Micro-scale study of the first stage of cake formation for the microfiltration of model particle and yeast suspensions : In-situ and real-time experimental approach

Alberto Jorge Valencia Navarro

To cite this version:

Alberto Jorge Valencia Navarro. Micro-scale study of the first stage of cake formation for the microfiltration of model particle and yeast suspensions : In-situ and real-time experimental approach. Fluid mechanics [physics.class-ph]. Institut National Polytechnique de Toulouse - INPT, 2020. English. NNT : 2020INPT0007 . tel-04165727

HAL Id: tel-04165727
https://theses.hal.science/tel-04165727

Submitted on 19 Jul 2023

THÈSE

En vue de l'obtention du

DOCTORAT DE L'UNIVERSITÉ DE TOULOUSE

Délivré par :
Institut National Polytechnique de Toulouse (Toulouse INP)

Discipline ou spécialité :
Dynamique des fluides

Présentée et soutenue par :
M. ALBERTO JORGE VALENCIA NAVARRO
le lundi 20 janvier 2020

Titre :

Micro-scale study of the first stage of cake formation for the microfiltration of model particle and yeast suspensions: In-situ and real-time experimental approach

---

Ecole doctorale :
Mécanique, Energétique, Génie civil, Procédés (MEGeP)

Unité de recherche :
Laboratoire d'Ingénierie des Systèmes Biologiques et des Procédés (LISBP)

Directeur(s) de Thèse :
M. PHILIPPE SCHMITZ
MME CHRISTINE LAFFORGUE-BALDAS

Rapporteurs :
M. JOSE TEIXEIRA, UNIVERSITE DE MINHO BRAGA
Mme JULIE MENDRET, UNIVERSITE DE MONTPELLIER

Membre(s) du jury :
Mme MARTINE MEIRELES, CNRS TOULOUSE, Président
M. JEFFREY MORRIS, CITY COLLEGE OF NEW YORK, Invité
Mme CHRISTINE LAFFORGUE-BALDAS, INSA TOULOUSE, Membre
Mme MELANIE JIMENEZ, UNIVERSITY OF GLASGOW, Membre
M. PHILIPPE SCHMITZ, INSA TOULOUSE, Membre
M. PIERRE JOSEPH, CNRS TOULOUSE, Invité

A mi familia:

A Mamá, su amor y dedicación… Sin lugar a dudas la persona más fuerte que conozco. A Papá, mi modelo a seguir... Espero infundir la seguridad que siento cuando estoy a su lado

A mí hermana, mi mejor amiga, quién me llena de orgullo y ternura

A mí hermano, mi mejor amigo, la persona en quien más confío

¡Qué sería de mí sin ellos!

Acknowledgments

I would like to express my gratitude to the people that during these last years had a positive influence academically, professionally and personally. Not only for their guidance and good advice that helped me to reach the “ups”, but also their support that smoothed the “downs”.

I had the nurturing opportunity of working under the guidance of three amazing supervisors; I would like to thank them for giving me the opportunity of working on this project. I am deeply grateful with Christine LAFFORGUE-BALDAS for her relentless encouragement, commitment and accurate advice. I have most appreciated the constructive attitude, scientific exchange and the unconditional support of Philippe SCHMITZ. In the same way, I highly value the willingness and availability of Jeff MORRIS, his scientific curiosity and kindness. All of them pushed me beyond and provided me with many tools for carrying this research to a satisfactory outcome.

I would like to thank the members of the jury for being part of the defense, the exhaustive review of the scientific content and their critical point of view. I appreciate their comments and suggestions as well as the perspectives they arose with their accurate queries.

A special thanks to Christophe ELLERO, Claude LE MEN and Pierre JOSEPH for their mayor support and intervention during the fabrication of the experimental set-up and campaign. The scientific exchanges, their creativity and advice were of most worth.

I would also like to thank my colleagues and friends. I cherish this experience and I always remember… the friends back home, Roberto, Vicky, Sebastian M. Let us keep creating memories… the friends found overseas, Fefe, Vivi, Kike, Jose, Jorge, Ramon, Naïla, Will and Isabella. You’ve made easier being far from home… the friends and colleagues from the lab, Alexandre, Francesco, Mohamed, the list is long, but a special word to Carlos “Pura vida”, our tea time was always refreshing, philosophically but also recreationally.

… My dearest friends Oscar, Sebastian R. and Santiago, words are not enough.

This work was done with the support of FERMAT Federation in the frame of the research grant program AAP 2015 from Idex UNITI “NEMESIS” conv-ANR-11Idex-0002-02.

Contents

Figure index

Acronyms

AFM: Atomic force microscopy

CGM: Cake growth monitoring module

CLSM: Confocal laser scanning microscopy

DOTM: Direct observation through membrane

LAAS: Laboratoire d’analyse et d’architecture des systèmes

LED: Light-emitting diode

MF: Microfiltration

NF: Nanofiltration

OD: Optical density

PCM: Particle concentration module

PS: Polystyrene

PVM: Particle velocimetry module

RO: Reverse osmosis

SAD: Sum of absolute differences

SDCLSM: Spinning disk confocal laser scanning microscopy

SEM: Scanning electron microscopy

UF: Ultrafiltration

YPD: Yeast peptone dextrose

Published article

A. Valencia, C. Le Men, C. Ellero, C. Lafforgue-Baldas, P. Schmitz, and J. F. Morris, “Direct observation at the microscale of particle deposition during the first stage of the microfiltration process,” J. Membr. Sci., vol. 599, p. 117823, Apr. 2020, doi: 10.1016/j.memsci.2020.117823

Abstract

Filtration is a widely used industrial process, which nature and purpose result in fouling and hence reduction of its efficiency with associated economic losses. This project aims to better understand the fouling through the microscale monitoring and analysis of the filtration process. For that, a new dead-end microfiltration apparatus is constructed and coupled with an imaging system to provide direct observation (DO) from the side. Particle deposition is characterized in-situ and in real time for four different suspensions: a cultivated yeast (*Saccharomyces Cerevisiae*) suspension and three suspensions of model particles in the same size range as the yeast cells (spherical particles, non-spherical particles and polydispersed particles in both size and shape). Model membranes are used to achieve fluid-particle separation, and different membrane geometries were created for studying the pore configuration effect on particle deposition and cake structure. Image processing is used to measure the observed cake height and to evaluate the concentration and particle velocity. This information is combined with the continuous pressure measurement and the qualitative description of the acquired images to provide a complete analysis of the microfiltration process. A mass balance is performed to estimate the porosity and the Kozeny coefficient (K_K) along with complementary analysis using Darcy equation and the Carman-Kozeny formula.

The system is validated for model conditions using the suspensions of spherical particles. The filtration performance for the different membrane geometries is similar. However, the initial cake structure is conditioned by the membrane geometry. This has an influence on pore blocking and further cake growth, which impacts on the pressure drop across the cake. Numerical simulations were used to investigate the initial behavior (pore blocking and hydraulic resistance) when the cake is forming and show good agreement with the experimental data.

Monodispersed particle suspensions show a very similar behavior in terms of porosity and permeability regardless of the different particle shapes. However, for a higher specific surface K_K coefficient decreases. For monodispersed particle suspensions, K_K behaves linearly with the porosity. In the case of the cake formed by the polydispersed particles, an exponential evolution for K_K coefficient is observed, which resembles more the yeast cake behavior. Additionally, when analyzing the porosity evolution of the four suspensions, the cake of

polydispersed particles shows an intermediate behavior between the monodispersed cases and the yeast cells. This confirms the influence of polydispersity and explains partly the yeast cake behavior, the high specific resistance and low permeability. Yeast cake behavior is explained by the combined effect of cell polydispersity and the compressibility of the cake. Yeast cakes were the only to exhibit a compressible behavior, which was confirmed by a volume expansion after transmembrane pressure was removed. The analysis of this expansion results in a porosity after relaxation close to the estimate for polydispersed particles ~0.26. It remains to explain the nature of this compressibility.

The experimental protocol is an accurate approach for the study of the filtration cake formation for different suspensions. The DO resolution was improved (~ 0.6 µm) allowing better imaging of particles in the microfiltration size range. Combining the velocity information with the pressure measurements makes it possible to characterize filtration processes where both pressure and flowrate are variables.

Résumé

La filtration est un procédé industriel dont l'efficacité est toujours réduite par le colmatage. Ce projet vise à mieux comprendre le colmatage par l'observation et l'analyse du processus de filtration à la micro-échelle. Pour cela, un dispositif original de microfiltration frontale a été conçu et réalisé. Il est couplé à un système d'imagerie qui fournit une observation directe (DO) latérale. Le dépôt de particules est ainsi caractérisé *in-situ* et en temps réel pour quatre suspensions : levure cultivée (*Saccharomyces cerevisiae*) et particules modèles dans la même gamme de taille et de forme (particules sphériques, particules non-sphériques et particules polydispersées). Des membranes modèles dont les pores sont des fentes parallèles régulièrement réparties sont utilisées pour la séparation fluide-particules. Différentes géométries ont été créées pour étudier l'effet de la taille et de l'espacement des pores sur la structure du gâteau. Avec le traitement d'images on mesure la hauteur du gâteau de particules observé et on estime le champ de concentration et la vitesse moyenne des particules avant leur dépôt. Des mesures de pression couplées à la description qualitative et quantitative des images permettent une analyse complète du processus de microfiltration. Un bilan de masse est ainsi effectué pour estimer la porosité puis le coefficient de Kozeny (K_K) en utilisant l'équation de Darcy et la formule de Carman-Kozeny.

Le système est validé sous conditions modèles avec la suspension de particules sphériques. Le processus de filtration pour les différentes géométries de membrane est similaire. Cependant, la structure initiale du gâteau de particules est conditionnée par la géométrie de la membrane. Cela a une influence sur le blocage des pores et la croissance du gâteau, et donc un impact sur la différence de pression et son évolution. Des simulations numériques ont été effectuées pour calculer l'écoulement dans une configuration géométrique périodique de référence comportant un blocage des pores optimal lorsque le gâteau se forme. Elles sont en bon accord avec les données expérimentales.

Les suspensions de particules monodispersées présentent un comportement similaire en termes de porosité et de perméabilité, indépendamment des différentes formes de particules. Cependant, pour une surface spécifique plus élevée, le coefficient K_K diminue. Pour les suspensions de particules monodispersées, K_K varie linéairement avec la porosité. Au contraire, le gâteau formé par les particules polydispersées présente une évolution exponentielle du

coefficient K_K,, plus proche du comportement des gâteaux de levure. Lors de l'analyse de l'évolution de la porosité des quatre types de suspension, le gâteau de particules polydispersées montre un comportement intermédiaire entre les cas des particules monodispersées et de la levure. Cela confirme l'influence de la polydispersité et explique partiellement le comportement du gâteau de levure, sa haute résistance spécifique et sa faible perméabilité.

Les caractéristiques du gâteau de levure s'expliquent par l'effet combiné de la polydispersité de la levure et de sa déformabilité. Le gâteau de levure est le seul à présenter un comportement compressible, confirmé par une expansion volumique remarquable du gâteau après la relaxation de la pression transmembranaire. L'analyse quantitatif de cette expansion fournit une porosité après relaxation proche de l'estimation faite pour les particules polydispersées ~0,26. Il reste donc à expliquer la nature de cette compressibilité.

Le protocole expérimental est une approche pertinente pour l'étude de la formation du gâteau de filtration pour différentes suspensions. La résolution de la DO a été améliorée (~ 0,6 µm) permettant une meilleure imagerie des particules dans la gamme de tailles de la microfiltration. La combinaison des mesures de vitesse et de pression permet de caractériser les processus de filtration où la pression et le débit varient simultanément.

Chapter I: Context and aims

I. Context and applications

Filtration is a widely used industrial process involving the transport and the separation of suspensions of matter with different nature, size and shape, as well as complex physical and chemical phenomena. Despite its wide usage, the nature and purpose of this process result in the fouling of the filter and hence the reduction of its efficiency with the associated economic losses. The multi-scale characteristics and the diverse nature of the suspensions mean that the problem involves a large number of variables. Moreover, the existence of different filter types and operating conditions adds even more complexity. This makes it difficult to perform an extensive characterization from which to develop comprehensive understanding of the fouling mechanisms involved in all situations. That is why the present work is dedicated to membrane microfiltration. Some of the applications of membrane filtration are presented below.

Water treatment

Worldwide, water demand is constantly under pressure due to the increasing population and the scarcity of sources. Being a limited resource, the issue of water is one of the modern society paradigms. Globally improving standards of living place demands on society's ability to provide sufficient clean water [1].

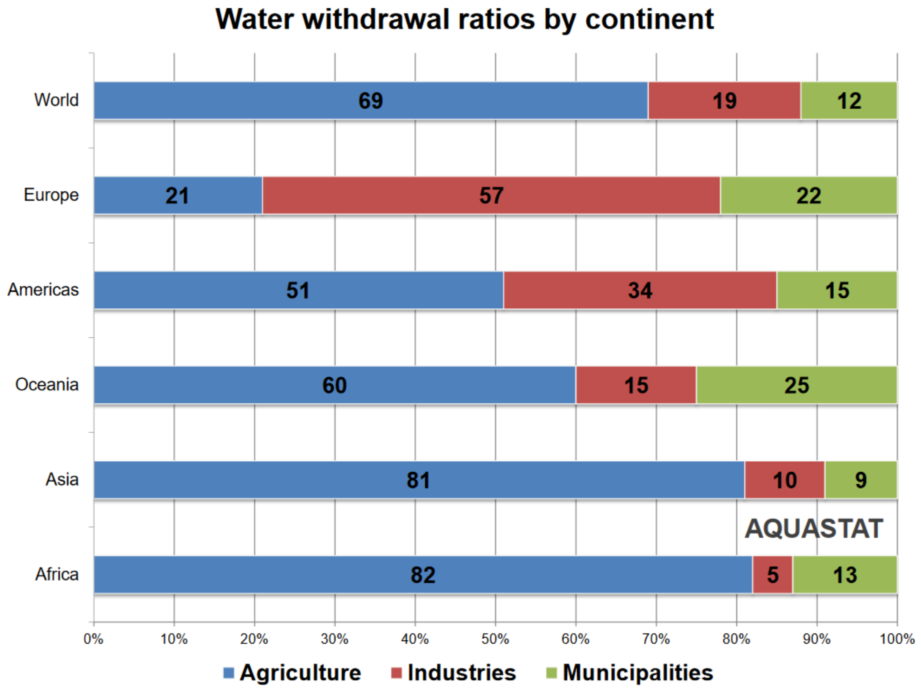

Figure 1. Water withdrawal ratios by continent and usage in 2015 [2]

In this field, membrane technologies have been valuable, as they are widely used for water purification at large scale, and, in fact, water treatment is one of the most important single application of membrane technology. Membrane usage for water treatment is of interest to both the industrial manufacturing sector and water management authorities. Human water consumption is divided in three main categories: domestic use, industry and agriculture. Figure 1 shows the ratios of water withdrawal by continent for each category of consumption.

Even if classical water treatment is firstly associated with chemical addition for coagulation, flocculation and disinfection, some microorganisms are resistant to chemical disinfectants. Membrane treatment appears as a better solution as it requires minimal addition of aggressive reagents and produces almost no by-products. For this reason, membrane processes are more and more used in many water treatment applications.

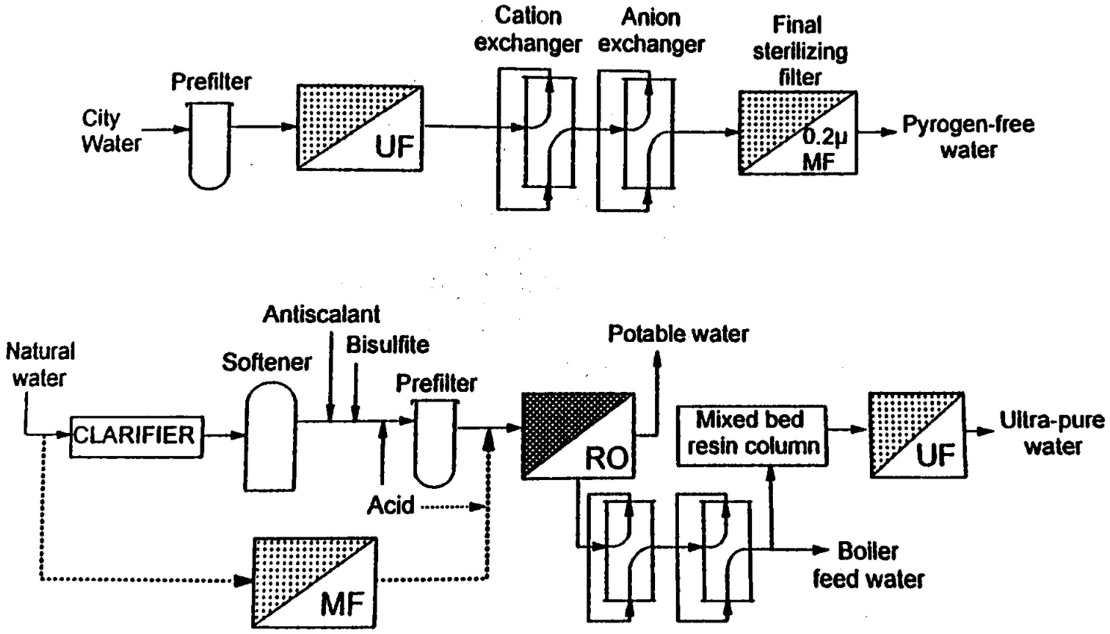

Figure 2. Hybrid membrane systems [3]

Normally membrane technologies work as a combined hybrid system. Hybrid membrane systems are conceptually viewed as a series of steps based on the membrane range of material rejection from RO to MF [4]. MF is used to remove turbidity and larger microorganisms; many studies have demonstrated MF rejection of microorganisms like yeast (*Saccharomyces cerevisiae*) and *E. coli* (Ben Hassan et al., 2014; Li et al., 2003; Zhang et al., 2010). UF allows inorganic compounds and large molecules retention such as heavy metals, suspended solids, organic compounds and virus. Both UF and MF are standard processes for oil-water separation. The NF and RO are able to reject colorant molecules and ions, so that it can be applied as the final step to produce potable water. Figure 2 depicts the concept of hybrid membrane systems for water treatment.

Regarding sewage (or sludge), the high demand on membrane treatment by the industry and its wastes provide the motivation for the development of this technology. Forward osmosis is an emerging technology for separation and treatment of a broad range of wastewaters, including produced water from oil and gas [8], [9]. Forward osmosis was proposed as a breakthrough in the desalination technologies due to its potential for reducing the power consumption associated with the high pressure gradients of RO.

Industry

Some industrial applications need a certain quality in the input water and environmental regulations demand a certain quality in the output as well. As an example, about 15% of the industrial input water used by United States manufacturing is ultrapure water produced by MF and UF techniques (see Figure 2).

Not all common contaminants in water can be removed by only one method, so that different water treatment processes are applied according to the type of disposed water and the residue that must be eliminated from the permeate. Table 1 presents a comparison between the different methods.

Table 1. Comparison of water purification techniques [3]

Purification process	Dissolved ionized solids	Dissolved ionized gasses	Dissolved organics	Particulates	Bacteria	Pyrogens
Distillation	E	P	G	E	E	E
Deionization	E	E	P	P	P	P
Reverse osmosis	G	P	G	E	E	E
Carbon adsorption	P	P*	G**	P	P	P
Filtration	P	P	P	E	E	P
Ultrafiltration	P	P	G++	E	E	E
UV oxidation	P	P	G++	P	Gs	P

E: excellent G: good P: poor

* Activated carbon will remove chlorine by adsorption

** Special grades of carbon

\+ Depends on molecular weight of organics

++ Some types will remove organics

s Selected bactericidal capabilities, depending on intensity, contact time and flowrate

Some of the industrial applications using filtration processes in order to capture the desired product or for water treatment are:

- Dairy industry: in the food industry, dairy is the most important field of application of membrane technology. The lactose industry in particular has many products involving MF and UF as shown in Figure 3, but also NF and RO processes can be applied to obtain different lactose by-products. One example is the patented 3-step membrane filtration for production of lactose-free dairy products [10]. Vasileva et al. also use hybrid membrane system for the hydrolysis of whey lactose, which is used in the products such as dairy, confectionery, baking and soft drinks [11].

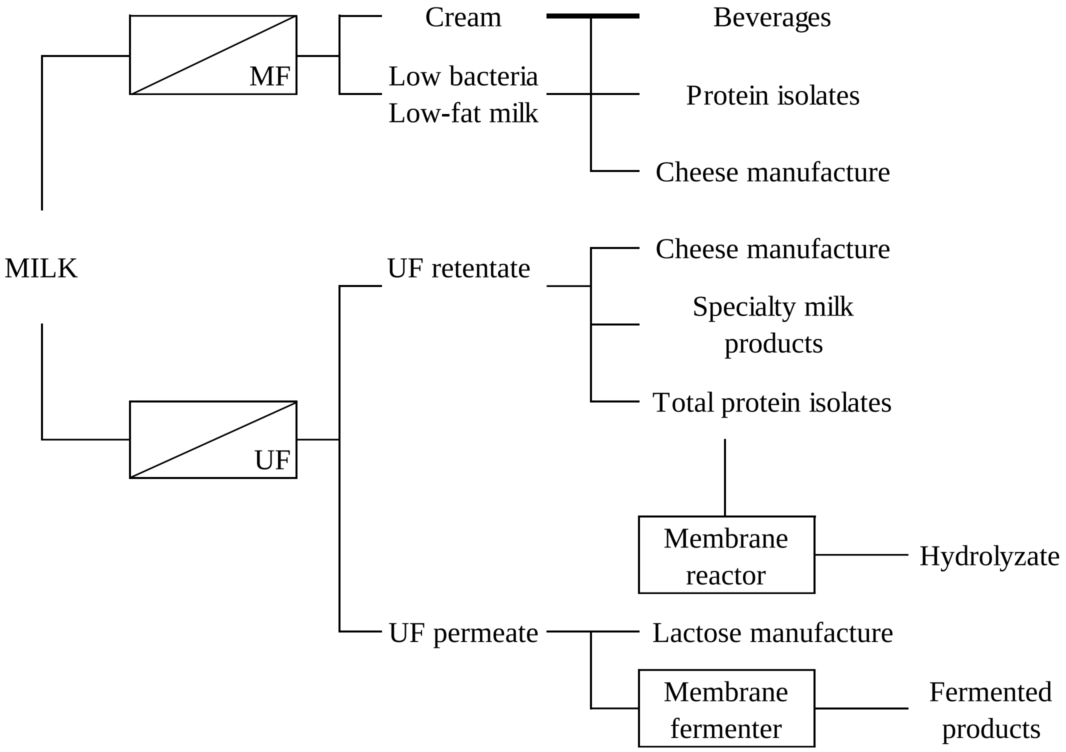

Figure 3. Some milk industry filtration processes and the resulting products [3]

- Industrial waste treatment: interest in green technologies and integrated processes has increased efforts and investment in development of new techniques and protocols for water reuse and waste reduction. Besides technological development and economical profit, political aspects play an important role as there are new legislations regarding the quality of waste effluents to the environment [1]. There are many examples of separation processes that are already in place. Reverse osmosis and nanofiltration membranes were investigated for treatment of wastewater that is food industry effluent in order to reduce the chemical oxygen demand [12]. Also, during ethanol production yeast fermentation of sugars produce 8-12% of ethanol from the total volume, and the remaining products are waste. This waste has 5% of solid content, formed by dead yeast cells, cell debris and traces of residual sugars. By using MF the resulting waste, or "stillage", can be clarified [3] [13]. Combination of other techniques with filtration has also been practiced, for example in the treatment of leather industrial effluents by filtration and coagulation processes [14].

Other examples among many where membrane filtration processes are used are the ink industry, latex emulsions production, pulp and paper industry, sugar refining, vegetable oils, and protein processing [3].

Biotechnology pharmaceutical applications

“Pharmaceutical industry can be viewed as a complex system of processes, operations, and organizations involved in the discovery, development, and manufacturing of drugs” [15]. Biotechnology applications include a wide range of biological processes to obtain different product inputs or the final product itself. The pharmaceutical and biotechnology industries having some mutual objectives, and thus are overlapping in some sectors of development and sharing in certain expertise and techniques. Separation techniques are widely present in both industries and play a role in recovery of molecular and particulate components, protein concentration, suspension clarification, sterilization, and more. Ultrafiltration and microfiltration are widely used to recover macromolecules and retain suspended colloids, particles and microorganisms. One of the main applications of membrane technology in this field is the separation and harvesting of enzymes and microorganisms. An example is the sterile filtration for bacterial removal at the initial stage of the production line of many products and laboratory procedures. Sterile filtration is normally performed in a dead-end configuration [16]. Another application is the membrane bioreactor technology, where membranes are used for numerous purposes: enzymatic and microbial conversion processes [17], tissue culture, for the production of aminoacids, antibiotics, anti-inflammatories, anticancer drugs, vitamins, optically pure enantiomers and isomers [18], enrichment of nitrogen or oxygen, and filtration of exhaust air [3].

Adsorptive membranes have also been used as an alternative to resin-based chromatography columns, because shorter diffusion times are obtained. This could allow maintaining high efficiencies at high flow-rates using large biomolecules with small diffusivities (Charcosset, 2006).

II. Aims

As seen before, real filtration applications involve the separation by membrane processes of a large spectrum of materials in the same feedstock, which are different in size, shape and nature. From now, solid matter will be referred as particles. These differences bring a wide variety of interactions between particles like enhanced diffusion due to small sized particles, attraction or repulsion depending on the surface charge, deformation as function of the mechanical properties, etc. The flow and operating conditions may result in enhanced mixing or focalization due to particle migration, the fouling layer compaction, relaxation and reorganization caused by changes in pressure. Finally, the carrying fluid properties like the pH have an important effect on particle interactions. All these variables define the filtration performance, its efficiency and limitations.

The present work aims to better understand the membrane fouling mechanism through the monitoring and analysis at the micro-scale of particle accumulation at the membrane surface using model suspensions of solid particles and cultivated yeast (*Saccharomyces cerevisiae*).

An accelerated development made of yeast technology a highly productive and economic industry [19]. Being metabolically diverse, yeasts are widely used in many industrial processes. Different yeast strains are used for the production of ethanol, vitamins, organic acids, carotenoids, and enzymes. Yeasts are also used to catabolize benzene compounds and may prove useful for cleaning up spills of industrial chemicals as well as for biosynthesizing new compounds. Some of the developments in the pharmaceutical industry are also based on the yeast technology for the synthesis of active proteins and other compounds [20]. Many of these fields involve the membrane microfiltration as a main or a secondary process, which drives the attention to the study of the yeast filtration performance. Yeast is a microorganism whose properties like cell metabolism, mechanical response and size and shape polydispersity have been studied. However, the characteristics of yeast filtration cakes rises some question with regards the high cake hydraulic resistance and the consequent permeability and efficiency loss. These effects can be present in many real filtration applications. The interest of framing the project into a realistic filtration scenario led to focus the present study on the analysis of the microfiltration of cultivated yeast suspensions.

The choice of three model particle suspensions answer the interest of characterizing the system by a simpler scenario that allows to establish a valid protocol and the easy comparison with simulations. In addition, each model suspension assesses some of yeast characteristics: the yeast shape related to the budding behavior and the polydispersity. Model polymer particles are produced by emulsion, dispersion, or suspension polymerizations. [21]–[23].

Focusing in a more dynamic approach this project constitute the follow-up of the work achieved by Beaufort [24] and Ben Hassan [25]. In this work, an *in-situ* direct observation of the filtration cake growth is done using confocal laser scanning microscopy (CLSM). This method allowed to study the effect of the membrane geometry and the suspension nature and size disparity on the cake morphology. Even though the confocal microscopy is a powerful tool that allows the acquisition of 3D data, it falls short regarding acquisition rate necessary to analyze the filtration from a dynamic continuous approach. This is caused by the time required to scan an entire volume with high resolution. That is why the previous work analyzed the filtration cake formed layer by layer and not in real-time. In addition the thickness of the studied deposits was limited by the laser penetration, which only allows the examination of relatively thin fouling layer < 35 µm thickness.

III. Technical scope

The design and creation of a new microfiltration set-up is done so that particle deposition could be investigated *in-situ* and continuously. The configuration provides direct observation from the side of a wide field of view, thus permitting characterization of the vertical concentration profile, the cake structure and the rheology transition between the suspension behavior and the growing cake zone on the membrane surface.

This new set-up must satisfy certain specifications to achieve the desired coupling to optical devices and techniques, with optical resolution for model particles allowing continuous examination and data acquisition of the filtration phenomenon. The assistance and facilities of LAAS (*Laboratoire d'analyse d'architecture des systèmes*) are essential to determine the feasibility and guide design of the device; a critical expertise brought by these collaborators is their knowledge of techniques for creating micro-scale architectures.

The idea for the device is a dead end microfiltration cell consisting of a channel with a filter to achieve the separation. The device must be easily attached to a pump, the tubing, the suspension reservoirs and allows the observation. For that, a mechanical support must be designed to act as the interface between the microfiltration cell and the tubing allowing the connection to the pump and a manometer to register pressure variations. Taking these demands into account, the following considerations are studied:

- Filtering unit: the filtering unit is placed in the middle of the dead end microfiltration channel. The structure consists of a series of parallel walls forming an arrangement of slots (analogue to pores for common membranes). The slots width is given by the distance between the walls and must be smaller than the particle/cells minimum size. The filtering structure must guarantee that all particles and cells are rejected by size selectivity, i.e. only the sieving mechanism controls the system fouling by partial blocking and cake filtration (see Table 2). The length of the channel upstream and downstream of the filtering structure must be sufficiently long to insure that the flow reaches a stable flow regime, i.e. a fully developed flow can be assumed.

- Geometric constraints: the geometry of the experiment must be set at different scales. First of these is the macro-scale related to the assembly of the whole set-up. The microfiltration cell support is the key component to guarantee the flow conditions on the microfiltration cell and the observation of the filtration phenomenon. It must hold the microfiltration cell at the right position to achieve both the sealed connection to the flow system and the configuration of the microscope observation.

The meso-scale is associated with the channel dimensions, which define the main flow parameters, e.g. flow velocity, and the important contribution of the channel friction to the total pressure drop of the system. The aim is to study the filtration under laminar conditions and more specifically Stokes flow for $Re < 1$. For this regime under dilute conditions, particles follow closely the streamlines with negligible particle-fluid relative velocities. Hence, the flow velocity must be in agreement with optical set-up acquisition

Finally, the micro-scale is associated with the filtering structure. Varying the slots width and the distance between them (wall thickness); it is possible to study different membrane permeabilities and the effect of membrane geometry on the cake structure.

- Optical features: the main optical parameters are the working distance of the microscope objective as well as the optical equipment performance in terms of acquisition rate, memory, observable field, and image resolution. The principal feature regarding the camera choice is the pixel size of the acquired image, i.e. the resolution. The resolution should allow observing clearly both model particles and yeast cells. The model particle diameter is 8.4 µm with standard deviation of 0.9 µm and the yeast cells size ranges from 2-10 µm. A pixel size of 1 µm or less is targeted, so that, even the smallest yeast cells are resolved. Besides the resolution, the observed field must capture the entire membrane as well as a representative domain above the filter to characterize the cake and the suspension. In this way, it is possible to study the behavior of the suspension in the different concentration zones and the whole surface of the filtering unit, in order to estimate the feedstream concentration and to determine cake homogeneity. For that, the optical set-up should be able to observe a 1 mm by 1 mm field in *x* and *y* corresponding to the channel width and the domain above the membrane. Another constraint regarding optics is the camera dimensions and the coupling with the whole set up.

- Feasibility: the small dimensions, particularly at the filtering structure, present a challenge. The most suitable technique for creating the filtering module is photolithography followed by plasma etching; nonetheless, the plasma etching technique capability is limited when working at very small sizes such as those of the membrane microchannels. Having a channel length of 1 mm and the minimum slot width of 2µm, the technique can provide depths around 25-30 µm. The limited channel depth could lead to clogging issues for the model particles and yeast cells of approximatively 8.4 and 6.0 µm (mean for yeast cells) diameter, respectively. The studies by van de Laar et al. [26] and Dressaire et al. [27] conclude that aggregation could lead to channel clogging before reaching the filtering unit. In addition, an intermittent bridging phenomenon is common. An aggregation of 2-10 particles could lead to the formation of particle arches; then if one dimension of the channel is equal or less than 10 times the particles diameter, which is the case, bridging is likely to happen. However, it is important for this study to have a limited depth to allow focusing throughout the depth; this allows observation of all the particles in the depth dimension. It is also important to guarantee that particles are not aggregated in the suspension.

Previous tests were performed during the internship of Alice Gornall [28] in order to gauge the effect of salt concentrations on settling rates and the possibility of aggregation of yeast particles. To minimize later downstream processing, salt concentrations were kept below 0.5%, the maximum concentration of fresh water. There is very little effect on settling rates. It was therefore concluded that such low salt concentrations have little to no influence over particle aggregation and so the remainder of experiments were carried out in a 0g/L salt solution.

The outline of this document is organized as follows:

Chapter II presents and extended bibliographie with a general overview of the filtration principle for then focus on the membrane microfiltration, the fouling mechanisms and the fundamental relationships considered for the further analysis. Different fouling characterization methods are reviewed.

Chapter III describes the experimental set up and protocol as well as the model conditions for the numerical simulations.

Chapter IV is focused on the validation of the experimental set-up for the filtration of a suspension of monodispersed spherical particles. The filtration performance for this suspension is analyzed and the results are used for further comparison.

Finally, Chapter V evidences yeast cake behavior and offers explanation to its morphological properties and filtration performance by evaluating yeast cells features, like size distribution and shape, using model particle suspensions.

Chapter II: Bibliographic review

I. Filtration

Transport and separation processes are present in several branches of industrial development. Among them, filtration is widely used and has a strong presence in the biotechnology and pharmaceutical industry [29], the drinking water and waste water treatment sectors [30], [31] and the food and beverage industry [32]. Giving its presence, it is natural to seek new ways to enhance the filtration performance and effective solutions to filtration and separation problems [33].

The main hindering features related to filtration system failure are the fouling and clogging phenomena. Mechanisms such as sieving, bridging and particle aggregation [27] result in permeate flux decline and lower efficiency of the process.

I.1. Principle

Filtration is a selective process that allows separation of two or more constituents from a fluid stream. This separation is often based on the size but also may rely on different properties including diffusion, ionic charge, density, temperature and surface activity as depicted in Figure 4. The separation is achieved using a filter through which the fluid passes and leaves behind certain components.

The filter is the selective barrier that allows retention of specific components from the fluid feed stream. The retained material is known as retentate and the passing material is called permeate. The filter represents an obstacle to the flow, thus it has an associated hydraulic resistance and a consequent energy loss related to a pressure drop. To establish the flow through the filter either a pressure gradient or a chemical potential gradient is needed.

I.2. Classification

There are multiple criteria to classify the separation processes, some of them are: the separation range of usage, the filtration operating mode, the flow condition and the filtrate retention zone.

Separation range of usage

Figure 4 shows different processes classified by the range of usage and the dominant separation factor. Filtration process can be applied in a wide range of particle sizes from reverse osmosis (RO) being able to retain components in the range of simple ions of sub-nanometer scale to common filtration of coarse particles.

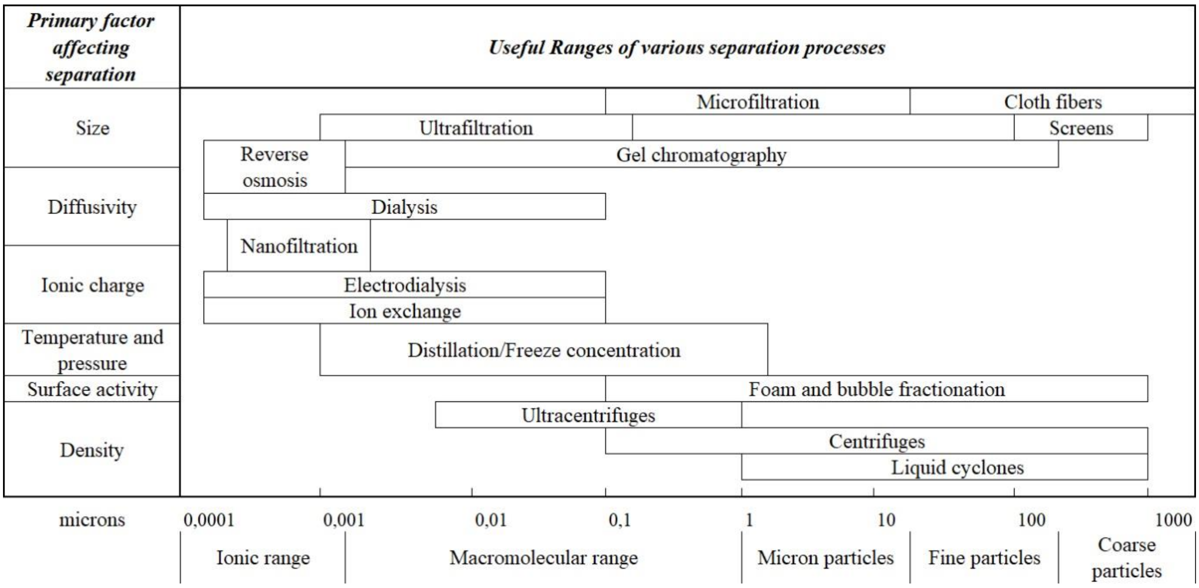

Figure 4. Useful ranges of various separation process [3]

The present study is focused on membrane separation by sieving i.e, surface size rejection. Concerning particle size, the filtration processes retaining particles of size equal or inferior to the microfiltration range are also known as membrane separation processes. For these cases the main role of the membrane is to act as the selective barrier, the filter. Membrane filtration extends its applications further in order to include the separation of dissolved solutes in liquid streams and also separation of gas mixtures [3]. RO and nanofiltration (NF) are used to separate particles in the ionic range from 10^{-4} to 10^{-3} µm. Both are widely used for single-stage seawater or brackish water desalination [34] and it is possible to remove pollutants such as the hydrolyzed reactive dyes, mineral salts and organic compounds [35]–[37]. RO and NF have a high rejection performance but also require very high transmembrane pressures (and thus high absolute) which results in important capital and operational costs. In the case of ultrafiltration (UF), separation units are able to reject particles from 10^{-3} to 0.1 µm. UF membranes remove inorganic contaminants such as heavy metals along with suspended solids and organic compounds from a bulk suspension [38]. In the case of microfiltration (MF), particles within the range of 0.1 to 10 µm are retained. Microorganisms like *Saccharomyces Cerevisiae* and *E. Coli*, colloids and smoke particle from suspensions and gases are some of the examples of the retained material. The advantage of both MF and UF ultrafiltration is the low driving force required. However, problems associated with fouling limit their application. Both are usually used as hybrid or integrated membrane processes, which means that they are integrated with other membrane processes, either with or without conventional unit operations to increase performance depending on the type of feed and product quality required; this is the case for desalination and water purification by reverse osmosis (RO) [4].

Filtration operating mode

In terms of flow direction, the process is mainly classified in two operating modes: frontal (also known as dead end) and crossflow filtration. In the case of dead end filtration, the main flow direction is perpendicular to the filter. In this configuration, all retentate accumulates on the filter surface with no opportunity for flux-induced cleaning. The advantages of dead-end filtration are the high percentage of rejection and product recovery as well as simplicity of operation. The main drawbacks remain the flux and capacity limitations. The flux is largely determined by permeability of the filter, which is related to the pore diameter, pore distribution [39] and membrane surface properties [40]. The thickness of the porous medium as well as tortuosity of filter channels are important factors, especially for depth filtration. Besides the characteristics of the filter, the feed suspension properties will generally affect dead-end filtration performance: the viscosity and density of the feed suspension as well as the nature of the retained materials may result in lower fluxes due to fouling layers with high hydraulic resistances [41]–[43]. All these factors can accentuate or attenuate the fouling phenomena. The observed effects depend on the imposed flow conditions: fouling results in the transmembrane pressure rising for constant flux conditions, whereas flowrate reduction is observed when the pressure is constant. The growth of the fouling layer may result in system failure due to unacceptably high pressures or low flowrates) which limits the filtration capacity.

In crossflow or tangential filtration, the primary flow direction is tangential to the filter. Crossflow filtration tends to improve the hydrodynamic flow conditions, with shear stresses as an antifouling factor. In this configuration it is possible to attenuate the retentate accumulation at the filter as function of the flow parameters [44]. This can enhance the filtration efficiency since the fouling phenomenon resulting from the cake formation results in high operational costs. It is because of this feature that the potential for improvement based on the control of the hydrodynamic conditions has been the motivation of many studies. These studies are focused on the influence of different membrane geometries and operating modes to induce higher levels of shear rate associated with higher turbulence to hinder cake formation [45]–[47].

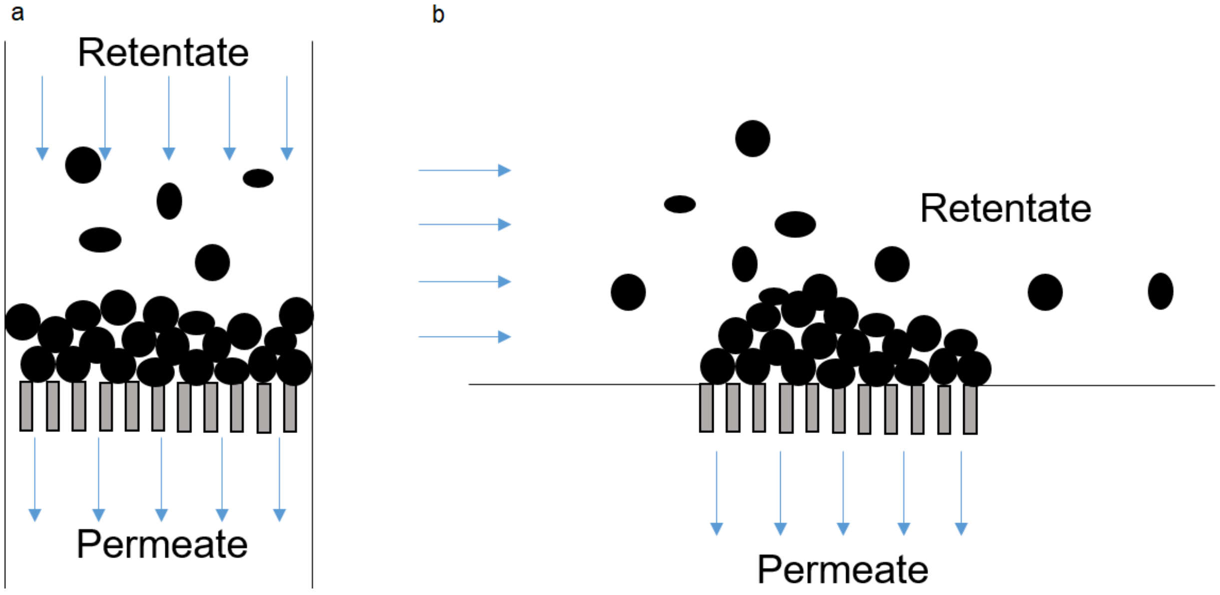

Figure 5 Representation of: a) Dead end and b) Crossflow filtration

Flow condition

Filtration studies typically seek to determine such flow parameters as the pressure-velocity relation, or the hydraulic resistance of the deposit, among others. These parameters are obtained through experiments that are conceived according to the objectives under different flow conditions:

- Constant pressure
- Constant flux

At **constant pressure,** the flow rate can be obtained according to Darcy's equation, i.e.

$$J = \frac{1}{A}\frac{dV}{dt} = \frac{\Delta P}{\mu(R_m + R_c)}$$

Eq. 1

where R_m (m^{-1}) is the membrane hydraulic resistance, R_c (m^{-1}) the cake hydraulic resistance, A (m^2) the filter surface and μ (Pa.s) the dynamic viscosity. The quantity R_c increases, typically linearly or faster, with the deposited solid mass per filter surface unit m (kg/m^2). Then R_c is expressed as the product of an average specific cake resistance and m:

$$R_c = \alpha m = \frac{\alpha C V}{A}$$

Eq. 2

Here, C represents the effective bulk concentration (g/m³), α (m/kg) is the average specific resistance and V (m³) is the cumulative permeate volume. Through substitution of Eq. 2 in Eq. 1 and integration, one finds

$$\left[\frac{\mu\alpha C}{\Delta P A^2}\right] V + \frac{\mu R_m}{\Delta P A} = \frac{t}{V}$$

Eq. 3

The slope $\mu\alpha C/2\Delta P A^2$ is known as the Modified Fouling Index (MFI). Previous reported experimental data for filtration under constant pressure shows approximately linear behavior of t/V vs. V over a broad range of varying flux J for small foulant concentration [48].

The approach described by Eq. 3 allows determination of a mean specific fouling resistance α if all the other measurable quantities are known. Nevertheless, it is often not possible to characterize accurately the temporal evolution of α. For this reason, another approach is formulated using Eq. 1 and Eq. 2 and the definition of membrane permeate flux $J_0 = \Delta P/\mu R_m$ at $t = 0$. Upon substitution and rearranging one obtains:

$$\alpha_i = \left(\frac{\Delta P A}{\mu C J_0}\right)\left(\frac{J_0 - J_i}{J_i}\right)\frac{1}{V_i}$$

Eq. 4

Substituting the instantaneous values of cumulative permeate volume V and permeate flux J one obtains the specific resistance α throughout the entire filtration process.

For **constant flux** condition the total pressure drop in the filter-cake system is

$$\Delta P_t = \Delta P_m + \Delta P_c$$

Eq. 5

with ΔP_m and ΔP_c being, respectively, the pressure drops across the membrane and cake only. For a constant flowrate J, the cake resistance R_c, knowing the concentration C and recording ΔP as a function of time, one can directly compute the evolution of α throughout the filtration run as follows:

$$\alpha_i = \frac{\Delta P_{c,i}}{J\mu m}$$

Eq. 6

Filtrate retention zone

There are two types of filtration regarding the zone of retention, surface and depth filtration. **Surface filtration** works by direct interception. Particles whose size is bigger than the pores are stopped at the upstream surface of the filter. **Depth filtration** employs a medium with a significant thickness providing filtering in its depth. For this type of filtration, both of the phenomena of direct interception and retention occur; nonetheless, retention in depth remains the principal filtration mechanism. This kind of filters are density graded so that larger particles tend to be trapped at the surface and finer particles are trapped within the depth of the filter [33].

When filtration takes place there are two driving phenomenon:

- Retention of smaller passing particles within the pores by adsorptive forces and hence pore size reduction.
- A fouling cake formation that acts like a filter itself and grows progressively during the filtration process.

I.3. Filtration media

There are two main kinds of filters depending on the deposition area: the **surface filtration media** and **depth-type media** (Figure 6**)**.

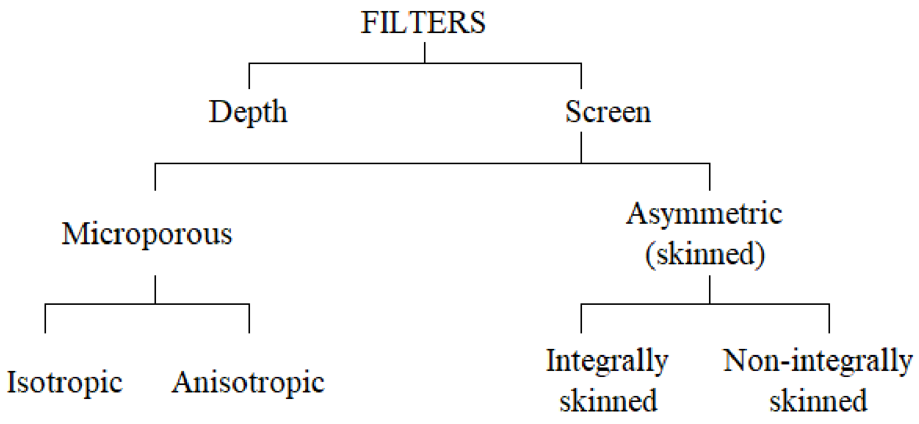

Figure 6. Filter classification [3].

Depth type media are often density-graded, with density increasing from the upstream to the downstream. This graded structure increases the probability of retaining fine particles on their passage and is constituted by a matrix of randomly oriented fibers forming a tortuous assembly of flow channels [3]. These filters are categorized as fibrous, porous or cake-like media.

Surface filtration is due mainly to sieving; it means particles whose diameter is greater than the characteristic pore size at the surface on which flow is incident are retained on the filter surface. However, particles whose size is smaller than the pore can clog the system by different mechanisms as bridging and aggregation [26], [27], [49]. Surface filtration media are basically of three types:

- Screen type filter
- Edge type filters
- Stacked disk filters

The present study is focused on membrane filtration. Here below, a more detailed characterization of membranes is done.

II. Membranes

Membranes are classified as surface filtration media of screen type, they are currently used widely in engineering applications for the filtration of micron and sub-micron size particles from liquids, and gases.

There are different kinds of membranes, which are designed to be resistant to both feed and cleaning fluids; membranes should be mechanically and thermally stable, while having a high permeability and selectivity. The design of the membrane unit responds to the specific requirements of the target process, so that a compromise of the previous noted characteristics as well as the cost are taken into account to guarantee a stable and efficient operation.

Membranes vary in material composition, pore size, structure and relative isotropy. Regarding the material composition, they are made of synthetic polymers (polypropylene, perfluoropolymers, elastomers polyamides and polysulphones), modified natural products (cellulose based) and miscellaneous other materials (inorganic, carbon, ceramic, metals dynamic and liquid membranes). Membranes whose physical and chemical properties are the same among the whole structure are known as isotropic membranes, otherwise they are known as anisotropic membranes [33].

Recent studies have highlighted the advantages of dynamic membranes over the conventional microfiltration and ultrafiltration membranes by exploiting the fouling cake as a means of achieving solid-liquid separation [50]. An improvement in membrane manufacture yielded the development of microsieves, which are extremely fine screen filters (~1 µm) with identical pores in regular distributions and high permeabilities [25].

II.1. Membrane fouling and cake formation

Membrane fouling is the primary limiting issue in membrane filtration technology, and for this reason filtration optimization is intrinsically related to understanding of particle deposition at the membrane. Particle deposition is not only the first step, but also one of the major reasons for filtrate flux decline with time under flow and the associated membrane fouling [51]. Fouling causes a permeability decay, high energy consumption and a need for frequent cleaning or replacement [52].

Almost all feed components will foul the membrane to an extent that depends on the physicochemical nature of the membrane and the solute, and thus how they interact with each other [3]. There exist some fouling features that are inherent to feed stream flux:

- Changes in membrane properties: result of physical or chemical deterioration of the membrane. Depending on the pressure, the membrane can undergo a slow deformation, i.e. “creep” or compaction that is permanent. Chemical deterioration is related to pH, temperature and other agents that attack the membrane material.
- Change in feed properties: variations in the feed stream viscosity and diffusivity could be expected as the solid concentration varies within the cake layer, the transition and polarization zones or the suspension.

An extensive work on membrane fouling has been done. Fouling phenomena are the main cause of filtration efficiency loss and they are related to system clogging. Different clogging mechanisms related to suspended particles have been identified and models developed in order to predict flux decay and pressure rise.

Sieving is one of these mechanisms and is due to the surface accumulation of particles whose sizes are larger than the pores. This particle accumulation creates a porous medium of increasing thickness that continuously adds resistance to the flow [53]. However, this mechanism cannot be simplified into a simple geometrical problem. While for rigid particles it is a size exclusion phenomenon, the different nature of the feed suspension adds complexity for the filtration of anisotropic and soft deformable particles, which is the more common case in industrial applications.

Particle bridging is another fouling mechanism. The combination of geometrical and hydrodynamic effects increase the particle volume fraction allowing the particles to form arches at constrictions like the pores. Converging flow and high particle concentration generates bridge-like structures composed of a few particles, typically between 2 and 10. Bridging happens most commonly for dense suspensions close to the jamming value, but can also occurs for low concentrations [27], [49].

The last mechanism is associated with particle aggregation. Short-range attractive van der Waals forces result in the formation of colloidal particle clusters in the bulk suspension or liquid interfaces when particles are close enough, and the same forces may cause adhesion to the pore boundaries. The work by van de Laar [26] used transient state theory to describe a balance of the driving forces resulting from advection and diffusion to rationalize how particles interact with each other and accumulate on the channel walls. This mechanism is associated with internal fouling as particles with smaller diameter than the pores (constrictions) are able to flow into, and partially through, the pores and start aggregating on the walls.

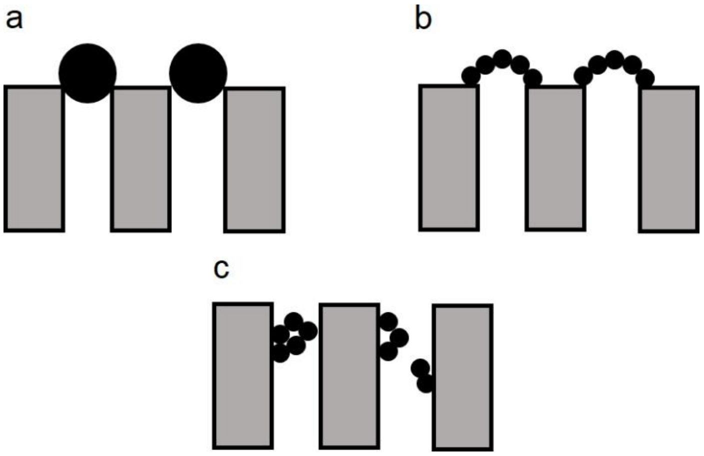

Figure 7. Different particle clogging mechanisms a) Sieving, b) Bridging and c) Aggregation

Figure 7 illustrates the previous clogging mechanisms. The extension of the membrane fouling associated with each fouling mechanism depends on different filtration parameter; however, the common denominator is the contribution to the formation of a fouling layer, the cake. Many approaches addressing cake structure and the influence of particle interactions have been applied in order to better understand these mechanism involved in the filtration phenomenon [54], [55]. The filtration cake structure has been characterized through different *in-situ* and *ex-situ* observation techniques. The typical cake structures exhibit a porosity and concentration gradient. The study by Tarabara et al. [56] investigated the structure of membrane cakes for conditions of variable particle size and solution ionic strength. In all cases, the observation reveled a stratified structure where very dense regions of the cakes were observed adjacent to the membrane. These dense regions rapidly transitioned to a more porous layer towards the cake-suspension interface. Figure 8 shows the previous described cake structure. Also the 2007 study by Le-Clech et al. [57] used direct observation from the side to study fouling formation on a hollow fiber membrane. This configuration revealed a similar concentration gradient during filtration deposition of an alginate/bentonite suspension. In both studies the optical resolution of the acquired images did not allow examination at the particle level.

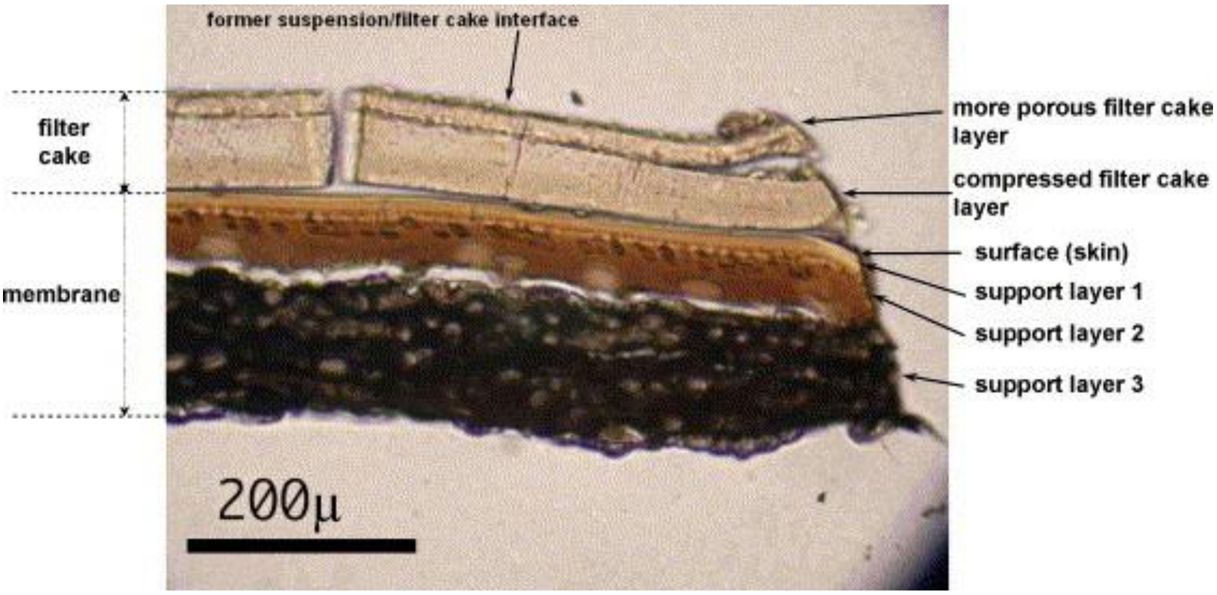

Figure 8. Filter cake cross-section [56]

To reach universally applicable rules with respect to membrane fouling is a difficult task. This is because the complete phenomenon involves multiple mechanisms and several factors that are related to each particular case: among these, there are the feed stream zeta potential, concentration, inter-particle interactions and the solutes nature (i.e. macromolecular compounds, proteins, polysaccharides…); the membrane chemical constitution, pore size and distribution as well as flow velocity, temperature and hydrodynamic conditions in general. There are three main categories with regards of the fouling factors: the membrane material properties, the solute properties and the filtration operating parameters.

Membrane, suspended particles and solute properties

- **Hydrophilicity**: ideal membranes should be hydrophilic. Hydrophobic behavior leads to feedstream component adsorption and consequent fouling [3]. The wettability and water permeability of a membrane is evaluated by water contact angle and water flux tests [40].

- **Surface topography**: membrane surface topography describes the roughness of the membrane. Smoother surfaces generally yield higher flux values [58]. The irregular structure of rough membranes increases the retention as the surface depressions constitute preferential locations for deposition.

- **Charge**: repulsion between the particles and the membrane makes convenient the use of a charged membrane. One example is the use of a positively charged membrane for cathodic electrocoating paint; a positively charged nanofiltration membrane for use in organic solvents induces higher rejection to positive organic molecules due to charge repulsion [59].

- **Pore size:** the pore size of the membrane with respect to the particles size has an important influence on the flux. Numerous examples in the literature show that larger pore membranes will initially have higher flux than smaller-pore membranes but will eventually have lower flux. This is explained by the different fouling mechanisms. Understanding relatively large pores as pores whose size is approximately that of the particles, it is observed that particles preferentially block the pores leading to a rapid drop in flux. On the other hand if the pores are smaller than the particles to be separated then particles will not get caught within the pores but will roll off the surface under the induced shear forces [3].

- **Surface modification**: membrane surface modification can lead to altered surface properties that can enhance the filtration process. A catechol-based biomimetic strategy combined with surface mineralization to enhance hydrophilicity and anti-fouling properties of polytetrafluoroethylene (PTFE) flat membranes is an example of surface modification. Using this low-cost and simple modification method, the PTFE flat membrane was endowed with excellent hydrophilicity, high water permeation flux and superior anti-fouling [40].

- **Feedstream composition**: fouling implies interaction between the membrane and the different feedstream components, so the nature of these components is a major concern.

- Proteins are complex foulants because of their multiplicity of functional groups, the charge density within these molecules, the degrees of hydrophobicity and the interactions with other feedstream components. Various operating parameters influence these properties adding even more complexity to the fouling phenomenon.
- Salts as function of different operating parameters can highly reduce its solubility, hence inducing precipitation so that membrane surface accumulation is strongly enhanced, with a consequent lowering of the flux. Also, salt can change the ionic environment, altering surface potentials or charge interactions and consequently the solute-solute and solute-membrane interactions.
- Lipids, fats and oils can reduce the flux depending on the membrane hydrophobicity. The same issues are involved with antifoams that can increase membrane fouling when a membrane is hydrophobic [3].

Operating parameters

- **Temperature**: normally at higher temperatures flux increase as result of a lower viscosity and higher diffusivity from the side of the fluid. On the other hand, the interaction between fluid and particles or molecules may reduce the flux and increase the fouling. In the case of proteins, denaturation and other heat damage will result in flux reduction [3].

- **Flow rate and turbulence**: High shear rates at the membrane surface tend to shear off deposited materials and thus reduce the hydraulic resistance of the fouling layer. However depending on particles size and size heterogeneity high shear could lead to stratification of small particles at the membrane surface. Shear affects large particles than small ones, when an induced lateral lift gives rise to this phenomenon [3]. This lateral lift has been shown to be related to shear-induced normal stresses (SIM) introduced by Nott and Brady in 1994 [60] and modified later by Morris and Boulay in 1999 [61]. The impact of SIM on membrane filtration has been reviewed by Vollebregt et al. [62]. In terms of sizes, smaller particles (< 1µm) are more affected by Brownian motions and turbulence recirculation, contrary to bigger particles whose motion in these cases is driven by shear-induced normal stresses.

- **Pressure**: initially the pressure is directly proportional to the flux but it also affects the cake layer density. An increase in pressure means an increase of flux at the first stages, but with compaction of an increasingly thick cake layer the flux is severely reduced [3].

II.2. Membrane fouling models

Fouling models have been formulated through the mathematical expression of the experimentally characterized fouling mechanisms. Authors refer to four different mechanisms: complete pore blocking, intermediate pore blocking, cake filtration and pore constriction. These are the result of only one or the combination of the previously described particle-particle and particle-membrane interactions when clogging takes place (sieving, bridging and particle aggregation). Hermans and Breede [63] proposed different expressions for the four mechanisms. These expressions were grouped under a common differential equation when the filtration is done under constant pressure conditions [64].

$$\frac{d^2t}{dV^2} = K\left(\frac{dt}{dV}\right)^n$$

Eq. 7

with n the blocking index and K the resistance coefficient both functions of the blocking model. Table 2 summarize the four mechanisms including a schematic representation of each one.

In the cake filtration model, particles form uniform cake layers with an associated hydraulic resistance. The evolution of the cake layer resistance is a function of the material sieving on the membrane. For the complete pore-blocking model, the accumulation of material on the membrane surface reduces the flowrate exponentially with the blocked pore area as the filtration progresses. The rate of area blockage is a function of the material concentration in the feedstream and the filtrate flowrate. In this model, particles are assumed to exclusively block the pores. On the other hand, intermediate blocking considers the possibility of non-uniform layer formation in the early filtration stages. Particles can land on top of other deposited particles. In this case, pore blockage is proportional to the ratio of unblocked area to the total area. The pore constriction model takes into account the pore area reduction as it implies an internal membrane fouling. The flowrate reduction is proportional to particle accumulation on the pore walls, due to adhesion at the wall and then particle aggregation and bridging [65].

Table 2. Pore blocking mechanisms and resulting from the normalized flowrate [65]

Blocking mechanism	**n**	Physical concept	Schematic	Normalized flowrate
Cake filtration	0	Effect of the cake formation on the surface of the filter due to sieving	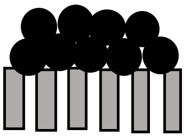	$\frac{Q}{Q_o} = \left(1 + f'R'\frac{2\Delta P}{\mu R_m^2} C_b t\right)^{-\frac{1}{2}}$
Intermediate blocking	1	Effect of both, the cake formation and partial pore blocking related to sieving and bridging	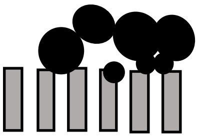	$\frac{Q}{Q_o} = \left(1 + \alpha'\frac{\Delta P}{\mu R_m} C_b t\right)^{-1}$
Pore constriction	1.5	Refered to the internal membrane fouling caused by bridging and aggregation	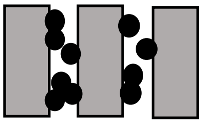	$\frac{Q}{Q_o} = \left(1 + \alpha_{in}\frac{Q_o}{\pi r_o^2 \delta_m} C_b t\right)^{-2}$
Complete blocking	2	The area open to flow is blocked due to sieving	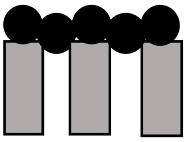	$\frac{Q}{Q_o} = \exp\left(-\alpha\frac{\Delta P}{\mu R_m} C_b t\right)$

Many experimental studies assess the fouling by one or a combination of the blocking mechanisms. Intermediate blocking and complete blocking models were found to fit experimental data for BSA protein filtration [66]. Other authors propose modeling the fouling phenomena as the transition from one mechanism to another. An initial membrane coverage is observed which is consistent with a complete blocking model. As the membrane coverage becomes more important, particles start depositing directly on the fouling layer according with the intermediate blocking mechanism. Finally with an increasing fouling layer, the system dynamics are controlled by the cake filtration [67].

II.3. Membrane cleansing and antifouling strategies

In order to reduce membrane fouling and overcome filtration issues, different approaches have been studied. The work on membrane surface modification by Xue et al. [40] provides guidance toward an efficient method capable of improving membrane wettability and water flux, by applying surface coating and mineralization. The influence of different membrane geometries to induce higher levels of turbulence and hence hinder cake formation [45]–[47] has been also studied. Various studies on the filtration parameters suggest better ways to optimize the operational conditions by manipulation of the pressure and the flowrate [68], [69]. While much work has been devoted to reducing fouling, there is also significant work in a different direction, namely on different ways to recondition the membrane performance to its initial state through cleaning methods as backwash [30], [70], [71].

III. Fundamental relationships

Darcy equation describes mathematically the low Reynolds steady-flow of a single-phase incompressible fluid through a porous media. The expression was empirically determined in 1856 and further derived from Navier Stokes equations [72], [73].The relationship depicts the proportionality of the flowrate to the pressure drop.

$$J = \frac{K}{\mu L} \Delta P$$

Eq. 8

With J the flow-rate (m/s) and ΔP (Pa) the pressure drop through the porous medium. The proportionality factor combines the properties the permeating fluid and porous media, the length and internal structure. The Darcy permeability K in (m^2) assesses the porous medium internal structure effect on the flow, and represents the ability of the porous media to let the fluid pass through it. The viscosity of the fluid μ in (Pa.s) and L in (m) the length of the porous medium.

With μ and L easy determinable, K remains the only parameter to set. The permeability depends on the microstructure of the solid phase in the porous medium and is independent from the fluid properties. There are many approaches to assess the structural properties of the porous medium to model the permeability; some of these properties are the specific surface of the medium, the shape of the pores, the porosity and the tortuosity of the pore channels. The two main approaches are the analytical and the phenomenological approach. The analytical approach focuses on the drag theories analyzing the permeation flow as flow around particles. The phenomenological approach instead, considers the permeation flow through a system of capillaries [74].

The Carman-Kozeny theory follows the phenomenological approach to model the permeability. Kozeny simplifies the porous medium as a set of capillary channels with the same radius.

$$J = \frac{\Delta P d_h^2}{32\mu L}$$

Eq. 9

Combining Hagen-Poiseuille velocity equation (Eq. 9) with Darcy's law and taking into account the tortuosity of the capillaries, the next expression was obtained for the permeability K:

$$K = \frac{\epsilon d_h^2}{32T}$$

Eq. 10

With ϵ the porosity, d_h the hydraulic diameter and T the tortuosity, which represents the ratio of the capillaries length to the porous medium thickness. The permeability equation of Kozeny was further developed by Carman [75]. The porous medium is assumed as a network of non-cylindrical capillaries for which solid-fluid contact surface is represented by the ratio of the porosity ϵ to the internal surface per unit volume. Then Carman-Kozeny formula for the Darcy's permeability results was introduced as follows:

$$K = \frac{\epsilon d_h^2}{16K_k}$$

Eq. 11

with K_K the Kozeny coefficient to be determined empirically. Defining the pore hydraulic diameter d_h as:

$$d_h = \frac{4\epsilon}{S_p(1-\epsilon)}$$

Eq. 12

With S_p the specific surface (m^{-1}). Then replacing d_h in Eq. 11 one obtains the expression found in literature for the Carman-Kozeny permeability:

$$K = \frac{\epsilon^3}{K_k S_p^2 (1-\epsilon)^2}$$

Eq. 13

Carman introduced a pore shape factor k_s (from experiments) which combined with the effect of the tortuous capillaries evaluate the K_K for a bed of spherical particles. From the analysis of the experimental data, Carman found that the shape factor varies from 2.0-3.0 and concluded that the tortuosity T is rather constant over a wide range of porosities $\sim\sqrt{2}$. Carman broke down the Kozeny coefficient into the product of the pore shape factor k_s and the tortuosity squared T^2. From this study, it raises the well-known value of $K_K = 4.8 \pm 0.3$ for a bed of spheres. Later studies have shown that the tortuosity depends on the porosity and T^2 can reach values of 50 [76] for very low porosities. Table 3 shows different studies on the determination of K_K for specific porous medium depending on the geometry of the particles forming the deposit.

Table 3. Literature studies on determination of Kozeny coefficient [77]

Researchers	**Type of study**	**Porous medium**	**Proposed constant or relationship**
Xu and Yu (2008)	Theoretical	Cross flow, Inline cylindrical bars	Graphical presentation
Carman (1937)	Experimental	Uniform spheres	$K_K = 4.8 \pm 0.3$
Ergun (1952)	Experimental	Spheres	150 (Blake-Kozeny constant which equals to $36k_K$ for spheres)
Nakayama et al. (2007)	Computational	Square rods, cubes, cylinders	$K_K = 7.5$ for square rods in cross flow $K_K = 9.5$ for cubes $K_K = 9$ for circular cylinders in cross flow
Heijs and Lowe (1995)	Computational	Random spheres and soil sample	Graphical and table presentations
Li and Gu (2005)	Experimental	Fibrous and granular beds	$K_K = 12.81$
Mathavan and Viraraghavan (1992)	Experimental	Peat beds	$K_K = 3.4$
Eidsath et al. (1983)	Computational	Cross flow, In-line blocks, Inline and staggered cylinders	Table presentation
Terual and Rizwan-uddin (2009)	Computational	Cross flow, Staggered square cylinders	$K_K = 8.1875$ for $\varepsilon < 55$
Vidal et al. (2009)	Computational and experimental	Spherical particles and blocks	$4.9 < K_K < 7.1$
Koponen et al. (1997)	Computational	Random porous media constructed with square obstacles	$6.5 < K_K < 10.4$
Kyan et al. (1970)	Theoretical and experimental	Fibrous beds	$k_K = \frac{\left[62.3\left(\sqrt{\frac{2\pi}{1-\varepsilon}} - 2.5\right)^2 (1-\varepsilon) + 107.4\right]\varepsilon^3}{16\varepsilon^6(1-\varepsilon)^4}$
Happel and Brenner (1986)	Theoretical	Parallel flow along cylinders, Cross flow through cylinders, Flow through random orientation of spheres, flow through spheres	For parallel flow along cylinders: $k_K = \frac{2\varepsilon^3}{(1-\varepsilon)\left(2\ln\left(\frac{1}{1-\varepsilon}\right) - 3 + 4(1-\varepsilon) - (1-\varepsilon)^2\right)}$ For cross flow through cylinders: $k_K = \frac{2\varepsilon^3}{(1-\varepsilon)\left(\ln\left(\frac{1}{1-\varepsilon}\right) - (1-(1-\varepsilon)^2)/(1+(1-\varepsilon)^2)\right)}$ Table presentations
Pacella et al. (2011)	Experimental	Hollow fibres bundle	$BK = 542\varepsilon - 128$ (Blake-Kozeny constant which equals to $36k_K$ for spheres)
Davies and Dollimore (1970)	Theoretical and experimental	Bed of sedimenting spheres/ fluidized beds	$k_K = 1/[2\varepsilon^{n-3}(1-\varepsilon)]$

IV. Cake characterization techniques

Membrane fouling and particularly cake characterization are an increasingly studied field since membrane technology is gaining ground in many industrial branches. These studies are focused on the analysis of cake formation during filtration phenomenon at different characteristic zones:

i. The membrane
ii. The membrane-cake interaction: associated initially to blocking and the transition to cake controlled dynamics.
iii. The fluid boundary layer including the membrane-fluid and cake-fluid interface
iv. The bulk fluid

There are different approaches in order to study the many parameters during the process. The direct measure of variables includes the flux, the pressure, as well as cake thickness, particle concentration and arrangement through image processing. These measurements enable further analysis through the calculation of cake properties like the hydraulic resistance, permeability and porosity. Some approaches involve *in situ* and online acquisition. Such approaches are necessary to understand the real dynamics of the phenomenon. *In situ* live data acquisition is aimed to be a non-invasive method. Also live data or online acquisition implies quick response time to signal change. These two characteristics must be exploited at a convenient image resolution so the analysis is done with the desired precision [78]. Some non-invasive observation techniques applied to membrane processes are listed and compared in Table 4.

Table 4. Non-invasive methods applied to membrane processes [78].

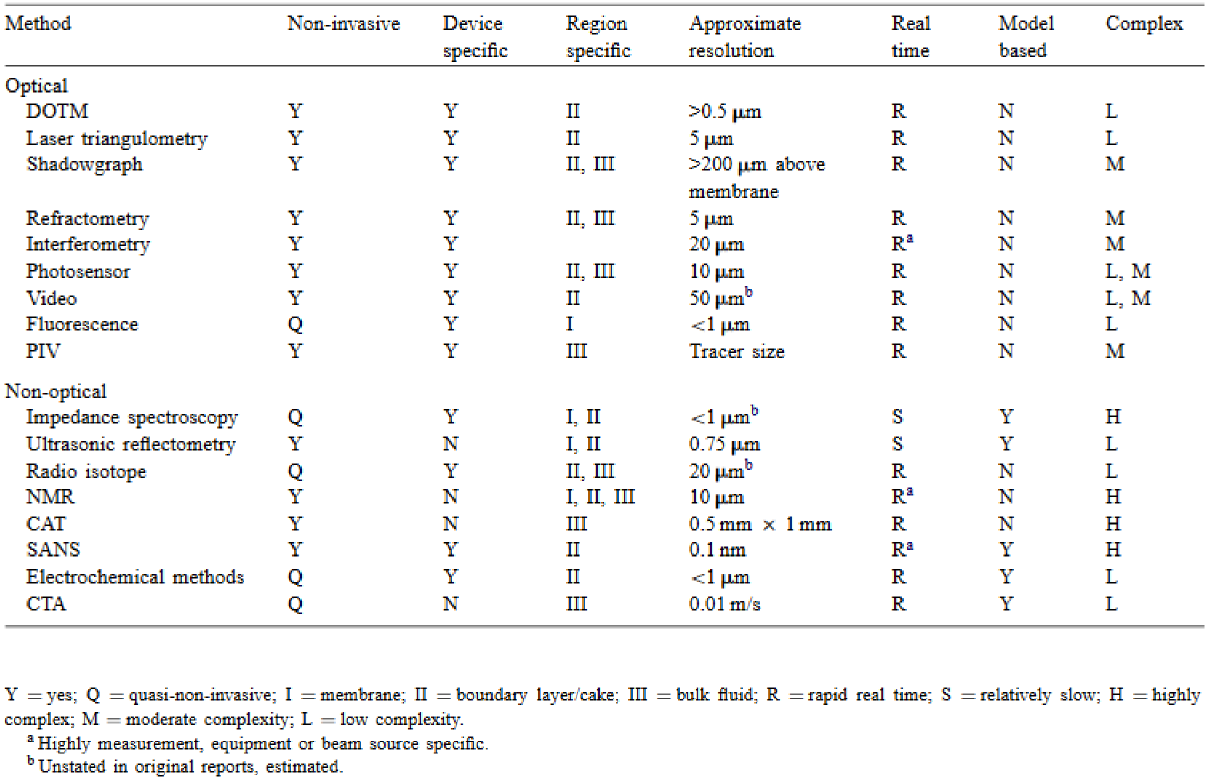

Method	Non-invasive	Device specific	Region specific	Approximate resolution	Real time	Model based	Complex
Optical							
DOTM	Y	Y	II	>0.5 μm	R	N	L
Laser triangulometry	Y	Y	II	5 μm	R	N	L
Shadowgraph	Y	Y	II, III	>200 μm above membrane	R	N	M
Refractometry	Y	Y	II, III	5 μm	R	N	M
Interferometry	Y	Y		20 μm	R[a]	N	M
Photosensor	Y	Y	II, III	10 μm	R	N	L, M
Video	Y	Y	II	50 μm[b]	R	N	L, M
Fluorescence	Q	Y	I	<1 μm	R	N	L
PIV	Y	Y	III	Tracer size	R	N	M
Non-optical							
Impedance spectroscopy	Q	Y	I, II	<1 μm[b]	S	Y	H
Ultrasonic reflectometry	Y	N	I, II	0.75 μm	S	Y	L
Radio isotope	Q	Y	II, III	20 μm[b]	R	N	L
NMR	Y	N	I, II, III	10 μm	R[a]	N	H
CAT	Y	N	III	0.5 mm × 1 mm	R	N	H
SANS	Y	Y	II	0.1 nm	R[a]	Y	H
Electrochemical methods	Q	Y	II	<1 μm	R	Y	L
CTA	Q	N	III	0.01 m/s	R	Y	L

Y = yes; Q = quasi-non-invasive; I = membrane; II = boundary layer/cake; III = bulk fluid; R = rapid real time; S = relatively slow; H = highly complex; M = moderate complexity; L = low complexity.

[a] Highly measurement, equipment or beam source specific.

[b] Unstated in original reports, estimated.

IV.1. *In-situ* characterization techniques

In-situ characterization refers to the investigation of a phenomenon in the same place it is occurring. It is normally preferred because of the representativeness of the analysis, as an isolation or alteration of a sample is minimal or not required. The *in-situ* characterization can be invasive or not-invasive, this depends on the information signal generation and detection [78]. Some *in-situ* characterization experiments allow the real-time data acquisition; this is approachable with optical methods and some of the non-optical.

This review is focused on the optical techniques. Optical techniques use high magnification cameras or microscopes that might be coupled with a video recorder device. Some of these techniques allow the images to be observed during the experiment or to be stored for subsequent analysis. Usually this kind of approaches require the use of specially designed set ups [78]. Down below some optical tools are explained.

Direct observation (DO)

Direct observation technique was first reported in 1993 [79] and further developed to observe particle deposition during filtration process. This non-invasive technique allows *in situ* live-data acquisition. The direct observation facility includes an optical microscope and an attached video camera. Improved resolution (1µm/pix) allow particles larger than 1 µm to be relatively well identified. This technique allows multiple configuration; Li et al. [80] were the firsts observing particles deposit using a transparent membrane and the microscope objectives at the permeate side, this configuration is the well known as direct observation through membrane (DOTM). Otherwise, Mores and Davis [71] set the system configuration in order to observe the upstream side of the membrane.

For the observation of sub-micron particles, the facility can be adapted using fluorescence microscopy. Li et al. [6] used this technique in their study of the deposition and removal of bacteria on the membrane surface during crossflow microfiltration. This work extended the DO technique to observe deposition and removal of model bacteria SW8 with a mean size of 0.8 µm. Their results showed that the shear-induced diffusivity (SID) models underestimate the critical fluxes for smaller particles. They gave a possible explanation, addressing the presence of bacteria aggregates causing higher critical flux. This raises the possible interest in “preflocculation” of bacteria prior to microfiltration to reduce particle–membrane interaction. Also Liu et al. [81] in their recent work studied bacterial deposition and detachment of fluorescent *E. coli* from nanocomposite membranes embedded with silver nanoparticles through a DO set-up; the system allows online visual monitoring of bacterial deposition on a membrane surface during membrane filtration. The deposition experiments showed that the bacterial deposition rates were the same for both membranes, nonetheless for rinsing assays a high bacterial detachment for nanocomposite membranes of 75% was observed compared with 18% for the polysulfone membrane. They suggested that the antibacterial effect of the silver nanoparticles hindered the irreversible fouling caused by bacteria permanently attaching to the membrane.

This method is limited as the fluorescent dye loss the emitting property after certain time of strong fluorescent light excitation, which makes difficult the observation of bacteria deposition on the membrane and thus the estimate of the critical flux. The observation configuration allowed the surface characterization of the membrane and the forming deposit, which is enough for critical flux analysis but does not allow cake structure characterization

The configuration used by Le Clech et al. [57] made possible the side direct observation of the fouling layer formation resulting from the filtration of model solutions to study membrane bioreactors (MBR) fouling phenomenon. The filtered suspensions aimed to model the polysaccharides, which is one of the main foulants in MBRs; alginate/bentonite and alginate/bacteria suspensions were used. This study enabled to identify different zones of the cake layer. They found three different characteristic cake zones result of a particle concentration gradient (Figure 9):

- The viscous layer formed after few minutes of the filtration run and characterized by a velocity decline by half the initial value after 15 min. This decline was explained by the viscous effect of the formed alginate hydrogel and was rapidly identified in the whole observed domain (up to 240 µm)
- The stagnant layer is caused by the immobilization of the bentonite particles in the alginate hydrogel above the membrane surface, creating a visible cake of approximately 65 µm. Is within the stagnant layer that concentration gradient is observed as the filtration runs and allows to differentiate a high concentration layer of approximately 50µm after 60 min. Both are considered sublayers of the fouling cake.

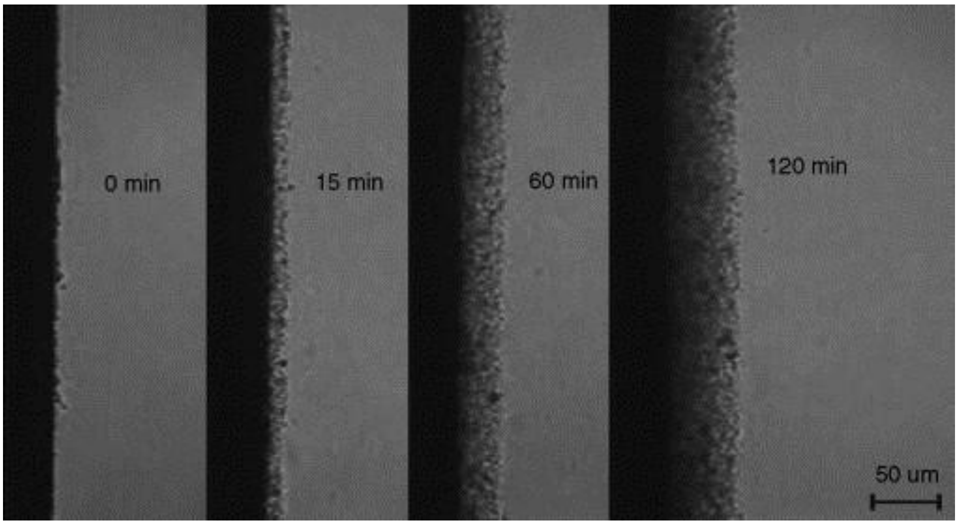

Figure 9. Direct observation of fouling formation on hollow fiber [57].

Of note also is the recent work of Lorenzen [82], who used direct observation to study the influence of charged particles on the fouling phenomena during crossflow filtration. The use of a side view configuration allowed them characterize the formation through the analysis of the cake thickness. They found that increasing the particle surface charge increases both the specific resistance and compressibility of the cake while lowering the charge increases the cake growth rate and the steady-state thickness. Non-charged cake thickness was ~40 µm after 300 min of filtration, whereas charged particles at the same concentration and flow-rate conditions growth up to 20 µm thickness. The maximum cake hydraulic resistance for highly charged particles was found 3 times larger compared to non-charged particles. They also study an effective cake removing technique through the combination of backwash and high cross-flow shear. Particles behavior was observed under compression and relaxation cycles varying the trans membrane pressure (TMP). Charged particles exhibited a rapid response, regrouping fast under compression and swelling in when the TMP is reduced. An important relaxation happened within a few seconds. Even if further relaxation could be observed, it happened more slowly.

Laar et al. [26] and Zwieden et al. [83] used direct observation for the study of the clogging phenomenon of micro-channels. They used similar set-ups adapted for frontal and crossflow microfiltration. By this means, they explored different features of the clogging phenomena like the geometry of the pores, the effect of “pore communication”, particle interactions and the membrane clogging mechanisms. They found that crossflow does not change the primary clogging rate; instead, crossflow has an influence on the communication between pores in a multi-pore membrane. When one pore is clogged, the subsequent filter cake grows and it can form an overhanging structure, which in turn could affect the probability for the neighboring pores to clog. This phenomenon was analyzed quantitatively by the probability for the next clogging event to occur within a distance to a previously clogged pore. Therefore, if an open pore is closer from a clogged one, it is more likely to be blocked. The geometry parameter shed light on the design of membranes, as the entrance angle of a pore is steeper (θ = 0), the characteristic clogging time is reduce by a factor of 4 comparing to θ = 55. The clogging time affected by the entrance angle and particle-interactions. They found that clogging time is 30 times higher for repulsive particles.

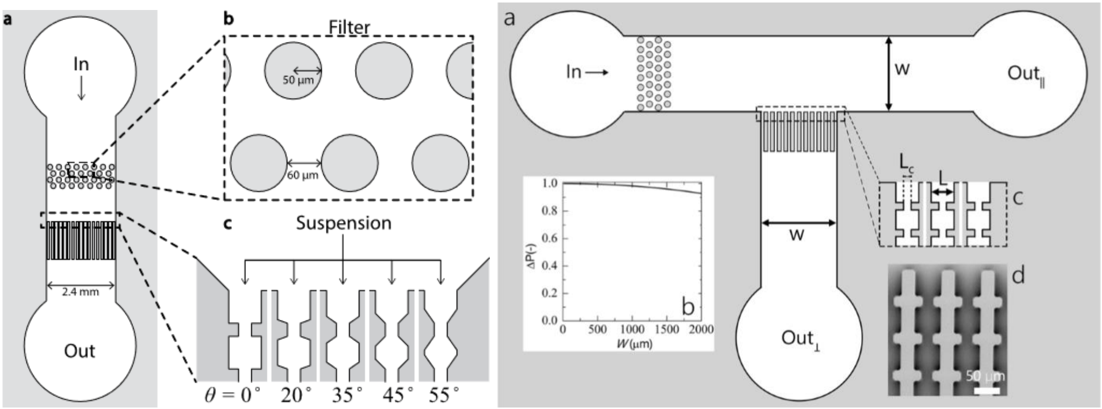

Figure 10. Frontal and cross-flow set-ups used by Laar et al. [26] and Zwieden [83] for clogging

The DO technique allows the *in-situ*, non-invasive and real-time data acquisition. The resolution > 1 µm is enough to approach the microfiltration study. However, for lower sized pollutants the resolution is insufficient and the analysis at the particle scale is not possible. The acquired information does not allow a 3D characterization and the observation is limited to the optical depth of the lighting set-up. This causes the loss of information in the depth direction and brings the study to the hypothesis of homogeneity.

Laser triangulometry

The principle of the technique of laser triangulometry is based on the reflection of laser light from the membrane surface or the cake surface. The angle of the laser varies as a function of the layer thickness, this variation is assessed by a detector allowing the cake layer recognition [78]. Figure 11 illustrates the principle.

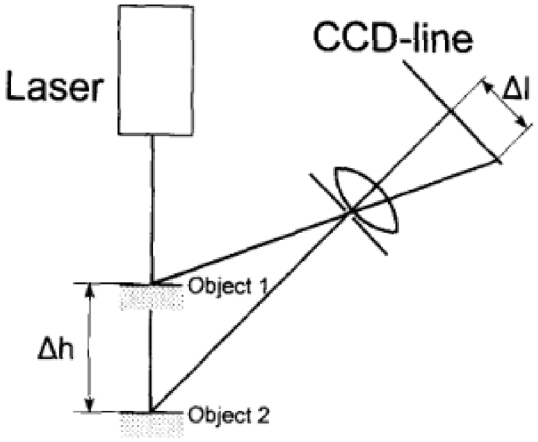

Figure 11. Laser triangulometer principle [54]

In flux-step mode it is possible to observe the cake formation. Mendret et al. [70] studied deposits formed by filtration of yeast and bentonite with different concentrations and under various constant transmembrane pressure (TMP). Backwashes were performed with different operating conditions (TMP and duration). Using the laser triangulometry in their experiments shed light on the cake growth kinetics (Figure 12) and backwash efficiency, measured in terms of remaining cake in dead-end filtration in a confined channel.

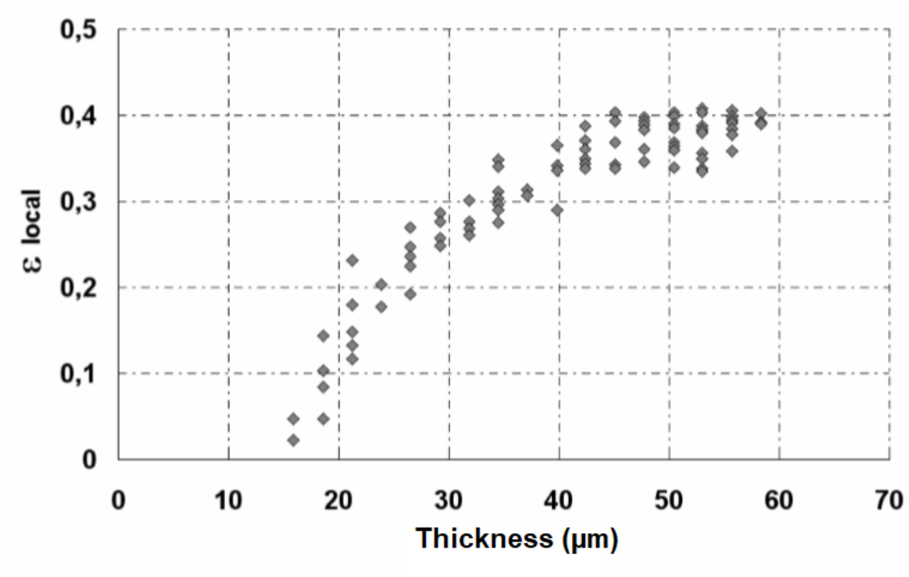

Figure 12. Local porosity as a function of the cake thickness.[84]

Further development by Mendret [84] use the principle of the laser triangulometry. Instead of common laser beam, the use of a fine laser sheet with a grazing incidence allows to obtain the cake thickness profile throughout the investigated length (laser sheet thickness = 400 µm) and to register the *on-line* cake formation. The resolution of this technique is 3 µm and the laser sheet allows investigating a length of 400 µm. By using this technique to investigate the cake height and a mass balance, it was possible to assess the porosity of the cake. A gradient of porosity varying from <0.05 near the membrane to 0.38 for cake thickness around 40 µm (Figure 12) was found. The cake exhibits a high hydraulic resistance that rises with a steep slope to a value of 1.5 x10^{13} m^{-1} when the first layer form (10 µm) and then get to 2.3 x10^{13} m^{-1} around 40 µm.

The work of Schluep and Widmer [55], applied the laser triangulometry method to measure the thickness of a yeast deposit after crossflow filtration. With a 2µm precision, the assays were compared to numeric simulations finding a deviation around 20%. The yeast cake hydraulic resistance varies from 2 x10^{10} to 1.4 x10^{11} m^{-1}. They identified three different stages of the yeast cake formation: first the build-up of the filter cake show a constant specific cake resistance which corresponds to non-compressible behavior at this stage. In the second stage the compression of the cake causes an increasing in the cake specific resistance on average by 1.79 x10^{14} + 2.18 x10^{13} m^{-2}. In the third phase, the reduction of the flux with no change in the cake height makes the authors suggest the fouling of the filter cake, which is explained by the cell debris and macromolecules depositing in the pores.

Altman and Ripperger [54] also used laser triangulometry technique to study the particle deposition and the cake layer formation during crossflow microfiltration. They filtrated diatomaceous and silica particles. The assays shown a rapid formation of cake layer and more slowly decrease of the flux. This phenomenon is explained by particles size distribution. Bigger particles contribute to the cake layer thickness while the smaller ones contribute to flux reduction. Through the *ex-situ* investigation of the formed cake structure using the SEM, they found a graded structure in terms of particle size and depending on the operational filtration parameters. Particle segregation due to hydrodynamic forces and shear induced migration associated with the crossflow filtration define the graded structure in term of size; they observed larger particles near the membrane and smaller at the cake surface under constant TMP conditions.

This technique offers a good resolution that could reach up to 2 µm which is enough for studying the cake growth. The technique principle does not allow studying single particle deposition and cake structure. In addition, this technique captures only the zone corresponding to the polarization zone, the cake surface only, this could be the source of error when there is heterogeneity in the cake surface and important structural information about the cake, like the porosity is calculated indirectly.

Fluorescence microscopy

The use of fluorescence combined with a suitable optical device becomes a quantitative technique widely used in different fields of research, and is adapted for the observation of sub-micron particles. The fluorescence is a phenomenon caused by light excitation at specific wavelengths. Some molecules can absorb this excitation and then re-emit the light at a different wavelength; such molecules are called fluorochromes. The difference between the maxima of the absorption and emission spectra is known as the Stokes shift and determines the energy difference between the absorbed and emitted photons. The absorption and emission are normally placed in the interval of the visible and UV electromagnetic spectrum. Each fluorescent molecule is characterized by its absorption and emission spectra that represents the energetic probability distribution.

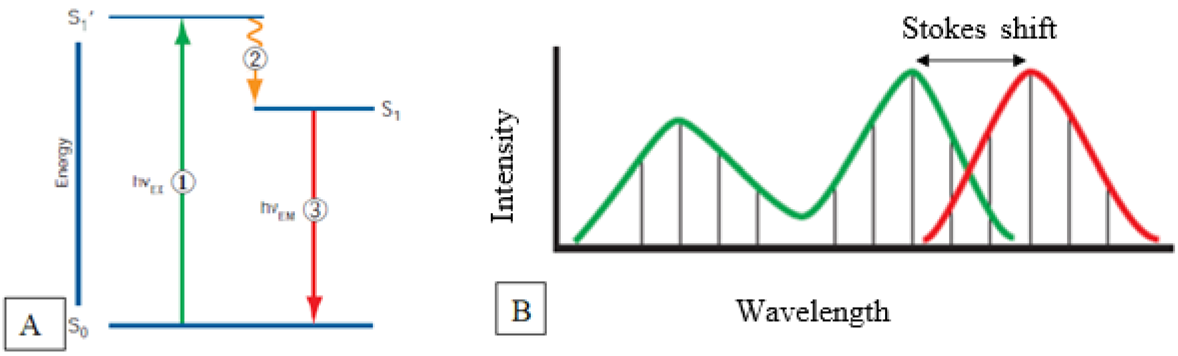

Figure 13. (A) Jablonski's scheme (1. Excitation, 2. Relaxation, 3. Emission); (B) Excitation and emission spectra [85]

Fluorochromes or fluorophores can be used to determine the location of certain structures and compounds. One example is the yeast cell dyeing process using eosine for yeast filtration cake characterization by confocal laser scanning microscopy [25]. The technique can also be used to identify enzymatic activity [86]. In order to make use of fluorescence requires an epifluorescence microscope or the CLSM. The epifluorescence microscope works by illuminating the sample with a certain wavelength so the fluorophores of the sample absorb the input light and then emit the light. The emission is detected through the microscope objective by a photodiode. The input light is filtered by a dichroic mirror and then produces 2D images. Figure 14 shows the configuration of the epifluorescence microscope.

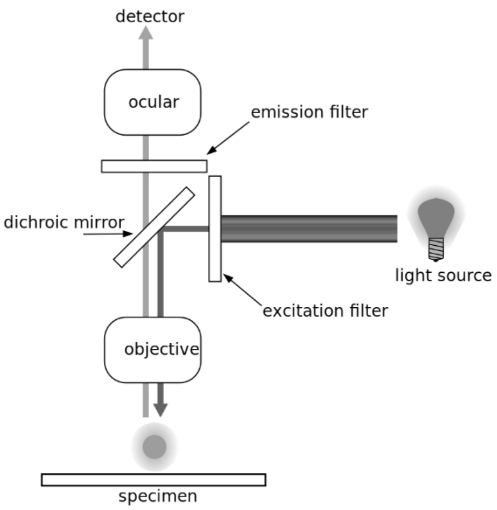

Figure 14. Configuration of epifluorescence microscope [87]

The resolution of the microscope depends on the numeric aperture of the objective, denoted NA, the excitation wavelength λ, and the refraction coefficient of the medium n. The resolution dx, dy are calculated as follows:

$$dx = dy = 0{,}61 \frac{\lambda}{\sqrt{2}NA}$$

Eq. 14

Confocal laser scanning microscope (CLSM)

In order to better characterize the samples confocal laser scanning microscope offers the capability of 3D acquisition of information relaying on principle of fluorescence and image sectioning. Conventional microscopy, illuminate the entire depth or volume of the sample continuously resulting in the detection of out-of-focus emitted light. The fundamental concept of confocal microscopy is the elimination of out-of-focus images thanks to the incorporation of a confocal pinhole [88]. The confocal pinhole acts as a spatial filter removing out-of-focus emitted light that allows imaging only from the focal plane of interest. This allows improvement of the lateral resolution. Furthermore, by scanning through focal planes, it allows the acquisition of 3D information and thus can provide an axial spatial resolution [89]. The axial resolution dz is calculated as follows:

$$dz = 0{,}61 \frac{1.4\, n\lambda}{NA^2}$$

Eq. 15

In practice, the best lateral resolution of a confocal microscope can be as small as 0.2 µm, and the best axial resolution can be as fine as 0.5 µm [88]. Figure 15 shows the configuration of the CLSM and the principle of the confocal pinhole blocking out of focus light for better resolution and image sectioning.

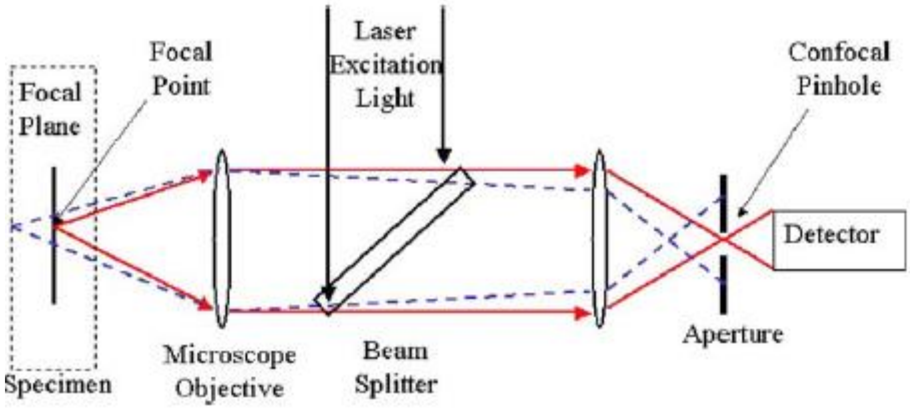

Figure 15. Confocal laser scanning microscope configuration [88]

Zator et al. [90] used the confocal microscope for membrane fouling characterization by model solutions containing a protein (BSA) and a polysaccharide (dextran). The use of the confocal microscope made possible to calculate the fraction of pore surface where the solutes were detected for depths up to 3 µm inside the membrane. The results of this study showed the predominant influence of internal fouling for all the studied scenarios. Experiments with different fluorescent and non-fluorescent protein/dextran solutions performed with different types of membranes to determine the effect of fluorescent tagging on the fouling behavior. Some studies have suggested that fluorescent tagging could alter physicochemical characteristics of BSA such as molecular size and relative charge, which may affect the fouling behavior of the protein. Fluorescent tagging can modify proteins charge and so affects the interaction between particles and the membrane. Further studies of Zator et al. [91] use the same technique for the fouling characterization of ternary solutions containing a fluorescent protein (BSA-FITC), a polysaccharide (dextran-RITC) and a polyphenol to get closer to the complexity of biological mixtures. They found that the presence of the polyphenol, even if it is not perceptible using the confocal microscope, plays an important role contributing to a larger fouling layer formation. All the solutions containing polyphenol exhibit an additional 8.5-17.5 µm layer that was absent in the two components solution. They also studied the effect of chemical cleaning using an enzymatic agent. Even though the complete removal of the cake layer was achieved including particles deposited/adsorbed inside the membrane, the original water flux was not restore reaching a cleaning efficiency between 35 – 55%.

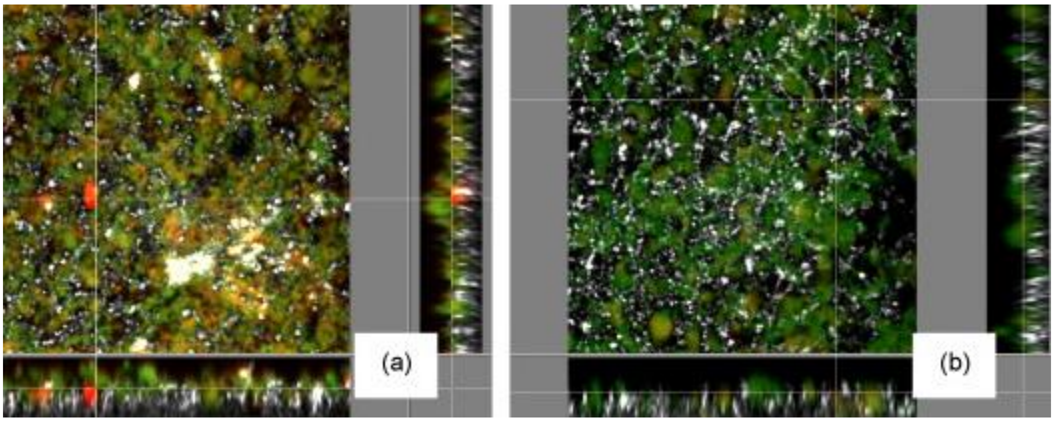

Figure 16. 3D reconstruction of image stacks obtained after filtration of BSA–FITC/dextran–TRITC using a Metricel membrane: 70 kDa (a) and 150 kDa (b) (green corresponds to BSA–FITC signal, red corresponds to dextran–TRITC signal) [90]

Bakhshayeshi et al. [92] used confocal microscopy to study the capture phenomenon in virus filtration process. For this purpose, they used fluorescence-labeled bacteriophages. The confocal images provided quantitative information on the location of the captured phage and the penetration profile. Thus, they could analyze the performance of two type membranes in different configurations.

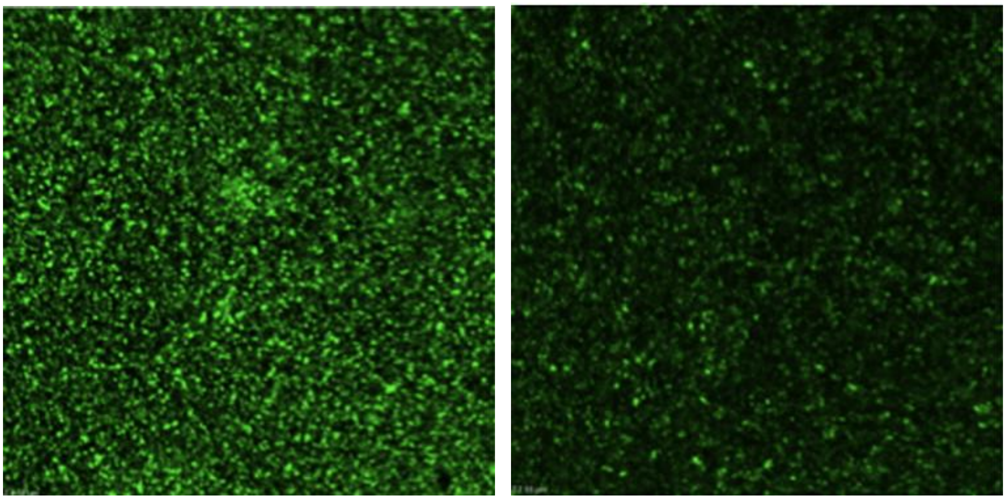

Figure 17. Confocal scanning laser microscopy images of a DV20 membrane after filtration of 15 ml of a 1 x10^8 pfu/ml suspension of bacteriophage fluorescent labeled under constant pressure of 210 kPa [92]

The images show a very high degree of phage capture within the upper layer of the filter with only a few isolated phage seen in the lower layer. The two configurations studied (both sides of the membrane) show that the “skin-side down” configuration allows the virus penetration, meanwhile the “skin-side up” captures the phages in a narrow band beneath the surface of the membrane.

Conventional confocal microscopes use a point-scanning confocal system, meaning that each point of the field in the target focal plane must be scanned. The scanning task requires an time to generate a full-frame image. This time varies depending on the scanning parameters. Finding a fair compromise in terms of image size, resolution and scan frequency leads to an optimal acquisition. However, conventional confocal acquisition frame-rate is not fast enough for studying dynamics in many microfluidics systems and exploit the capability of acquiring 3D information. For this reason, it is often used for static examination after the filtration is finished or in step experiments as in the work of Ben Hassan [39].

Even though, CLSM provides a fine resolution *dx*, *dy* ~0.2 µm, the best axial resolution is ~ 0.5 µm. This cause a deformation of the perceived shape of the imaged objects. This deformation can be easily accentuated when the optical set of the sample (observation window, glass slide thickness, refraction index, see Annexes, item III) is not optimal, leading to the distortion of the object in the *z* dimension by a factor ranging from 2.5 to 40.

Spinning disk confocal laser scanning microscope

Implementation of a confocal system coupled with a multi-pinhole provides a novel solution to overcome this speed limitation. This has been developed in the spinning disk confocal microscope (SDCLSM). The SDCLSM uses a rotating disc known as Nipkow disc that consists of several thousand pinholes usually arranged in a helical pattern. The Nipkow disc spins at rates of 1800–5000 rpm and so multiple spots of the focal plane can be scanned which makes it possible to capture images in real time [89].

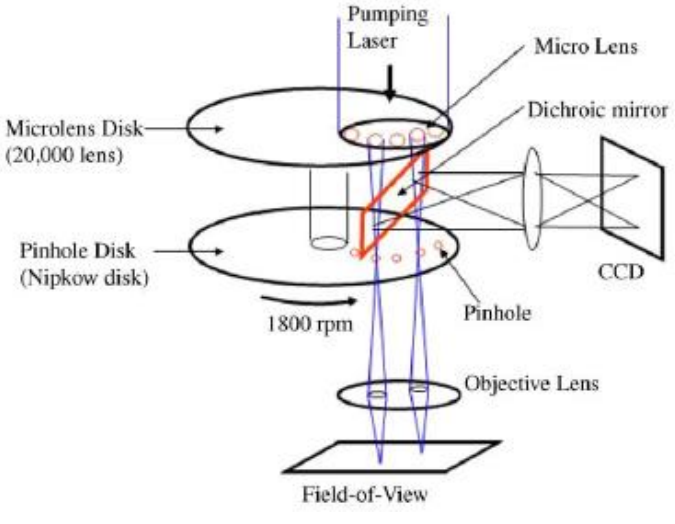

Figure 18.Principle of the spinning disk confocal laser scanning microscope [89]

This spinning disk feature has already been used, showing great promise for observing intracellular fluorescent protein dynamics at high spatial and temporal resolution, being able to reach acquisition frame rate up to 1000 fps [93].

Even if the SDCLSM improve the acquisition time, another factor limiting the scope of the confocal microscopy is the laser penetration in the sample. The laser penetration defines the thickness the domain that the microscope is able to investigate, thus the thickness of the studied sample. In the work of Ben Hassan [25] only the top 30 µm of the fouling yeast cake could be investigated.

μ-PIV

Particle image velocimetry is an optical technique that uses a sequence of recorded images taken at a framerate 1/ Δt where Δt is the time between subsequent frames, with a correlation between images adjacent in time to visualize the flow velocity field. The flowing fluid is seeded with tracer particles. The flow field is illuminated by the dual-pulse laser system and so tracer particles are highlighted for the camera to acquire a clean image. The laser system is conveniently triggered with a pulse rate matched to the camera acquisition rate. Consecutive images are correlated in order to stablish the tracer particles displacements. Hence the instantaneous velocity of particles can be calculated having Δt and the individual displacements. Figure 19 depicts the experimental set up for the PIV technique.

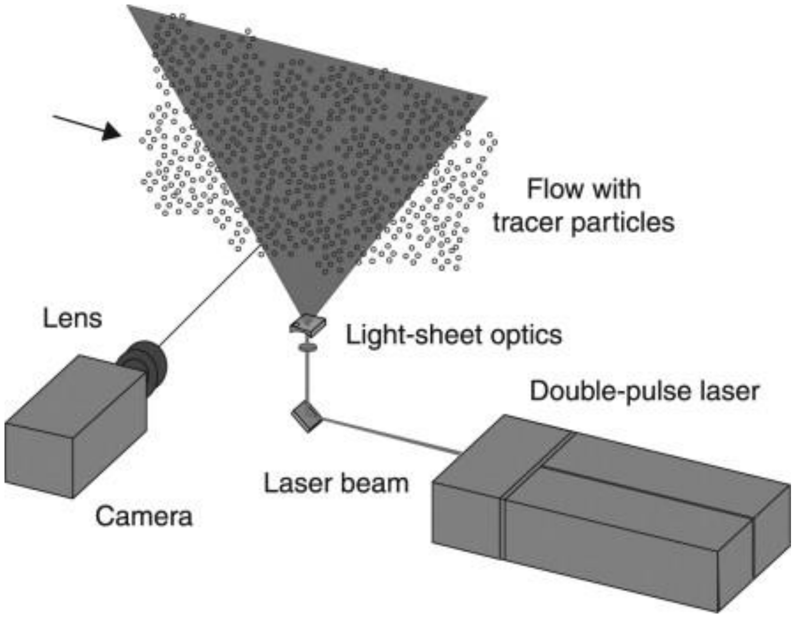

Figure 19. Experimental set up for PIV technique [94]

One of the special requirements for PIV measurement in membrane application is that the seed (or tracer) particles diameter must be of the order of microns. Also, tracer particles must have a low settling rate, as well as be highly reflective to guarantee clear image acquisition. The concentration of the tracer particles must be sufficiently high to resolve the stream lines of the flow field [78]. Finally particle displacement in Δt must be smaller than half the size of a cell of the matrix in which the complete image is divided.

Lately the µ-PIV technique has become an important tool for quantitative and instantaneous measurements of microscale flow. Recent work [95] on capillary flow characterization in open rectangular microgrooves heat sinks using the µ-PIV technique allowed a detailed characterization of some features of the flow under different heat flux and inclination angles conditions.

The work of Liu et al. [45] examined the flow patterns for saw-tooth spacers in membrane filtration. The flow patterns were characterized through µ-PIV in order to compare the filtration efficiency with the conventional zigzag spacer, the results showed that saw-tooth spacers enhance the turbulence behavior and reduce membrane fouling. Figure 20 shows the enhancement in turbulence as result of using saw-tooth (STS) spacer instead of zig-zag spacers (ZS). Higher velocities are achieved for STS driving cleaning and antifouling effects. They found that stronger turbulence can be produced by the STS due to the periodic generation and break of the recirculation region in the membrane channel. The average membrane shear in the STS were ~8.7 times higher than ZS, which leads to attenuate particle deposition thus fouling. They test two different STS units for which the on with higher tooth spacers result in an increased shear rate from 2.7-7.7%. Finally they observed that the potential of the shear enhancement of STS is higher at low Reynolds regimes $Re = 750$.

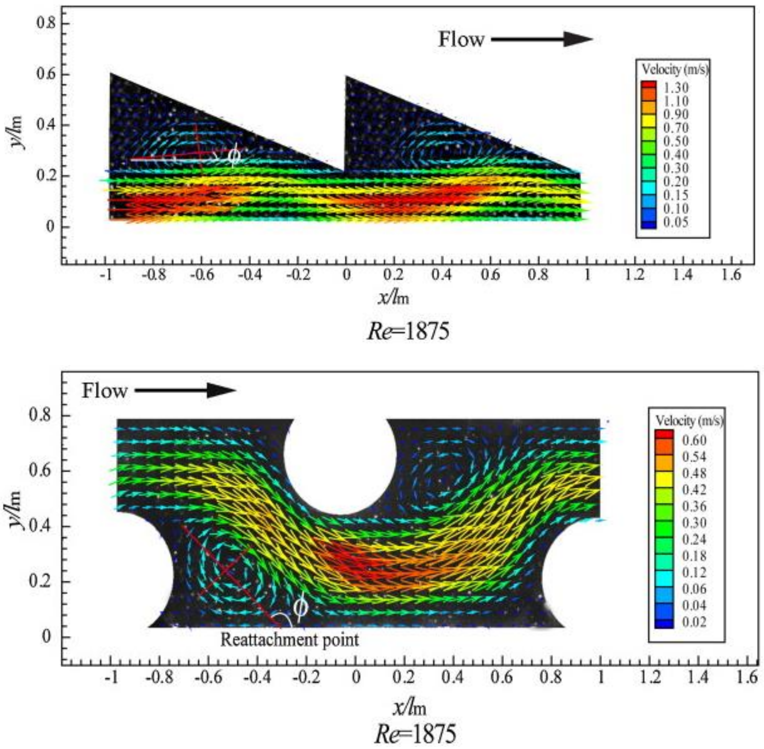

Figure 20. Flow field showing turbulence generated by different kinds of spacers [45].

The advantages of this technique relays in the capability of analyzing flow phenomena by a dynamic approach. The resolution of the technique depends on the tracer size, which is normally in the order of 1 µm. On the other hand, even if the technique results interesting when characterizing the flow it has not been adapted to study the hydrodynamics within the filtration cake and regarding the filtration study is focused on the specific region of the bulk fluid. Also µ-PIV only allows to image flow fields in a target focal plane.

Confocal µ-PIV

The confocal µ-PIV technique combines PIV with new developments on confocal microscopy. A novel use of CLSM makes the truly focused field of view with well-defined depthwise resolution possible for µ-PIV applications [88]. The basic setup consist of an inverted microscope combined with a confocal scanning unit and laser pulse system. The images are recorded by a high speed camera. The confocal µ-PIV system has the capability to acquire series of optical sections along the focal (or z) axis.

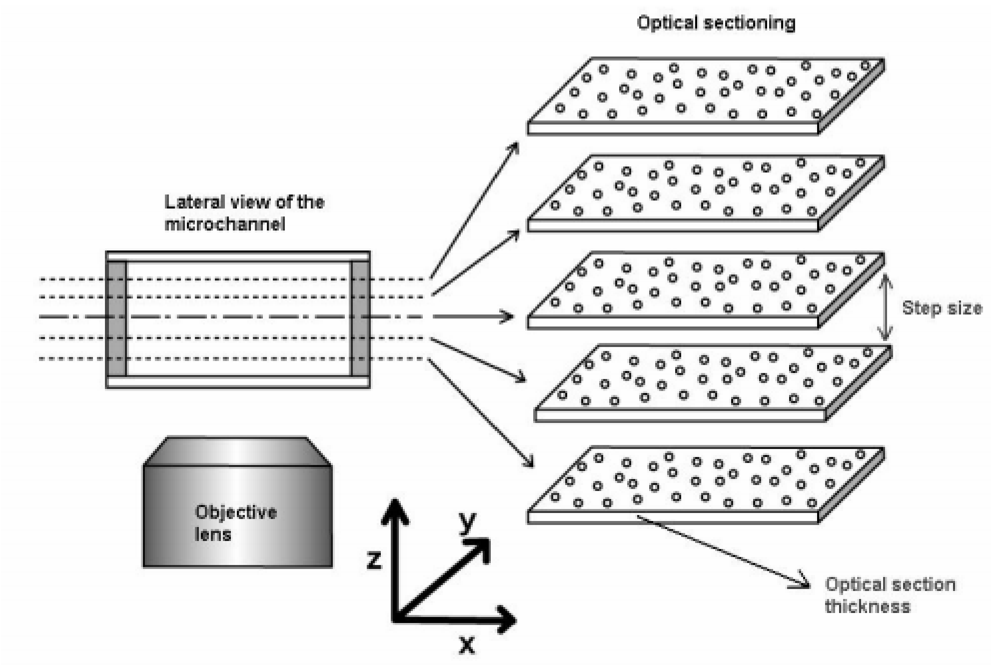

Figure 21. Optical sectioning for PIV measurements (1)

The work by Lima et al. [89] on flow field measurements of blood flow exploited the capacity of the enhanced SDCLM to reduce the data acquisition time and to produce 3D flow information (See Figure 21). The work presents the blood flow profile measurements in micro channels. This team worked with homogeneous (pure water) and non-homogeneous fluids in order to better model a suspension of blood cells (Hanks solution containing 10% human blood). The flow was studied in a square glass micro-channel, thus making possible the observation.

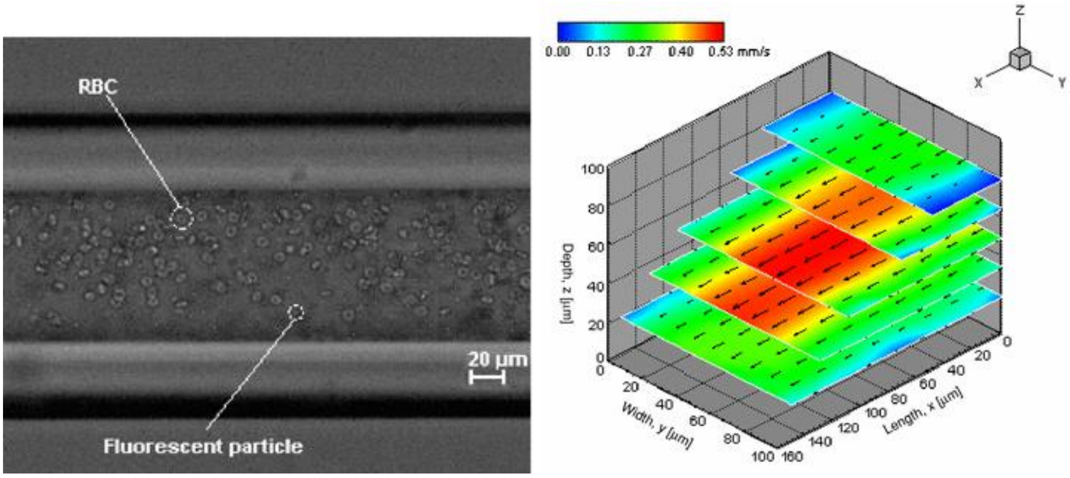

Figure 22. a) An image of the physiological fluid used in this experiment with halogen illumination. The fluorescent particles are observed as very small points and RBCs as dark-grey rings. b) Velocity vector fields at different z positions [89].

Figure 22.a shows an untreated image where it is possible to see the red blood cells as well as the tracer particles of one depth section. Figure 22b shows PIV velocity results for several depthwise layers.

The work done by Li et al. [96] for an experimental investigation on the 3D structures of elastic turbulence in a curved microchannel is prove of the scope of this technique. It presents measurements of the three-dimensional structures of a micellar solution flow in a curvilinear microchannel. The observation area using the 40x objective lens was 227.2 µm × 170.4 µm at a full size of 800 × 600 pixels, which gives a resolution of ~0.28 µm/pix. The use of fluorescent beads as tracers and SDCLM allows using the particle image velocimetry (PIV) technique in a microscale with real time data acquisition and multilayer analysis (3D feature by layers). Changing the PIV interrogation window (32x32 pix) combined with a high acquisition rate of 2000 fps, they were able to measure velocities up to 9 mm/s. They were able to characterize the flow in different parts of the microchannel and conclude that the internal flow of a viscoelastic fluid is not completely chaotic, but oscillates with two twisted sub-streams near the wall region. Also, the viscoelastic flow field inside the curved microchannel shares the main features of elastic turbulence.

There are many possible application of the confocal µ-PIV and specially combined with the SDCLM. The acquisition rate is very interesting; even with a top reported performance of 2000 fps, the acquisition time of the entire volume containing the 3D information is associated with the number of sections following the *z* direction for which the depth is divided.

IV.1. *Ex-situ* characterization techniques

In the case of *ex-situ* characterization, the phenomenon is not examined where it occurred. These techniques require an isolation or extraction of the sample, which often compromise the experiments. The *ex-situ* makes complicated the real-time data acquisition.

Scanning electron microscope

The scanning electron microscope produces an image of the sample by scanning with beams of electrons. The incident electrons on the sample generate different kind of signals. The result is 3D image with high resolution that allows to characterize the sample topology. The scanning electron microscope does not allow internal exploration of the sample nor live-data acquisition. Most of the times the sample must be prepared (drying and metal coating) and finally put in an isolated chamber for the observation. For the particular case of filtration cake analysis, the sample could be compromised due to the preparation which involves recuperate the sample from the filtration facility and perform a surface treatment for the observation. This method has been used to observe the cake layer surface and allows to determine the size, shape and the nature of the foulants.

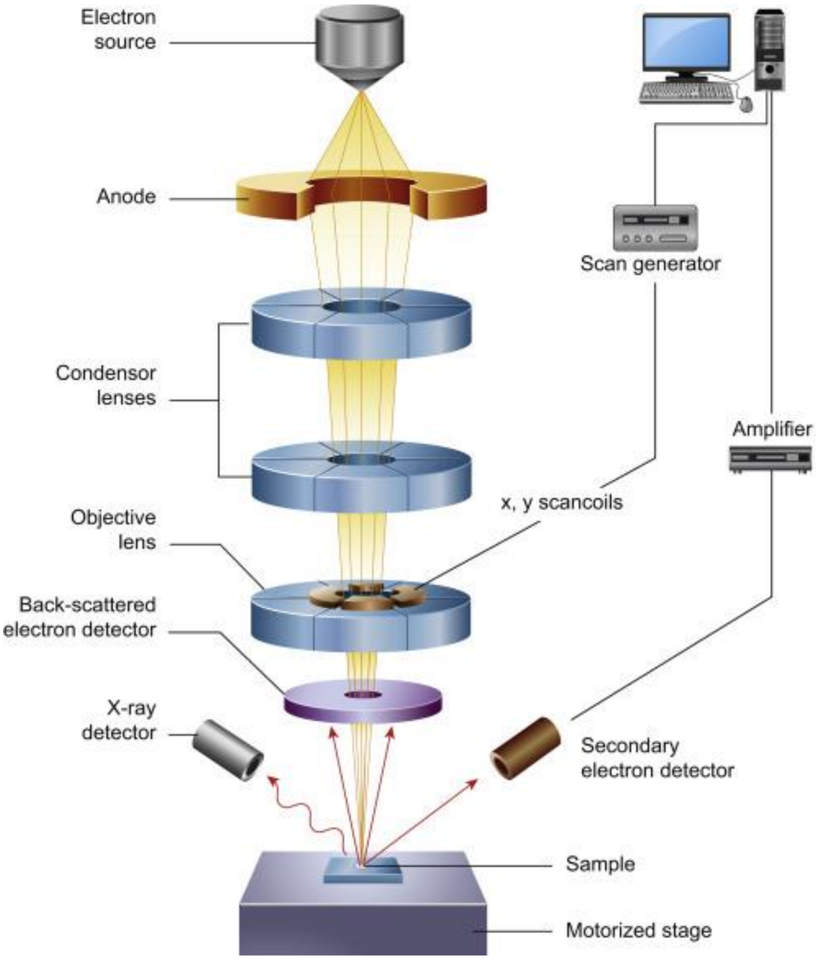

Figure 23. Scanning electron microscopy: schema and principle

Recent applications of the scanning electron microscope in the filtration field aim the characterization of the membrane and the cake layer. Boissier [97] et al. studied the respective impact of wine particles, yeast (*Saccharomyces cerevisiae*) and fines (lactic bacteria and colloidal aggregates Figure 24), on the performances of cross-flow microfiltration under different permeate flux rate and wall shear stress conditions. The cake properties were assessed by the filtration performance rather than the direct characterization. Alternating the TMP allows to study the cake fouling reversibility by using the SEM to observe the membrane surface. Pure yeast suspension always formed reversible filtration cakes differing from suspensions containing fines, which adhesive properties were observed. This technique did not allow to characterize the cake inner structure.

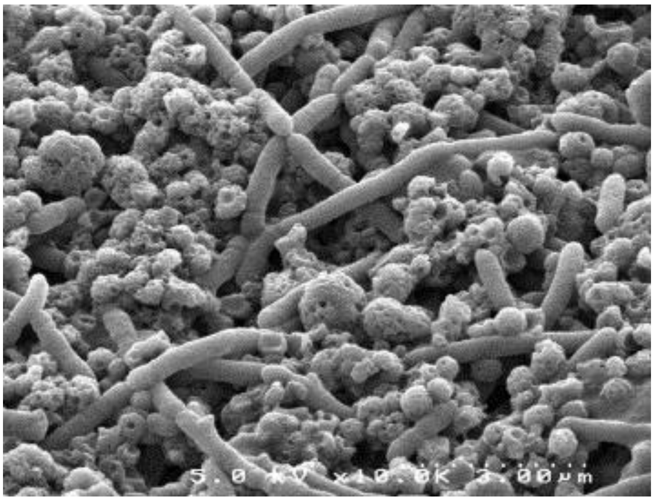

Figure 24. SEM observation of the wine deposit after crossflow microfiltration [97]

Reingruber et al. [98] used environmental SEM (ESEM) for the characterization of microfiltration membranes. This method allows membrane characterization under wet conditions. A qualitative description of the membrane structure is achieved through the observation of the wetting and drying process of the pores. Contrary to the conventional high vacuum mode (HV) the ESEM mode works with pressures in the specimen chamber from 1 – 70 mbar which enables the investigation of wet samples. The number, size and distribution of the pores are determined recording successive images of the drying membrane surface. This SEM mode allows the investigation of samples under conditions that are closer to the “natural” ones with minimum sample preparation [99], however it is under very particular conditions regarding pressure. Also, the characterization is only done at the surface level. Both conditions limit the use of this technique for analyzing the filtration process.

Atomic force microscope

The atomic force microscope (AFM) has been also used for the characterization of filtration cake mechanical properties. This technique generates 3-D high-resolution images, which make possible to characterize the cake surface morphology. After the review of Cappella [100] an intense development has occurred. Other applications are related to the measure of adhesive forces. This technique allows studying local material properties. The force data related to this feature make it valuable in many different fields of research such as surface science, materials engineering, and biology [101].

The principle of this technique is based on the forces experienced between the cantilever’s pointer and the sample surface. The cantilever is displaced as a result of the interaction with the sample. A laser is used to detect the displacement of the cantilever. The laser reflection due to the cantilever displacement allows an estimation of the sample surface. Figure 25 illustrate the principle of the AFM.

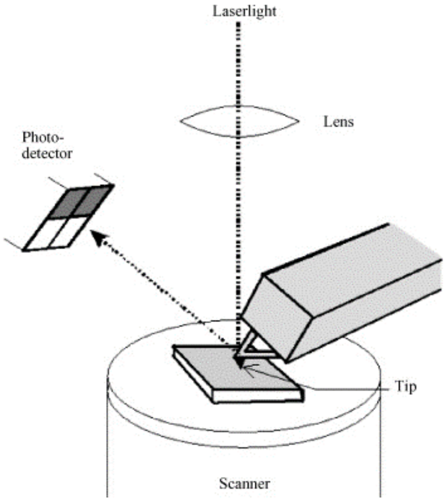

Figure 25. Atomic force microscope principle [101]

In the work made by Bowen et al. [102] the AFM was used to measure the adhesion force of activated yeast (mixed with bovine serum albumin BSA, Figure 26) to different type of membranes. For that purpose, a special coated colloid probe and cell probe techniques were used. A single yeast cell was immobilized on tipless cantilever. The adhesion was measured as the required force for detaching the probe coupled at the tip of the AFM cantilever from the membrane surface. The force curves produced by the AFM depicts the following probe-membrane interaction first from an initial state after probe-membrane contact, the probe and membrane move together with no displacement relative to the piezo. Then, there is a stretching causing a relative movement that continues until the contact between the probe and the membrane is broken. The difference in force between the moment when the stretching begins and the contact is broken measures the adhesive force. This way they were able to measure yeast-membrane adhesive forces in the range of 1.4nN to 9.9 nN.

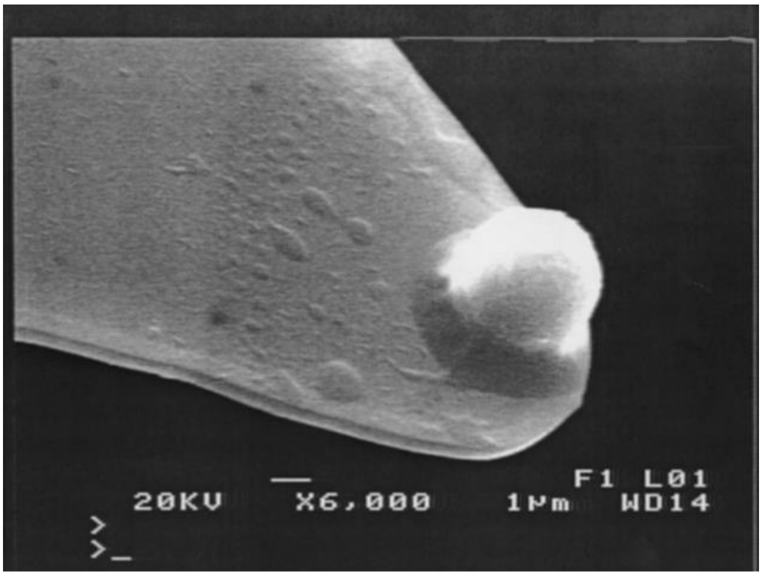

Figure 26. SEM image of yeast (*Saccharomyces cerevisiae*) attached to an AFM cantilever – a cell probe [102]

The work done by Gong et al. [103] to optimize wastewater treatment plants, used the AFM tool characterize the adsorbed irreversible deposit. The objective was to characterize the organic recovery of the membrane. For a better characterization, dead end filtration experiments were set to characterize the additional resistance due to irreversible fouling. After the three filtration cycles the hydraulic resistance was as high as 20.84 $x10^{10}$ (m^{-1}) which is 3 times the membrane resistance before fouling.

The AFM is powerful tool that allows not only high resolution imaging, but also to perform a mechanical characterization by force spectroscopy based on the ability to measure forces of a few pN with a vertical and axial resolution of 0.1 and 25 nm respectively [101]. In addition, the AFM allows the investigation without the risk of changing or damaging the sample with an special treatment. By the other hand, the AFM is only able to investigate an open system with limited domains, with a maximum scanning area of 150x150 µm and a maximum height of the sample of 10-20 µm. The acquisition rate of the AFM is also limited, it takes several minutes for scanning an image [104], which make it inadequate for characterizing dynamic processes.

IV.2. Summary

Table 5 summarize the main feature of the different optical techniques. After studying the different techniques and their performance, the DO appears as an adequate technique regarding the present work context and aims.

Table 5. Characterization techniques in membrane processes

Method	In-situ	Non-invasive	Filtration region	Approximate resolution	Real time	Complexity
SEM	N	N	I, II	< 1µm	N	H
ESEM	N	N	II	< 1µm	N	M
DO	Y	Y	I, II, III, IV	> 1 µm	Y	L
Laser triangulometry	Y	Y	I, II, III	> 3 µm	Y	L
AFM	N	N	I, II	0,1 nm, ≈1 pN	N	M
CLSM	Y	Q	I, II, III, IV	x, y = 0,2 µm; z > 0,5 µm	Q	H
SDCLM	Y	Q	I, II, III, IV	x, y = 0,2 µm; z > 0,5 µm	Q	H
µ-PIV	Y	Y	IV	Tracer size	Y	M
Confocal µ-PIV	Y	Y	I, II, III, IV	x, y = 0,2 µm; z > 0,5 µm; tracer size	Q	H

Y = yes; N = No; Q = quasi; I = membrane; II = membrane-cake; III = cake-bulk fluid; IV = bulk fluid

H = high; M = moderate; L = low

The DO relative low complexity makes it an approachable technique of fast implementation, which allows studying the microfiltration phenomenon. The DO resolution of > 1 µm can be improved by using new equipment and an adapted optical set-up. By this means, resolutions ~ 0.6 µm are reachable, allowing better imaging of particles in the micrometric size range. The lateral DO also allows the real-time characterization of the microfiltration phenomenon in the regions of interest (The membrane, the cake interaction, the fluid boundary layer and the bulk fluid). This allows relating the local phenomena to the global behavior to check the correctness of the analysis. The 2D observation hinders the analysis of a 3D phenomenon, particularly in the depth direction. However, reducing the domain matching the available optical depth, allows minimizing the loss of information with low compromise of the filtration physics.

Chapter III: Materials and methods

In filtration processes, a wide range of scales are of concern, but this study is focused on the microscale. The formation and characterization of the cake layer deposit above a microfiltration membrane is one of the main objectives of this study. This characterization is approached by means of the DO technique. Different kinds of suspensions were used in the experiments to characterize the system and to provide a realistic characteristics filtration scenario.

I. Experimental set-up

An original DO experimental set-up was constructed to provide direct observation of a micro-filtration cell. The side filtration monitoring uses bright field microscopy and an acquisition camera attached to the adapted microscope in order to register the filtration process by sequence of images. A microscope objective attached to a camera (Basler acA 1920-155µm) is used for real-time imaging and data acquisition Figure 27a. A syringe pump (Harvard Apparatus 33) is used to provide suspension flow-rates in the range of 1 to 20 µl/min resulting in linear velocity of 0.5 - 15 mm/s at the filter. A digital pressure gauge (Type E2 - Sika) is used to measure pressure. Figure 27 shows the scheme of the experimental set-up.

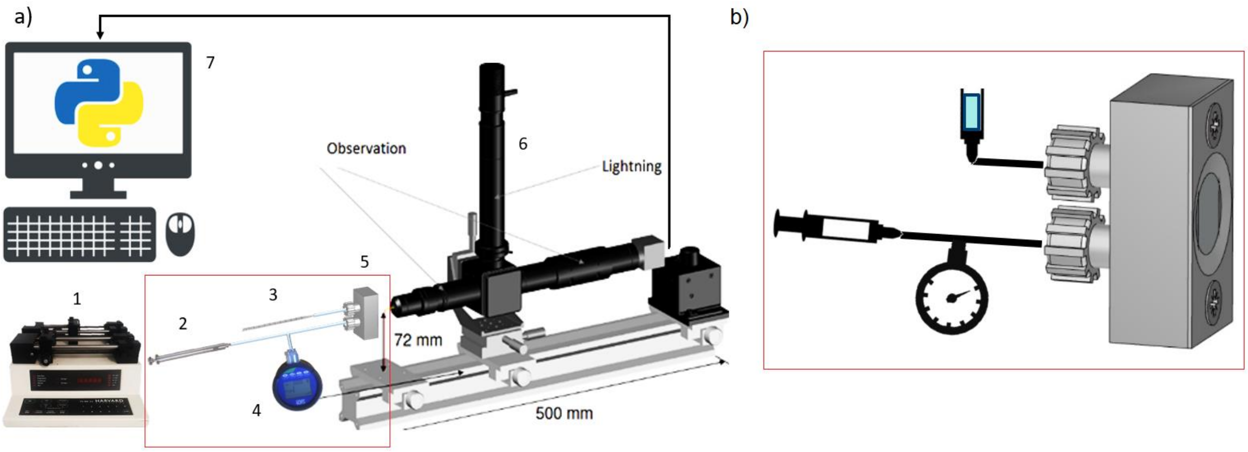

Figure 27. Side DOTM set-up. a)Scheme of the experiment set-up: 1) Syringe pump, 2) Syringe, 3) Reservoir, 4) Manometer, 5) Mechanical support of the microfiltration cell, 6) Optical bench, 7) Acquisition PC. b) Scheme of the zoomed zone: microfiltration cell support and, connections to syringe, reservoir and manometer

It is important to guarantee system cleanliness; the presence of dust particles can disturb the experimental results and compromise the deposit properties. The wettability of the system is a key parameter in order to run the experiments properly and stablish the flow. The water and glycerin mixture (78.9%W, 21.1%G for latex particles and 91.0%W, 9%G for yeast cells) is used as suspending fluid to match the particle density and guarantee the neutrally buoyant condition. In order to avoid dust particles in the system the water and glycerin solution is filtered (0.2 µm diameter pore syringe filters) before preparing the suspension. It was necessary to degas both the solution and the suspension prior to each experiment to avoid the formation of gas bubbles when the fluid passes through the system; a vacuum pump (Knf, Laboport) is used for this purpose. After dust and dissolved gas are removed, the system is filled with the water and glycerin mixture and then the filtration unit is characterized. With the characterization, the stationary flow condition before fouling is known. When the stationary condition is reached, the suspension is injected. The filtration starts and real-time imaging and data acquisition is launched when the first particles arrive. All the experiments are conducted at room temperature 21 ± 1 °C

II. Model suspensions

Four suspensions were used: A cultivated yeast (*Saccharomyces cerevisiae*) suspension aged for 50 h (stationary phase) and three suspensions of model particles, spherical particles, non-spherical particles with peanut shape, and a size/shape polydisperse suspension in the same range of size of the yeast cells (Figure 28).

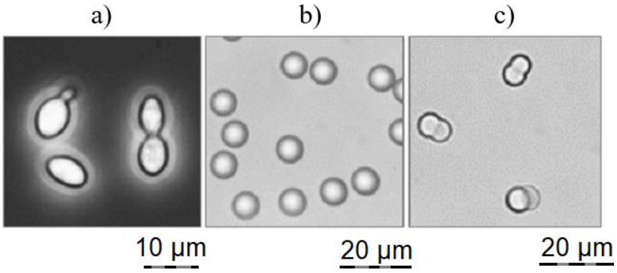

Figure 28 a) Yeast cells, b) Spherical particles and c) Non-spherical particles with peanut shape

II.1. Yeast suspension

In order to prepare the yeast suspension at a given concentration, the growth behavior of the *Saccharomyces cerevisiae* strain was studied in a preliminary stage. The dry mass per unit of volume and the optical density (OD at 600 nm) were measured (spectrometer Biochrom Libra S4) at different ages of the yeast cultivation. It is then possible to relate the concentration of cells to an easily measureable parameter as it is the optical density throughout the whole culture.

The growth medium used for the culture was Yeast Peptone Dextrose (YPD 10g/l Yeast extract, 10 g/l Bactopeptone and 10 g/l Glucose, SIGMA Aldrich©). Once the nutritive materials are combined the medium is separated into batches of 50 ml for pre-culture and 200 ml for culture. The medium is sterilized in an autoclave for 20 minutes at 120 ºC before inoculation. Yeast inoculum are stored in 1 ml cryo-tube with 20% glycerin at -20 °C. Yeast inoculum is pre-cultured in a cotton-plugged flask with baffles, incubated at 30 ºC and stirred at 120 rpm for 24 h in the 50 ml medium to ensure a standardization for the further culture. After the 24 h a 4 ml sample of the standardized pre-culture is added to the 200 ml medium (in baffled Erlenmeyer flask) under sterile conditions, then incubated at 30 ºC and stirred at 120 rpm.

At least 22 ml are sampled under sterile condition each hour for the analysis. A test probe is fill with 1 ml of the cell suspension for measuring the OD. Figure 29 shows the evolution of the OD as a function of the culture age.

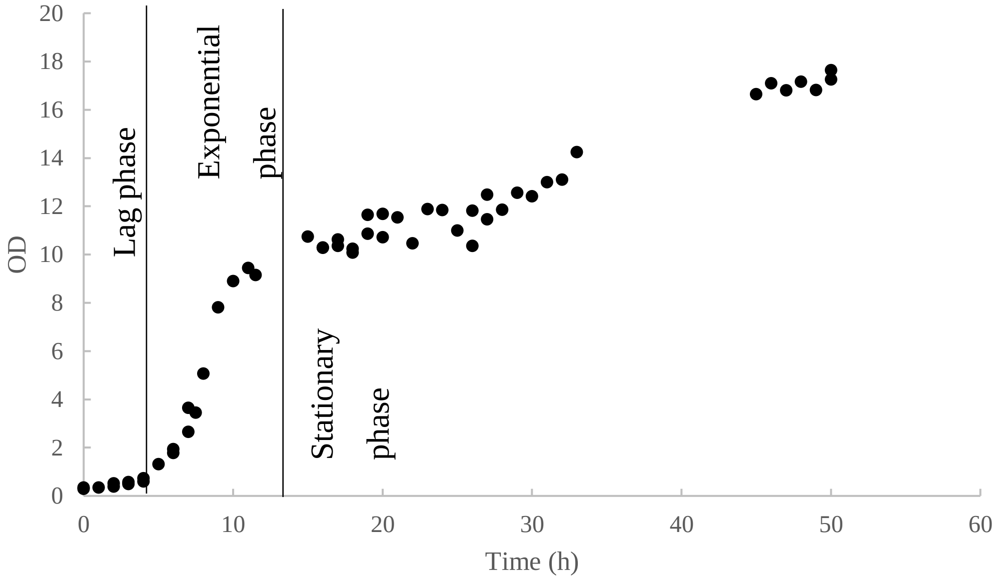

Figure 29. OD evolution through the culture. Identification of the different growth stages: lag, exponential and stationary phase

Then, a volume of 20 ml is filtered (Nalgene™ Reusable Filter Holder and Masterflex, Bioblock scientific pump) using a polyamide membrane (0.2 µm pore size, Sartoryus©) to retain the cells and measure the total mass (membrane + yeast cells) after drying m_d.

The membranes are previously dried and weighted (m_{md}) to calculate the cell concentration as follows:

$$C_c(g/l) = \frac{m_d - m_{md}}{V_s}$$

Eq. 16

for V_s the filtered volume sample. Figure 30 shows the concentration evolution throughout the yeast culture.

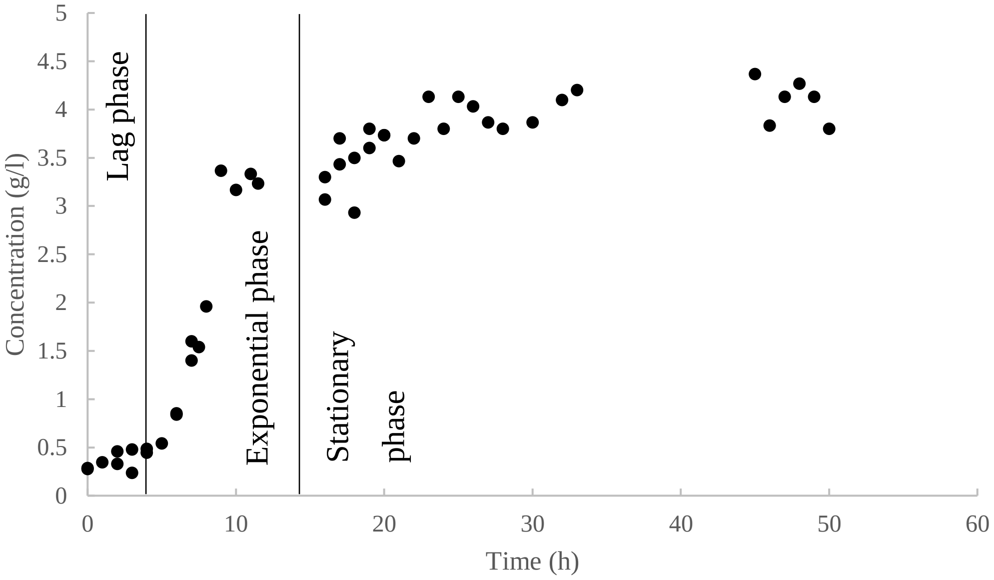

Figure 30. Concentration evolution through the culture. Identification of the different growth stages: lag, exponential and stationary phase

In order to cover the culture at each hour, two batches delayed in time were prepared for sampling. The different behavior at the stationary phase for the OD and the concentration is caused by the change of predominant shape of the yeast cells. When the cells have consume most of the nutrients, cell division stops and the shape of cells tend to be more spherical instead of buds. This has an influence on light interference and consequently the OD measurement.

It is possible to relate the cell concentration to the OD. Figure 31 shows a linear relation of the cell concentration as a function of the optical density $C = 0.255\, OD + 0.558$. This way it is possible to calculate the concentration of the culture when preparing the yeast suspension for the filtration experiments. In order to take into account the shape cariation on the OD measurement the concentration correlation at 50 h is done and yields $C = 0.236\, OD$.

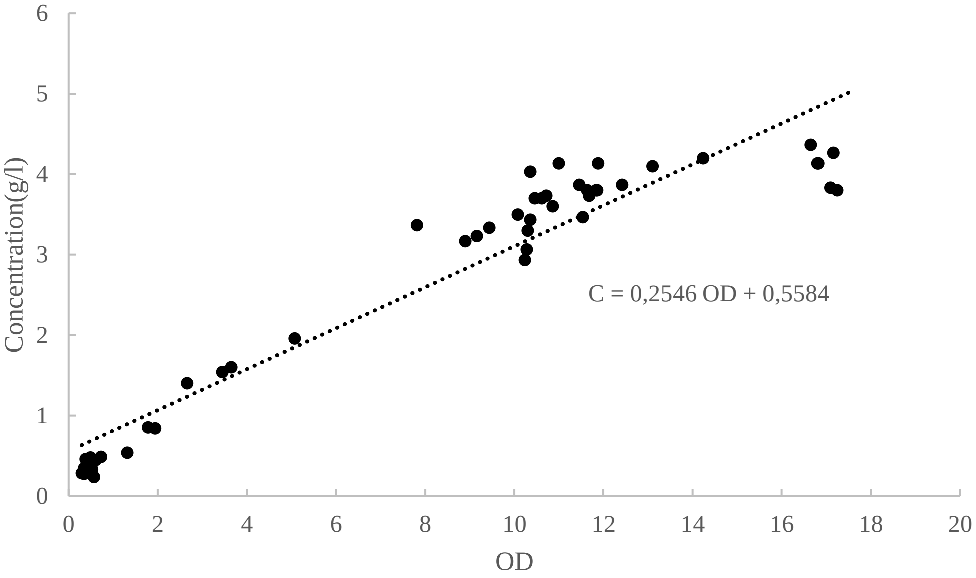

Figure 31. Yeast cell concentration (Dry mass/liter) as a function of the optical density

After studying the yeast growth behavior, it is possible to controllably prepare the cell suspension for the experiments. When the cultivation reaches 50 h age, the OD is measured and the concentration is calculated using the previous relation. The right volume of culture suspension is collected for preparing the desired concentration. The obtained suspension is centrifuged, the supernatant is removed and the cells pass through two washing cycles before being re-suspended in a density matching (1.024 g/cm3) water and glycerin mixture (91%W, 9%G).

II.2. Model polystyrene (PS) particles

Micron-sized polymer particles have been used to mode different phenomena and have application in different fields of development like medicine, research and biotechnologies. Some important properties of polystyrene (PS) micro-particles are the following:

- High mono-dispersity and uniform spherical shape
- Hydrophobic surface
- Non-specific adsorption of proteins
- Non-aggregation
- Density of 1.055g/cm3
- Refractive index of 1.59

Spherical particles suspension

The spherical particles suspension used for the experiments consists of the noted water – glycerin mixture (79%W, 21%G matching PS microparticles density) and latex beads (Micro Particles GmbH PS-R-8.4) of mean diameter of 8.4 µm with and standard deviation of 0.09 µm, and a density of 1.055 g/cm^3. Spherical model particles were chosen in order to characterize the system and to compare with simulations, as their shape is easier to model but also resembles the shape of individual yeast cells.

Non-spherical particle suspension (peanut shape)

Latex non-spherical particles with peanut shape (Magsphere PNT005UM) were suspended in a water–glycerin mixture (79%W, 21%G). The peanut shape has a longest dimension of $a = 7.4\ \mu m$ µm from two identical particles merged while the other two characteristic lengths correspond to the particle diameter of 5.1 µm. The particles density is 1.055 g/cm^3. This particle suspension was used in order to being closer to the yeast buds shape and so the resulting cake structure.

Polydispersed suspension

The polydispersed suspension consists of a discrete distribution of three kind of model particles equally apportioned in volume. Two sizes of spherical particles (Micro Particles GmbH) with diameters of 5 and 8.4 µm and non-spherical particles with a peanut shape (Magsphere PNT005UM) suspended in water –glycerin mixture (79%W, 21%G). This suspension was used in order to being closer to the yeast suspension. In terms of shape, the budding behavior is represented by the non-spherical particles and the individual cells size distribution by the two different particle sizes.

Table 6. Particles characterization

Code	Description	Characteristics	Specific surface, S_p x10^6 (m^{-1})
Yeast	Saccharomyces Cerevisiae	Cultivated 50 h	1.13
NS	Non-spherical “peanut”	a = 7.4 µm; d=5.1 µm	1.10
S	Spherical	d = 8.4 µm	0.71
		d = 5 µm	1.20
SD	Polydisperse	$S_{8\mu m}$-NS-$S_{5\mu m}$ (1:1:1 Vol.)	0.98

All suspensions are calibrated in order to have an estimated filtration deposit height. The mother suspension of 1% (w/w) is diluted so the proper volume of particles and concentration is achieved depending on the test. In the case of the cultivated yeast, every test used new cultivated cells for which the growth curve (OD vs. Dry mass) is calibrated and monitored so the suspension concentration is calculated using the OD information at the sampling instant.

III. Filtering cells for side direct observation

Because interest here is in the cake formation, the microfiltration device and its inner filtration unit were designed based on the expected cell size of the yeast in order to achieve fluid-particle separation by sieving. Yeast cell size distribution ranged from 2 to 10 µm and the latex particles mean diameters were 5 and 8.4 µm; following this, membrane smallest pore size dimension was 2 µm, which allows the retention of particles and cells on the surface.

A set of micro-filtration cells was specially designed and created using two main techniques, photolithography and plasma reactive etching in collaboration with the LAAS laboratory (*Laboratoire d’analyse et d’architecture des systèmes*). The geometries are defined by two parameters: the slot width and the distance between consecutive slots (wall thickness), related to the slot periodicity. These two parameters aim to change the permeability and the preferential configuration of the particles when the cake layer is forming. This geometry is the first to be determined in order to fabricate the photo-mask to be used at the photoresist activation (see Figure 32).

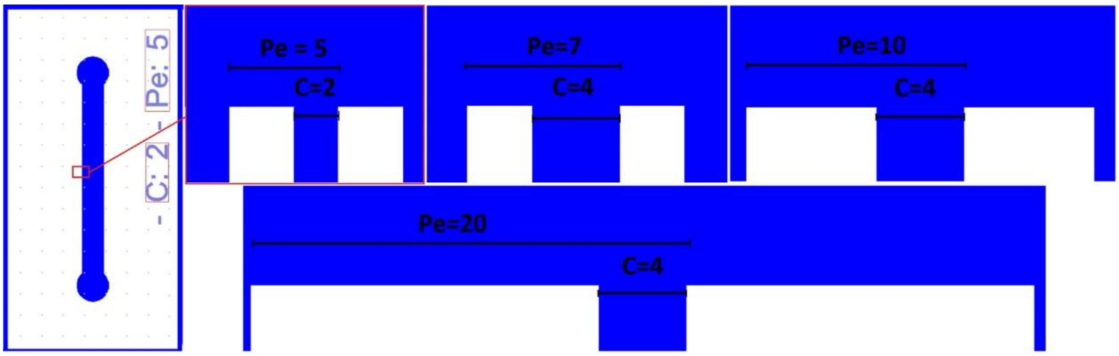

Figure 32. Microfiltration cell configurations. The C is the identification of the slot width and Pe the slot periodicity. The difference Pe- C corresponds to the distance between consecutive slots. Highlighted is the zoom of the corresponding entire cell, C2Pe5. At the side is the corresponding information of each different geometry, the information is summarized in Table 7 (units are in µm).

The cell consists of a straight channel for frontal or dead-end filtration and a filtering structure at the middle. The channel length is 11.5 mm, 1 mm width and depth of 30 µm. The membrane is placed in the middle of the channel and consists of a series of consecutive walls forming slots that selectively let fluid pass and retain particles. The walls are 25 µm length, with height equal to the channel depth, and the width depends on which of the membrane configurations is considered. Figure 32 shows the described geometry while Table 7 presents the different consecutive wall configurations.

Table 7. Membrane geometries characterization

Geometry reference	Slot width, C (µm)	Periodicity, Pe (µm)	Slot distance, d_p (µm)
C2Pe5	2	5	3
C4Pe7	4	7	3
C4Pe10	4	10	6
C4Pe20	4	20	16

The use of dead-end filtration operating condition is accurate for analyzing the first layers of cake and the first stage of cake formation; even under crossflow operation conditions it is well known that some particles accumulate at the membrane surface as the flow direction in the vicinity of the membrane is perpendicular to the filtration surface [105]. In addition, dead-end operating condition is adequate for performing the mass balance, which is the basis of the quantitative analysis.

III.1. Photolithography

The photolithography technique creates a desired pattern using the property of a material known as a photoresist. The photoresist is a resin, whose properties change after UV light exposure. After UV exposure, the photoresist is able to endure the effect of solvent substances known as developers. Photolithography technique usually uses a mask that allows the selective exposure of the surface coated with the photoresist. The photoresist layer is selectively marked using UV radiation. The photomask allows the UV radiation to pass through according to the mask pattern. There are two types of photoresists: positive photoresists become soluble with the action of the developer after exposition; for negative photoresists, unexposed regions are soluble with the action of the developer. The photolithography process is conducted at the LAAS cleanroom.

The photomask is made in glass and covered with chrome following the desired pattern depicted in Figure 32. A silicon standard wafer of 525µm thickness is used. Each wafer is set to contain 41 microfiltration cells; there are 11 units of the C2Pe5 configuration and 10 units of each C4Pe7, C4Pe10 and C4Pe20 (Figure 32, Table 7). The 41 units are engraved on the silicon wafer surface though the combination of the photolithography and plasma etching techniques and are distributed as shown in Figure 33.

The first step of the photolithography technique is to coat the wafer with the photoresist. For this, the wafers are cleaned using "piranha" treatment followed by a 15 min MOS plasma oxygen (LAAS recipe #2); this is the standard LAAS protocol for cleaning. Previous engravings made at LAAS laboratory suggest a 2.5 µm layer of AZ ECI 3012 photoresist for an engraving penetration of 20-30 µm. Before covering the wafer with the photoresist, hexamethyldisilazane (HMDS) is applied on the wafer to enhance photoresist adherence to the silicon.

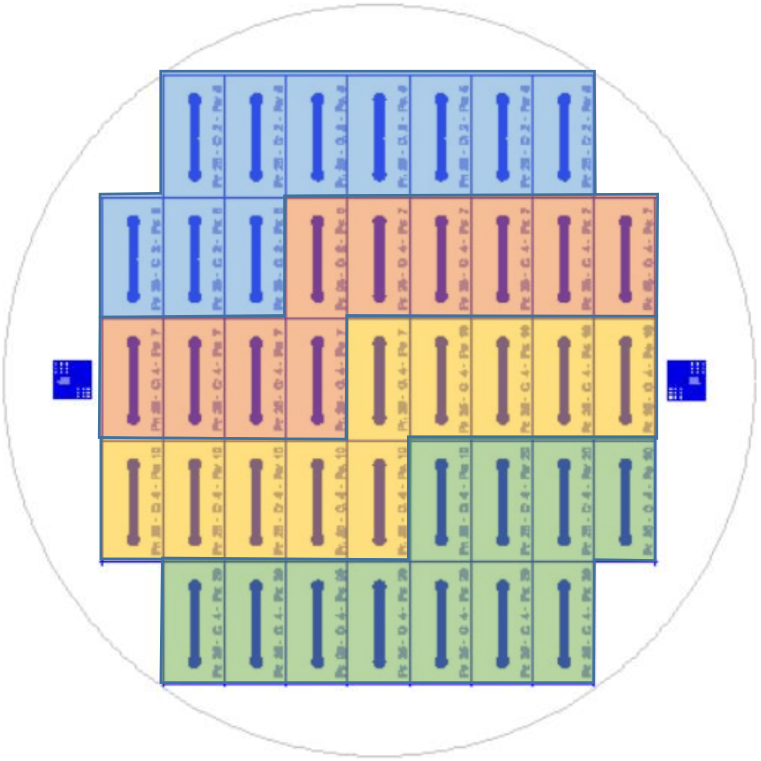

Figure 33. Microfiltration cell distribution on the wafer. Blue zone correspond to C2Pe5 units, orange C4Pe7 units, yellow C4Pe10 units and green C4Pe20.

The wafer is covered with a 2.5µm ECI photoresist by spin coating. Shortly after coating the wafer is exposed to a soft bake (90-110°C) to eliminate solvents in the photoresist/substrate interface and to solidify the photoresist film. It is important to control the soft bake step to avoid the appearance of bubbles in the photoresist layer. The EVG 120 equipment (EVG) is used for automated coating, baking and development.

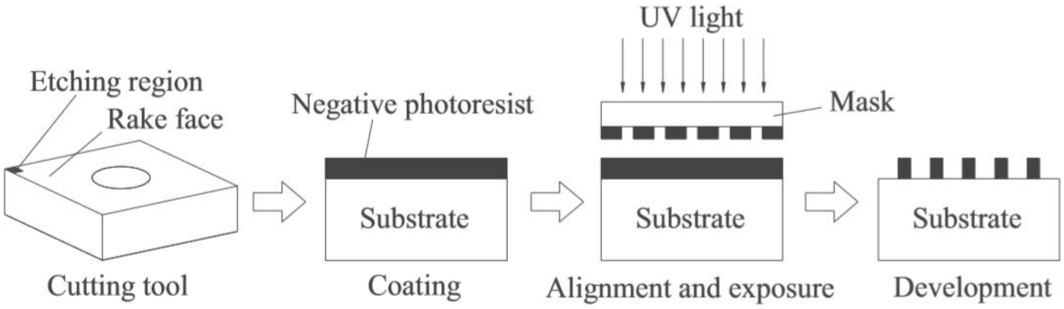

Figure 34. Schematic diagram of the photolithography technique [106]

After the wafer is coated the photoresist is activated with UV rays using the photomask and the mask aligner (MA150 Suss Microtec). By this means, the desired pattern remains after developing the photoresist using the solvent. Three photoresist developments (5s solvent exposure under spinning conditions) have been performed in order to fully remove the undesired zones. After developing, a post exposure baking (PEB) is conducted to stabilize the printed features and avoid negative construction-destruction interference effects.

After concluding the photolithography process, the characterization of the wafer is performed. A first characterization is made using a mechanical profilometer (Tencor P16+) in order to confirm if the thickness of the photoresist is effectively 2.5 µm or more. It was found for the wafers, a thickness between 2.69-2.79 µm that is satisfactory for the engraving purpose. The function of the photoresist coating is to protect the desired zones from the etching effect of the later texturing process.

III.2. Plasma etching

The Alcatel P1-BOSCH (Multiplex Alcatel AMS4200) process is used to engrave the desired pattern on the surface of the silicon wafer. The reaction chamber is filled with the etching gas that is turned into reactive plasma using a coil activated by a radiofrequency generator. The plasma produces a physicochemical attack on the silicon wafer surface and the protective photoresist, etching the silicon at a rate of 2 µm/min. The etching rate allows setting of the reaction time.

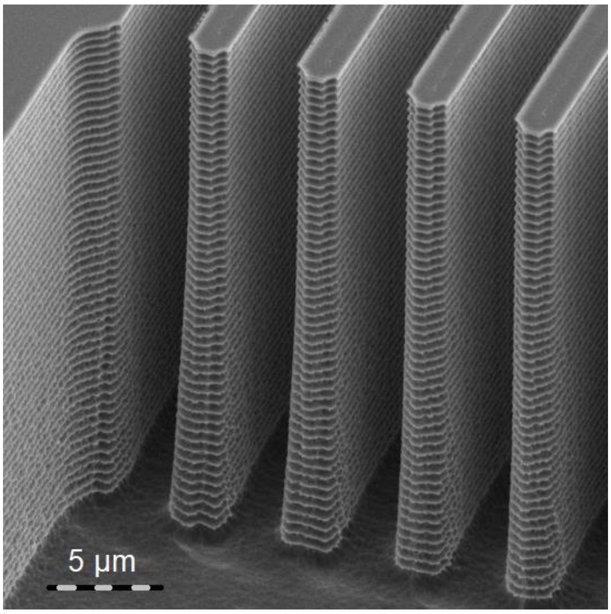

Figure 35. Plasma etching result C4Pe7 unit.

After the etching, wafers are characterized to investigate the etching performance and quantify the effect on the photoresist layer.

Even if the plasma etching produces the desired patterns (Figure 35. Plasma etching result C4Pe7 unit.), it is important to highlight some features that differ from the initial design. The section is not constant in depth, this is caused by the over-exposure of the walls to the plasma attack as they were closer to the surface before etching starts (Figure 35). Fringe effects are spotted in Figure 36a and b at the bottom of the walls. Another feature is the local effect of the plasma etching, which is uneven in the center and the borders of the wafer. These issues could led to slight differences in the performance of the different filtration units even among units of the same configuration.

A non-uniform permeability along the membrane is associated with the precision of the filtration unit fabrication at the membrane fine structures. According to previous literature, a uniform cake surface is formed on the membrane when the filtration dynamics are controlled by the cake. However, in the first stages of the filtration, non-uniform membrane permeability could influence the formation of the first layers [107]. Mendret et al. [108] used numerical simulations to investigate the effect of non-uniform permeability on the cake formation. A sinusoidal function modeled the variation of the membrane permeability along the channel; the results revealed that the non-uniform initial permeability becomes uniform as the cake grows.

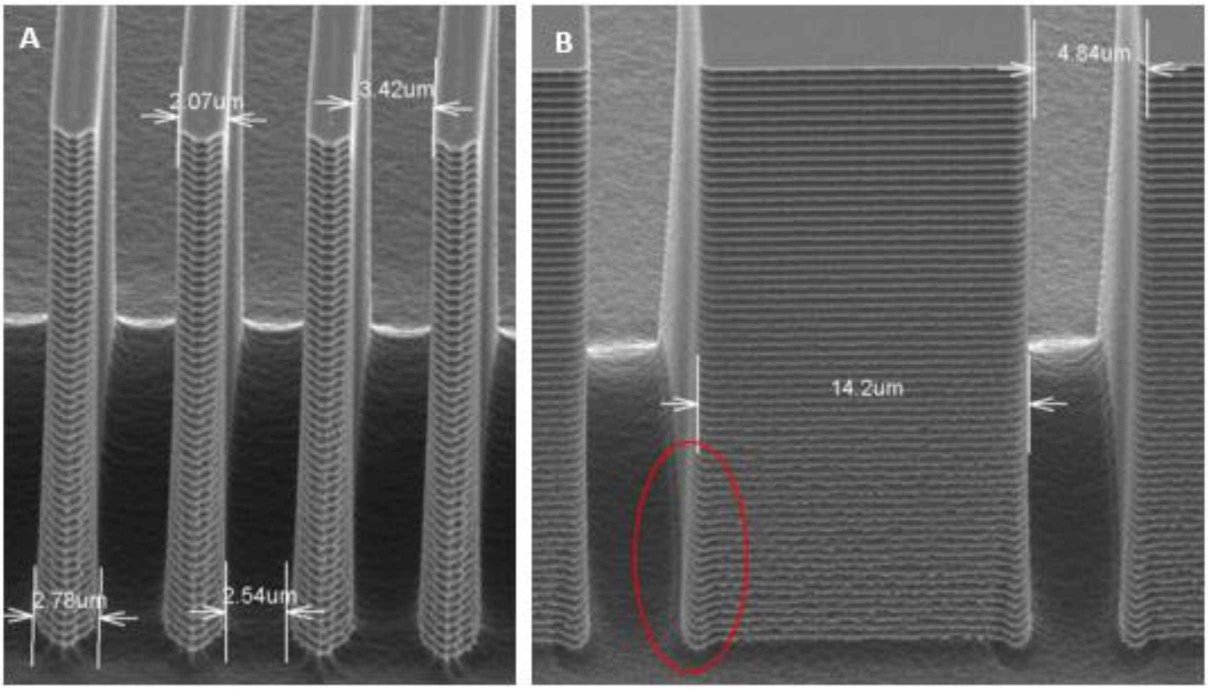

Figure 36. Irregularities of the engraving

III.3. Piercing and anodic weld

With the pattern engraved on the wafer surface, the only step before covering the wafer with the glass slide (170 µm thickness) and cutting them apart into the individual filtering cells is to pierce the inlet and outlet openings using abrasive blasting.

Before covering the wafer with the glass, it must be properly cleaned. The covering process is known as anodic weld and is performed by the AML Aligned Wafer Bonding machine (AWB 04). Silicon wafers are 525µm of thickness and they are covered with a glass wafer of 170µm for a total thickness of 695µm. The AWB machine makes a vacuum so both wafers stick together (silicon + glass). When contact is established both wafers are heated to 370°C and then exposed to high voltage (600V). Under this condition, cations migrate to the glass surface creating an electric field at the glass-silicon interface and the permanent chemical bonding. Under vacuum and high temperatures Van Der Waals bonding between two surfaces is achieved.

IV. Image acquisition

Before the experiments, the membrane structure of the microfiltration cell is characterized. The last steps of the cell fabrication could lead to membrane damage, thus the structure integrality is checked to guarantee the membrane capability of retaining particles/cells.

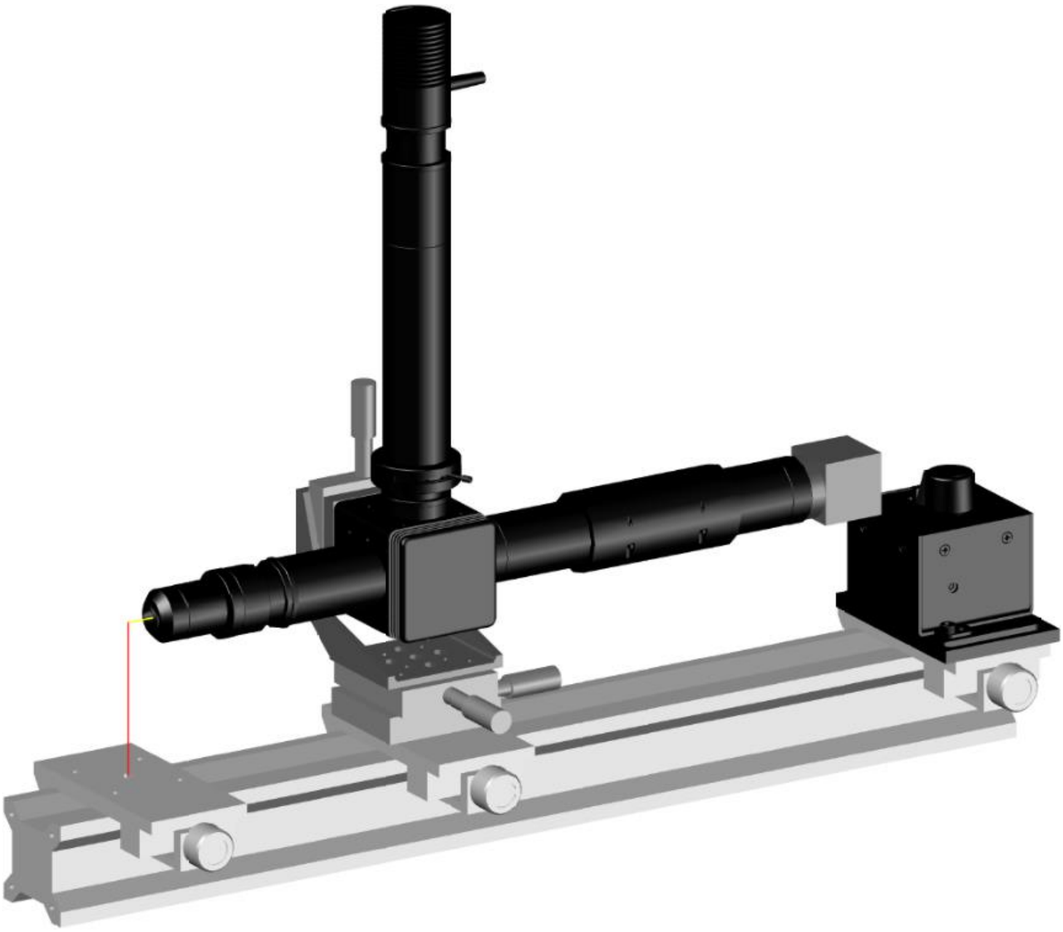

Figure 37. Optical bench design

An optical bench is configured to make possible the observation and the image acquisition (Figure 37). The system principle is the same as a bright field microscope. The sample is lighted through the microscope objective. A light-emitting diode (LED) is used to light the microfiltration observation window. The LED light passes through a collimator to narrow the beam into parallel rays. The narrow beam enters into a fluorescence cube containing a dichroic mirror, which acts as a light filter based on the light wavelength. The mirror reflects the LED light in the direction of the microscope objective lens to light the sample. The sample emitted light pass through the objective lens to the dichroic mirror, this time letting the light to reach the camera sensor. Figure 38 describes in detail the principle of the optical set-up. The optical system is capable of a 10x zoom, being able to observe all the channel width (1 mm) and a limited zone above the membrane (0.8 mm). The image resolution is about 0.6 µm/pix, which is an improvement compared to previous DO set-ups, which were around 1 µm/pix.

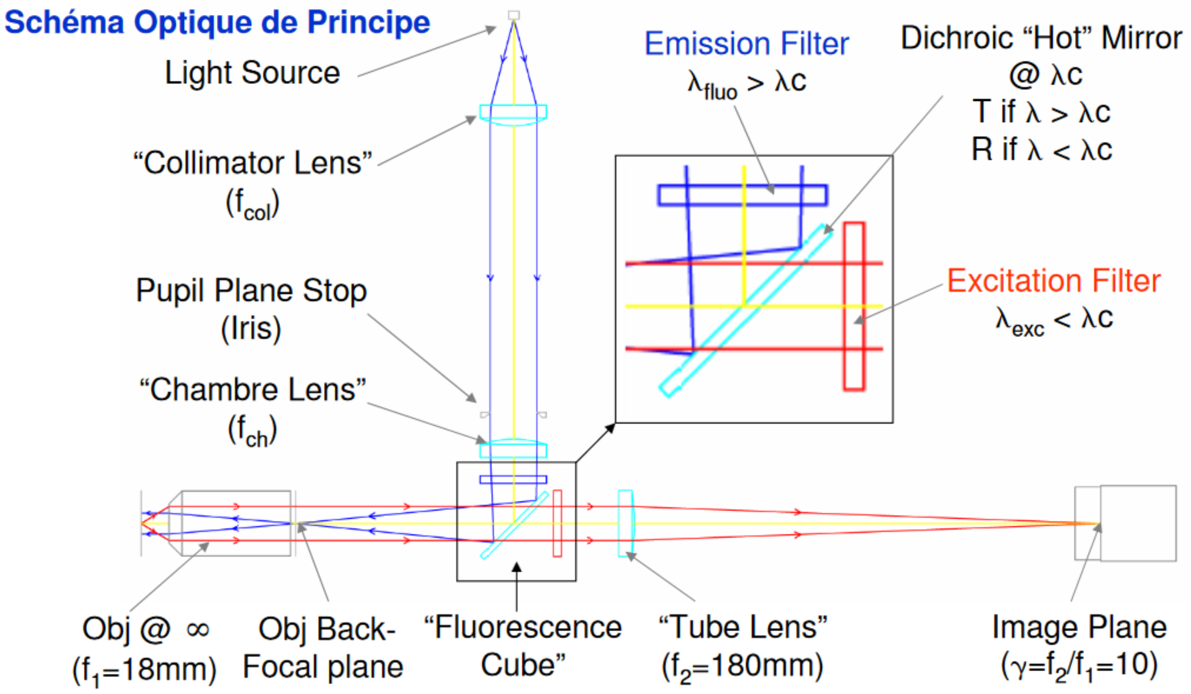

Figure 38. Optical principle of the designed optical set up (By Claude Le Men)

The microfiltration cells are held by an aluminum support. The aluminum was chosen as the support material based on the manufacturing convenience and the material properties. The support allows coupling hydraulic system with the optical bench. The system sensitivity to the pump and surrounding vibrations was studied and considered negligible.

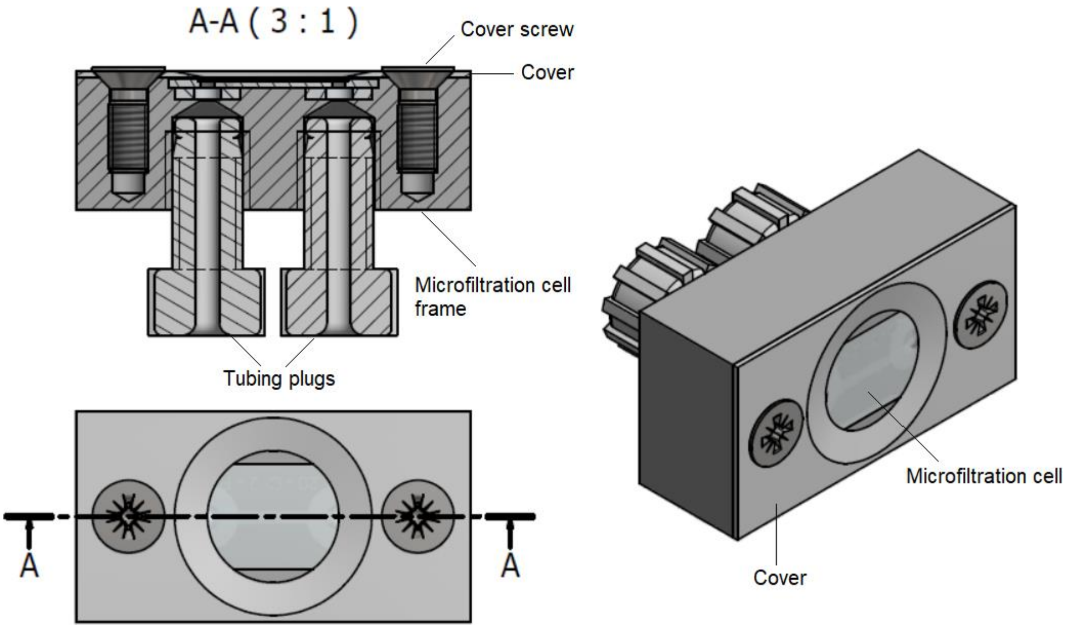

Figure 39. Support for the microfiltration cell

The studied parameters using the image processing are the cake growth, cake mean height, the particle/cell vertical concentration and the local fluid velocity. The cake growth is investigated by measuring the cake mean height throughout the filtration experiment and the concentration is estimated by quantifying the particles/cells in the suspension above the cake. The accurate estimation of these two variables rely on the image size; however, the velocity estimation depends also on the acquisition frame rate. The design of the filtration experiment is determined by the optical set up performance. The following parameters of the optical set-up are key to achieve the aims of the study and design the experiment:

- Image size: to analyze quantitatively the cake height, particle/cell concentration and the velocities, the observation of the whole channel length (*x* direction) is necessary. This way it is possible to capture cake heterogeneity and particle focalization in the flow due to channel imperfections or permeability gradients. These phenomena could lead to false concentration measurements in case of reducing the observation domain in *x*. Besides, a representative zone above the cake (*y* direction) must be observed for the concentration and velocity estimation. The observation window is set of 1650x800 (Figure 40a); this corresponds to a domain of 1000 µm in *x* to observe the whole membrane, 480 µm in *y* (1.25 MB image size). Even if acquiring a square domain was possible, 480 µm height is enough to observe the membrane, the cake and a representative domain above the cake for the concentration and velocity estimations. This choice responds also to the requirements associated with the acquisition framerate for the velocity estimation and the storage capacity.

- The acquisition framerate: it is a function of the observation field and the exposure time. This parameter must be set conveniently in order to register the particle/cell velocity. The exposure time corresponds to the shutter speed and is related to the amount of light reaching the camera sensor. The choice of the exposure time relays on the uniformity of the image background (bottom of the channel) and the particles resolution. A slightly over-exposure leads to a flat background caused by the loss of highlight detail. The texture of the channel bottom is “washed out” from the image to observe clearly the cell and particles with no background interference (Figure 40). For exposure times varying from 100-120 µs an optimal image quality is obtained. At this low exposure time, the key parameter defining the acquisition rate is the image size, which leads the choice of a rectangular domain. A convinient acquisition rate is set at 100 fps to capture particule movement and it is also in agreement with storage capacity.

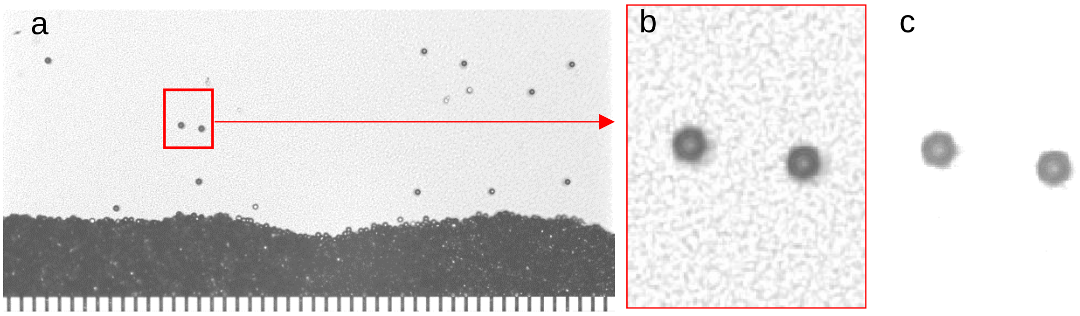

Figure 40. a) Rectangular acquisition domain, b) Lower exposure times reveal the channel bottom texture (zoom) and interfere with further image processing, c) Image using an exposure times in the range of 100-120 µs

- Storage capacity: the last parameter to take into account for the acquisition is the buffer capacity of the computer RAM. The buffer uses the RAM memory to store the acquired images while they are saved on the hard drive and it is necessary as the acquisition rate is higher than the saving rate. When the buffer is full, the upcoming new images are dropped until enough storage capacity is released. Dropping images makes impossible to keep a constant acquisition framerate; this yields an uncertainty in the time between two consecutive images, which hinders the velocimetry analysis. The buffer maximal capacity is 8000 frames and is calculated as the RAM capacity divided by the size of an image in MB. The acquisition is finished when the buffer is full, this limits the filtration experiment duration.

V. Image processing

A specialized Python code is used to analyze the acquired information. This code has three modules: the particle velocimetry module (PVM), the particle concentration module (PCM), and the cake growth monitoring module (CGM). All modules use an identification function and a dedicated algorithm to extract the desired information: the cake height or the deposited mass, the velocity and the concentration. Once the objects are identified, they are parametrized based on the shape and size, for the particles/cells and the position for the cake. In addition PVM has a correlation function that allows to identify particle trajectories. The standard platform for Python data science Ananconda is used.

V.1. Cake growth monitoring

After contours are identified, the CGM uses the position filter to classify a contour as a part of the cake. When the cake is found, the coordinates of the surface are extracted and then the cake mean height and heterogeneity are determined.

Identification function

A contour is the set of coordinates defining the bounds of a shape or object. The Python's Open CV library find the contours in an image and allows the calculation of the specific properties associated to the objects. The contours properties used in the identification code are the contour coordinates, the area, the minimum enclosing circle and the extreme points.

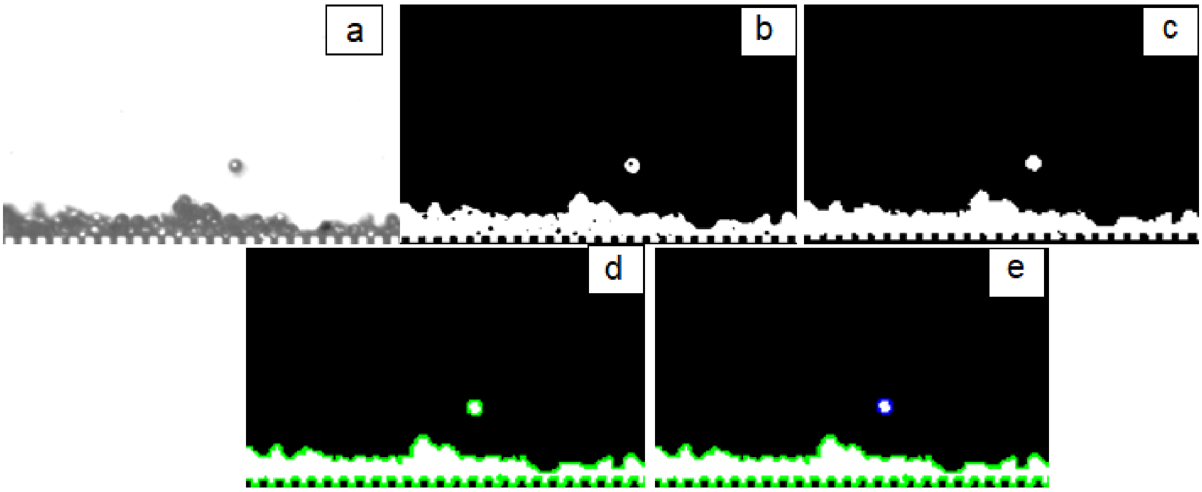

Figure 41. Results from the different steps of the identification code

In order to find the set of coordinates of every contour in an image the following protocol is used: first, the raw image is imported (Figure 41a). After that, the image is binarized so the contours can be found easily (Figure 41b). Having the image binarized the voids are filled to avoid finding concentric contours (Figure 41c), then contours are identified (Figure 41d) and so their coordinates. The contours properties are calculated; in the case of the deposit identification, only the contour coordinates are used to classify the object. Then, if at least one of the contour y_i coordinate matches with the membrane coordinate y_m the contour is considered as part of the filtration cake. The diagram in Figure 42 explains the deposit identification algorithm.

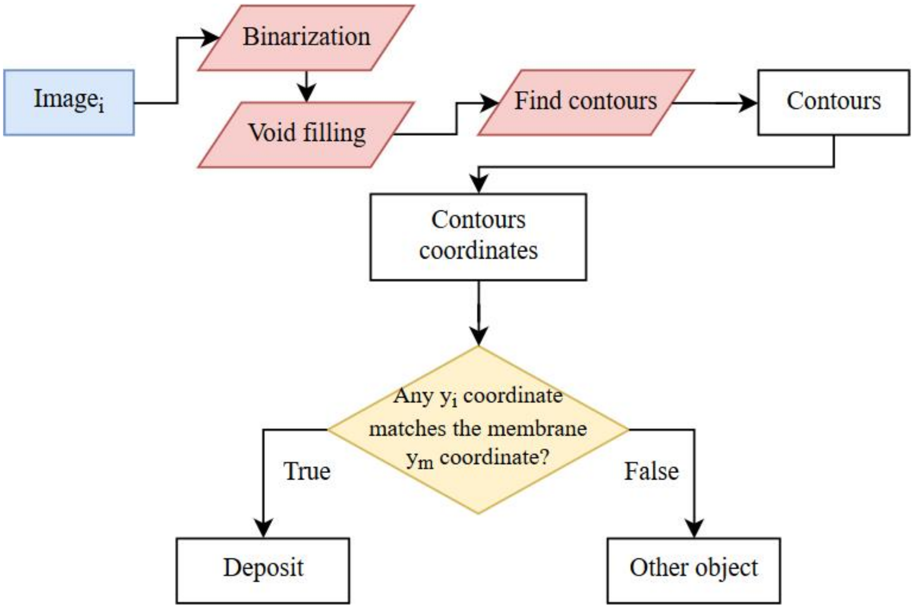

Figure 42. Code diagram for cake deposit identification

V.2. Particle concentration module (PCM)

Once the contours are classified, there are two approaches to calculate the concentration. For the first approach, the number of contours is related to individual spherical particles, which have a known volume. Then, dividing the particles cumulative volume by the observable channel volume provides an estimate of the concentration.

$$C(\%) = \frac{n \cdot \frac{4}{3}\pi r^3}{V_c} \cdot 100$$

Eq. 17

The second approach consists in inspecting each pixel line to evaluate the particle presence as a 1D binary signal. The 1D signal is extended into 2D surface information assuming that particles/cells cross section corresponds to spheres of a characteristic size, which is a fair approximation even for yeast cells. Figure 43 illustrates the signal operation. The ratio of the total estimated particles surface to the channel cross section yields a measure of the vertical concentration profile.

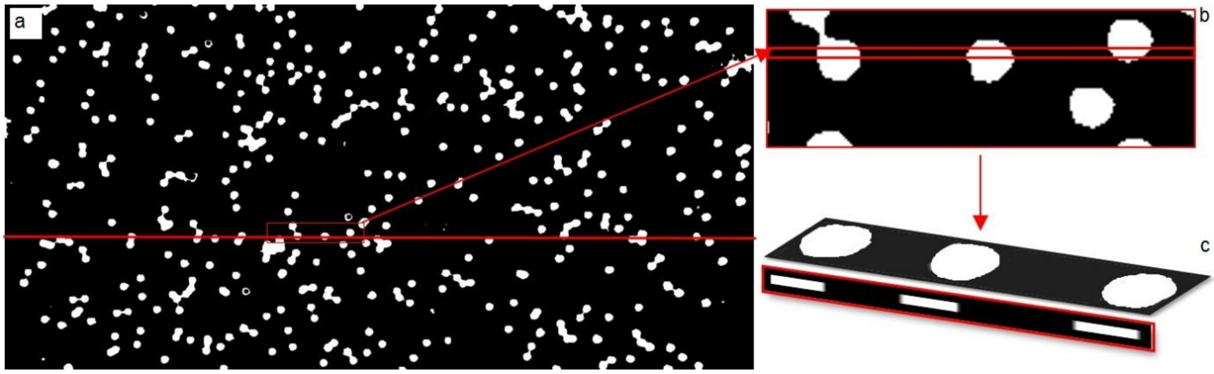

Figure 43. a) Inspection of a line of pixels for the concentration estimation, b) The particle presence is evaluated for a fragment of the line, c) The 1D presence signal extended to 2D surface information assuming spheres as particles/cells cross section

The first approach obtains a mean value of the concentration. This method results accurate when estimating the concentration of spherical particles. When calculating the concentration of non-spherical particles the assumption of spherical volumes for the *n* identified objects becomes less accurate. Changing the characteristic volume V_c by the volume of a peanut particle solves the problem. Nonetheless, this problem does not have such an evident solution for the calculation of yeast cells concentration due to the size distribution and the presence of aggregates. The second approach can be applied for all the suspensions. The assumption of circular cross sections is more accurate than the first method for yeast and peanut shapes and it takes into account the possibility of yeast cell aggregation. The first approach is used for spherical and peanut particles while the second approach is applied for the polydispersed and yeast suspensions.

V.3. Particle velocimetry module (PVM)

For the PVM the algorithm is developed according with previous studies [109], [110]. This function allows one to relate particles at consecutive instants and hence re-construct the trajectory of a single particle. Knowing the time interval Δt between the acquisition of consecutive images, it is also possible to calculate particle velocities. However, while individual tracking of particles is possible, it takes a long calculation time. This method is mainly used to study particle trajectories when a preferential flow in a certain zone of the membrane is observed. Another approach is used to estimate the mean velocity and it is based on the vertical concentration profile calculated using the PCM. The autocorrelation of the concentration profiles at two consecutive instants is used in order to find the velocity at which the concentration front arrives to the cake. This provides an estimation of the mean velocity. For each method, a sampling is done to compare the code results to the values calculated directly from the images. The two approaches are explained below.

Identification function

The same algorithm used for the cake identification is applied to identify the particles; the difference lays in the applied filters. Instead of using the position obtained from the contours coordinates, the size and shape properties are used as the filtering parameters. Only the objects with surface higher than 30 (characteristic pixel surface) and a shape ratio over 0.8 are considered particles (Figure 41e). The diagram in Figure 44 explains the particle identification algorithm.

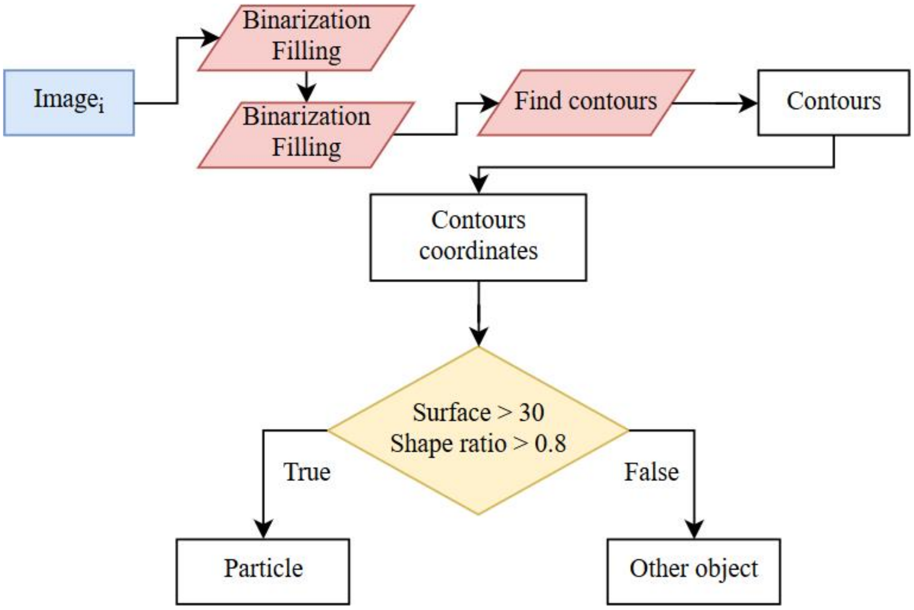

Figure 44. Particle identification code applied to every image of the data set

Correlation for particle tracing

The correlation code makes possible to relate an identified particle at a given instant i with the corresponding particle at the instant $i + 1$. To achieve that, two matrix are created at the two consecutive instants *i* and *i+1*. First, the reference matrix *R (m,n)* at the instant *i* is constructed with the pixel values (0-255 grayscale) of the image enclosing the particle. Figure 45 exemplifies the definition of the reference matrix at the instant *i*, the zoomed zone corresponds to the image that represents *R*.

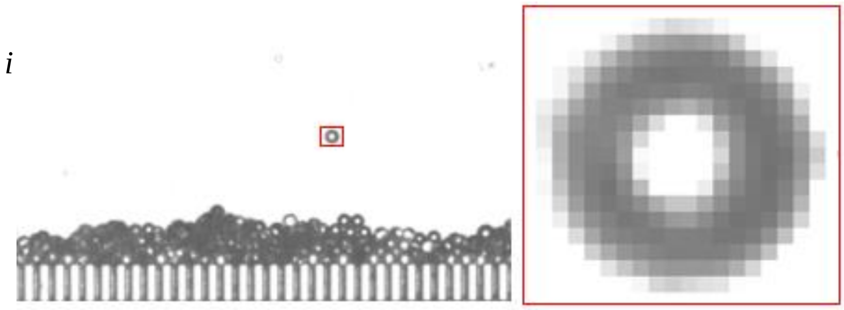

Figure 45. Example of a particle deposit. Extraction of the reference matrix

The second matrix is called research matrix T. This matrix is constructed using the pixel values from the image at the instant $i+1$. The size of the research matrix (M,N) is defined based on the theoretical maximum velocity of a particle in the fluid, which is $V_{max} = 1.5\bar{V}$. With the velocity and the acquisition frame rate it is possible to calculate the expected maximum displacement in pixels. This expected displacement in pixels helps to define the research zone at image $i+1$. Even if the research matrix size is predefined it could change if the particle is not found in the zone. This suggests a possible unexpected acceleration being the cause of the particle getting out the research zone. Figure 46 illustrates the concept of the research matrix, the research zone (zoom) is defined using the paticle coordinates at the instant i and the expected displacement.

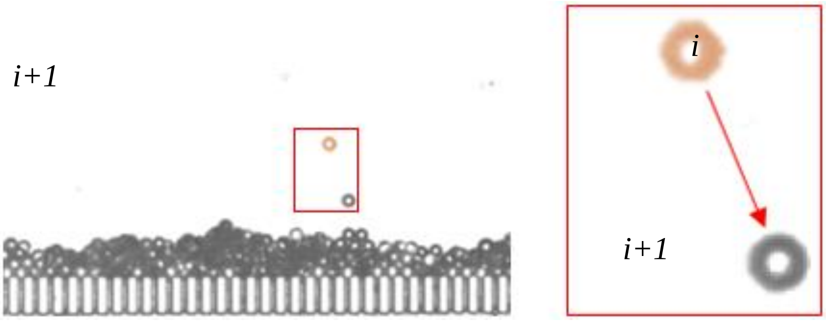

Figure 46. Construction of the research matrix at the instant (i+1). The particle in red shows the position at the instant (i) as it is possible to compare in Figure 45.

After the definition of the two matrices R and T, the Sum of Absolute Differences (SAD) method is applied and so the correlation matrix is calculated. This matrix allows to find the position of R in T with the highest correlation. The SAD method creates a matrix for which each entry corresponds to the difference between the pixel values of the identified particle at the instant i and the pixel values of the image at the instant $i+1$. The SAD algorithm is given by the following expression:

$$S(i,j) = \sum_{x,y=0}^{M-N} |T(i+x, j+y) - R(x,y)|$$

Eq. 18

The size of the SAD matrix is given by the size of the tracking matrices *(M-m,N-n)*. Figure 47 shows the diagram of the correlation algorithm, when the highest correlation of the SAD matrix is lower than an estimated minimum correlation, the matrix *T* is re-sized *(M,N')* with *N' > N*. Then the SAD method re-applied and the correlation checked.

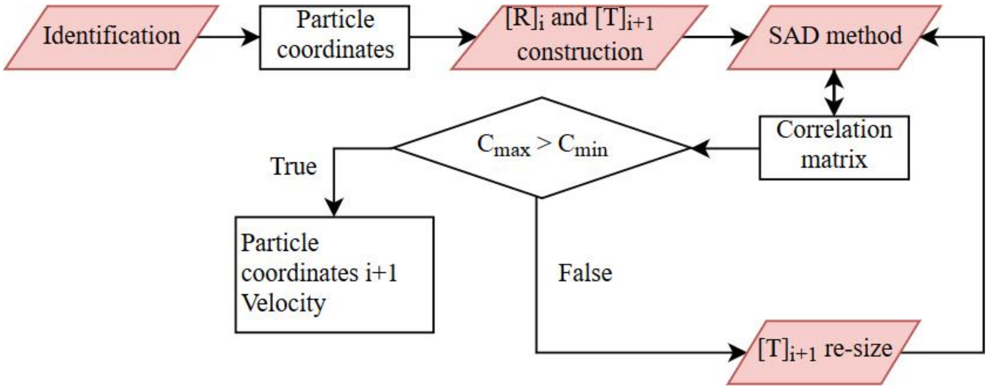

Figure 47. Diagram of the correlation algorithm

Figure 48 explains in detail a simplified case using the SAD where the reference matrix *R*, is square matrix of (2,2), and the research matrix (3,3). It's possible to observe the four available position of *R* in *T*, and how the correlation is defined by de difference in the pixel values of the two matrices at each position. The minimum value corresponds to the highest correlation and the most probable position of the particle at the next image.

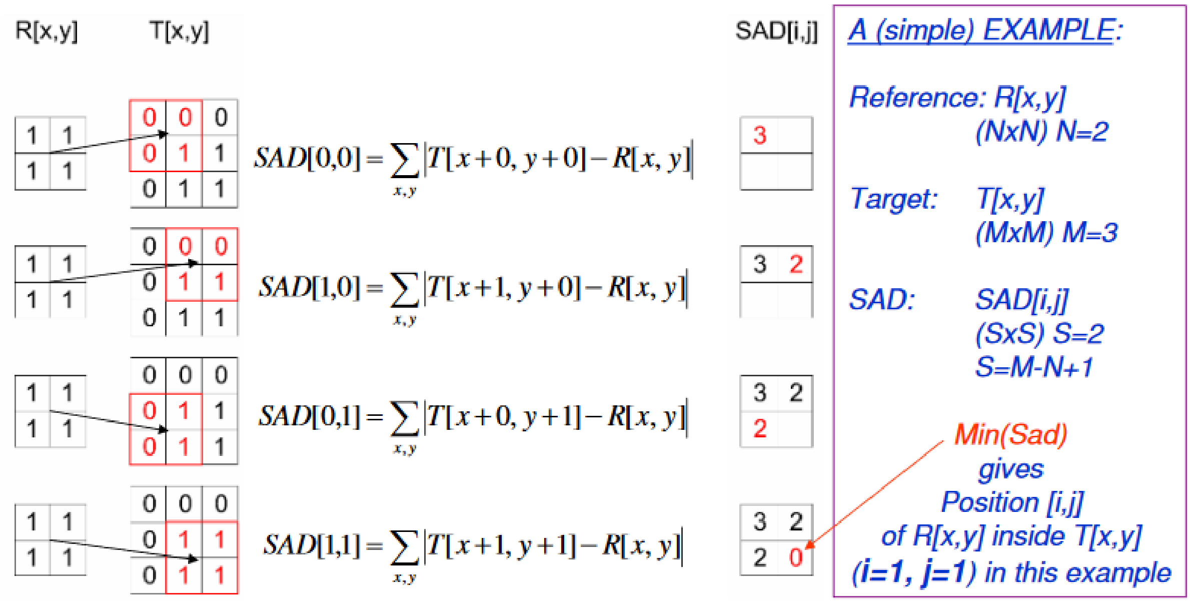

Figure 48. Simple example of the SAD method

Figure 49 shows the diagram of the particle tracing code. Double lined entities (Images, Objects Particles, Tracing) represent group objects that are either iterated in a loop or used as storing vectors, lists or information matrices. Simple lined color entities correspond to a single element from the group of the corresponding color. Red boxes are code functions and gray boxes are control flow statements or simple python operators (for, append). The diamonds represent conditions. The “for” boxes are always related to the group of entities they operate in the loop by a double direction arrow. It is important to follow the color code as well as the sub-indexes, which denote the time instant.

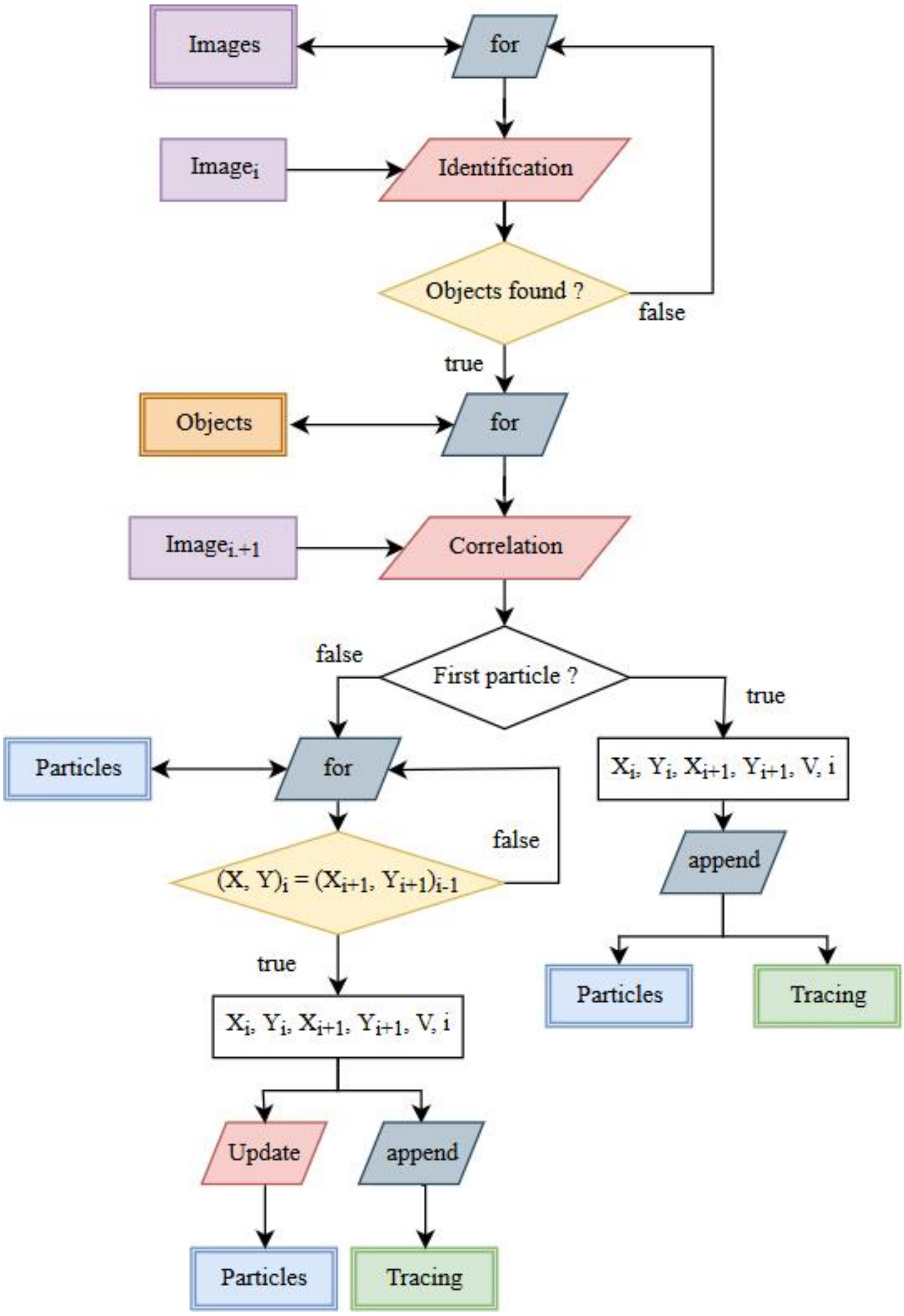

Figure 49. Diagram of the particle tracking code

The particle tracing component of the PVM module produces a **Tracing** list. The Tracing list contains *n* entries, with *n* the total number of filtrated particles in the analyzed period. Each entry is created when the particle is first spotted and it registers the instantaneous information of the particle: the current coordinates $(x,y)_i$ in pix, the coordinates at the next instant $(x,y)_{i+1}$ in pix, the current particle velocity V_i in pix/frame and the instant number *i*. All the particle positions are registered until the particle arrives to the filtration cake. First a “for” loop is used to affect the desired **Images** from the experiment registered in a file directory. The first image ($i=0$) is analyzed using the identification function. In case there are no particles the “for” loop pass to the next image until at least one particle is found. When the first particle or group of particles are found, the **Objects** temporary list is created with the coordinates $(x,y)_i$ an the given ID of all the identified particles at the instant i. Then, a “for” loop allows to use the correlation function to find the coordinates of every particle at the next instant $(x,y)_{i+1}$ and to deduct the velocity (with Δt=1/fps). The **Particles** list is created and contains only the updated information of an identified particle. For that, the **Objects** information at the at the instant $(x,y)_i$ are compared with the **Particles** information updated at the previous instant $(x,y)_{i-1}$. For the matches the information is updated in the **Particles** list, otherwise it means that a new particle entered in the observed domain. The **Tracing** list keeps all the information of any identified particle (not only updated) so the traces are re-constructed.

Concentration front autocorrelation

An intermediate stage of the application of the PCM module quantifies the presence of particles in each pixel line before obtaining the actual concentration. The result at this stage is the vertical profile addressing particle presence in the suspension above the cake. This information is registered as a signal. The velocity is then estimated through the autocorrelation of the particle presence signal $\vec{r}(1,n)$ and $\vec{t}(1,N)$ at the instants i and $i+1$ respectively ($N > n$).

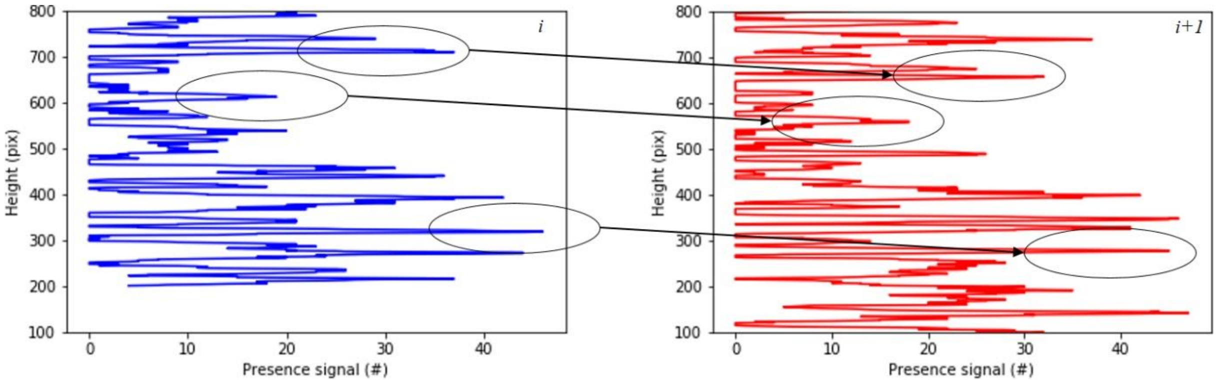

Figure 50. Particle presence vector at to consecutives instants of a filtration experiment. The displacement of this signal in time gives an estimation of the velocity.

The SAD method principle is used for the autocorrelation of the presence signals (Figure 50). This way it is possible to estimate the particle concentration front displacement from the instant i to $i+1$. The SAD algorithm adapted for operate the presence vectors is:

$$\vec{S}(1,j) = \sum_{y=0}^{N-n} |T(1,j+y) - R(1,y)|$$

Eq. 19

VI. Numerical simulations

In order to characterize our system from a numerical point of view it was analyzed using the commercially available finite element code COMSOL Multiphysics^{TM}. The simulations are addressed in order to dimension and check the measurement tools related to the pressure and particles velocity and thus to have theoretical insight on the behavior of the system. The simulations were focused on the microfiltration cell performance as well as the early stage of the cake formation. The stationary laminar flow was solved for the entire system without the membrane, with the membrane, and the membrane-cake interaction simplified geometry. For that, a simplified geometry and domain are defined. The mesh is selected using a sensitivity analysis and the results are analyzed using the Darcy equation.

VI.1. First layer hydraulic resistance:

Geometry and equations

The simulated domain in COMSOL is defined according to the ideal case where the migration of latex particles is initially and preferentially to the slots defined by the spaces between the consecutive walls. An optimal distribution of the space in the filtering channel allows a limited number of particles to lie above the filter. Regarding the previous description of the ideal case, the geometry is simplified taking into account the symmetry of the system. Figure 51 shows the different simulated domains as well as the simplified zone, all to be divided into several finite element for the calculations. Figure 32 shows the different configurations for which the system is parametrized.

The model is built and parameterized as function of the slot width *C* and the periodic feature of the different configurations *Pe*. Navier-Stokes equations are simplified for the Stokes flow regime ($Re < 1$) of an incompressible fluid. The three dimensional domain (Figure 51) is modeled; as the channel depth is small, wall effects should be taken into account for the depth dimension of the filtration unit (30 µm). Navier-Stokes momentum and continuity equations are then simplified. The equation system solved by COMSOL is:

$$0 = -\nabla p + \nabla.\left(\mu(\nabla u + (\nabla u)^T)\right)$$

Eq. 20

$$\rho\nabla.(u) = 0$$

Eq. 21

The boundary conditions when the system is entirely simulated (Figure 51a and b) were set as walls with no slip condition besides the inlet and the outlet (red and blue surfaces respectively. For the membrane-cake interaction from the upper view in Figure 51d, the bottom and top boundaries (edges) were considered walls while the side boundaries were considered symmetric to simulate a periodic domain. This is a fair assumption as the membrane length ratio to the channel depth is much higher than 1. The inlet corresponds to the red highlighted surface at the top in Figure 51c and the outlet corresponds to the bottom blue surface.

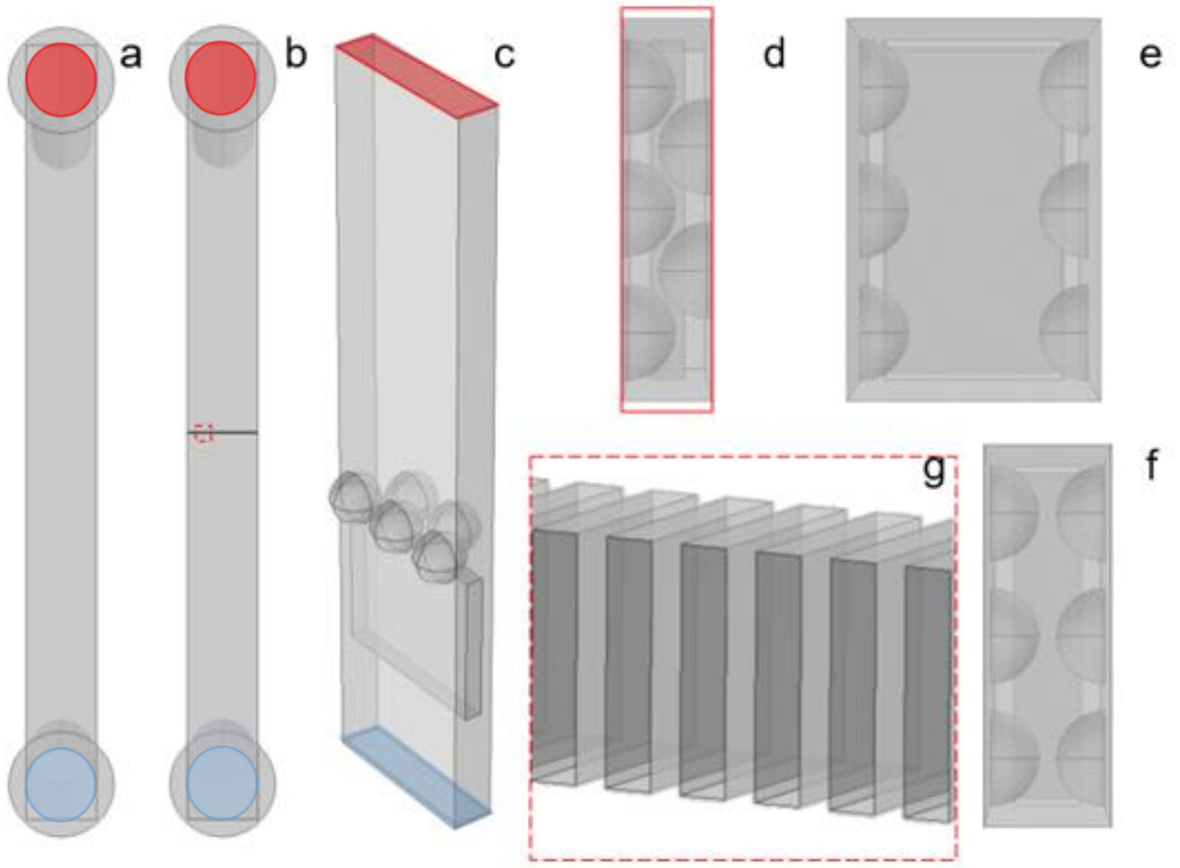

Figure 51. a) Entire geometry without the membrane*. b) Complete geometry with the membrane*. c) Simplified geometry for cake-membrane interaction (first layer C4Pe7)*. d,e,f) Upper-view of the simplified geometry for C4Pe7, C4Pe20 and C4Pe10 units respectively. g) Detail on the membrane for the simulated geometry (channel + membrane for C4Pe10 unit). * The red surface corresponds to the inlet and the blue to the outlet.

The evolution of the velocity was studied through all the channel length, providing knowledge of where the flow is fully developed under the influence of the channel entrance, exit and the membrane.

Initial conditions

For the initial conditions a reference pressure of 0 Pa is set on the outlet (Figure 51c blue plane) so it is possible to measure the transmembrane pressure (TMP) as the pressure difference at the inlet (Figure 51c red plane). The initial velocity is calculated based on the experimental flow rate of 10 µl/min divided by the corresponding section and set as the normal velocity at the inlet. The domain upwards the membrane is long enough for the flow to be fully developed. The fluid is set as 20° C water /glycerin mixture with a density of 1060 kg/m^3 and a viscosity of 2x10^{-3} Pa.s.

Hydraulic resistance model

Knowing the TMP as well as the velocity it is possible to use Darcy's equation to calculate the serial hydraulic resistance model for the membrane and the thin layer of particles:

$$J = \frac{1}{\mu(R_m + R_c)} TMP$$

Eq. 22

Where J (m/s) is the filtration flow rate, μ (Pa·s) is the dynamic viscosity, $R_{m,c}$ (m^{-1}) the membrane and cake resistances and TMP (Pa) the transmembrane pressure.

VII. Data analysis

The cake observed height obtained from the CGM, the concentration from the PCM and mean velocity from the PVM combined with the manometer continuous pressure logs yield important quantitative information. This information leads to a dynamical analysis of the microfiltration process. Combining the quantitative information with the qualitative interpretation of the acquired images also allows concluding on important cake structural features.

Mass balance: porosity and K_K

A mass balance is performed to estimate the porosity and the Kozeny coefficient. First, the system behavior is characterized for the spherical particles for which the K_K is known equal to 5 [75]. The mass balance is achieved comparing the observed cake height $\bar{h}_o$ to the integration of the particle flowrate variation *QC* through the experiment. This allows calculating the height $\bar{h}_c$ corresponding to a cake with no porosity. In Eq. 23 the result of the mass balance yields the porosity estimation ϵ_h as a function of the observed and calculated heights ($\bar{h}_o$ and $\bar{h}_c$ respectively).

$$\epsilon_h = 1 - \frac{\int QCdt}{S}\frac{1}{\bar{h}_o} = 1 - \frac{\bar{h}_c}{\bar{h}_o}$$

Eq. 23

with *Q* ($\mu m^3/s$) the flow rate, *C* (% V/V) the concentration computed using the PCM and *S* (μm^2) the area of the channel cross section. When comparing the calculated height $\bar{h}_c$ with the observed height obtained from CGM, the porosity is estimated.

Nonetheless, in order to validate the previous analysis, the porosity is also calculated using the Darcy equation (Eq. 8) and the Carman-Kozeny formula (Eq. 13). It uses also the definition of the hydraulic resistance to assess the effect of both the membrane and the cake on the global dynamics.

$$\frac{Q}{S} = \frac{\Delta P}{\mu(R_m + R_c)}$$

Eq. 24

The series model of the total hydraulic resistance ($R_T = R_m + R_C$) allows decomposing it into the sum of the membrane and cake resistances, R_m and R_c respectively. The cake hydraulic resistance is $R_c = L/K$, with $L = \bar{h}_o$ the observed cake height and K as presented in Eq. 13. The Eq. 25 provides another estimate value for the porosity of a cake of spherical particles, using the pressure data and $K_k = 5$.

$$\frac{Q}{S} = \frac{\Delta P}{\mu\left(R_m + \frac{\bar{h}_o K_k S_p^2 \left(1-\epsilon_p\right)^2}{\epsilon_p^3}\right)}$$

Eq. 25

with ΔP (Pa) the trans-membrane pressure, μ (Pa·s) the dynamic viscosity, R_m (m^{-1}) the membrane hydraulic resistance, $\bar{h}_o$ (m) the cake height, S_p (m^{-1}) the specific surface of the particles and K_k the Kozeny coefficient. The porosity ϵ_p, is the only unknown parameter and is calculated as a function of the pressure. This approach is accurate since the whole channel depth remains within the optical depth field of the observation set up, hence the information loss in the depth dimension when calculating the concentration and the cake height is negligible. The estimated values of the porosity are compared and then the analysis is validated for implementing the methodology for the other suspensions (Peanut, polydispersed and yeast suspensions). For the experiments with peanuts, polydispersed and yeast suspensions, only the porosity ϵ_h is estimated (Eq. 23) and then used as an input for estimating the K_K from Eq. 25.

The different components of the total resistance $R_t = R_m + R_c$ are calculated from the raw data. Then the permeability of the cake $K_c = \bar{h}_o / R_c$ is used in order to characterize the filtration performance throughout the filtration. In order to analyze the compressibility of the cakes formed by different particles, the hydraulic resistance $R_c = \alpha m$ is expressed in terms of the deposited mass per unit surface m (kg/m2) and the specific resistance α (m/kg). The compressibility has an effect on the specific resistance which can be expressed as a function de the pressure as follows:

$$\alpha = \beta \Delta P^n$$

Eq. 26

For β (m^{-1}) the specific resistance coefficient and n the compressibility index. The compressibility index is 0 for non-compressible behavior and it reaches values of 0.9 for highly flocculated compressible sludges [42], and compressible cakes; Higher values than the unity are reported for highly compressible cakes [111]

Chapter IV: System validation and cake microfiltration characterization using a model suspension of spherical monodispersed particles

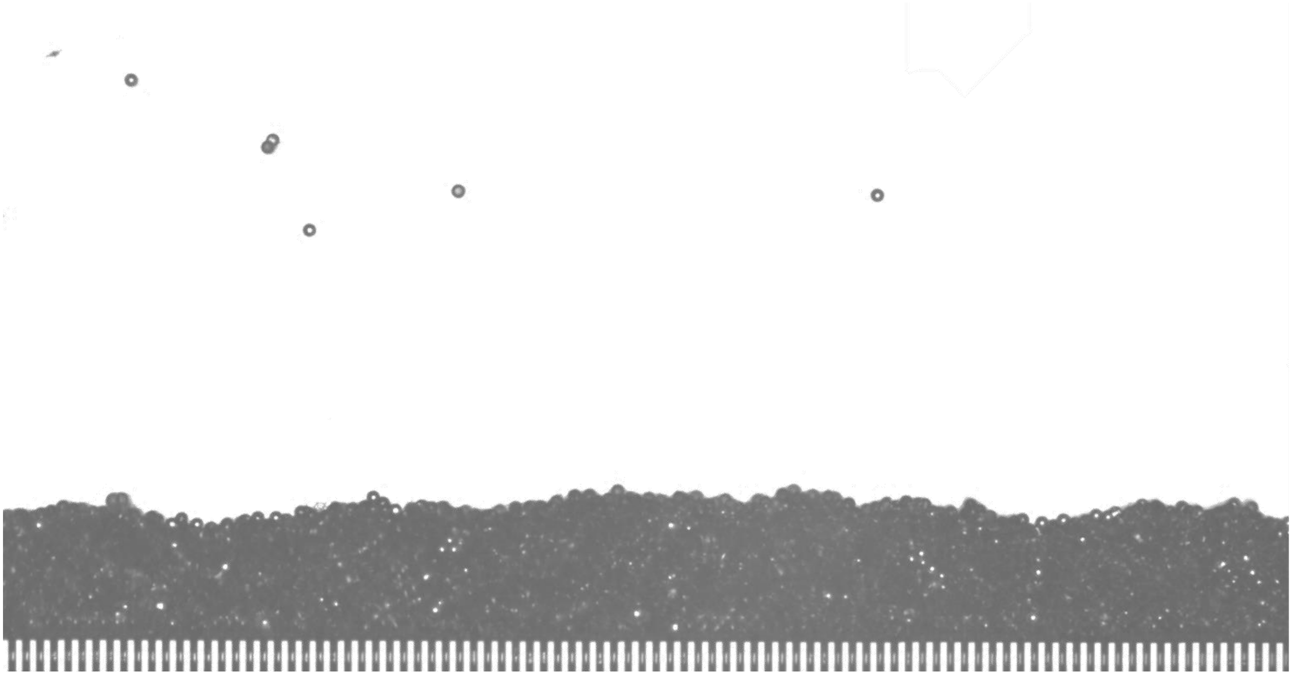

Before starting an experimental campaign to explore the mechanism of microfiltration fouling phenomenon, a validation of the whole system is conducted to ensure the capability of the experimental set-up to perform the experiments and the reliability of the optical device and image acquisition system. Further investigation leads to the characterization of the filtration fouling addressed by the suspension of monodispersed spherical particles.

The experimental protocol and analysis guidelines described in Chapter III: Materials and methods are the result of the validation and characterization stages and they were applied in all the filtration experiments for the different suspensions. Only the protocol regarding the suspension preparation is different for the yeast and polydisperse suspensions. Various adaptations of the initial protocol are required to avoid drawbacks like the presence of dust and gas in the system, to ensure the reliability of the pressure measurements and to avoid leaks in the system. The image processing procedure was first developed based on a preliminary filtration tests and it was further adapted to better analyze the different observed phenomena that are involved in membrane blocking, particle deposition and organization in the cake. The model suspension of spherical particles was used to validate both the system and the analysis and to characterize the fouling addressed by monodispersed spherical particles. The experiments analyzed in the present chapter contribute to create a database for further comparison, thus allowing better understanding of the fouling and cake behavior of more complex suspensions. In the results here below, three type of experiments are compared, the reproducibility of the presented data (standard deviation) is not shown to make the analysis clearer. The information is presented in the annexes for C4Pe20 membranes, for which three experiments were performed to investigate the reproducibility. Supplementary experiments should be conducted in order to provide data and be conclusive on C4Pe7 and C4Pe10 units reproducibility.

I. System characterization

The four different configurations of the filtration units (C2Pe5, C4Pe7, C4Pe10 and C4Pe20 shown Figure 32) were characterized and compared with the theoretical values. The characterization consists in checking the filtration unit condition (membrane integrity, absence of collapsed walls, no misplacement of the inlet or the outlet, etc), as well as the filtration performance by measuring the pressure drop of the clean membrane and the volume required to fill the system.

To do so, the system is filled (at 10 µl/min) with the water - glycerin solution in the opposite direction to that used in the filtration experiment (pushing mode) until fluid reaches the reservoir (Figure 27 and Figure 52b). The time to fill the system is registered; with a known constant flowrate

(10 µl/min), it is thus possible to check the volume of the system. To measure the pressure drop of the clean membrane, after the solution reaches the reservoir, the flow direction is set in the filtration direction (pulling mode) and the pressure evolution is registered until the stationary condition is established.

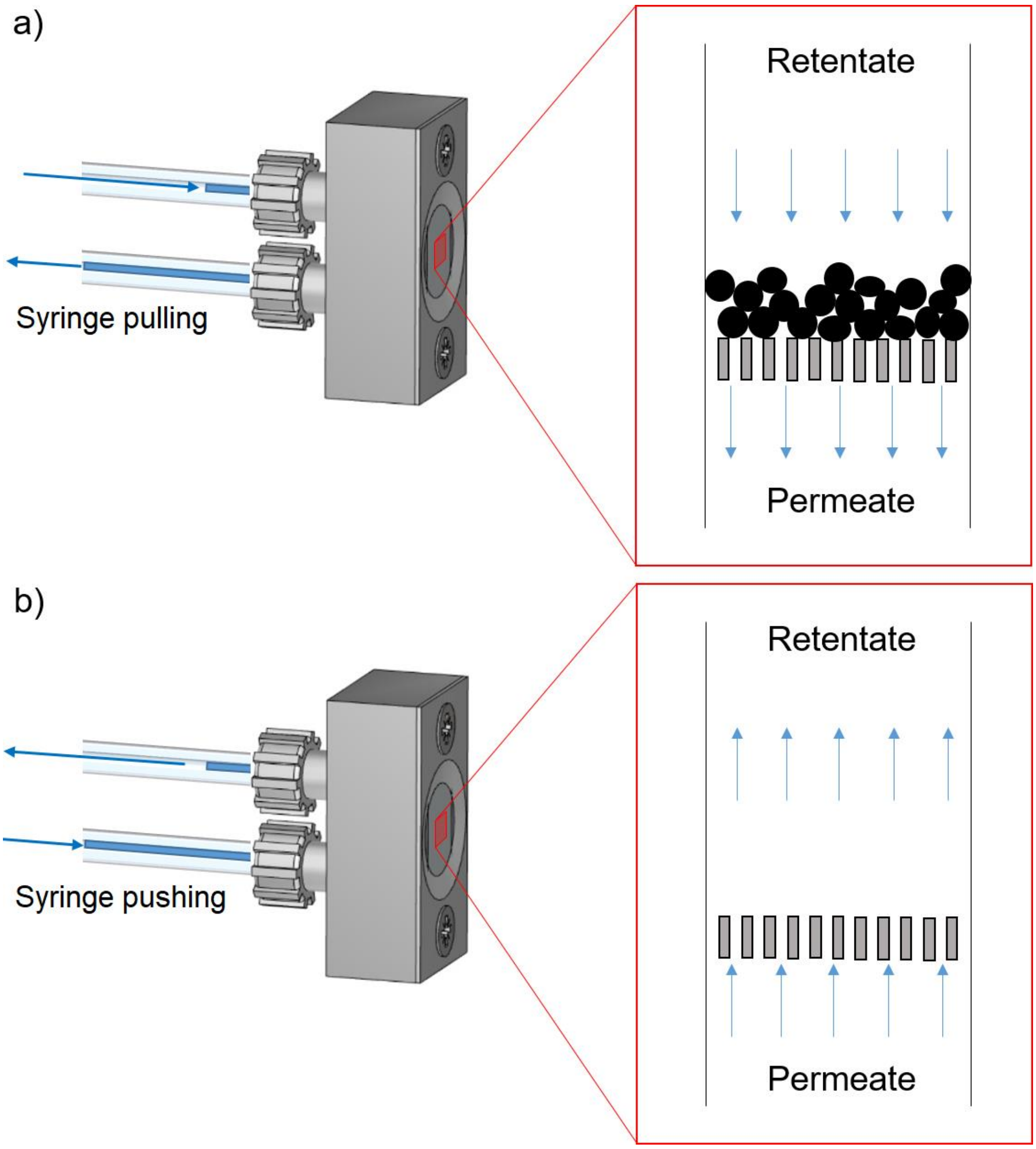

Figure 52. a) Syringe pulling to establish the flow in the filtration direction. b) Syringe pushing to fill the system

For the validation, the experimental results are compared to theoretical calculations of the system volume and the pressure based on the geometrical design. Darcy-Weisbach equation is used to calculate the pressure drop.

$$h_f = \lambda \frac{L}{D_h} \frac{v^2}{2g}$$

Eq. 27

with L (m) the length of the channel, D_h (m) the hydraulic diameter (tubing, channel and slots), v (m/s) the flow velocity and g (m/s^2) the gravity constant. The Darcy coefficient λ is calculated assuming laminar regime as 64/Re. Table 8 and Table 9 summarize the pressure drop calculations in the system. The viscosity used for the calculation of Re is μ = 2x10^{-3} Pa·s for the water-glycerin solution.

Table 8.Calculations for the pressure drop in the tubing and the channel upstream and downstream the membrane

Element	Dh (m)	L (m)	v (m/s)	Re	λ	ΔP (mbar)
Tubing	1,00E-03	9,00E-02	2,12E-04	1,12E-01	5,69E+02	0,02
Channel	5,83E-05	1,15E-02	5,56E-03	1,72E-01	3,73E+02	12,05

Table 9. Calculations for the pressure drop due to the different membrane configurations. ΔP total takes into account the pressure drop in the tubing and the channel previously calculated in Table 8.

		C2Pe5	C4Pe7	C4Pe10	C4Pe20
Number of slots	N (units)	200	142	100	50
Slot width	C (m)	2,00E-06	4,00E-06	4,00E-06	4,00E-06
Slot distance	d_p (m)	3,00E-06	3,00E-06	6,00E-06	1,60E-05
Porosity	ϵ	0,40	0,57	0,40	0,20
Velocity in the slot	v_p (m/s)	1,39E-02	9,72E-03	1,39E-02	2,78E-02
Slot hydraulic diameter	Dh_p (m)	3,75E-06	7,06E-06	7,06E-06	7,06E-06
Reynolds slot	Re_p	2,76E-02	3,64E-02	5,20E-02	1,04E-01
Darcy Coefficent, λ	f_p	2,32E+03	1,76E+03	1,23E+03	6,16E+02
ΔP slot	ΔP_p (mbar)	15,80	3,12	4,46	8,92
ΔP total	ΔP_t (mbar)	27,88	15,20	16,53	20,99

The pressure drop across the clean membrane is important for the further analysis of the filtration cake properties and must be taken into account for decomposing the contributions of the tubing, channel, membrane and the cake to the total hydraulic resistance of the system. The hydraulic resistance of the device when the membrane is clean R_m must be known, then R_m is subtracted from the total resistance R_t when cake is forming to yield the cake contribution to the resistance and the estimate of the cake permeability.

Table 10. Volume of the system (*V*) and pressure drop (*ΔP*) obtained for the different microfiltration units. Comparison between the calculated values and the experimental results from the characterization

Filtration unit	Calculated V (µl)	Mean V (µl)	Std (V) (µl)	Calculated ΔP (mbar)	Mean ΔP (mbar)	Std (ΔP) (mbar)
C2Pe5	19.6	21.1	1.62	27,87	37.00	8.00
C4Pe7				15,19	15.67	4.89
C4Pe10				16,53	22.50	7.50
C4Pe20				20,99	25.20	3.44

The statistical analysis in Table 10 confirms that the measured volume of the system is in agreement with the calculated volume from the cell design. The deviation of the measured volume from the mean value remains small. The pressure drop measurements exhibited a higher deviation from the mean value especially for C2Pe5 units; however, pressure always reached the stationary condition. This could be explained by the precision of the plasma etching technique when the geometry detail is very fine like in the membrane slots, which could have an effect on the pressure difference. Another factor conditioning the plasma etching result, that could have an effect on the pressure drop, is the position of the filtration unit in the wafer as explained in Chapter III: Materials and methods, Section I.III.

The operating flowrate (10µl/min), obtained with the syringe pump, is also checked using the experimental set-up. Following the characterization procedure, the system is filled until the water – glycerin solution reaches the reservoir (in "pushing mode" Figure 52b); at this point, the reservoir is detached from the tubing and filled precisely using a micro-pipette (in the range from 1-10 µl) with the desired volume to test the flowrate. To do so, the reservoir can be easily attached to the pipette, which makes it an easy procedure to control the injected volume with precision. The filled reservoir is reconnected to the system and the syringe pump is turned on in the filtration flow direction (pulling mode Figure 52a). The time required for the pump to empty the reservoir is registered and so the flowrate is checked. This process confirmed that the syringe pump was delivering the desired flowrate. The whole validation and characterization leads to the conclusion that the microfiltration cells are consistent and the syringe pump provides the set point flowrate.

Knowing the pressure at the stationary condition and the volume required to fill the system, it is easier to check each microfiltration unit before performing the filtration to run a successful experiment. The characterization is always followed by a filtration experiment. When the system volume is filled and pressure difference reaches the steady state value, the particle/cell suspension is injected. The image acquisition starts approximately when the system volume has been discharged for a flowrate of 10 µl/min.

The validation and characterization process allowed to get information regarding the imaging performance of the optical device for different parameters that are studied (Exposure time, contrast, image size vs. acquisition rate compromise). From these preliminary tests conducted to validate the filtration set-up, the experimental protocol and the conditions for image acquisition could be optimized (camera exposure time, calibration of the image processing parameters).

II. Experiments with a model suspension of spherical monodispersed particles

The experimental strategy previously described for the system characterization and the protocol presented in Chapter III: Materials and methods, was followed for the filtration of spherical particles and to study the influence of the membrane geometry on the initial blocking and the cake structure. From the instantaneous mean height of the cake, the mean concentration above the cake surface and the particle velocity it is possible to monitor the cake growth, to perform a mass balance and to describe the cake structure related to the porosity. The porosity (Eq. 23) and the Kozeny coefficient (Eq. 25) of the resulting deposit are calculated and analyzed. The estimated porosity is checked using Eq. 25 with $K_K = 5$. The permeability is also calculated for characterizing the cake properties and further comparing with the other suspensions.

A qualitative analysis of the filtration is achieved through the observation of the acquired sequence of images. The images of the first layer formation allows observation of the characteristic induced structures related to the different membrane configurations. As the cake layer grows, the corresponding zone becomes darker, and it is no longer possible to differentiate single particle contours in the image. The experiments using model particle suspensions are conducted using the filtration units with slot width $C = 4$, i.e. C4Pe7, C4Pe10 and C4Pe20.

III. Qualitative analysis

The first stages of the filtration exhibit behavior strongly dependent on the membrane geometry. As shown in Figure 53 after the first particles reach the membrane, the relation between the particle diameter and the distance between consecutive slots induces different cake structures. The characteristic Stokes flow corresponds to Reynold's number Re < 1 [112] which is the case for the filtration experiments as shown in Table 8. The viscous forces are higher than the inertial forces; as a result, particles in the dilute suspension follow closely the fluid flow streamlines with negligible particle-fluid relative velocities. Consequently, particles are driven by the flow and the first particles preferentially block to the slots. The slot distribution plays a role on the organization of the particles in the first layers; once the slots are blocked, the following particles approaching to a blocked slot are driven the membrane surface zone corresponding to the walls separating the slots. Depending on the distance between slots, a certain number of particles can deposit on these zones, causing the particles to arrange differently in order to fill the whole membrane surface.

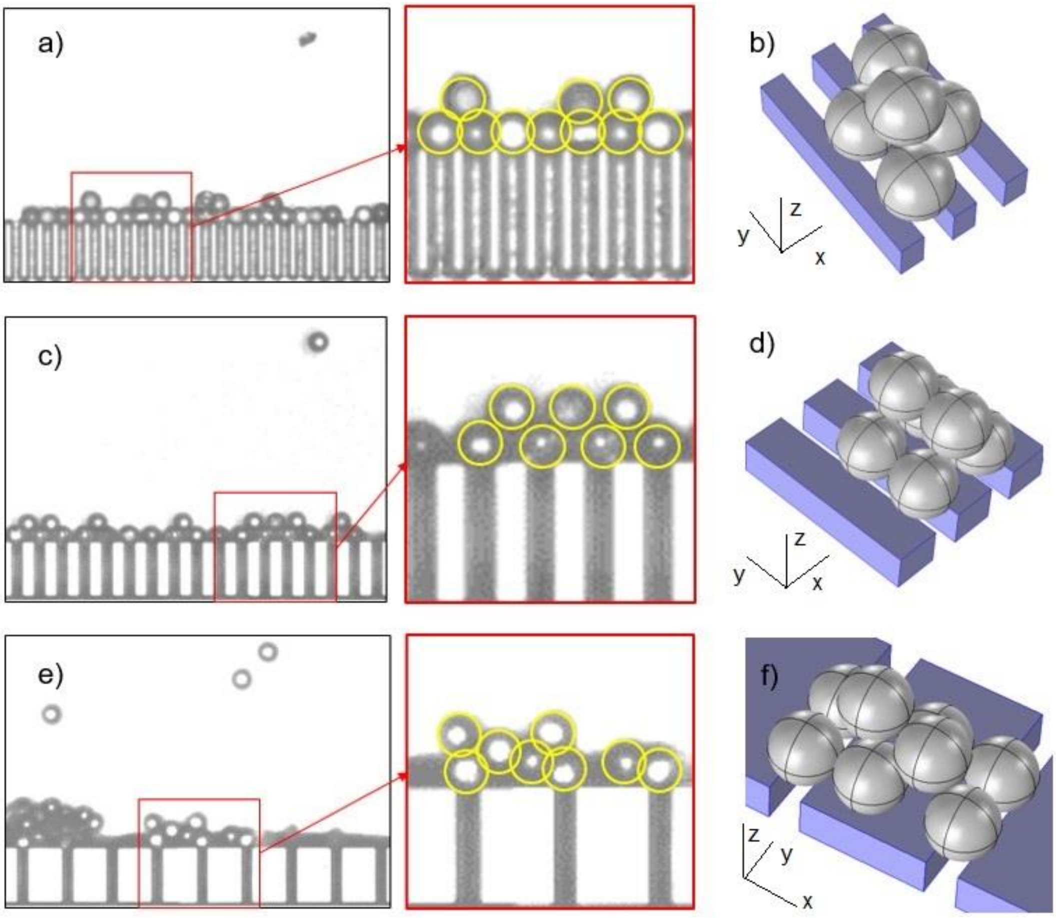

Figure 53. a,c,e) First stage of cake formation for C4Pe7, C4Pe10 and C4Pe20 configurations, respectively. b,d,f) Sketches of the typical structure of particle arrangement for the corresponding membrane configuration

For C4Pe7 units, d_p is small compared to the diameter of the particles (8.4 µm) and the slot width is $C = 4$ µm; with $d_p = 3$ µm, particles are not able to lay on the walls, moreover d_p is too small and their arrangement results in a moderate slot blocking since they cannot be closely aligned over a slot. According to this arrangement, particles centers are not on the same axis following the membrane length direction (*x*), hence causing a shift of the particles in the depth direction (*y*). This causes the overlaying highlighted by the circles in Figure 53a, as some particles are displaced in *y*, they cannot be observed in the focus plane. Figure 53b illustrates the previous analysis: for the C4Pe7 configuration, particles are spread over all the membrane with large spaces between each other and in a limited depth, thus relatively large voids are formed in the first layers resulting in high porosity. This phenomenon has been reported as the pore "protection phenomenon" and it yields a more porous blocking layer [39]. The membrane blocking remains moderate and this slot configuration induces a pyramidal arrangement as it is possible to see in Figure 53a and b.

In the case of C4Pe10 $d_p = 6$ µm, which corresponds almost to the space that allows particle centers to align on the membrane length axis (*x*). In C4Pe10 membranes, the "pore protection phenomenon" is no longer detected, as due to membrane configuration there is no particle shift in the (*y*) direction. The distance between slots d_p allows particles to align in the *x* direction, however it is not enough for particle to reach the walls of the membrane surface. The resulting packing for C4Pe10 membrane appears higher than for the case of C4Pe7 units. The membrane surface blocking is accentuated, the structure of the first layer tends to be regularly organized in a pyramidal structure similar to the body-centered cubic packing (Figure 53c and d). The filtration cake formed for C4Pe10 units results consistently in less voids and a less porous cake first layers.

For C4Pe20 units, particle distribution over the slots is similar to that observed for C4Pe10 units with no "pore protection phenomenon". The slot distance $d_p = 16$ µm is large enough and particles are optimally organized on the slots with their centers aligned on the membrane length axe (*x*). In addition, particles can deposit on the walls due to the larger distance between pores that allows the particles to arrange in random structures. This leads to more disorganized layers as shown in Figure 53e and f. The first arriving particles mainly block the slots and the following are driven by the fluid to the zones of the slots that are still open to the flow. This leads to a more complex and disorganized structure that could result in more compact cake layers.

Pore protection

In order to assess the "pore protection phenomenon" for the filtration of a suspension of monodispersed spheres, the geometric parameter called the "pore protection coefficient" p_p is introduced as*:*

$$p_p = \frac{Pe - C}{d - C}$$

Eq. 28

This parameter relates the distance between slots/pores d_p and the relative size of the particle to the slot $d - C$. Figure 54 shows the membrane configuration and the parameter considered in the calculation of p_p for the model membranes used in the present study and for conventional ones.

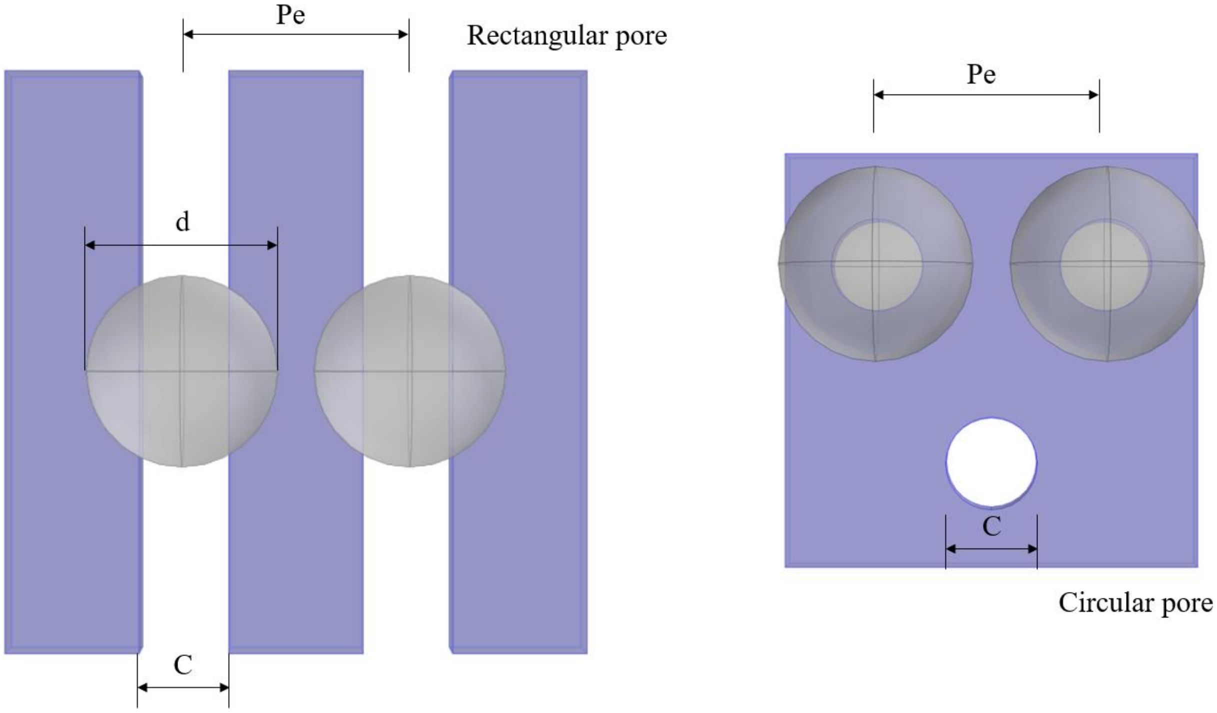

Figure 54. Slot/pore configuration and variables intervening in the calculation of p_p for membranes with circular pores and for the characteristic geometry of the current experiments

Only for the following explanation of p_p, both slots and pores, are referred as pores. As the only separating mechanism is sieving, the relative size of the particles to the slot $d - C$ takes positives values, which makes p_p strictly positive. For $p_p \geq 1$ pore blocking is the dominant condition. For $p_p = 1$, pores are blocked by particles centered on the pore (center of the cylindrical pore and longitudinal axe of the slot). In this case, particles are in contact with each other creating an organized structure that will strongly influence the further cake structure. This organized structure, where particles come in contact, tends to be more stable under the action of the rising pressure, as they are better distributed. For $p_p > 1$ particles are able to center on the pores and are not in contact with neighboring pore-blocking particles as d_p (Pe-C) brings particles far from each other. In the particular range corresponding to $1 < p_p < 2$, particles are not able to lie on the membrane wall due to the reduced space. Since particles tend to center on the pores, the further cake structure of the forming layers is conditioned by the membrane geometry. As p_p becomes higher than 2, d_p is large enough to allow particles to lay on the membrane surface. With more space between pores there are more possible arrangement of particles, which promotes a more random packing contributing hence to lower porosities. On the other hand, for $p_p < 1$ the "pore protection" phenomenon effect appears. The first particles are able to center on the pores, but neighboring pores cannot be blocked. The presence of voids in the first layers is higher and yields cakes with higher porosity, at least in the initial layers.

From now, "pore" and "slot" are used to differentiate previous studies form the current work. The "pore protection" phenomenon and preferential arrangements were previously described. In the work published by Ben Hassan et al. [39] using CLSM for direct observation of a thin cake formation (~35µm), it was possible to obtain evidence of particle organization patterns related to the ratio of particle size to distance between pores. This was achieved by using two type of membranes with different pore size and distance between pores. In that work, for the filtration of spherical particles (4.8 µm diameter) the current definition of the "pore protection coefficient" is used and yields p_p of 0.2 and 0.36. Even if the membrane geometry is different, particles are initially and preferentially driven by the flow to the pores. In both cases, the value p_p suggests a strong influence of the pore protection phenomenon. It was observed that pore distribution affects the level of membrane blocking since particles with a size large compared to the pore distance protect neighboring pores from being blocked. The case with $p_p = 0.2$ presented a fraction of open pores of 0.91 after the deposition of a monolayer, whereas the case with $p_p = 0.36$ has a mean fraction of open pores of 0.72. As p_p is smaller, the fraction of open pores after membrane surface covering is higher.

It is thus evident that different membrane geometries affect blocking mechanisms and particle arrangement. These effects persist to a certain degree into the later cake formation, but they become attenuated as the cake grows. Indeed, as the cake becomes thicker, filtration dynamics are dominated by the cake properties rather than the membrane and the membrane-cake interaction. Membrane and membrane-cake interactions have a stronger influence in the initial partial blocking phase. Nonetheless, these results could lead to the optimization of the membrane design. For low values of p_p, it is possible to attenuate the membrane permeability reduction due to initial pore blocking. This could be achieved either by reducing C or d_p, or both; however in terms of operational TMP it would be more relevant to reduce d_p. The calculations summarized in Table 9 shows that for the same d_p, C2Pe5 membrane yields higher pressure drop than C4Pe7 with p_p of 0.47 and 0.68 respectively and for spherical particles (8.4 µm diameter). The two membranes induce the “pore protection phenomenon”, however, even if C2Pe5 have a lower p_p resulting in an enhanced “pore protection”, the pressure drop associated to the slot width (pore size for common membranes) produces a higher pressure difference.

C4Pe10 and C4Pe20 membranes have a $p_p > 1$, which corresponds to the possibility of an optimal slot blockage. In the case of C4Pe10 p_p is 1.36, being close to the unity the cake presents the most organized and stable structure (Figure 55c and d). This will be analyzed below. C4Pe20 has $p_p = 3.64$ leading to a more random packing and compact cake structures.

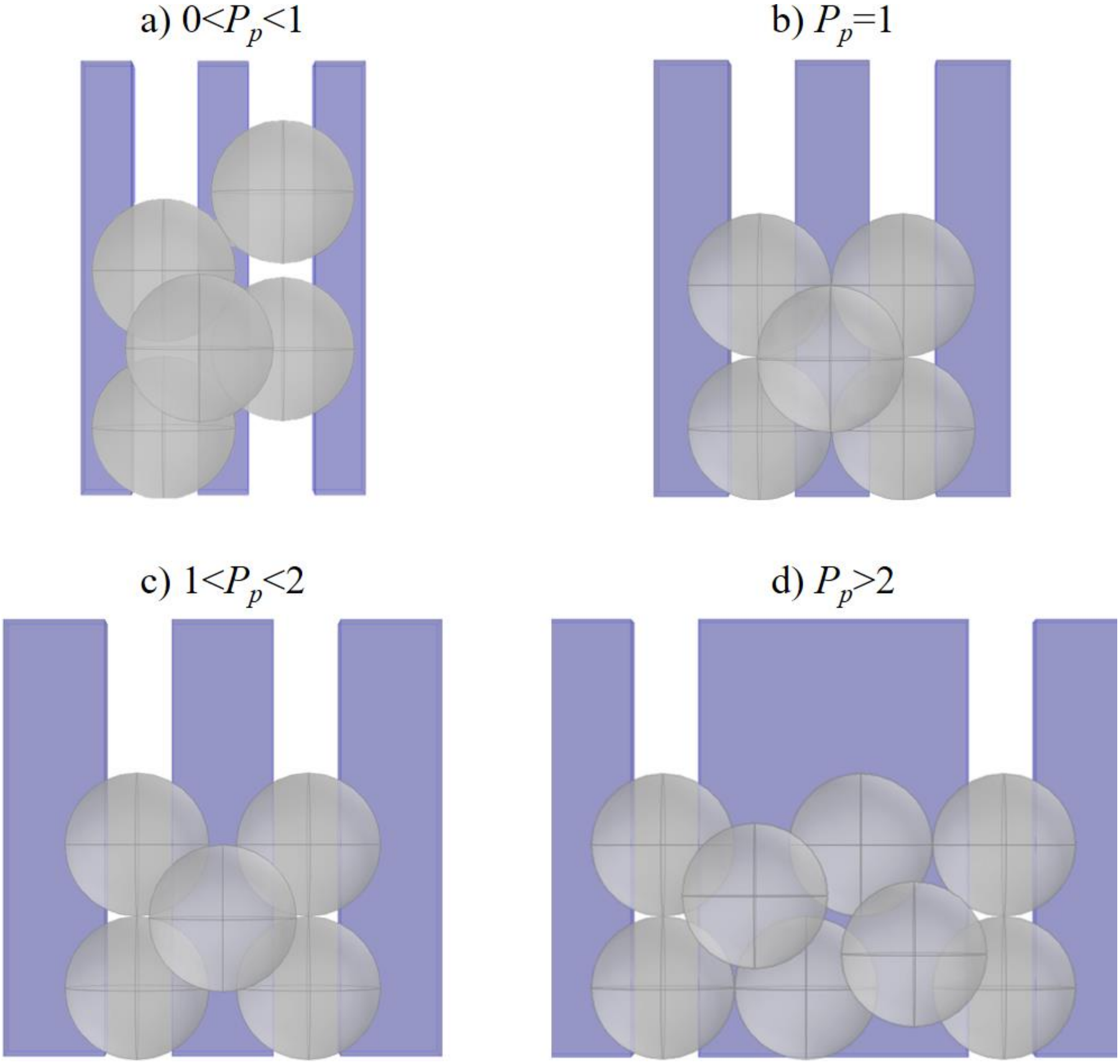

Figure 55. Different slot blocking configuration and first layers possible structure based on p_p. a) Particles are in contact with an organized structure but do not block optimally the slots for $p_p < 1$. b) Particles get in contact forming a well organized structure for $p_p = 1$. c) For $1 < p_p < 2$ particles

cannot place on the membrane walls after slots are blocked. d) Particles can lay on the membrane surface for $p_p > 2$.

IV.Quantitative analysis

The filtration phenomenon is studied from the “pore scale” where blocking takes place to the transition state between membrane and cake controlled dynamics (cake filtration). To analyze the filtration when the dominant fouling mechanism results from the cake (cake filtration stage) the observation window should be larger than (1650 pix) x (800 pix) for being able to observe thicker deposits. Whereas 1650 pix in length allows the observation of the whole channel width and the membrane, the observation window height of 800 pix allows observing a limited domain of ~475 µm at the magnification used (10x). In this domain, both the cake and the bulk fluid must be observed to assess the mean cake height, the concentration and the mean velocity, in order to perform the mass balance. However, in order to have an accurate estimation of the concentration a sufficiently large domain above the cake must be investigated. This limits the observable cake height in a filtration experiment.

IV.1. Cake growth and flowrate evolution

Figure 56 illustrates the behavior of the mean height of the cake, h_o, as a function of the deposited mass per membrane unit surface, *m*, over the course of the filtration. The differences in the slopes obtained for each membrane geometry suggest that the porosity of the deposits is not the same. In the case of C4Pe20 it is clear that for the same deposited mass *m*, the observed height is consistently lower than for the other two configurations. For C4Pe7 and C4Pe10 the behavior appears to be more similar, however the cake height for C4Pe7 is slightly higher except at the end of the experiment. Indeed, around $m = 55$ g/m^2, the curves for C4Pe7 and C4Pe10 filtration units tend to overlap. Further analysis of the pressure and the porosity allow explaining this feature.

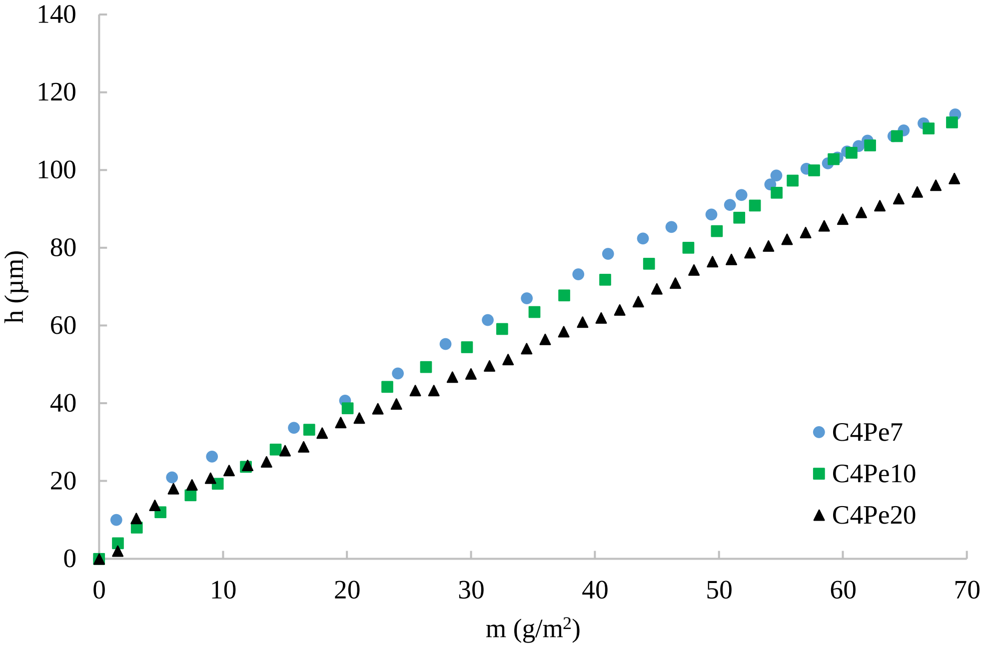

Figure 56. Mean height of the deposit obtained using the CGM module during the filtration of spherical particles for different membrane geometries

The flow rate is calculated from the mean velocity estimate using the particle velocimetry module (PVM). The flowrate is obtained by the product of the velocity at which the concentration front arrives (mean velocity) to the membrane (or the cake) and the channel cross section. This approach is accurate since for the Stoke’s flow there is no relative particle-flow velocity and so the particle mean velocity is the same as for the fluid. Figure 57 shows the evolution of the flowrate when the filtration cake grows. The initial flowrate exhibits a decreasing behavior from 10 µl/min towards a stable value of approximately ~5 µl/min. This is an unsettling behavior since the flow-rate set point is kept constant during the experiments and must be taken into account to perform the mass balance in the filtration unit. The possible presence of leaks due to improper sealing and loss of liquid at the connections was check and the system proved to be hermetic. Finally, it was found that the flowrate reduction was the result of the elasticity of the system downstream the membrane. This is causedby the gas expansion in the syringe for pulling operating mode (Figure 52a) as pressure difference becomes more important with the cake formation. However, the system sealing condition guarantees the pressure measurements while the PVM module ensures the correctness of the analysis taking into account the velocity variation. Thereby, despite the flowrate variation, the set-up provides an adequate analysis for filtration process where both pressure and velocity are variable.

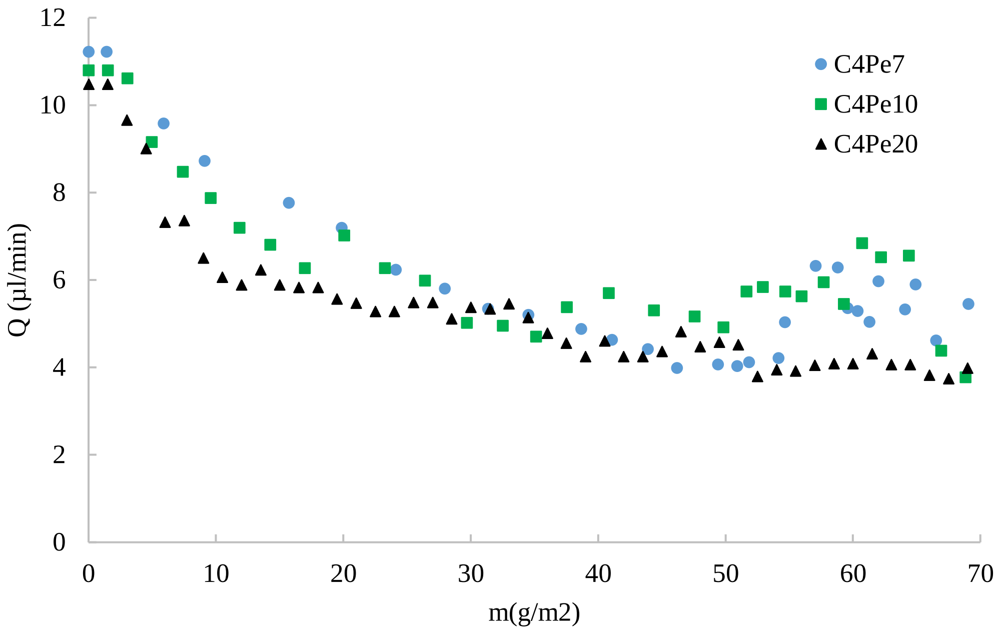

Figure 57. Flowrate evolution as a function of the deposited mass per membrane unit surface during the filtration of spherical particles for different membrane geometries.

IV.2. Pressure, porosity and K_K

The pressure difference across the cake and the porosity evolution as function of the deposited mass throughout the filtration are represented in Figure 58. The data is plotted for the three membrane units to analyze the influence of the previously identified membrane-induced particle organization on the global filtration hydrodynamics.

The cake formed on the C4Pe7 membrane exhibits a lower pressure drop than the cakes formed using the other filtration units and it presents a change of the pressure slope around $m = 55$ g/m². This change corresponds to the moment at which C4Pe7 and C4Pe10 porosity curves almost overlap and could suggest a rearrangement of the C4Pe7 cake structure into a more stable and compact organization. This possible particle rearrangement can be the result of a higher void fraction in the first layers caused by the short d_p as previously discussed and shown in Figure 53a and b. These voids could suffer a partial collapse under the effect of continuous cake growth and rising pressure, leading to a more compact organization that may explain the rise observed in the pressure gradient. Thereby, the pressure drop values for the filtration using C4Pe7 membrane tend to approach the values observed for C4Pe10 unit. The pressure drop corresponds to the qualitative description of the induced cake structure with regards the membrane geometry. As both cakes obtained for C4Pe7 and C4Pe10 membranes exhibit a similar pyramidal structure in the first layers, it is not surprising the agreement of the two curves when the initial voids (in the cake obtained for C4Pe7 membrane) are collapsed.

The properties of the cake formed on the C4Pe10 membrane shows an intermediate behavior between the C4Pe7 and the C4Pe20 units. The “quasi linear” pressure difference evolution for C4Pe10 membrane could suggest that the induced cake structure is more stable than for C4Pe7 membrane and that there is not a significant rearrangement of particles as the pressure increases and the deposit grows. A consistently higher pressure drop is observed for the C4Pe20 membrane cake. In this case, a more random particle arrangement within the first layers of the cake could result in a more compact structure, and hence lower porosities.

It is also interesting to consider the later behavior when the cake layer growth is large compared to the slot size. Pressure drop is consistently lower for the cake formed using the C4Pe7 membrane and higher in the case of C4Pe20 unit. This difference suggests that the arrangement of particles in the first layers combined with the initial slot blocking by the particles have an effect on later cake structure and the resulting mean porosity. An alternating change in the pressure gradient is observed for the C4Pe20 cake throughout the filtration. This could suggest two mechanisms interacting in the cake formation. The first mechanism is the particle deposition, as the concentration front arrives to the cake, a new layer is formed. The pressure keeps increasing as the cake grows. When the pressure reaches a level, high enough to induce the reorganization of the particles in the new layers, the compaction is accentuated making the pressure rise steeper. This is similar to the suggested pore collapse in the case of the cake formed on the C4Pe7 membrane, a rearrangement triggered at a certain pressure drop. The difference results from the induced structure for C4Pe7, which could change the time required for this alternating event. The pressure drop behavior is in agreement with the qualitative analysis. Membrane influence remains throughout the filtration experiments, up to 70 g/m^2; nevertheless further cake formation should drive the filtration dynamics to be determined by the cake.

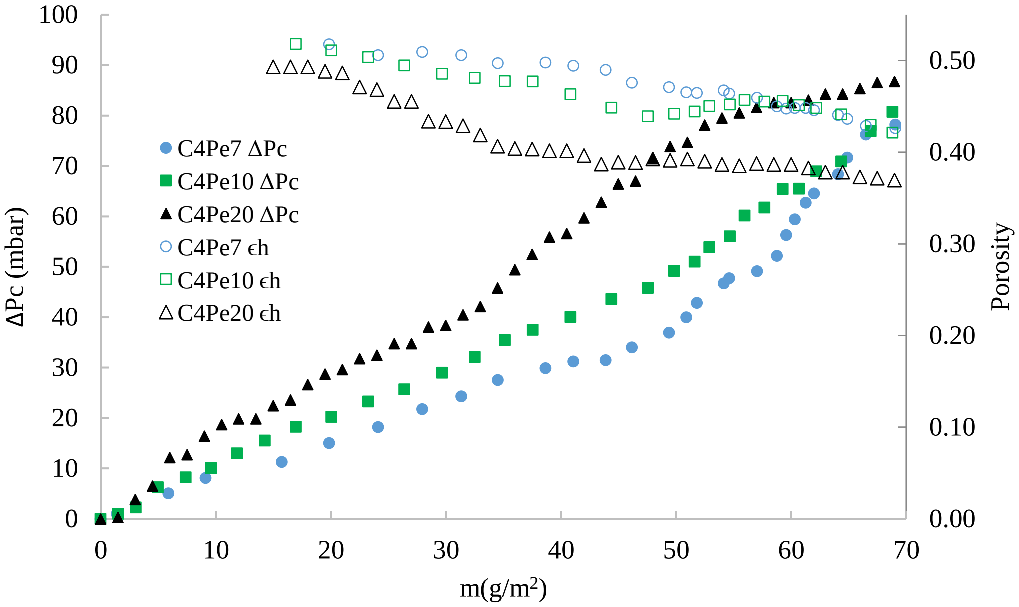

Figure 58. Pressure drop across cake alone and cake porosity evolution as a function of the deposited mass per surface unit for the filtration of spherical particles using different membrane geometries

Porosity is calculated when approximately 3-4 layers of particles are deposited, which corresponds to the limit of applicability of the Carman-Kozeny formula. The porosity values obtained in these experiments are in the same range that the values previously reported for spherical particles. In the work by Ben Hassan et al. [39] using different types of membranes (with a calculated $p_p = 0.2$ and 0.36) , the effect of pore size (*C*) and distance between adjacent pores (d_p) on the cake porosity for about 5 layers (~ 25µm, ~ 5 layers of spherical monodispersed particles of 4.8 µm diameter) was demonstrated. Porosity values of 0.41 and 0.49 were found for theses cakes of monodispersed particles when using two membranes with different geometries (pore size and spacing). The membrane with lower p_p exhibits a higher porosity, which is in agreement with the current results and relates the “pore protection” feature to higher cake porosities.

For a more developed and thicker cake layer, and comparing with theoretical packing models, the deposits obtained for C4Pe7 and C4Pe10 have a porosity evolution that corresponds to a packing varying from “loosest regular packing” (cubic lattice: 6 points of contact per sphere) to “random loose packing” with model porosities varying from 0.48 – 0.40, respectively. On the other hand, in the case of the deposit formed on C4Pe20 membrane the porosity changes from “random loose packing” to “random close packing” (as found in vibrated beds), corresponding to theoretical porosities of 0.40 to 0.36, respectively [113]. In the case of C4Pe7 and C4Pe10 filtration cakes, the theoretical packing models are in agreement with the observation as very regular structures can be observed in both cases.

These regular structures later evolved under the effect of increasing pressure to become more compact, especially prominent in the case of C4Pe7. In the case of C4Pe20, “pore protection coefficient” $p_p = 3.64$, thus the membrane does not influence the cake structure and the cake exhibits the “random loose packing” of particles from the beginning of the experiment. The effect of the rising pressure leads to a closer random packing

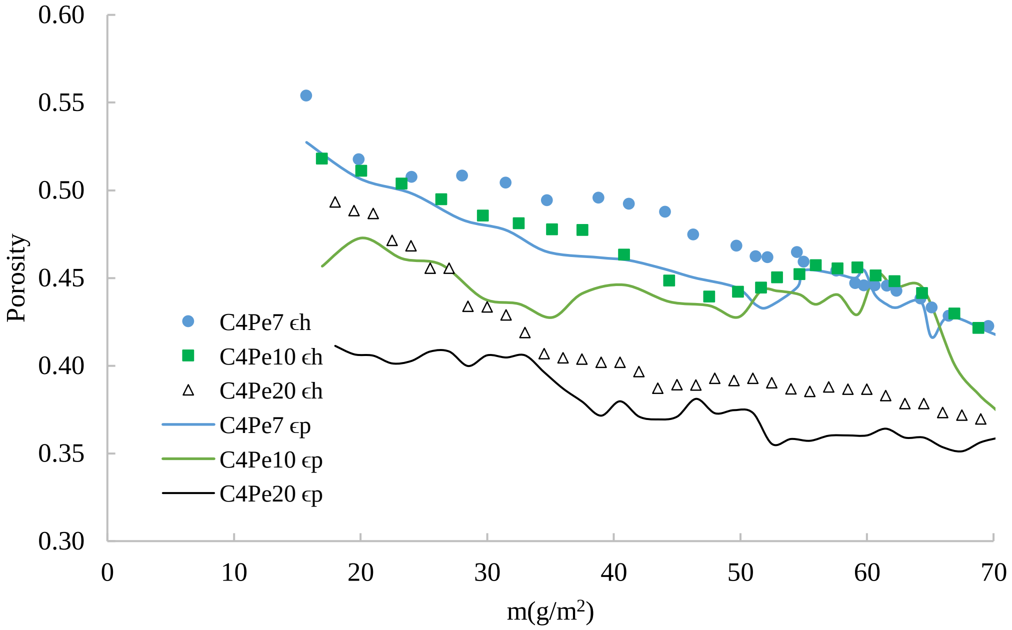

Figure 59. Estimated porosity from the mass balance ϵh (Eq. 23) compared to the calculated porosity ϵ_p (Eq. 25) for $K_K = 5$ for the filtration of spherical particles using different membrane geometries.

To provide a more complete characterization and validate the analysis, the porosity ϵ_h estimated using Eq. 23 is compared with the porosity ϵ_p calculated using Eq. 25 and the constant value of $K_K = 5$ for spheres. Figure 59 shows both ϵ_h and ϵ_p represented by symbols and solid lines respectively. The estimated (ϵ_h) and calculated (ϵ_p) porosities have a similar behavior for the cakes formed under the different membrane configurations; however, the values differ slightly, being ϵ_p consistently lower than ϵ_h. The difference could be explained by the assumption of a constant K_K coefficient when calculating ϵ_p. Previous work has reported the dependence of the K_K on the porosity [76]. Although the Kozeny-Carman formula provides a semi-empirical relation for the permeability, analytical development of the continuity and momentum equations for Stoke’s flow has been made. Vidal et al. [114] performed massive parallel lattice-Boltzmann simulations of the flow through monodispersed and highly polydispersed spherical particle packing formed using Monte-Carlo methods. Their results show a reasonable good agreement with Carman-Kozeny formula. For monodispersed particles, they found values of K_K ranging from 6.0 to 5.5 for high ($\epsilon = 0.46$) and low

(ϵ = 0.38) cake porosities respectively. The experimental results for ϵ_h and the previous literature findings show good agreement and validate the estimate regardless the slight differences with ϵ_p.

Considering K_K variable as a function of the porosity, then Eq. 25 is used to calculate the correspondent values for each estimated porosity ϵ_h. In Figure 60 K_K varies within a consistent range throughout the filtration experiment (as a function of the deposited mass), for the three geometries they are close, but generally above the typical constant value $K_K = 5$, for monodispersed spheres.

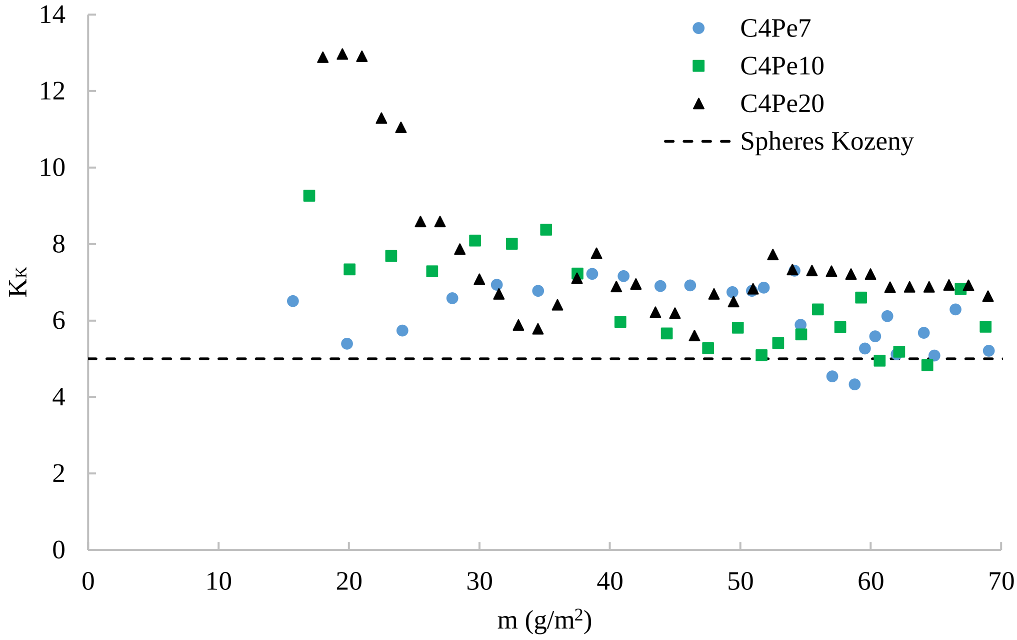

Figure 60. Evolution of the Kozeny coefficient throughout the filtration on different membrane geometries and a suspension of spherical monodispersed particles.

For C4Pe7 and C4Pe10 filtration cakes, K_K exhibits barely an evolution with mean values of 6.0 and 6.6 respectively; for C4Pe20 K_K starts at a higher value and decreases towards a stabilization around ~ 7.

IV.3. Permeability

Figure 61 shows the variations of the cake permeability as a function of the deposited mass per membrane surface unit. The cake permeability ($K_c = \bar{h}/R_c$) is calculated from the cake hydraulic resistance obtained from the difference of the total and the membrane resistance ($R_c = R_t - R_m$).

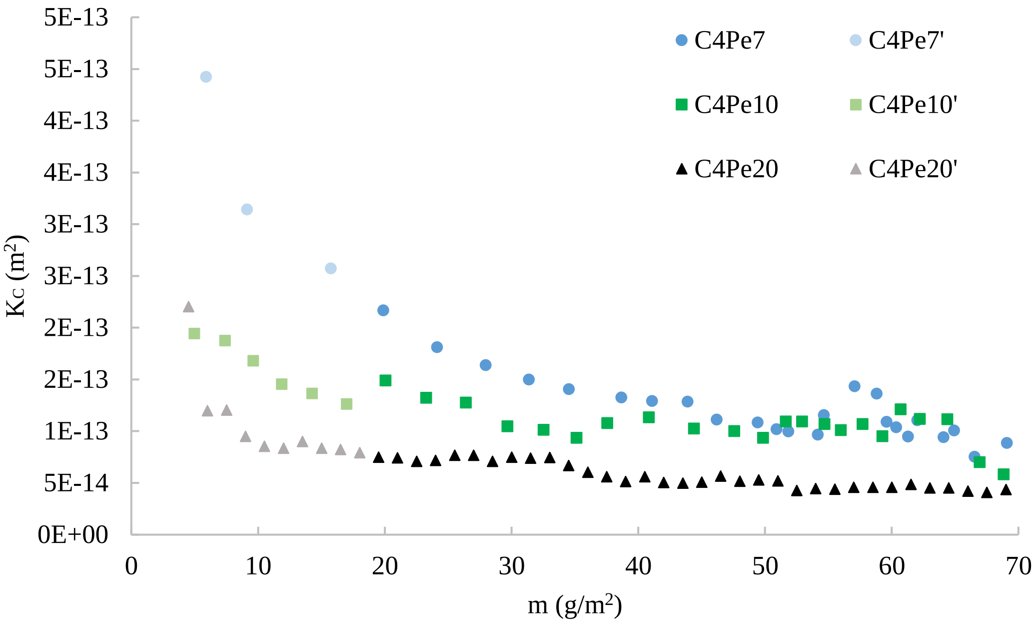

Figure 61. Evolution of the cake permeability for the three different membrane units when filtering suspensions of model spherical particles. Light symbols asses the permeability related to first particle deposition while dark symbols corresponds to a formed deposit ($\geq$ 3 layers)

The cake resistance allows the definition of the permeability resulting from the cake and the membrane blocking by particles. These two resistance components are observed in the permeability evolution, which exhibits a significant decrease as the first three layers are formed. The initial sharp decrease can be related to the blocking phenomenon. This can be confirmed from the variation of cake height as a function of the deposited mass (Figure 56) for which m = 10g/m^2 corresponds to ~20µm of cake height; regarding particle size, this corresponds to the second layer formation. The permeability becomes gradually more influenced by the continuous cake growth and decreases toward a stable value. This could be explained by a possible particle rearrangement in the deposits as the pressure rise. Two main features explain the differences in the initial permeability values of the different membrane configurations: the partial blocking phenomenon and the induced cake structure. For C4Pe7 membrane the initial permeability is higher. This is related to the geometry and the efficiency of slot blockage by the particles. As the distance between slots is small relative to particle diameter, “pore protection” plays a role. When more particle layers are deposited, the later cake formation controls the permeability as it approaches to a stable value. In the case of C4Pe10 and C4Pe20 units the absence of the “pore protection" phenomenon (Figure 53c and d) accentuates membrane blocking, which results in a lower permeability than C4Pe7, and particularly lower for C4Pe20. As the cake grows for C4Pe10 units, the permeability becomes stable around the same values as those found for C4Pe7. This is consistent with the porosity evolution that overlaps for C4Pe7 and

C4Pe10 around m = 55 g/m². The permeability and porosity results are also consistent for C4Pe20 membrane and it is confirmed by a lower stable value corresponding to a lower porosity.

IV.4. Numerical simulation

Membrane blocking

As described in "Chapter III: Materials and methods - Section V", three geometries were studied in order to analyze the particle deposition when the first cake layer is forming and to confirm the experimental results. In the current numerical simulations an optimal coverage of the different membranes was studied, corresponding to the sketches presented in Figure 53b, d and f. The results of the qualitative analysis were the base to define the simplified model geometries for the simulations (Figure 51). The pressure drop across the system for the three scenarios is calculated to assess the contributions of the membrane and the membrane blocking to the total resistance.

The simulation results allow the calculation of the hydraulic resistance of the first layer of particles (blocking layer), which are responsible for the partial blocking of the membrane. In order to compare the hydraulic resistance caused by the first layer with the experimental results, the mean height of the layer of blocking particles is calculated for the total surface based in the geometry of the membrane (specifically *Pe*). The number of particles depends on the spacing between the slots per unit of membrane surface, for this reason, the height is not the same for the three geometries. The lowest value of *Pe* (C4Pe7) yields a larger height of the blocking layer; for a higher distance between slots (C4Pe20) there are fewer slots and hence less particles blocking them, this makes the blocking layer height smaller. It must be pointed out that the height the blocking layer for each membrane configuration is always lower than *d*, the particle diameter, for the previous reason, but also due to particles embedding in the slots. As these simulations were run for the blocking layer, the resistance is represented by a single point for each membrane configuration, which corresponds to the three hollow symbols in Figure 62.

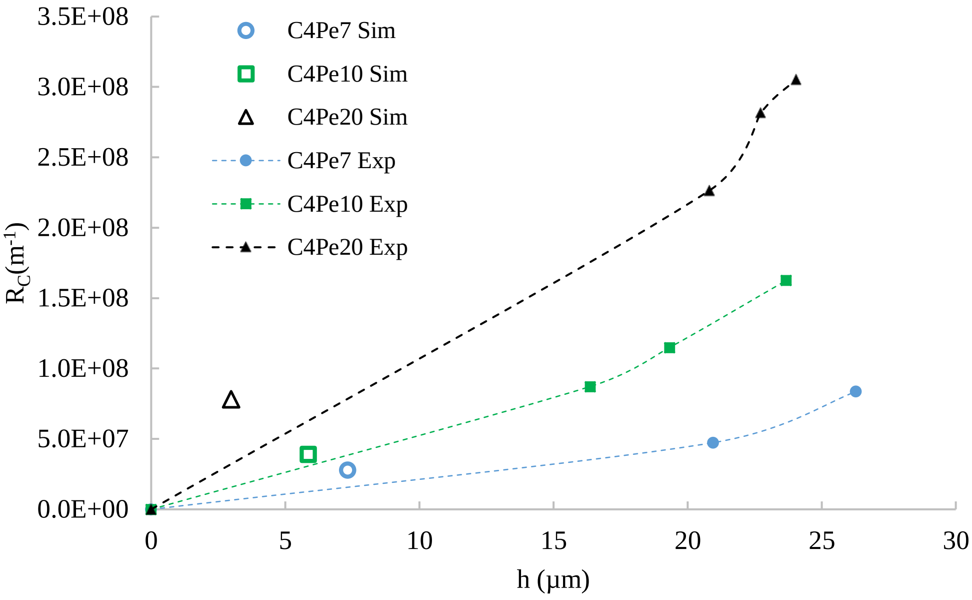

Figure 62. Experimental values of the hydraulic resistance caused by membrane blocking for the different geometries when the first layers are forming (dashed lines with symbols). Symbols represent the simulation results for the membrane blocking resistance (< 1 layer of particles).

Figure 62 shows the comparison of the simulated (<1 layer) and the experimental (~3 layer) hydraulic resistance caused by the cake and the membrane blocking as a function of the cake mean height during the beginning of the filtration. Hollow symbols represent the simulation results for the cake hydraulic resistance when the slots are optimally blocked for each membrane geometry. The values are plotted as a function of the mean height for the corresponding geometry. Note the proximity of the simulations with the respective experimental curve at the early membrane blocking (< 1 layer ~3-7 µm depending on the membrane geometry and particles embedded in the slots). This indicates that the experimental data is in a consistent range. However, there is a difference in the resistance obtained from the simulations for the different geometries. This could be explained by the assumption of an optimal blocking of the slots by the particles; this is not always the case in the real experiments and is likely a reason why the simulations are not in full agreement with the experimental curves. Here the experimental variations of R_c vs. h are assumed to be linear from 0 to the first measured point.

The results also validate the previous analysis regarding the “pore protection” phenomenon. Using again the definition of the pore protection coefficient p_p. The filtration experiment using the C4Pe7 membrane has the lowest $p_p = 0.68$, which leads to a higher “pore protection” effect. This is in agreement with the calculated hydraulic resistance, being the lowest of the three membrane configurations. Both C4Pe10 and C4Pe20 have $p_p > 1$ with values of 1.36 and 3.64 respectively, in this case there is no effect of the geometry on the “pore protection”. The higher hydraulic resistance for the blocking of the C4Pe20 unit is caused by the effect of a less permeable membrane geometry to the flow (Table 9).

V.Conclusion

The system and the methodology developed based on microfabrication techniques are found to be of high interest when characterizing the early filtration process of micrometric spherical particles. The cake growth and its heterogeneity are analyzed by the cake growth monitoring module (CGM), which easily tracks the cake surface. This information is coupled with the concentration and velocity estimates to evaluate the mass balance and perform an extensive quantitative analysis. An additional qualitative analysis is performed to characterize the structure of the first particle layers. The observations are used to characterize and model the cake geometry for the conducted simulations.

The velocity is assessed using image processing and it allows measurements of the flowrate. Combining the velocity information with the pressure measurements makes possible the characterization of filtration processes where both the pressure and the flowrate are variables. The analysis showed a good agreement with previous reported information regarding the porosity and Kozeny coefficient.

The filtration performance for the different membrane geometries is similar, but the pressure drop can be affected by the distance between slots. The initial cake structure is visibly conditioned by the membrane construction parameters, and it has an influence on slot blocking and further cake build up, which impacts the pressure drop. The introduction of the pore protection coefficient (p_p) offers a quantitative characterization of the membrane-particle interaction based on the geometry. It proves to be an accurate parameter when used to characterize and compare the results obtained by Ben Hassan et al. [39].

The numerical simulations provide a means of rationally evaluating the role of the initial conditions of the cake formed at the membrane. The simulation results for the initial layer hydraulic resistance are in close agreement with the experimental data for the current suspension.

With the validation and global characterization, the system is then used to study the filtration of more complex suspensions. The characterization of the filtration of yeast suspensions and the associated cake properties is addressed using the microfiltration set-up and the DO technique.

Chapter V: Experiments with cultivated yeast and model suspension

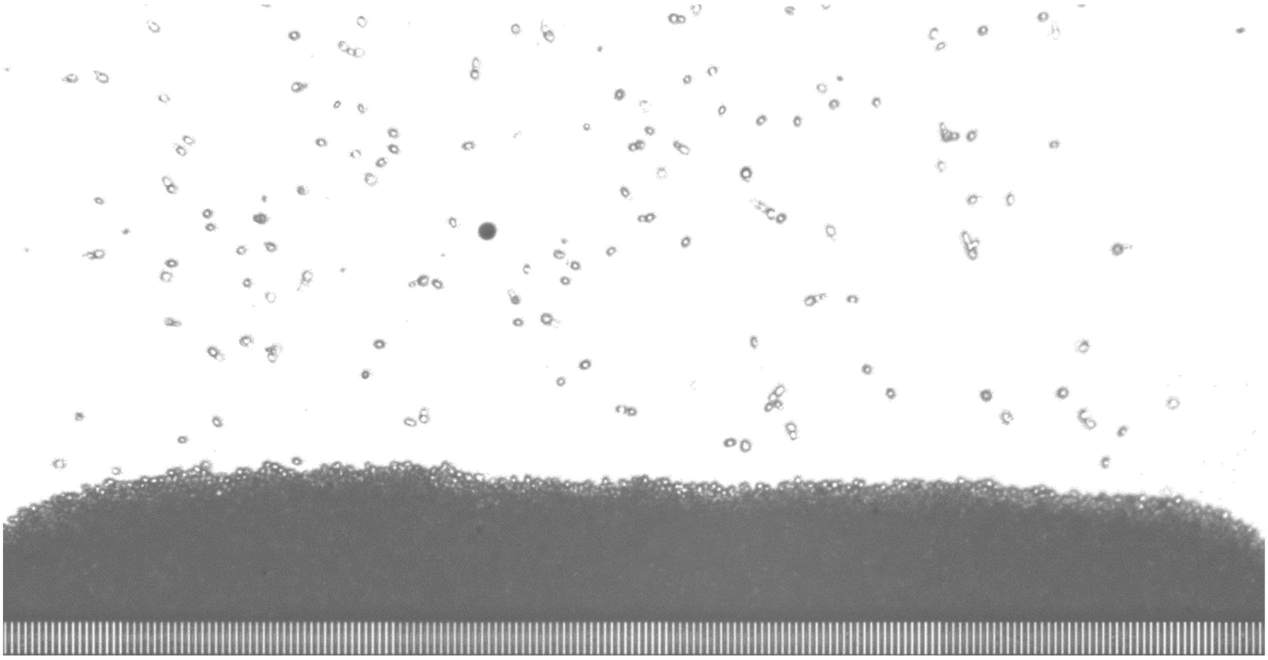

I. Cultivated yeast suspension

The filtration experiments with yeast suspensions were conducted using exclusively the C2Pe5 membranes. As yeast cells have a size distribution taking into account individual cells, buds and aggregates, C2Pe5 units are the only ones for which the slot size of 2 µm guarantees the sieving of all the cells. This is necessary to assess accurately the deposited mass and to perform the subsequent estimation of porosity, permeability and specific resistance of the cake. The results are presented as the mean value and come along with the standard deviation information to evaluate the reproducibility based on four filtration experiments.

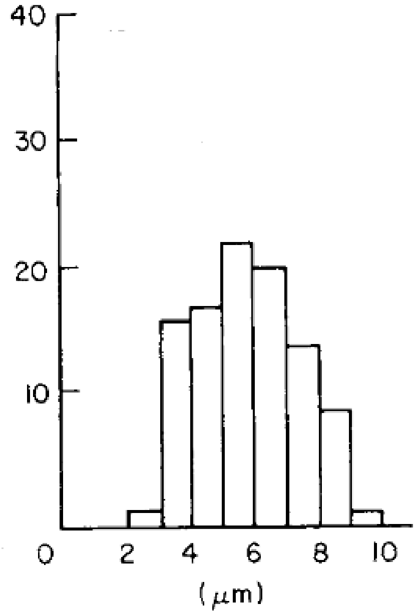

Figure 63. Yeast cell size distribution at 50 h of cultivation.

I.1. Cake growth and flowrate

The cake mean height as a function of the deposited mass per unit membrane surface is shown in Figure 64. The cake mean height shows consistence among the experiments according to the deviation bars, which confirms the reproducibility. A steep slope characterizes the initial stage of the cake formation. The slope, that is associated with the cake porosity, is higher at the beginning of the experiment due to the cake heterogeneous surface in length (*x*) and depth directions (*y*). However, this heterogeneity is rapidly compensated by the consequent non-uniform permeability. As the particles are not distributed homogenously over the membrane at the beginning of the experiment, there are zones of the membrane that remains open to the flow, i.e. zones with higher permeability, and particles are then driven towards them. This mechanism homogenize the cake surface during the filtration. The initial non-uniform permeability of the membrane is probably caused by the filtration cell fabrication.

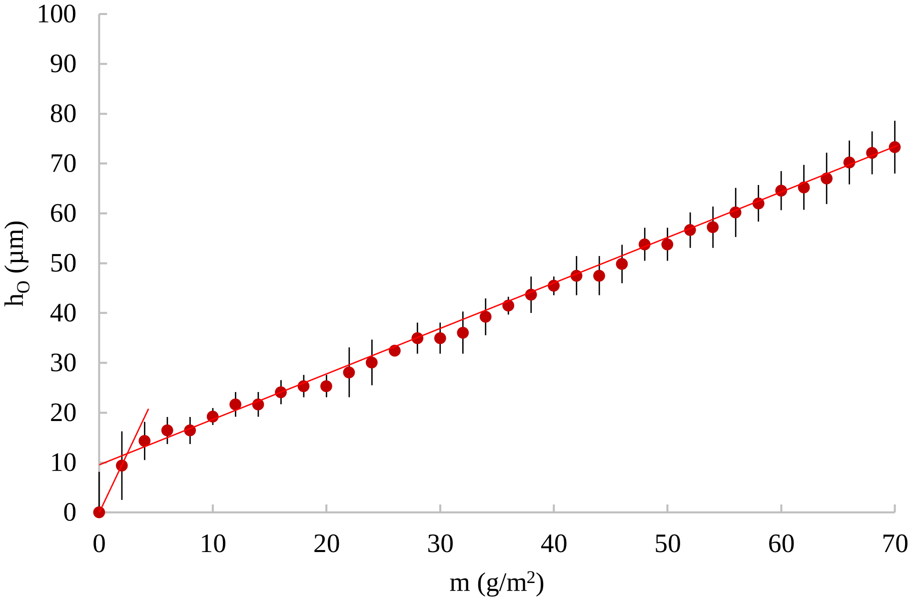

Figure 64. Yeast cake mean height as a function of the deposited mass per unit membrane surface. Mean values with the standard deviation.

Similarly than for monodispersed spherical particles, the flowrate reduction is also observed for the yeast suspensions as the cake grows (Figure 65). For the yeast cake the stable flowrate reached at the end of the experiment is around 10 times lower than the flowrate set for the syringe pump. This reduction is more drastic (~ 1 µl/min) than for the spherical particles, for which the value at the end is around 5 µl/min. The flowrate standard deviation is about 20% of the mean value at the beginning of the filtration; nonetheless, the standard deviation decreases over the filtration. One possible explanation of the larger standard deviation at the beginning could be that C2Pe5 filtration units exhibit a higher heterogeneity in the membrane because of the finer structure that is more difficult to construct.

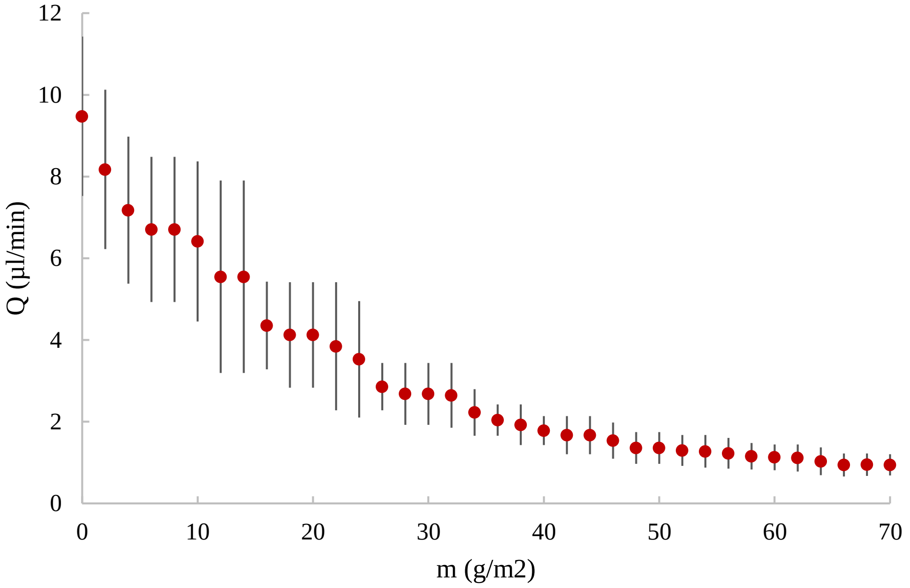

Figure 65. Evolution of the flowrate mean value throughout the filtration experiment as a function of the deposited mass per unit surface

I.2. Porosity, permeability and Kozeny coefficient

The estimated porosity ϵ_h (from the cake height and using Eq. 23) and the macroscopic properties calculated using the raw data, such as the permeability, the specific hydraulic resistance and Kozeny coefficient K_K are used henceforth to characterize and compare the filtration performance for the different suspensions. The cake porosity evolution during the filtration of the yeast cell suspension varies from 0.43 when cake first layers are formed to 0.15 at the end of the filtration run (Figure 66). This initial more porous behavior could be explained by the heterogeneity of the cake first layers. The cake continuous growth gradually attenuates the cake surface heterogeneity the same way it was explained before addressing the permeability non-uniformity for the evolution of the yeast cake height.

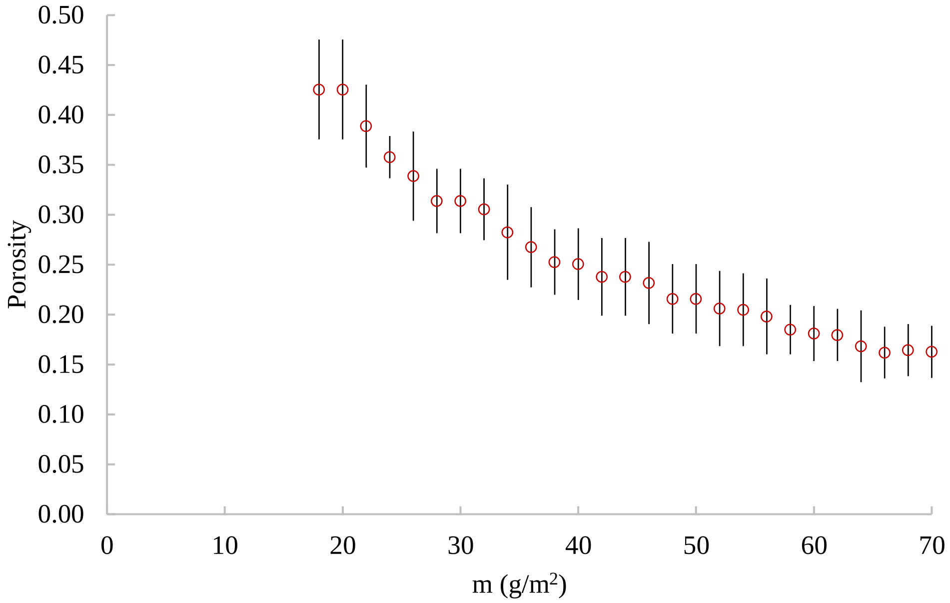

Figure 66. Porosity evolution. Mean values with the standard deviation plotted as a function of the deposited mass per unit surface

The porosity evolution for the yeast cake is consistent with the permeability variations throughout the filtration (Figure 67); both decrease with the same profile as the deposited mass increases. Different authors have reported porosity values for different microorganisms ranging from 0.40 to 0.10. Fane et al. [41] considered the effect of membrane surface properties and ionic strength using biomass microfiltration for controlled suspensions of *Escherichia coli*. For their experiments, they used membranes with pore size $C = 0.2$ µm and they analyzed the flux while filtering the bacteria suspensions at different ionic strengths and pressure difference. They performed an *ex-situ* analysis of the cake using SEM. They found that porosity values for *E. coli* varies from 0.18 to 0.10 for a pressure difference around 300 mbars. Nakanishi et al. [115] measured the mean specific resistance of the cakes (5.15 kg/m^2) obtained from filtering (at constant pressure 130 – 780 mbar) suspensions of different microorganisms. The observed a gradually decreasing flowrate that stabilizes over the time (2 h filtration). Different behavior was found depending on the size distribution and characteristic shape of the microorganism cells conditioning the cake structure. Particularly for yeast suspensions, the cake porosities were in the range from 0.30 to 0.20 in the pressure range of the study. Ben Hassan et al. [5] used confocal laser scanning microscopy (CLSM) to characterize the deposit of fluorescent dyed yeast obtained by dead-end filtration. They used different membrane units with 0.8 and 2.0 µm pore size, for which the cake porosity were 0.12 and 0.10 respectively. These values corresponds to the porosity estimation when the membrane were fully covered (~ 30 µm thickness) and they are in fair agreement with the results of Beaufort et al. [24] who found, also using CLSM, a porosity varying between 0.09 and 0.13 for yeast cakes of ~ 30 µm thickness obtained using 0.2 µm membranes for the filtration. These results are slightly lower than porosities obtained in the current study. The difference could be explained by the indirect estimation methods used in the previous work with regards the vertical resolution of the CLSM, which appears inaccurate to estimate the porosity from the image processing.

These experimental values are smaller than the lowest porosities reported for theoretical packing models of monodispersed and polydisperse spherical particles. For monodispersed particles densest regular packing for face-centered cubic and hexagonal close-packing is 0.26 [113] while for polydisperse particles the porosity value is around 0.29 [116], [117]. This difference between the experimental data and theoretical results can be explained by the assumptions made for these models, which consider solid particles with no deformation capacity and do not take into account the complexity addressed by living organisms such as heterogeneity in shape and deformability due to call age and physiological state.

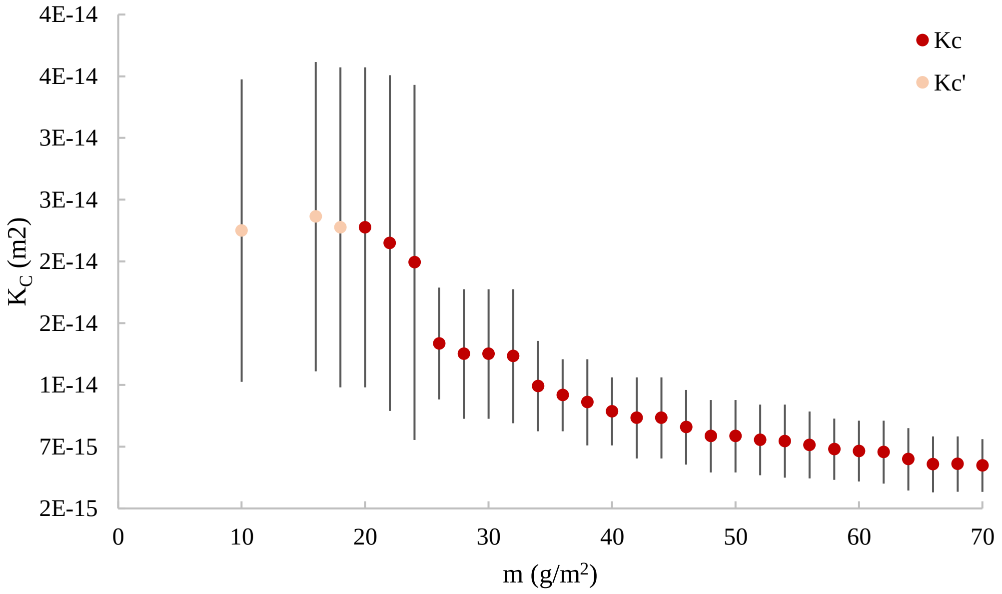

Figure 67. Evolution of the cake permeability during the filtration of yeast cell suspensions. Mean values with the standard deviation are plotted against the deposited mass per unit surface. K_C corresponds to the permeability for a formed deposit (m > 20 g/m^2) while K_C' for the blocking layers.

In the work of Ben Hassan [5] the total hydraulic resistance is estimated when the membrane is fully covered (~ 30 µm) and they obtained R_t ranging from 2.00 x10^9 – 2.25 x10^9 m^{-1} for membranes of 0.8 and 2 µm pore size respectively. These results are in agreement with the ones obtained in the present study: for a deposited mass of 25 g/m^2, the thickness is about 30 µm, at this stage the membrane is fully covered (Figure 64). For this $m = 25$ g/m^2 the calculation of the hydraulic resistance yields $R_t = 2.01 \times 10^9$ m^{-1}.

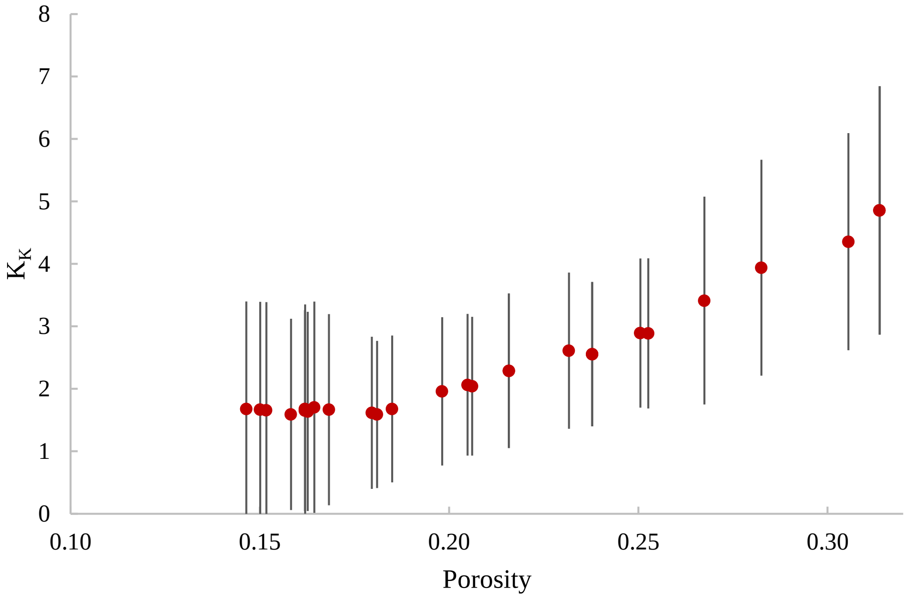

.

Figure 68. Kozeny coefficient as a function of the porosity for yeast cakes.

Yeast cell suspensions characteristics like size and shape depend on various parameters (strain, culture condition, culture age, etc.). It can be considered than suspended yeast have a non-spherical shape (ovoid and budding cells) and their size range from 2 to 10 µm [118]. This parameters have an influence on the Kozeny coefficient K_K, which depends on the tortuosity and the pore shape of the yeast cake porous medium. The K_K coefficient could differ from the values commonly adopted in literature when modeling porous media. In order to perform a more reliable analyze of the current experiments, K_K was calculated using the data obtained from the yeast filtration experiments. K_K coefficient is plotted as a function of the porosity (Figure 68) to relate both parameters. An exponential increasing profile is observed ranging from ~1.5 to 4.5. For porosity values lower than 0.20, corresponding to the end of the experiment, it seems that the K_K coefficient reaches a minimum value ~ 1.5. The exponential behavior could suggest that there is not only cell reorganization in the cake causing the porosity variation, and might be other features like cell local deformation, cell compressibility and polydispersity playing a role on yeast cake permeability. Cell compressibility and polydispersity are not usually taken into account in the classical Carman-Kozeny approach and this yields different values from the classical $K_K = 5$ for monodispersed spheres. In the work done by Beaufort [24], CLSM was used for the observation of the structure of biological deposits (*E. coli* and *S. cerevisiae*) formed during the dead-end filtration (ceramic membranes with 0.2 µm pore size). For porosity values in the range of 0.10 to 0.25, *Kk* is calculated and it was found that the coefficient varies from 1 to 10.

I.3. Compressibility and cake relaxation

Figure 69 shows the variations of the cake specific resistance as a function of the pressure drop across the cake only. A power law was found to fit the pressure dependency and reflects a compressibility feature of the yeast cake as the pressure increases. The compressibility of the system can be introduced by "n" the compressibility index for the relation $\alpha = \beta \Delta P^n$. For n = 0 the cake is considered non compressible with a rigid structure [115]. With higher values of n, the compressibility rises, reaching values of 0.90 for highly flocculated compressible sludges and cakes. Previous work reported yeast filtration cakes compressibility values lying between 0.25 and 0.9 [42]. Higher values than the unity correspond to highly compressible cakes [111].

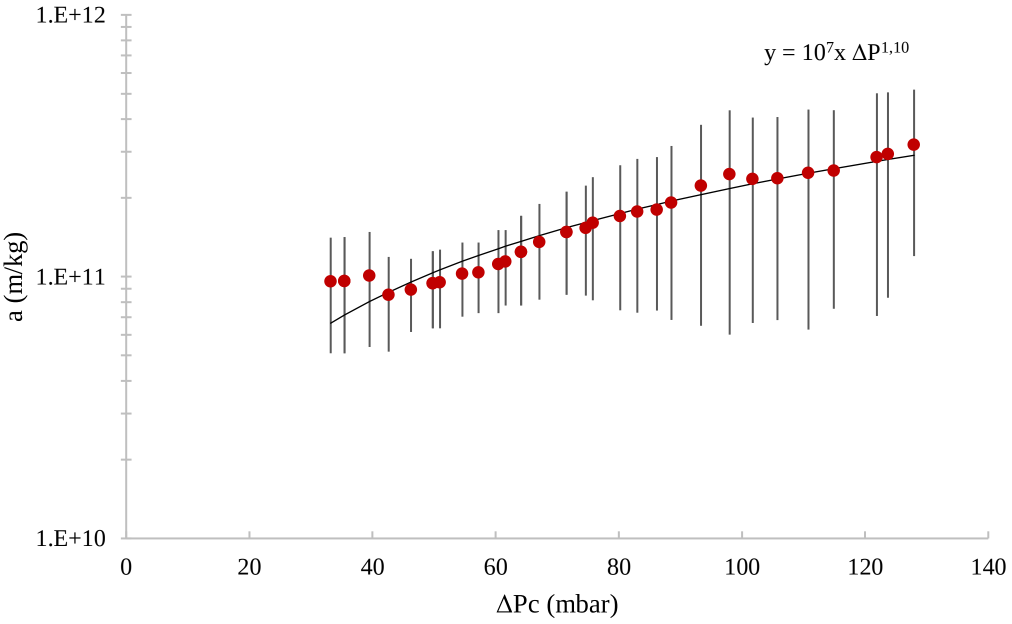

Figure 69. Specific hydraulic resistance as a function of the pressure

A compressibility index n = 1.10 with $\beta = 10^7$ m^{-1} was calculated using a regression analysis, which represents the compressible behavior previously reported for yeast.

In the work of Mendret [84], laser triangulometry provides the characterization of the cake formed by the filtration of bentonite suspensions. Values ranging from 0 – 70 µm of cake height were found for the same range of deposited mas per membrane surface unit that the current study. Even if bentonite suspension differs inherently in the shape of the particles (platelet shape) the compressibility index $n = 0.82$ corresponds to a compressible cake which is also the case for the current study ($n = 1.10$) and the particle size distribution is similar to the one of yeast cells. The comparison then lays in the compressibility of both cakes and how the observed height is in the same range for similar compressibility behaviors.

The compressibility index obtained in the current work is compared to that previously reported for yeast suspensions in several studies corresponding to different operating conditions. Rushton and Khoo. [118] investigated the filtration characteristics of cultivated yeast at different ages (24, 48 and 72h). They performed vacuum filtration with (i) varying TMP and (ii) drained compressibility test in order to characterize (i) the filtration performance and the (ii) yeast cake compressibility. This experimental approach did not allow deriving quantitative relationships as the influence of both ΔP and particle velocity were not clear. However, they conclude that for vacuum design purposes, cake specific resistances between $10^{11} > \alpha > 10^{12}$ m/kg may be expected. The compressibility tests yield a compressibility index $n = 0.9$. In the previous noted work of Nakanishi et al. [115] (Section I.2 of this chapter), they also evaluate the specific resistance of the cakes of different microorganisms assessing the flux variations under constant pressure (130 – 740 mbar). For the filtration cake (5.15 kg/m^2) of yeast cells, they found cake specific resistances ranging from $10^{11} > \alpha > 10^{12}$ m/kg and a compressibility index varying between $0.28 < n < 0.45$. Meireles et al. [42] studied the hydraulic resistances of the filtration cakes of yeast cells. They found the specific cake resistances in the order of magnitude ranging from $10^{11} < \alpha < 10^{12}$ m/kg at 100 mbar for a deposited mass ranging from 49 – 60 g/m^2. In addition, in their work they found a compressibility index $n = 0.80$. Mota et al. [43] found a compressibility coefficient $n = 0.7$ and specific resistance within the range $1.0 \times 10^{11} < \alpha < 3.0 \times 10^{11}$ m/kg (at 400 mbar filtration pressure) while studying the effect of the suspension concentration on the filtration of yeast cells.

.

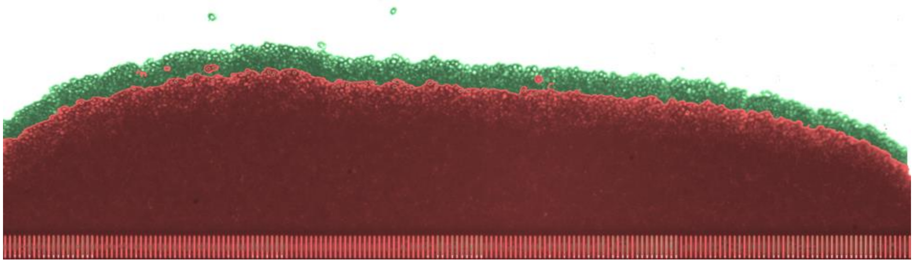

Figure 70. Compressibility of the yeast cake. Red surface corresponds to the cake at the final pressure, while green surface represents the difference between the compressed and relaxed cake.

The compressibility and the elasticity of the yeast cake were also investigated by releasing the pressure of the system after the cake was already formed. In all the experiments, yeast cakes exhibited a relaxation confirmed by the cake swelling as illustrated in Figure 70. The red surface corresponds to the compressed state of the cake at the end of the filtration and the green surface to the relaxed state of the cake when the pressure is released. While at the compressed state (~ 130 mbar) the porosity was 0.15, after pressure relaxation, the cake exhibited a rise in the porosity about ϵ ~ 0.26. Different mechanisms could explain the effect of pressure on the cake expansion when the pressure is removed like the yeast cell compression, deformation or cell reorganization (Figure 71).

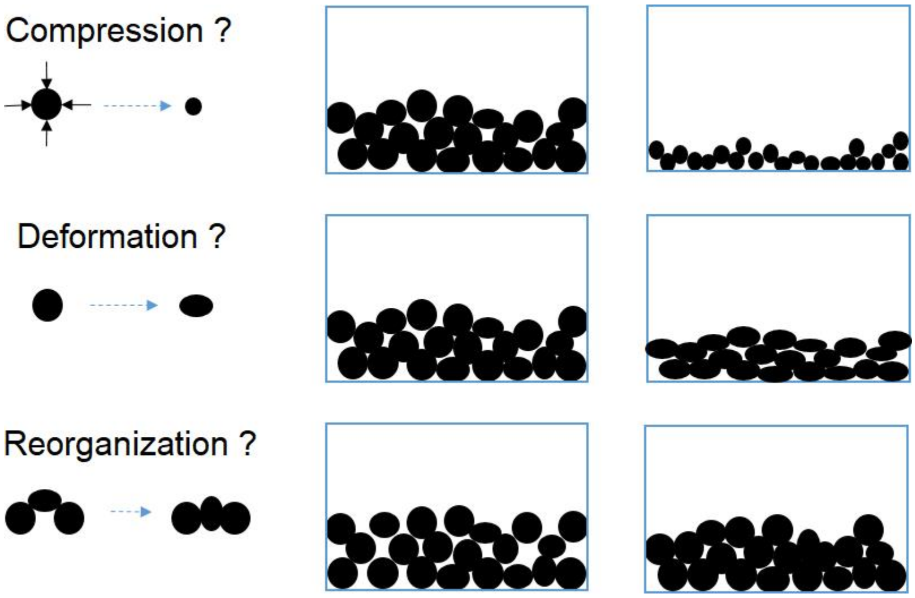

Figure 71. Cell compression, deformation and reorganization on yeast cake compressibility.

When considering the ratio of total deformation to the cake height after relaxation $\varepsilon = \Delta\overline{h_o}/h_o$ and the compressibility stress σ corresponding to the filtration final pressure, an apparent elasticity modulus of the cake, E (σ/ε) = 30 kPa is estimated for the yeast cake. Yeast mechanical properties certainly play a role on the cake behavior. However, the cake elasticity cannot be only correlated to the individual yeast properties, mainly because of the voids between the cells that could collapse and the experimental conditions for which the mechanical properties of individual cells are estimated.

Indeed, previous work addressed yeast cell mechanical properties, the reported Young's modulus can be much higher than the values obtained for the cake of the current study. However, Schiavone et al [119] studying the mechanical properties of wild and mutant yeast cells (*S. cerevisiae*) using atomic force microscopy found that ethanol causes a decrease of the Young's modulus. In particular, for the wild yeast strain, they found Young's modulus of ~675 kPa and ~135 after cells were treated with ethanol. Nevertheless, under the condition of yeast growth in the current study (low glucose concentration and no oxygen limitation) the ethanol concentration remains very low and cannot have such an effect. Another study by Delarue et al. [120] investigated yeast cells (*S. cerevisiae*) growing in a confined environment. Cell jamming produced by proliferation in the device leads to a partial confinement of the population and a gradual increase of the contact pressure up to 0.65±0.1 MPa. Whereas yeast cells in the absence of mechanical stresses are nearly spherical (ovoid shape), they observe morphological modification of the cells into convex polyhedra as the pressure becomes growth-limiting; at 0.5 MPa most of the yeast cells were consistently deformed exhibiting convex polyhedral shape. The work of Stenson et al. [121] also assess the yeast cell (S. cerevisiae) mechanical properties. In their study, an individual yeast cell is fully compressed between two parallel and rigid platens until it ruptures. They found a mean cell elastic modulus of 185±15 MPa. This result is even higher than the one found by Schiavone (previously noted) and this could be explained by the different techniques used for the estimation.

Comparing to the previous studies the level of pressure in present work (~ 130 mbar) should not lead to important deformation of the individual yeast cell and thus the cause of the global compressive behavior cannot be explained only by the cell deformation. While there have been studies devoted to yeast filtration and mechanical properties, most of these have focused either at the individual cell scale or on the empirical relations between flux and the operating pressure. There is a lack of information regarding the compressibility at the cake level during the actual filtration process. The previously noted work of Meireles et al. [42] compared experimental data on filtration through yeast filter cakes with a mechanical model developed to describe the behavior of a cake of deformable cells. They used a multiple speed equilibrium sediment height technique (MSESH) to assess the compressive yield stress. They measured the compressive yield stress for different solid fractions in the range 0.5–0.9 and observed that porosities as low as 0.15 can be reached for compressive yield stress in the range 100–500 mbar, which is in agreement with the present results. In addition, they suggest a relaxation of the cell cake once compression is stopped, which has been confirmed in the current study.

II. Filtration experiments using model suspensions: non-spherical and polydispersed latex particles

Non-spherical and polydispersed suspensions were studied to explore the effect of two different yeast features that could impact filtration performance: the presence of buds and the size distribution. The filtration was studied from the slot scale, when blocking takes place, to the transition state between membrane and cake controlled dynamics. The following results correspond to the mean value for three experiments for both suspensions.

The experiments with model particle suspensions (non-spherical NS and polydisperse SD) were driven using the C4Pe20 units as the minimum size of the particles is 5 µm for which sieving is normally achieved. Based on the results in Chapter IV: the further experiments for model particles are done using C4Pe20 units for which the cakes are more compact and thus should be closer to yeast cake behavior.

II.1. Non-spherical particle suspension

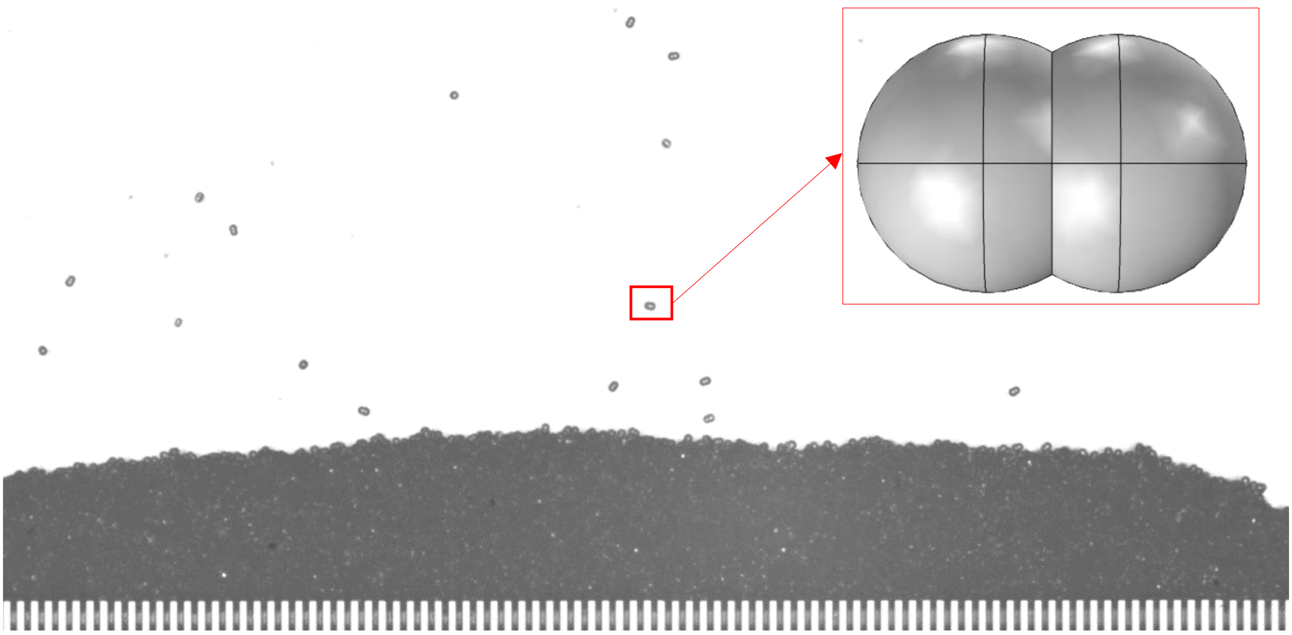

Figure 72. Cake obtained for non-spherical particles and scheme of the characteristic peanut shape.

The particles used in this experiments are peanut shaped. The peanut shape has a longest dimension of a = 7.4 µm from two identical particles merged while the other characteristic length correspond to the particle diameter of 5.1 µm (Figure 72). These particles are used for their resemblance to aggregates of two yeasts cell (mother and daughter cells before separation).

Cake growth and flowrate

Figure 73 shows the cake height and flow rate evolution as function of the deposited mass per unit membrane surface. The standard deviation for the measured cake height supports the good reproducibility of the experiments. An initial accelerated growth of the cake is observed as there is a steeper slope, that should correspond to the arrival of the first particles that mainly block the slots, then the height increase becomes linear a the cake becomes uniformly distributed. The flow rate also exhibits an important initial decrease from the initial value of ~ 9 µl/min, (close to the pump set-point), towards a stable flowrate ~ 4 µl/min. The flowrate standard deviation also confirms the good reproducibility of the experiments. The changes in the slope of the cake height and flowrate are obtained for a deposited mass of about 10g/m^2. This value appears to be consistent because it corresponds to the mass of particles required to fill all the slots taking into account the surface of the non-spherical particles and their corresponding volume and density. Thereby, two regimes clearly appear: the first one until all the slots are filled correspond to the membrane blocking phase (influenced by the membrane geometry) and the second one, when the slots are covered corresponds to the phase where the cake growth and particle organization in the cake become driven by the cake itself.

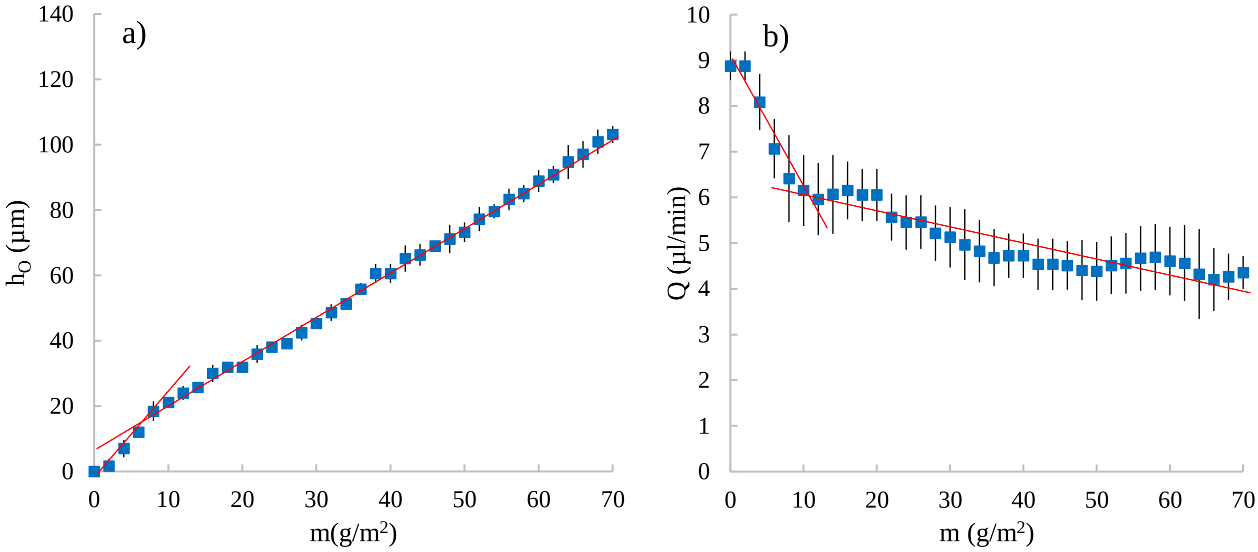

Figure 73. a) Cake mean height and b) Flow rate evolution. Both as a function of the deposited mass per unit membrane surface. The red lines differentiate the noted regimes of membrane blocking at the beginning of the filtration and the cake formation.

Porosity, permeability and Kozeny coefficient

The permeability of the cake represented in Figure 74b has been calculated when the cake is sufficiently developed (*m* ~ 20 g/m^2). The permeability evolution is consistent with the porosity variation (Figure 74a), which behaves similar to the case of monodispersed spherical particles and in the same range of values (0.50 to 0.38 shown in Figure 59a). This similar behavior could be explained by the monodispersity of both suspensions and the low aspect ratio of the peanuts particles. The previous studies [122]–[125] have also shown similar behavior in terms of porosity for the aspects ratios in the range $0 < \alpha < 2$, with $\alpha = 0$ corresponding to spheres.

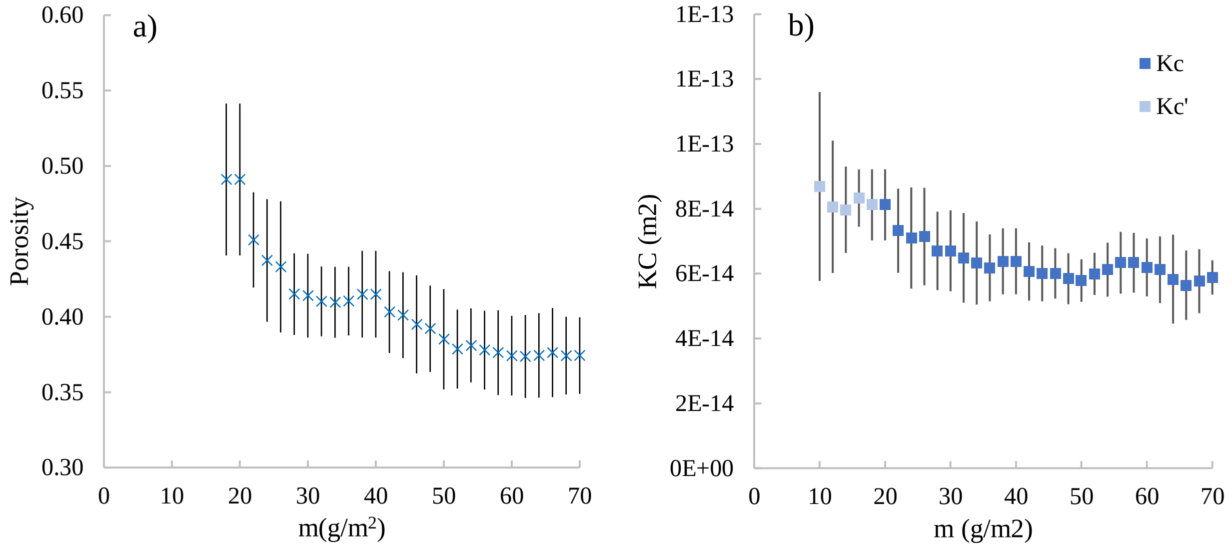

Figure 74. a) Porosity and b) Permeability evolution as a function of the deposited mass per unit membrane surface for non-spherical particles. K_C corresponds to the permeability for a formed deposit (m > 20 g/m^2) while K_C' for the blocking layers.

According to the theoretical models for spherical particles. The decreasing behavior towards a stabilization corresponds to a close random packing structure (ϵ = 0.36, vibrated beds) [113]. Particles with "peanut" shape have not been widely studied, nonetheless previous work with particles with similar shapes (Cylinders, beans, nail shaped particles) show good agreement with the current experimental results. Nolan and Kavanagh [126] performed experiments with different non-spherical particles (cylindrical, bean and nail shaped) and compared these results with simulations. They modeled non-spherical particle shapes by an assembly of spheres. The precision of their calculations depends on the number of component spheres for modeling the non-spherical shape. The experimental and simulation results were in good agreement; the mean close random packing porosities obtained were $\epsilon \sim 0.33$ for the cylindrical and bean shaped particles and $\epsilon \sim 0.48$ for nail shaped particles. Cylinders and bean shapes are more similar to the peanut shape particles, and the porosity for both shapes show good agreement with the experimental values found by the end of the filtration experiment in the current study ($\epsilon_h \sim 0.36$). Later work by Williams and Philipse [125] focused on the packing of monodispersed particles with spherocylindrical shapes. They simulated the packing for particles with different aspect ratios (a) and found a dependence of the porosity on this parameter. The spherocylindrical shape is very similar to the peanut shape for small values of a (a = 0 corresponds to spheres). The peanut shape for the current study corresponds to $a \sim 1.5$ and the obtained packing ($\epsilon = 0.38$) is in agreement with Williams and Philipse results, for which porosities of 0.34 and 0.38 were found for $a = 1$ and 2 respectively. Other authors also found similar results for the spherocylindrical shapes as a function of α [122]–[124].

Kozeny coefficient and compressibility

Even though porosity is similar between spheres and peanut particles, the shape difference has an effect on the Kk values that are consistently lower than the common value $K_K = 5$ as shown in Figure 75a. This is explained by the calculation of K_K (Eq. 13) and the difference in the specific surface S_p of both type of particles (Table 6 in Chapter III: Materials and methods, Section II). The coefficient Kk decreases as the S_p grows. Kk shows a linear increase with the porosity in contrast with the yeast exponential behavior (Figure 68). Ozgumus et al. [77] also found a linear relationship when simulating the flow through a porous media formed by particles with rod shape. They obtained Kk values within the range from about 3 – 12 for porosities between 0.2 to 0.4. This linear relationship could be related to the non-compressibility of the cake that is consistent for rigid latex particles.

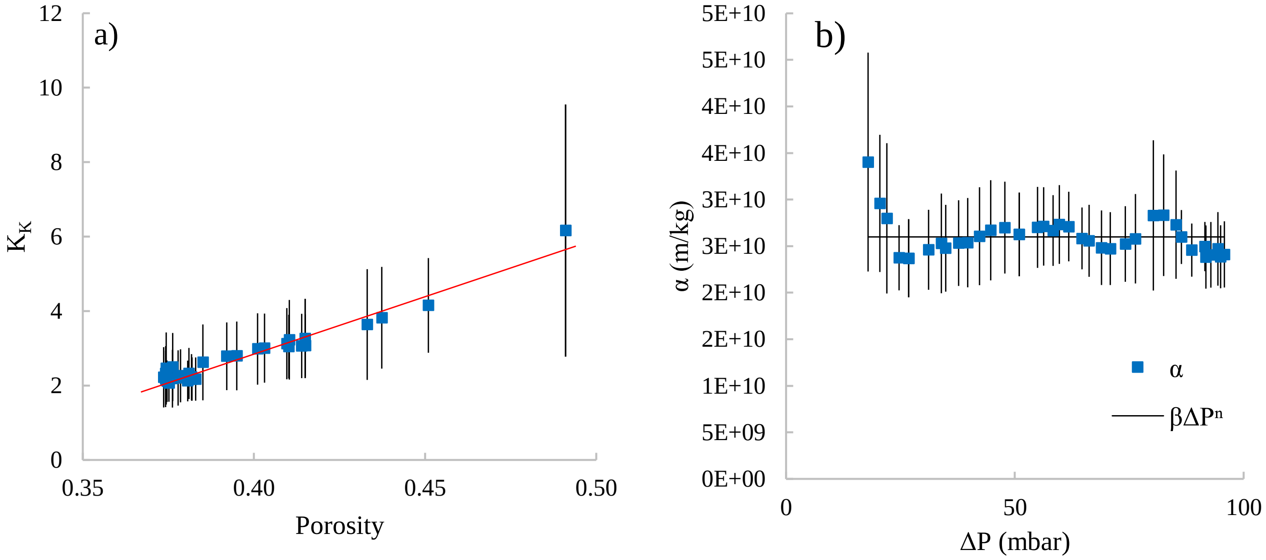

Figure 75. a) Kozeny coefficient K_K as a function of the porosity and b) Specific resistance as a function of the pressure drop across the cake alone during the filtration of non-spherical particles.

The non-compressibility feature of the cake can be confirmed from the specific resistance analysis in Figure 75b. The fitting curve of the specific resistance as a function of the pressure by power law leads to a compressibility coefficient $n = 0$. This compressibility index was previously found close to 0 by Nakanishi et al [115] for latex particle cakes with very high rigidity and low compressibility behavior.

II.2. Suspension of polydispersed model particles

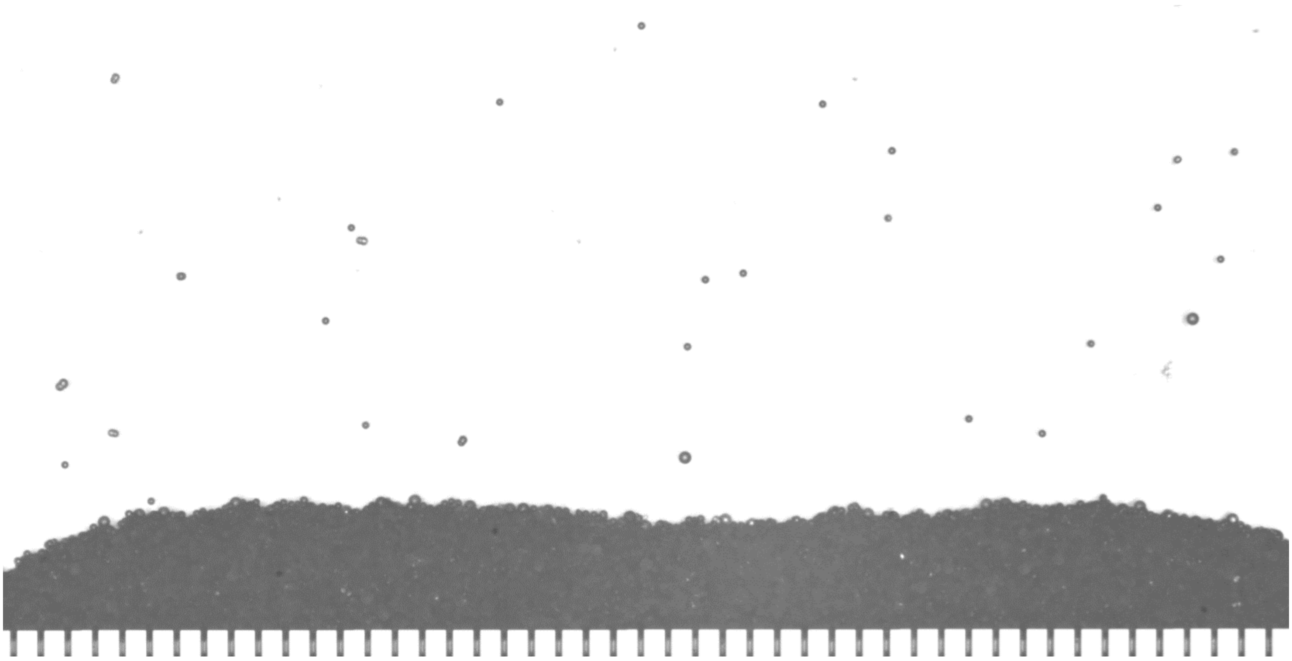

Figure 76. Cake obtained for the polydispersed suspension.

The similar behavior of monodispersed model particles (peanut and spheres) stands out the importance of analyzing polydispersed suspensions. In order to be closer to real filtration feeds, shape disparity was studied in addition to size distribution. Besides, both size distribution and shape are in agreement with that of cultivated yeast *S. cerevisiae*. For 50 h aged cells, previously reported size distribution [118] shows an important participation of individual cell size ranging from 4 to 8 µm. Thereby, in order to mimic a yeast suspension, the sizes of the used model particles for polydispersed suspension are chosen according to the size distribution of yeast cells of 50 h culture. In addition, the budding shape of dividing cells is comparable to the non-spherical “peanut” shape. Thus, by mixing spherical particles of 5 µm, 8.4 µm and peanut particles, equally apportioned in volume, the used suspension is considered a simplified representation of the yeast suspension. It is important to point out that, as particles are equally apportioned in volume, the number concentration of each kind is different (Figure 77).

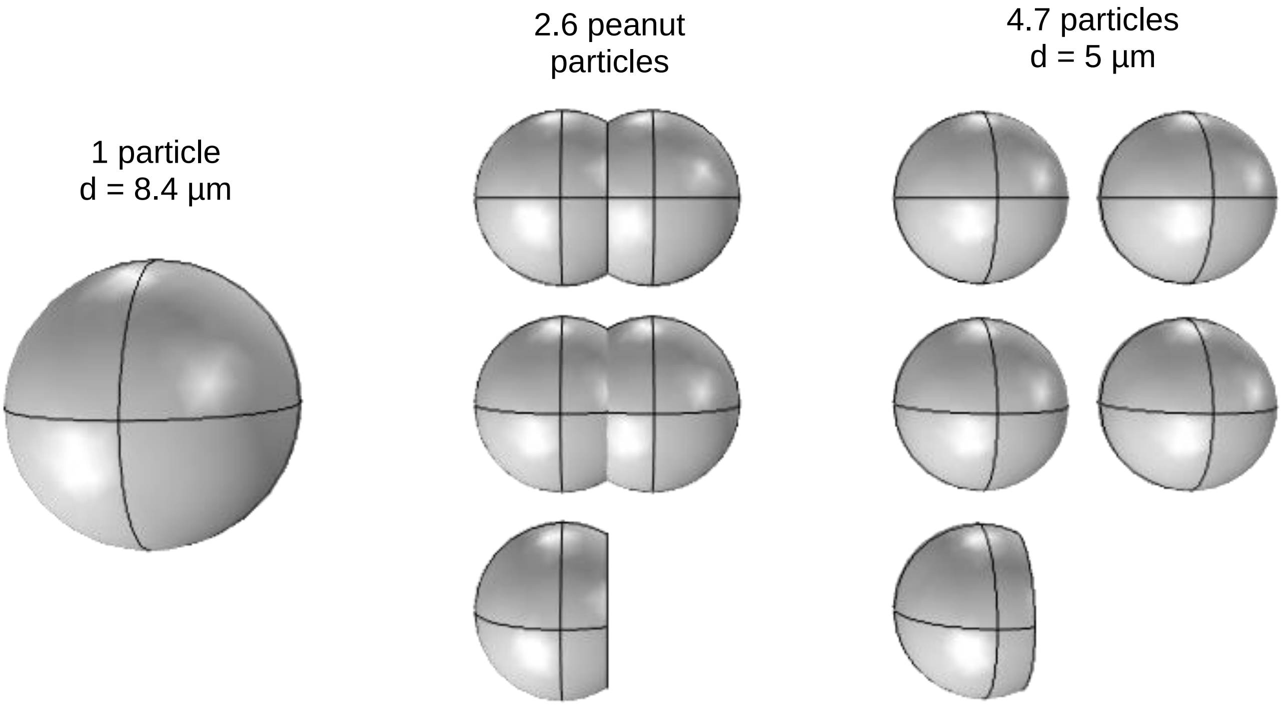

Figure 77. Particle number concentration for the polydispersed suspension.

Cake growth and flowrate

Figure 78a shows the cake height and flow rate evolution as function of the deposited mass per unit membrane surface. There is a negligible standard deviation of the data, which shows a good reproducibility of the experiments. Similar to the previous suspensions, the cake height exhibits fast growth at the beginning of the experiment, while the flowrate decreases sharply from the initial value ~9 µl/min, close to the set-point (Figure 78b). As the deposited mass reaches about 5g/m^2, the increase of cake height becomes linear with the deposited mass and the flow rate starts its transition to a linear and attenuated decrease. In this case the flowrate reduction is more important compared to the filtration of the monodispersed particle suspensions.

The establishment of the first blocking layer over the membrane slots of particles can explain the change in the slope for the linear relationship between the cake height and the deposited mass. Concerning the flowrate, it seems to be three behaviors: at the beginning (0 – 5 g/m^2), there is an accentuated blocking due to high number of particles with diameter d = 5 that causes a fast flowrate reduction. Smaller particles block more optimally the membrane. Then, it could be assumed the existence of a second slope that results from the effect of the different particles blocking the membrane. Even if there are more particles with d = 5 as the filtration continues, eventually the other particles (peanut and particles with d = 8.4 µm) contribute more to membrane blocking and they attenuate the fast decreasing. For a deposited mass higher than ~ 12g/m^2, the flowrate decrease becomes linear and it can be assumed that it corresponds to the cake filtration phase.

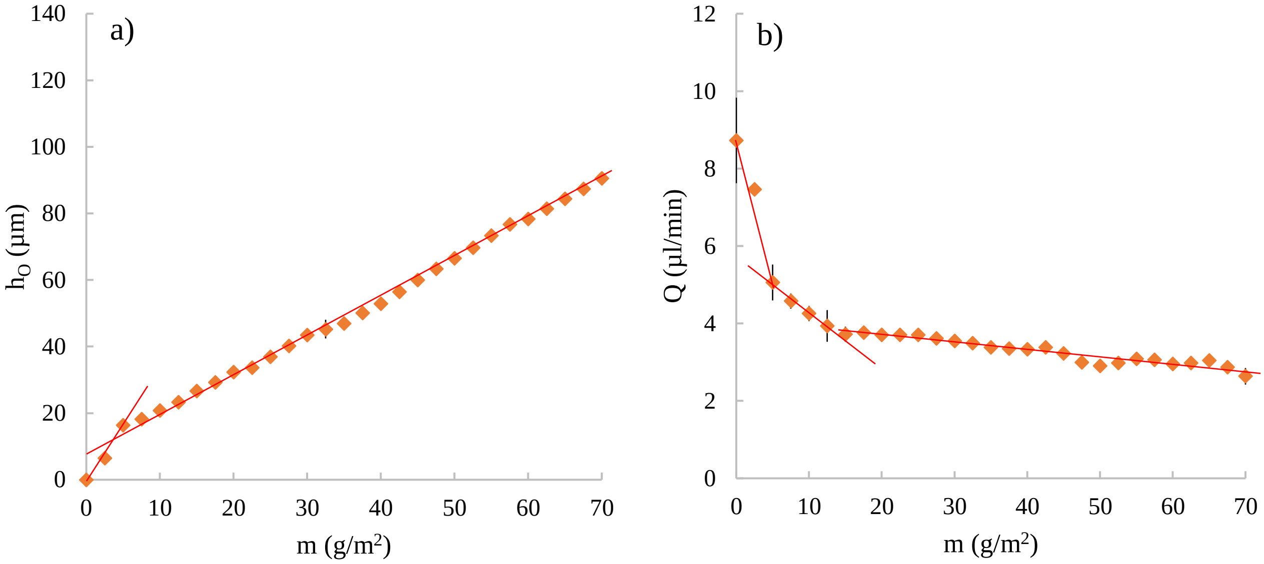

Figure 78. Cake mean height and b) Flow rate evolution for polydispersed suspensions. Both as a function of the deposited mass per unit membrane surface.

Porosity and permeability

Figure 79a shows the porosity evolution for the polydispersed particles cake. The porosity takes values from 0.55 in the first stages of the cake formation to 0.26 when the cake is more developed. Two different slopes are observed: a sharp zone that could be related to a promptly transition from an initial porous structure to a more compact; at this stage, smaller particles could be filling easily the spaces around the bigger ones. As the voids are filled the previous phenomenon is attenuated and the evolution of the porosity towards a stable value is decelerated. A previous study by Thies-Weesie and Phillipse [127] analyzed the packing of bi-dispersed suspensions with a size ratio R_1/R_2 = 1.4 and 2.6, and for different mixing percentages. The lowest porosity values corresponds to a percentage of smaller particles between 20 – 40% of the particle volume fraction in the suspension. They found porosities varying within the range 0.26 – 0.34, however they used an *ex-situ* and indirect porosimetry technique. A more recent study by Han et al. [128] used bi-dispersed particle suspensions and studied the evolution of the cake during the dead end microfiltration. Particles of 5 and 3 µm were used at different percentages in the suspension and the filtration was conducted on membranes with cylindrical pores of 2 µm. Using optical coherent tomography (OCT with resolution of 4 µm) they found a porosity gradient along the cake height. In particular, for equally mass-apportioned particles in the suspension they found a porosity of 0.7 at the surface of the cake, while in the zone were the cake is more developed and compressed, the porosity varies from 0.20 to 0.25. In the case of more continuous size distribution Kramadhati et al. [129] found porosity gradients along the cake height varying from 0.45 to 0.35. Theoretical models report porosity for continuous size distributions ranging from 0.25 to 0.40 depending on the particle size ratio of the size distribution [117], [130] and the skewness [116].

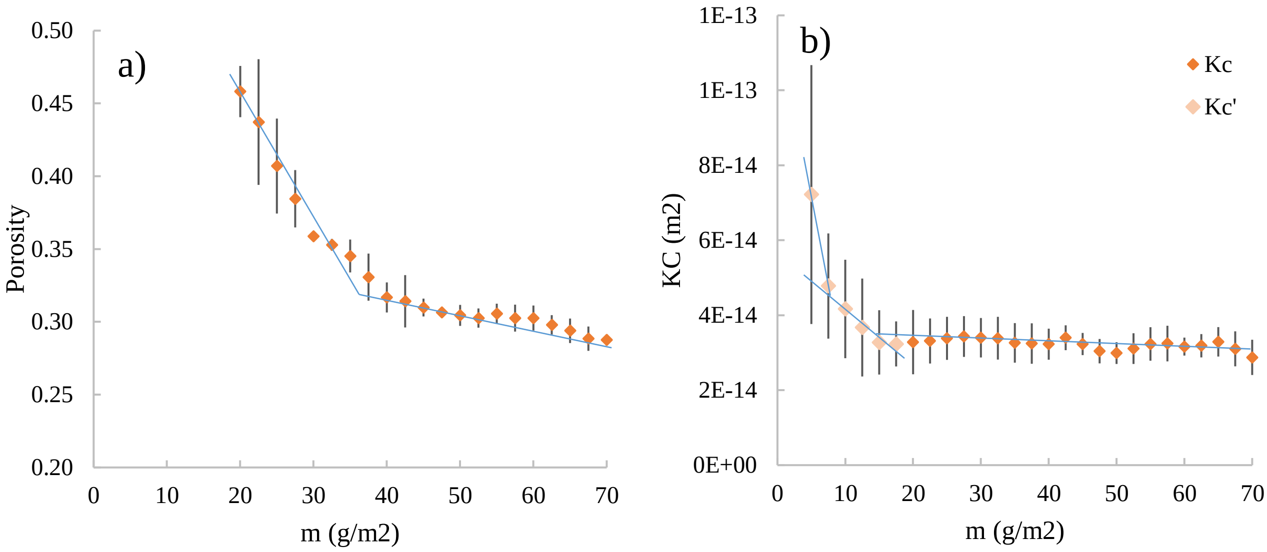

Figure 79. a) Cake porosity and b) permeability evolution for polydispersed suspensions. Both as a function of the deposited mass per unit membrane surface. Mean values with the standard deviation. K_C corresponds to the permeability for a formed deposit ($m > 20$ g/m^2) while K_C' for the blocking layers

The decrease in porosity does not seems have the expected influence on the permeability evolution (Figure 79b), which seems to reach the stationary for a deposited mass $m > 20$ g/m^2. However, the permeability still exhibits a decreasing behavior, but for low compared to the sharp decrease associated with membrane blocking for $m < 12$ g/m^2. The permeability K_C represents the combined effects of the initial membrane blocking and the growing cake. The presence of smaller particles (5 µm diameter) in the polydispersed suspension (equally apportioned in volume, i.e higher number of smaller particles compared to the others) could yield a higher coverage of the filtering surface. Consequently, membrane blockage could be accentuated in comparison with the experiments performed with peanut and spherical particles with diameter $d = 8.4$ µm. This phenomenon may result in an increase of the hydraulic resistance, which combined with a more dense packing of the polydispersed particles in the first layers, leads to the drastic reduction of the permeability at the beginning of the filtration.

Kozeny coefficient and compressibility

The Kozeny coefficient *Kk* shows a sharp exponential increase with an increase in the porosity. The *Kk* coefficient behaves consistently in almost the entire range besides the higher porosities for which the dispersion becomes important (Figure 80a). The specific hydraulic resistance exhibits a non-compressible behavior with n value close to zero and with β the mean specific resistance. Different from yeast cakes, the cakes obtained from the filtration of model particle suspensions do not exhibit elastic behavior after pressure is removed, with nearly no detectable variation of the cake height and hence porosity; this is in agreement with the behavior observed for the specific resistance. The work by Rushton and Khoo [118] and Nakanishi et al. [115]also found no compressible behavior for latex particle cakes.

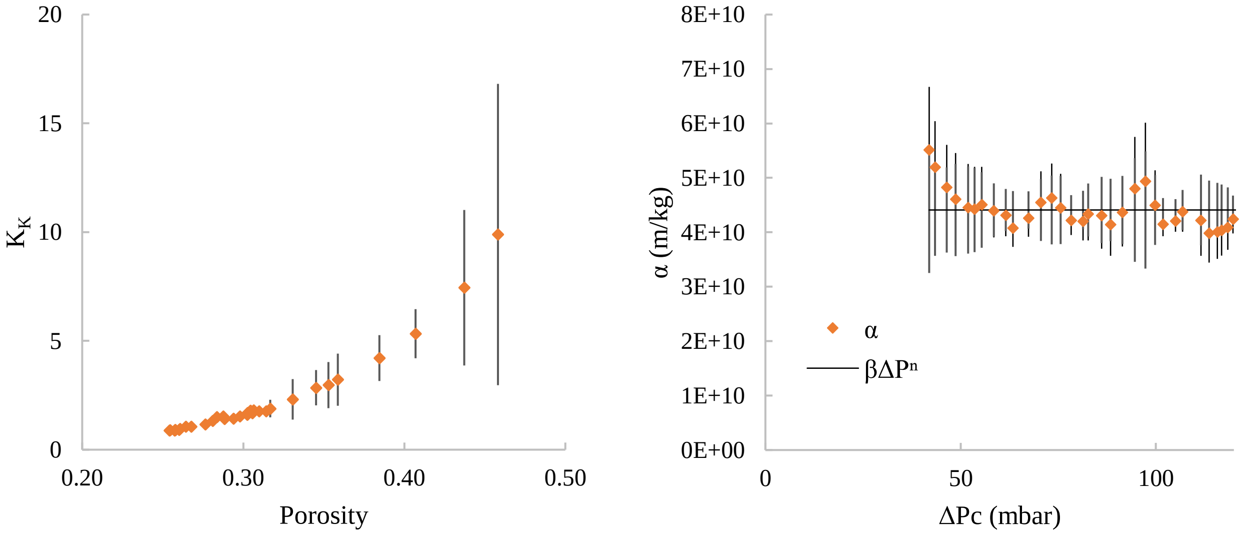

Figure 80. a) Kozeny coefficient as a function of the porosity and b) Specific resistance as a function of the pressure difference across the cake alone for the filtration cake of polydispersed particles.

III. Comparison

In this section, the objective is to compare the results obtained for the different model suspensions with those obtained with yeast suspension in order to better understand the parameters involved in fouling, such as cake structure and its relation to particle shape, organization and polydispersity. In order to have clearer graphical representation of the data and results, the information regarding reproducibility (standard deviation) is not presented (see Sections I and II of the current chapter and Annexes). The comparison is made for the filtration using C4Pe20 units, which exhibited (for spherical particles) a more compact behavior that is closer to that observed for yeast cakes.

Cake observed height

Figure 81 illustrates the cake growth as function of the deposited mass per unit membrane surface. The monodispersed suspensions (spherical "S" and peanut shape particle "NS") overlapped in the whole domain, which means that porosities behave similarly as it is confirmed in Figure 82. Yeast cakes exhibited the lowest cake height for the studied range of deposited mass. This means that yeast cakes should be the most compact. The height of the polydispersed particle cake is intermediate between the cake obtained for monodispersed particles and the yeast cells.

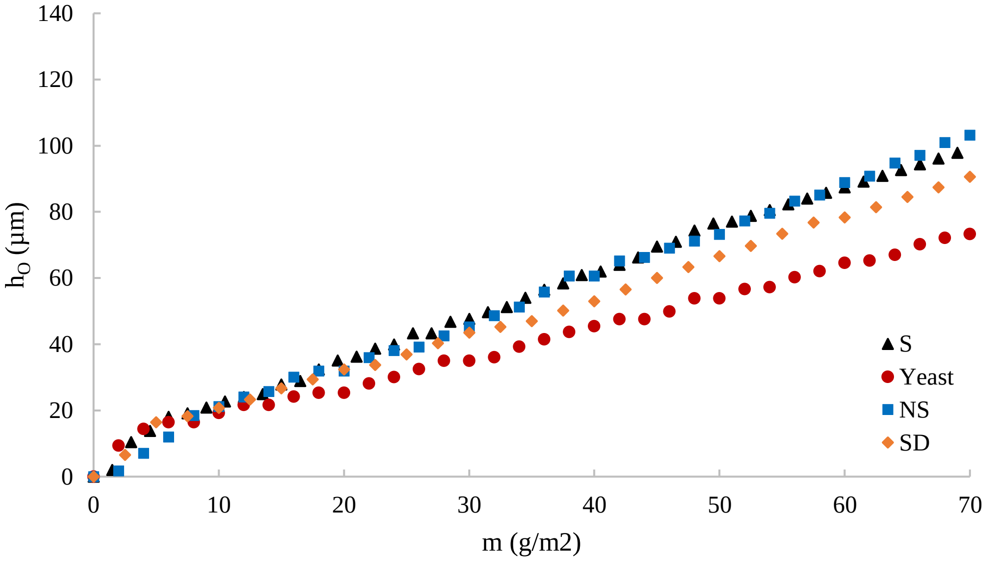

Figure 81. Comparison of the cake height evolution for the different suspensions.

Porosity, permeability and Kozeny coefficient

The porosity and permeability evolution for the different suspensions is observed in Figure 82 and Figure 83. Monodispersed particles (spherical and non-spherical) cakes have a quite similar behavior.

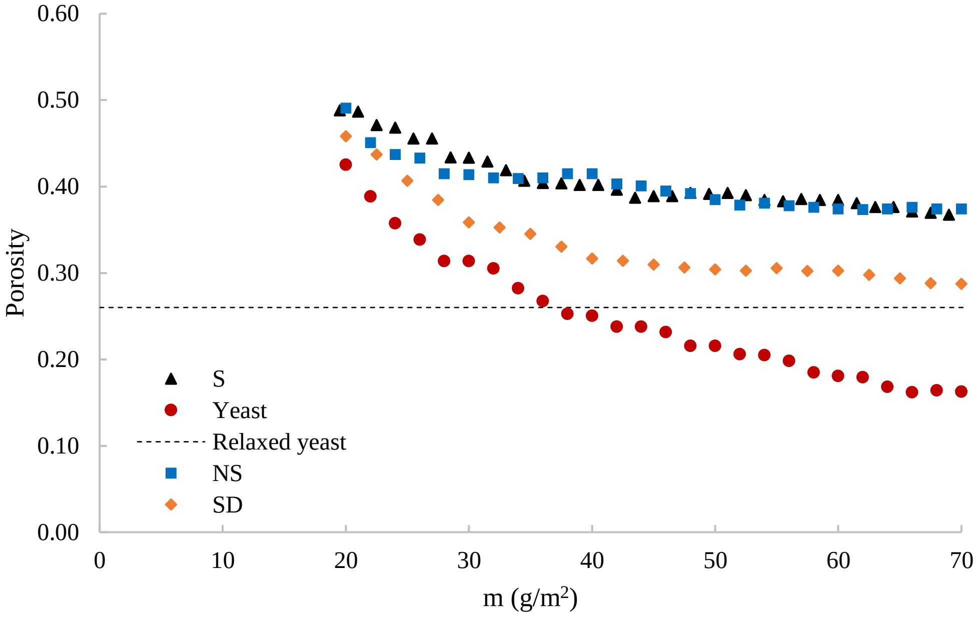

Figure 82. Comparison of the porosity evolution of the cakes obtained for the different suspensions.

The analysis starts at 20 g/m^2, after the first membrane blocking phase when the cake construction begins, corresponding to a cake height between 2 – 3 layers for monodispersed particles and 3 – 4 for yeast and the polydispersed suspensions (as a function of the mean diameter). Porosity evolution starts from different values for the four different experiments, being ~0.49 for the monodispersed suspensions, ~ 0.46 for the polydispersed suspension and ~0.43 for the yeast suspension. These differences become larger as the cake keeps forming during the filtration. Yeast cake exhibits 62% reduction of the porosity, while for monodispersed particle cake is 25% and for polydispersed particle cake is 37%. These results present more clearly the role of polydispersity on the global filtration dynamics for the yeast suspension. Polydispersity is related with lower porosities, the smaller particles can fill the voids around the bigger ones, which reduces the void fraction of the cake. This phenomenon has been previously observed experimentally and modeled theoretically. Ben Hassan [25] observed this particle arrangement for a bi-dispersed suspension (4.8 and 1 µm latex beads) while performing microfiltration experiments with microsieves (0.2 µm pore size). A porosity of 0.40 was found for the bi-dispersed particle cake whereas for monodispersed particles the porosity was 0.45 and 0.42, for 4.8 and 1 µm particles respectively. Similar results in term of particle arrangement have also been described by Thies-Weesie and Philipse [127]. Other authors conclude that the packing depends on the particle size ratio and the mixing percentage of the particles of different sizes [116], [117], [127], [130]. The permeability evolution is consistent with the previous analysis of the porosity (Figure 83) as lower permeabilities are found for yeast and polydispersed particles suspensions.

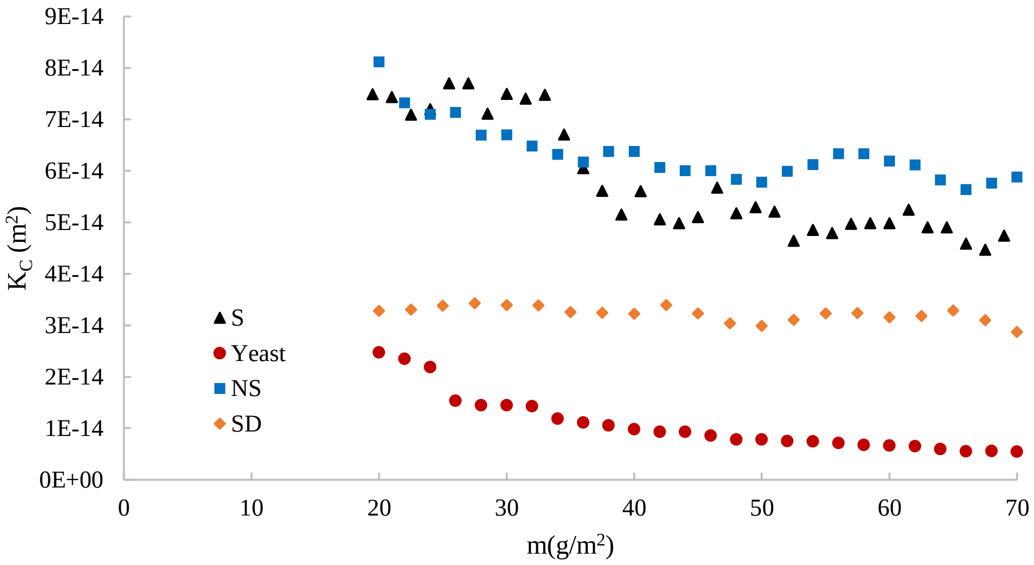

Figure 83. Comparison of the cake permeability evolution for the different suspensions against the deposited mas per unit membrane surface.

Even if the cakes obtained for the monodispersed particle suspensions (Spherical “S” and peanut shape “NS”) exhibited a similar behavior when analyzing porosity and permeability, the *Kk* coefficient varies in a higher range for the spherical particles. This is explained by the specific surface, which is lower for spherical particles (S_p = 0.71 and 1.10 µm^{-1}) as shown in Table 6 (Chapter III: Materials and methods, Section II). For the same range of porosities (0.4 – 0.5), *Kk* is consistently above 5, while for the cake obtained for peanut particles *Kk* is consistently under 5. For peanuts particle suspensions, K_K behaves linearly with the porosity increase in the whole range of the experiment. However, for the spherical particles the K_K coefficient decreases linearly when the porosity decreases from 0.5 to 0.4 and under this value K_K seems to stabilize around 7 and porosity remains higher than 0.36. This suggests that the cake formed with spherical particles reaches a stable particle arrangement.

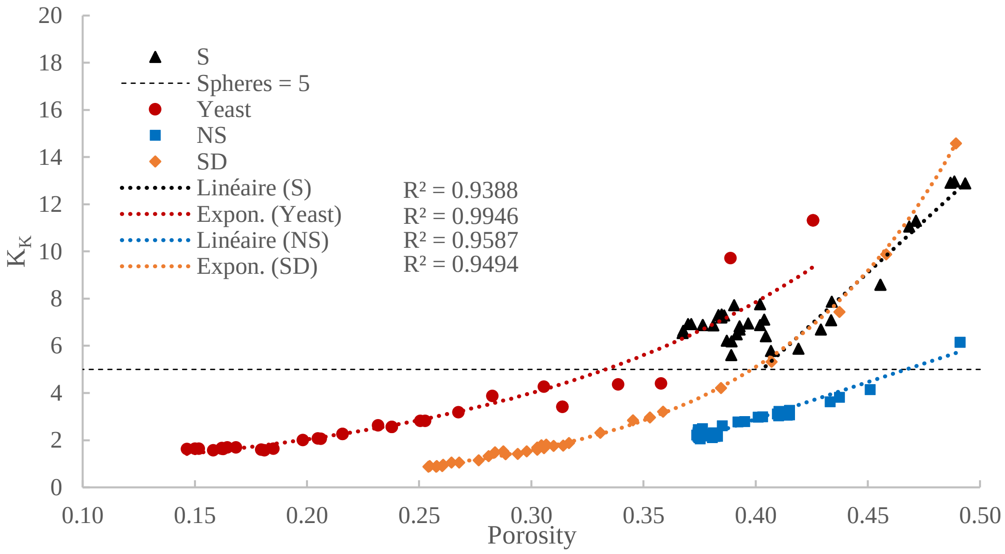

Figure 84. Comparison of the Kozeny coefficient as a function of the porosity for the different suspensions.

The cakes formed by the polydispersed particles and yeast cells present a quite similar relation between K_K and the porosity that can be fitted to an exponential law (Figure 84). The specific surfaces related to particle shape are 0.98 and 1.13 µm^{-1} for the polydispersed particle and the yeast cell suspensions respectively; this parameter is involved in the Carman-Kozeny formula used to calculate K_K and could explain the difference obtained among the suspensions and particularly for the spherical particles. Porosity and K_K reach lower values for the cakes of yeast cells and polydisperse particles; this might be consequence of particle/cell re-arrangement in the cakes when pressure increases. This suggests that polydispersity enhances particle reorganization in the cake, which yield denser packing structures.

Nevertheless, even if polydispersity was proved to have an important influence on the overall analysis of the different variables (porosity, permeability and K_K), there is a remaining gap between the behavior yeast and polydispersed particle cakes; this suggests that polydispersity feature does not fully explain the yeast cake properties.

Cake compressibility

The compressibility of the cakes is analyzed through the specific resistances (Figure 85) in order to explain the remaining gap regarding the porosity and permeability for polydispersed particle and yeast cell cakes. All the cakes formed by latex particles show an incompressible behavior with a compressibility index close to zero. This means that the specific resistance scatters around a mean value, thus it is independent from the pressure difference. For yeast cakes, a compressibility index *n* = 1.10 is obtained and corresponds to a compressible behavior and is close to what has been previously reported. The possible reason of this compressibility was previously discussed (Chapter V: Section I.3).

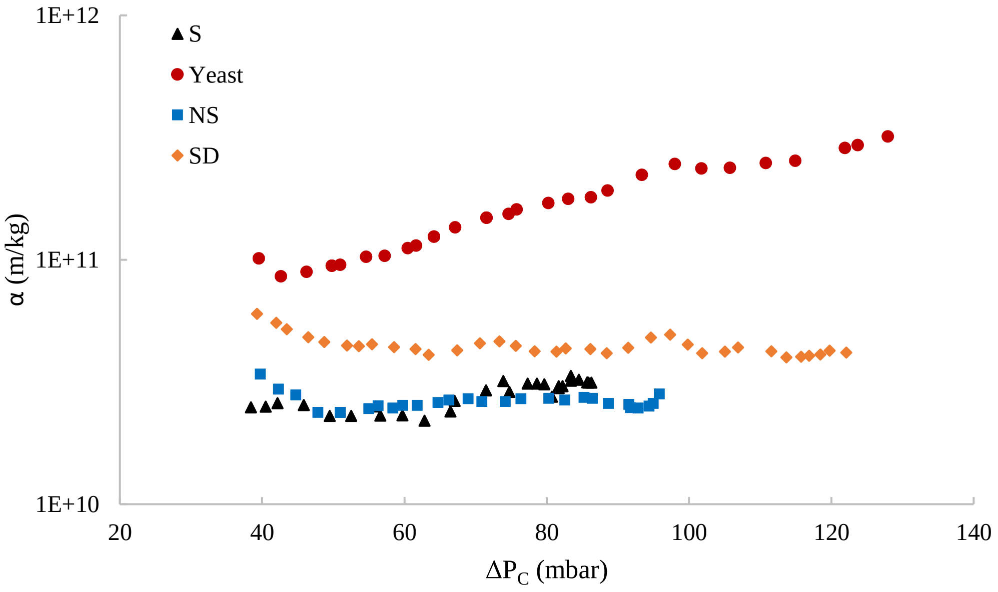

Figure 85. Comparison of the specific resistance as a function of the pressure across the cake alone for the different suspensions.

IV. Conclusion

The experimental protocol proposed in this study appears to be reliable to perform an accurate study of the filtration cake formation for different suspensions. The experiments for the different suspensions have shown a good reproducibility. The permeability is used as the macroscopic parameter to analyze the microfiltration performance.

Cakes formed by monodispersed particle suspensions show a quite similar behavior in terms of porosity and permeability regardless of the different particle shapes, spheres and peanuts.

The cakes formed by monodispersed rigid particles exhibit a similar incompressible behavior with higher cake permeability than those obtained for the filtration of polydispersed particle and yeast cell suspensions. The different shapes (spheres and peanuts) for the two monodispersed suspensions did not have an important effect on the overall hydrodynamics of the filtration; only the Kozeny coefficient was affected as it is strongly dependent on the porous medium geometry related to the particle specific surface that are different as shown in Table 6.

The combined analysis of the porosity, the Kozeny coefficient K_K and the permeability stand out the role of the porosity on the yeast cake behavior compared to K_K. The Kozeny coefficient values were roughly similar for the yeast and for non-spherical and polydispersed particle suspensions. However, the three suspensions exhibited different behaviors regarding the permeability and porosity.

Polydispersity proves to be one of the major features playing a role on the filtration properties of yeast cakes. However, it does not fully explain the yeast cake behavior. The evidence of yeast cake compressibility when removing the pressure drop contributes to explain the cake behavior. It was concluded that the low permeability of the yeast cakes might be caused by the combined effect of cells polydispersity and cake compressibility. The origin of this compressibility would require deeper investigation taking into account the complexity of living cells. Previous studies reported low cell deformation [120], [131], this low deformability corresponds to Young's modulus (~150 MPa) much higher than the 30 kPa estimated based on the yeast cake relaxation. Nonetheless, other authors report lower Young's modulus from 70kPa to 1 MPa for wild-type or mutant yeast cells [119].

Chapter VI: General conclusion

The present study was focused on characterizing the fouling phenomenon for membrane microfiltration and particularly the first fouling layer properties. The proposed strategy consisted in performing direct lateral observation (DO) of particle deposition over a model membrane during dead-end microfiltration process. The experimental set-up designed for the study allowed the *in-situ*, non-invasive and real-time acquisition of images of the particles arriving to the membrane and of the forming deposit. From these images, the cake height, the particle concentration field and the mean flow velocity were estimated using a dedicated image processing. The pressure was also recorded to provide a complete analysis of microfiltration evolution with the increase of deposited mass, taking into account both, the flowrate and pressure drop across the cake formed.

The dead-end microfiltration cell consisted of a channel (11.5 mm) with a model membrane composed by a series of consecutive slots (2µm and 4µm width as the filtering zone). The experimental set-up satisfied the required specifications to achieve DO and to record real-time data for further analysis. The following conditions of the conceptual design were achieved:

- Overall operation: the system support and connections guaranteed the effective seal of the system, hence there were no leaks disturbing the pressure measurements and compromising the system operation. The geometry of the model membranes (slot width) guaranteed the rejection of all particles and cells for all the experiments.

- Geometric constraints: The channel cross section yields flow velocities of 5.6 mm/s for the initial set-point flow rate corresponding to Stokes regime with Reynold's number $Re < 1$. In consequence there is negligible particle-fluid relative velocities; i.e. individual particles follow the flow streamlines. The image acquisition rate is high enough for capturing the particles arriving to the membrane, leading to an accurate mass balance. The limited channel depth match the optical depth of field; this allowed observing all the particles in the channel without losing information due to particles being out of focus.

- Optical features: The optical set up offers a high spatial and time resolution for the acquired data. The DO resolution was improved (~ 0.6 µm/pix) in comparison to previous reported studies. This allowed a better imaging of particles in the microfiltration size range. Also, the entire membrane (*x* direction) and a considerable distance above the membrane (*y* direction) were observed (1650 x 800 pix ~ 1000 µm x 480 µm). These features allowed the identification of the deposit contour but also the estimate of the concentration field and the mean velocity from image processing. Combining all the information recorded at a fast acquisition rate (up to 250 fps) made possible the real-time data analysis.

- Feasibility: thanks to plasma photoetching technique it was possible to obtain the fine geometry for the different membrane of the microsystem especially for the different configurations with relative small geometric irregularities. The channel depth remains in the limit of the theoretical Kozeny-Carman approach for studying porous media (3 - 6 particles for model suspension and from 3 – 10 cells for yeast suspension) and wall effect was examined for the complementary simulation analysis. Also, as a matter of evidence, no significant specific behavior of the particles close to the wall was observed, like particles stuck on the walls. The domain depth match the available optical depth field and so minimizes the loss of information without overly compromising the filtration physics.

The present research is characterized by model conditions that constitute a fundamental experimental approach to study the fouling mechanisms due to the accumulation of particles at the membrane surface at the beginning of microfiltration. Theoretical packing models for monodispersed spheres have been extensively studied. The experimental set-up and the analysis protocol were then validated for the filtration of monodispersed spherical particles suspensions, comparing with previous literature results.. In order to investigate the effect of multi-scale characteristics of complex suspensions, always keeping in mind the industrial applications, filtration of cultivated yeast (*Saccharomyces cerevisiae*) suspensions were performed. Complementary experiments using model latex particles with different morphologies, aimed a better understanding of yeast cake properties by studying cell individual features like shape and polydispersity.

In order to analyze the acquired images, a specialized Python code was developed. This code allows extracting the cake height, the deposited mass, the mean velocity and the concentration field from the sequence of images. Combining the quantitative information, including continuous pressure recording, with a qualitative interpretation of the acquired images provided insight on particle organization and thus the cake structure.

For spherical particles, a mass balance was performed to estimate the porosity ϵ_h and the Kozeny coefficient K_K along with complementary analysis using Darcy equation and the Carman-Kozeny formula. The analysis was in agreement with previous reported information. The characterization of membrane geometry influence on particle deposition and microfiltration performance was studied for the different filtration units (C4Pe7, C4Pe10 and C4Pe20). The initial cake structure is visibly conditioned by membrane geometrical parameters and it has an effect on slot blocking and further cake growth, which impacts pressure drop across the cake. The "pore protection coefficient" p_p, is then introduced to evaluate the effect of the membrane geometry. C4Pe7 membrane is characterized by $p_p < 1$ and exhibited pore protection phenomenon. In the case of C4Pe10, $p_p = 1.36$, being close to the unity, the cake presents the most organized and stable structure (Figure 53c and d). For C4Pe20, $p_p = 3.64$ leading to a more random packing and compact cake structures. The cake first layers for C4Pe7 and C4Pe10 exhibited an organized structure similar to theoretical cubic packing models. As the cake growths, for the different membrane geometries, permeability and porosity exhibited a consistent decreasing behavior. The cake porosity varied in the range 0.50 – 0.36, which corresponds to characteristic packing models from loosest regular packing to random close packing respectively.

The slot blocking and the first stage of cake formation were modeled using the commercially available finite element code COMSOL Multiphysics^{TM}. The simulations provided a means of evaluating the qualitative description of the membrane blocking in order to compare with the quantitative analysis of the experiments. Indeed, the qualitative analysis remains subject to the interpretation of 2D images, which leads to an uncertainty in the depth direction. However, even if the simulated 3D geometry is based on the qualitative description of pore blocking and particle arrangement, the calculations obtained from the simulations confirmed the consistency of the approach, as there is a fair agreement with the experimental results.

Monodispersed particle suspensions (spheres and peanuts) show a very similar behavior in terms of porosity (0.5 – 0.36) and permeability (final permeability ~ 5.5 $\times 10^{-14}$ m^2) regardless of the different particle shapes. Both parameters were stable by the end of the experiment (70g/m^2). However, the K_K coefficient varied in a higher range of values in the case of spherical particles (7 – 13), which is consistent with a lower specific surface. For the same range of porosities (0.37 – 0.50), K_K was consistently above 5, the well-known Kozeny coefficient for spheres. Particularly for spheres K_K displayed a linear decrease with decreasing porosities in the range 0.4 – 0.5. For porosities lower than 0.4 and as lowest as 0.36 it seems that K_K stabilizes about 6.9. For the peanut shape particles, K_K is consistently under 5 .

In the case of the yeast cell suspension, the cake porosity evolution shows a continuous decrease from 0.43, when cake first layers are formed, to 0.15 at the end of the filtration run (70g/m^2) and it is consistent with the permeability variations throughout the filtration. K_K exhibited an exponential increasing profile, as a function of the porosity, ranging from 1.5 to 4.5. For porosity values lower than 0.20, corresponding to the end of the experiment, it seems that the Kk coefficient reaches a minimum value ~ 1.5. The compressibility of the yeast cake was assessed by the compressibility index "n" for the specific resistance relation $\alpha = \beta \Delta P^n$. A compressibility index n = 1.10 with β = 10^7 m^{-1} was obtained using a regression analysis, which represents the compressible behavior, similar to that previously reported for yeast cakes.

The cake formed by the polydispersed particle suspension shows an exponential behavior for the K_K coefficient ranging from 1 to 10 for cake porosities between 0.26 – 0.46. Comparing the behavior of all the cakes obtained for the different suspensions, the cake for polydispersed particles resembles more to the one obtained for the yeast cells. Additionally, when analyzing the porosity evolution of the four suspensions, the cake of polydispersed particles shows an intermediate behavior between those obtained for the monodispersed particles and the yeast cells. The same is observed for the permeability (~ 3.0 $x10^{-14}$ m^2 at the end of the experiment for polydispersed particles). These results suggest an accentuated effect of particle reorganization in the cake and it explains the influence of polydispersity on yeast cake behavior. Yeast as polydispersed particle cakes exhibits a continuous decrease of the porosity and the permeability and does not seems to reach a clear stable value in the conditions of these experiments. Even if there is a certain level of similarity between the two experiments, yeast cake behavior remains not fully explained by the polydispersity of the cells.

Cake compressibility analysis assessing the specific resistances contributes to the explanation of yeast cake properties and reveals its influence on the filtration performance. All the cakes formed by latex particles show an almost incompressible behavior with a compressibility index close to zero while yeast cake exhibits a significant compressibility (n = 1.10). . Only yeast cake expands after transmembrane pressure relaxation which results in a porosity of ϵ_r ~ 0.26. This value matches the porosity for polydispersed particles and it explains the cake specific resistance. It might be concluded that the lower permeability of the yeast cakes is caused by the combined effect of the polydispersity of the cells and the compressibility of the cake.

The present work constitutes an original experimental approach and analysis method of membrane fouling. However, there is room for improvement to facilitate the experimental operation, guarantee more controlled conditions and extend the scope of the analysis. The main points that should be developed and investigated in further work could be the following:

- Further investigation of the “pore protection” phenomenon should be performed for suspensions of particles with different shape and size than those used in the present work. For spherical particles, p_p seems to be a reasonable parameter to characterize membrane blocking. However, in the case of complex polydisperse suspensions a deeper analysis of the effect of the shape of the particles could lead to an extended definition of the “pore protection coefficient”. A general parameter assessing size distribution and shape characteristics of the particles could be defined. This might be helpful for membrane design or selection for different industrial applications or research. Also, it would be interesting to perform filtration of bigger monodispersed particles to determine the optimal pore protection coefficient p_p, for which the permeability remains constant throughout the filtration. For more complex suspensions, it would be also interesting to evaluate how the macroscopic variables (Porosity, permeability, specific resistance) are sensitive to the size distribution characteristics like the size ratio, skewness and specific surface.

- The experimental set-up could be run under controlled pressure conditions. According to previous studies a reliable measurement of the flowrate (in the order of magnitude of the present study) could be an important issue. However, in the present study an accurate estimation of the flowrate is performed for low Reynold’s number ($Re < 1$). Controlling pressure would facilitate performing series of compression-relaxation (stress cycles) experiments after the filtration cake is formed for a deeper characterization of the cake mechanical properties like compressibility and elasticity. Complementary analysis for establishing the effect of macroscale measurable variables like pressure, on the local force distribution at the individual particle/cell scale in the cake, should be considered. Thereby, the porous structure and geometry could be better described as a function of the macroscale pressure and the particle/cell mechanical properties. This analysis could relate the local porosities to particle/cell local deformation and could help in developing the Carman-Kozeny approach.

  These compression-relaxation experiments could be complemented by using confocal laser scanning microscopy (CLSM) for acquiring 3D in situ information of the cake structure during stress cycles. The experiment could be easily adapted as the channel depth is in the range of laser penetration (30-40 µm). The use of fluorescent tagged transparent particles, or dyed cells would provide a mean of accessing another estimate of the porosity and more details about the 3D cake structure. According to the expected dynamics of the process, the acquisition rate of the CLSM should be enough to acquire the stack of images in order to investigate the evolution of the cake structure for slow stress cycles.

The experimental set-up could be improved and adapted for different applications:

- Using specific and monitored valves would significantly improve the system driving and facilitate the filtration operation. In addition, these valves should allow to better control the injection of the suspension and a more uniform concentration front profile in the channel.

- Another perspective of this study could be the set-up adaptation to crossflow filtration by changing the microfiltration cell units and adapting the flow system to the crossflow requirements. Interesting analysis could be performed based on the current image processing protocol to assess the cake growth, particle concentration and shear induced velocity. The PVM module and specially the particle-tracing feature could improve the mass balance, which has been a source of uncertainty in previous studies referring crossflow filtration. The information related to cross flow specific hydrodynamics could help for a better evaluation and description of the filtration performance addressed by the attenuation of particle accumulation at the membrane surface (anti fouling feature) due to shear induced migration (SIM). Experimental data could be useful for a deeper characterization of the parameters involved in the modeling of the SIM. The suspension balance model (SBM see Annexes) explains particle migration phenomenon observed in shear flows, which is ascribed to an inhomogeneous stress resulting from the presence of the particles in the suspension. A deeper and more precise experimental data will contribute to the definition of the parameters involved in the rheological model as the local viscosity.

This work was held in the frame of the research grant program AAP 2015 from Idex UNITI “NEMESIS”. One issue of this program was the investigation of the flow of non-colloidal suspensions. Particularly, the aim of the present study was to develop an experimental approach to characterize the behavior of concentrated particles near a membrane during filtration in order to implement the SBM Eulerian model. This model, which provides a fundamental and consistent approach for modelling the flow when the particles are fully mobile, has to be upgraded when the particles are at high concentration. The experimental approach developed in the current work, specially the original device designed for the study and the proposed methodology of analysis, will provide suitable tools to further investigate the filtration behavior of high concentrated suspensions in order to contribute to the issues raised by the NEMESIS program.

References

[1] A. Cano-Odena and I. F. J. Vankelecom, *Encyclopedia of Ecology*. 2008.

[2] A. FAO, “AQUASTAT - FAO’s Information System on Water and Agriculture.” [Online]. Available: http://www.fao.org/nr/water/aquastat/water_use/index.stm. [Accessed: 14-Oct-2019].

[3] M. Cheryan, *Ultrafiltration and Microfiltration Handbook*. CRC Press, 1998.

[4] R. Singh, “Chapter 3 - Hybrid membrane systems – applications and case studies,” in *Hybrid Membrane Systems for Water Purification*, R. Singh, Ed. Amsterdam: Elsevier Science, 2005, pp. 131–196.

[5] I. Ben Hassan, C. Lafforgue, A. Ayadi, and P. Schmitz, “Study of the separation of yeast by microsieves: In situ 3D characterization of the cake using confocal laser scanning microscopy,” *Food Bioprod. Process.*, vol. 92, no. C2, pp. 178–191, 2014.

[6] H. Li, A. G. Fane, H. G. L. Coster, and S. Vigneswaran, “Observation of deposition and removal behaviour of submicron bacteria on the membrane surface during crossflow microfiltration,” *J. Membr. Sci.*, vol. 217, no. 1, pp. 29–41, Jun. 2003.

[7] Y. P. Zhang, A. W. K. Law, and A. G. Fane, “Determination of critical flux by mass balance technique combined with direct observation image analysis,” *J. Membr. Sci.*, vol. 365, no. 1, pp. 106–113, Dec. 2010.

[8] A. Altaee, A. A. Alanezi, and A. H. Hawari, “2 - Forward osmosis feasibility and potential future application for desalination,” in *Emerging Technologies for Sustainable Desalination Handbook*, V. G. Gude, Ed. Butterworth-Heinemann, 2018, pp. 35–54.

[9] E. A. Bell, T. E. Poynor, K. B. Newhart, J. Regnery, B. D. Coday, and T. Y. Cath, “Produced water treatment using forward osmosis membranes: Evaluation of extended-time performance and fouling,” *J. Membr. Sci.*, vol. 525, pp. 77–88, Mar. 2017.

[10] O. Tossavainen and J. Sahlstein, “Process for producing a lactose-free milk product,” WO2003094623A1, 20-Nov-2003.

[11] N. Vasileva, Y. Ivanov, S. Damyanova, I. Kostova, and T. Godjevargova, “Hydrolysis of whey lactose by immobilized β-galactosidase in a bioreactor with a spirally wound membrane,” *Int. J. Biol. Macromol.*, vol. 82, pp. 339–346, Jan. 2016.

[12] I. Galambos, J. Mora Molina, P. Járay, G. Vatai, and E. Bekássy-Molnár, “High organic content industrial wastewater treatment by membrane filtration,” *Desalination*, vol. 162, pp. 117–120, Mar. 2004.

[13] A. Grelot, R. K. Dereli, F. P. van der Zee, J. G. M. van der Lubbe, and B. Heffernan, “Performances of Anaerobic Membrane Bioreactors Treating Thin Stillage from Bioethanol Plants at Different Sludge Retention Times,” *Procedia Eng.*, vol. 44, pp. 776–779, 2012.

[14] M. Chowdhury, M. G. Mostafa, T. K. Biswas, and A. K. Saha, “Treatment of leather industrial effluents by filtration and coagulation processes,” *Water Resour. Ind.*, vol. 3, pp. 11–22, Sep. 2013.

[15] S. Moniz, A. P. Barbosa-Póvoa, and J. P. de Sousa, “On the complexity of production planning and scheduling in the pharmaceutical industry: the Delivery Trade-offs Matrix,” in *Computer Aided Chemical Engineering*, vol. 37, K. V. Gernaey, J. K. Huusom, and R. Gani, Eds. Elsevier, 2015, pp. 1865–1870.

[16] R. Kuriyel and A. L. Zydney, “Sterile Filtration and Virus Filtration,” in *Downstream Processing of Proteins: Methods and Protocols*, M. A. Desai, Ed. Totowa, NJ: Humana Press, 2000, pp. 185–194.

[17] L. Giorno and E. Drioli, “Biocatalytic membrane reactors: applications and perspectives,” *Trends Biotechnol.*, vol. 18, no. 8, pp. 339–349, Aug. 2000.

[18] C. Charcosset, “Membrane processes in biotechnology: An overview,” *Biotechnol. Adv.*, vol. 24, no. 5, pp. 482–492, Sep. 2006.

[19] T. Deák, “YEASTS,” in *Encyclopedia of Food Sciences and Nutrition (Second Edition)*, B. Caballero, Ed. Oxford: Academic Press, 2003, pp. 6233–6239.

[20] C. P. Kurtzman and J. W. Fell, “16 - YEASTS,” in *Biodiversity of Fungi*, G. M. Mueller, G. F. Bills, and M. S. Foster, Eds. Burlington: Academic Press, 2004, pp. 337–342.

[21] K. E. J. Barrett, *Dispersion polymerization in organic media*. Wiley, 1975.

[22] T. Ono, M. Yamada, Y. Suzuki, T. Taniguchi, and M. Seki, “One-step synthesis of spherical/nonspherical polymeric microparticles using non-equilibrium microfluidic droplets,” *RSC Adv.*, vol. 4, no. 26, pp. 13557–13564, Mar. 2014.

[23] “Microparticle Synthesis & Properties,” *Sigma-Aldrich*, 2019. [Online]. Available: https://www.sigmaaldrich.com/life-science/cell-biology/detection/microparticles/learning-center/microparticles-synthesis.html. [Accessed: 22-Oct-2019].

[24] S. Beaufort, “Développement d’outils et de méthodologies pour l’étude de l’organisation et de la localisation in vivo de micro-organismes dans des structures biologiques complexes,” thesis, Toulouse, INSA, 2010.

[25] I. B. Hassan, “Analyse multi-échelle de la filtration sur microsive de particules modèles inertes et biologiques : caractérisation in situ du dépôt par microscopie confocale,” phdthesis, INSA de Toulouse, 2014.

[26] T. van de Laar, S. ten Klooster, K. Schroën, and J. Sprakel, “Transition-state theory predicts clogging at the microscale,” *Sci. Rep.*, vol. 6, p. 28450, Jun. 2016.

[27] E. Dressaire and A. Sauret, “Clogging of microfluidic systems,” *Soft Matter*, vol. 13, no. 1, pp. 37–48, Dec. 2016.

[28] A. Gornall, “Investigation of filter cake elasticity and reversibility during filtration of Saccharomyces Cerevisiae,” Internship report, Aug. 2017.

[29] C. Charcosset, “Procédés membranaires à application pharmaceutique et biotechnologique,” *ITBM-RBM*, vol. 27, no. 1, pp. 1–7, Feb. 2006.

[30] L. Qin *et al.*, “Anoxic oscillating MBR for photosynthetic bacteria harvesting and high salinity wastewater treatment,” *Bioresour. Technol.*, vol. 224, pp. 69–77, Jan. 2017.

[31] W. Pronk *et al.*, “Gravity-driven membrane filtration for water and wastewater treatment: A review,” *Water Res.*, vol. 149, pp. 553–565, Feb. 2019.

[32] A. Bennett, “Innovation trends in food and beverage filtration applications,” *Filtr. Sep.*, vol. 52, no. 2, pp. 28–33, Mar. 2015.

[33] T. Kudra, “FILTERS AND FILTRATION HANDBOOK 4th Edition (1997) By T. Christopher Dickenson Publisher: Elsevier Advanced Technology The Boulevard, Langford Lane, Kidlington, Oxford OX5 1GB, U.K.,” *Dry. Technol.*, vol. 17, no. 1–2, pp. 363–364, Jan. 1999.

[34] M. F. A. Goosen, S. S. Sablani, H. Al-Hinai, S. Al-Obeidani, R. Al-Belushi, and D. Jackson, “Fouling of Reverse Osmosis and Ultrafiltration Membranes: A Critical Review,” *Sep. Sci. Technol.*, vol. 39, no. 10, pp. 2261–2297, Jan. 2005.

[35] J. A. M. Hofman, “Removal of pesticides and other organic micrupollutants with membrane filtration,” *Water Supply*, vol. 11, pp. 101–111, 1993.

[36] T.-U. Kim, G. Amy, and J. E. Drewes, “Rejection of Trace Organic Compounds by Reverse Osmosis and Nanofiltration Membranes,” p. 15, 2005.

[37] S. B. Sadr Ghayeni, P. J. Beatson, R. P. Schneider, and A. G. Fane, “Water reclamation from municipal wastewater using combined microfiltration-reverse osmosis (ME-RO): Preliminary performance data and microbiological aspects of system operation,” *Desalination*, vol. 116, no. 1, pp. 65–80, Sep. 1998.

[38] R.-S. Juang and R.-C. Shiau, “Metal removal from aqueous solutions using chitosan-enhanced membrane filtration,” *J. Membr. Sci.*, vol. 165, no. 2, pp. 159–167, Feb. 2000.

[39] I. Ben Hassan, C. Lafforgue, A. Ayadi, and P. Schmitz, “In situ 3D characterization of monodispersed spherical particle deposition on microsieve using confocal laser scanning microscopy,” *J. Membr. Sci.*, vol. 454, pp. 283–297, Mar. 2014.

[40] S. Xue, C. Li, J. Li, H. Zhu, and Y. Guo, “A catechol-based biomimetic strategy combined with surface mineralization to enhance hydrophilicity and anti-fouling property of PTFE flat membrane,” *J. Membr. Sci.*, vol. 524, pp. 409–418, Feb. 2017.

[41] A. G. Fane, C. J. D. Fell, P. H. Hodgson, G. Leslie, and K. Marshall, “Microfiltration of biomass and biofluids: Effects of membrane morphology and operating conditions,” *Filtr. Sep.*, vol. 28, no. 5, pp. 332–331, Sep. 1991.

[42] M. Meireles, C. Molle, M. J. Clifton, and P. Aimar, “The origin of high hydraulic resistance for filter cakes of deformable particles: cell-bed deformation or surface-layer effect?,” *Chem. Eng. Sci.*, vol. 59, no. 24, pp. 5819–5829, Dec. 2004.

[43] M. Mota, J. A. C. Teixeira, and A. Yelshin, “Dependence of Saccharomyces cerevisiae filtration through membrance on yeast concentration,” 2004.

[44] C. Charcosset, “Procédés membranaires à application pharmaceutique et biotechnologique,” *ITBM-RBM*, vol. 27, no. 1, pp. 1–7, Feb. 2006.

[45] J. Liu, Z. Liu, X. Xu, and F. Liu, “Saw-tooth spacer for membrane filtration: Hydrodynamic investigation by PIV and filtration experiment validation,” *Chem. Eng. Process. Process Intensif.*, vol. 91, pp. 23–34, May 2015.

[46] J. Schwinge, D. E. Wiley, A. G. Fane, and R. Guenther, “Characterization of a zigzag spacer for ultrafiltration,” *J. Membr. Sci.*, vol. 172, no. 1–2, pp. 19–31, Jul. 2000.

[47] P. R. Neal, H. Li, A. G. Fane, and D. E. Wiley, “The effect of filament orientation on critical flux and particle deposition in spacer-filled channels,” *J. Membr. Sci.*, vol. 214, no. 2, pp. 165–178, Apr. 2003.

[48] D. C. Sioutopoulos and A. J. Karabelas, “Evolution of organic gel fouling resistance in constant pressure and constant flux dead-end ultrafiltration: Differences and similarities,” *J. Membr. Sci.*, vol. 511, no. Supplement C, pp. 265–277, Aug. 2016.

[49] O. Liot, A. Singh, P. Bacchin, P. Duru, J. F. Morris, and P. Joseph, “Pore cross-talk in colloidal filtration,” *Sci. Rep.*, vol. 8, no. 1, pp. 1–7, Aug. 2018.

[50] M. Saleem, L. Alibardi, R. Cossu, M. C. Lavagnolo, and A. Spagni, “Analysis of fouling development under dynamic membrane filtration operation,” *Chem. Eng. J.*, vol. 312, pp. 136–143, Mar. 2017.

[51] P. Schmitz, B. Wandelt, D. Houi, and M. Hildenbrand, “Particle aggregation at the membrane surface in crossflow microfiltration,” *J. Membr. Sci.*, vol. 84, no. 1, pp. 171–183, Sep. 1993.

[52] Y. Yu, Z. Yang, and Y. Duan, “Structure and flow calculation of cake layer on microfiltration membranes,” *J. Environ. Sci.*, vol. 56, pp. 95–101, Jun. 2017.

[53] A. Grenier, M. Meireles, P. Aimar, and P. Carvin, “Analysing flux decline in dead-end filtration,” *Chem. Eng. Res. Des.*, vol. 86, no. 11, pp. 1281–1293, Nov. 2008.

[54] J. Altmann and S. Ripperger, “Particle deposition and layer formation at the crossflow microfiltration,” *J. Membr. Sci.*, vol. 124, no. 1, pp. 119–128, Feb. 1997.

[55] T. Schluep and F. Widmer, “Initial transient effects during cross flow microfiltration of yeast suspensions,” *J. Membr. Sci.*, vol. 115, no. 2, pp. 133–145, Jul. 1996.

[56] V. V. Tarabara, I. Koyuncu, and M. R. Wiesner, “Effect of hydrodynamics and solution ionic strength on permeate flux in cross-flow filtration: direct experimental observation of filter cake cross-sections,” *J. Membr. Sci.*, vol. 241, no. 1, pp. 65–78, Sep. 2004.

[57] P. Le-Clech, Y. Marselina, Y. Ye, R. M. Stuetz, and V. Chen, “Visualisation of polysaccharide fouling on microporous membrane using different characterisation techniques,” *J. Membr. Sci.*, vol. 290, no. 1–2, pp. 36–45, Mar. 2007.

[58] S. H. Woo, J. Park, and B. R. Min, “Relationship between permeate flux and surface roughness of membranes with similar water contact angle values,” *Sep. Purif. Technol.*, vol. 146, pp. 187–191, May 2015.

[59] Y. Yao, C. Ba, S. Zhao, W. Zheng, and J. Economy, “Development of a positively charged nanofiltration membrane for use in organic solvents,” *J. Membr. Sci.*, vol. 520, pp. 832–839, Dec. 2016.

[60] P. R. Nott and J. F. Brady, “Pressure-driven flow of suspensions: simulation and theory,” *J. Fluid Mech.*, vol. 275, pp. 157–199, Sep. 1994.

[61] J. F. Morris and F. Boulay, “Curvilinear flows of noncolloidal suspensions: The role of normal stresses,” *J. Rheol.*, vol. 43, no. 5, pp. 1213–1237, Aug. 1999.

[62] H. M. Vollebregt, R. G. M. van der Sman, and R. M. Boom, “Suspension flow modelling in particle migration and microfiltration,” *Soft Matter*, vol. 6, no. 24, pp. 6052–6064, Nov. 2010.

[63] P. H. Hermans and H. L. Breede, “Principles of the Mathematical Treatment of Constant-Pressure Filtration,” *J Soc Chem Ind*, vol. 55, p. 1, 1936.

[64] J. Hermia, “Etude analytique des lois de filtration à pression constante,” *Rev Univ Mines*, vol. 2, no. 5, 1966.

[65] C. Duclos-Orsello, W. Li, and C.-C. Ho, “A three mechanism model to describe fouling of microfiltration membranes,” *J. Membr. Sci.*, vol. 280, no. 1, pp. 856–866, Sep. 2006.

[66] M. Hlavacek and F. Bouchet, “Constant flowrate blocking laws and an example of their application to dead-end microfiltration of protein solutions,” *J. Membr. Sci.*, vol. 82, no. 3, pp. 285–295, Jul. 1993.

[67] C.-C. Ho and A. L. Zydney, “A Combined Pore Blockage and Cake Filtration Model for Protein Fouling during Microfiltration,” *J. Colloid Interface Sci.*, vol. 232, no. 2, pp. 389–399, Dec. 2000.

[68] E. Iritani, N. Katagiri, and G. Inagaki, “Compression and expansion properties of filter cake accompanied with step change in applied pressure in membrane filtration,” *Sep. Purif. Technol.*

[69] Y. Zhang, Y. Zhao, H. Chu, B. Dong, and X. Zhou, “Characteristics of dynamic membrane filtration: structure, operation mechanisms, and cost analysis,” *Chin. Sci. Bull.*, vol. 59, no. 3, pp. 247–260, Jan. 2014.

[70] J. Mendret, C. Guiguir, C. Cabassud, and P. Schmitz, “Dead-end ultrafiltration and backwash: dynamic characterisation of cake properties at local scale,” *Desalination*, vol. 199, no. 1, pp. 216–218, Nov. 2006.

[71] W. D. Mores and R. H. Davis, “Direct visual observation of yeast deposition and removal during microfiltration,” *J. Membr. Sci.*, vol. 189, no. 2, pp. 217–230, Aug. 2001.

[72] S. Irmay, “On the theoretical derivation of Darcy and Forchheimer formulas,” *Eos Trans. Am. Geophys. Union*, vol. 39, no. 4, pp. 702–707, 1958.

[73] S. Whitaker, “The Forchheimer equation: A theoretical development,” *Transp. Porous Media*, vol. 25, no. 1, pp. 27–61, Oct. 1996.

[74] F.-J. Chen, “The permeability of compressed fiber mats and the effects of surface area reduction and fiber geometry,” Jan. 1975.

[75] Carman, “Fluid flow though granular beds,” *Chemical Engineering Research and Design*, pp. 415–421, 1937.

[76] M. A. Knackstedt and X. Zhang, “Direct evaluation of length scales and structural parameters associated with flow in porous media,” *Phys. Rev. E*, vol. 50, no. 3, pp. 2134–2138, Sep. 1994.

[77] T. Ozgumus, M. Mobedi, and U. Ozkol, “Determination of Kozeny Constant Based on Porosity and Pore to Throat Size Ratio in Porous Medium with Rectangular Rods,” *Eng. Appl. Comput. Fluid Mech.*, vol. 8, no. 2, pp. 308–318, Jan. 2014.

[78] V. Chen, H. Li, and A. G. Fane, “Non-invasive observation of synthetic membrane processes – a review of methods,” *J. Membr. Sci.*, vol. 241, no. 1, pp. 23–44, Sep. 2004.

[79] P. H. Hodgson, V. I. Pillay, and A. G. Fane, “Visual study of crossflow microfiltration with inorganic membranes: resistance of biomass and particulate cake.” 1993.

[80] H. Li, A. G. Fane, H. G. L. Coster, and S. Vigneswaran, “Direct observation of particle deposition on the membrane surface during crossflow microfiltration,” *J. Membr. Sci.*, vol. 149, no. 1, pp. 83–97, Oct. 1998.

[81] Y. Liu, E. Rosenfield, M. Hu, and B. Mi, “Direct observation of bacterial deposition on and detachment from nanocomposite membranes embedded with silver nanoparticles,” *Water Res.*, vol. 47, no. 9, pp. 2949–2958, Jun. 2013.

[82] S. Lorenzen, Y. Ye, V. Chen, and M. L. Christensen, “Direct observation of fouling phenomena during cross-flow filtration: Influence of particle surface charge,” *J. Membr. Sci.*, vol. 510, pp. 546–558, Jul. 2016.

[83] R. van Zwieten, T. van de Laar, J. Sprakel, and K. Schroën, “From cooperative to uncorrelated clogging in cross-flow microfluidic membranes,” *Sci. Rep.*, vol. 8, no. 1, p. 5687, Apr. 2018.

[84] J. Mendret, “Mise au point de méthodes de caractérisation non destructives du colmatage de membranes : application à la caractérisation in situ d’un dépôt particulaire en ultrafiltration frontale en lien avec les performances du procédé,” thesis, Toulouse, INSA, 2007.

[85] “Fluorescence Imaging, principles and methods.” Amersham Biosciences, 2002.

[86] W. T. Godbey, “Chapter 8 - Fluorescence,” in *An Introduction to Biotechnology*, W. T. Godbey, Ed. Woodhead Publishing, 2014, pp. 173–186.

[87] “Fluorescence microscope,” *Wikipedia*. 17-Dec-2017.

[88] J. S. Park and K. D. Kihm, “Use of confocal laser scanning microscopy (CLSM) for depthwise resolved microscale-particle image velocimetry (µ-PIV),” *Opt. Lasers Eng.*, vol. 44, no. 3, pp. 208–223, Mar. 2006.

[89] R. Lima, S. Wada, K. Tsubota, and T. Yamaguchi, “Confocal micro-PIV measurements of three-dimensional profiles of cell suspension flow in a square microchannel,” *Meas. Sci. Technol.*, vol. 17, no. 4, p. 797, 2006.

[90] M. Zator, M. Ferrando, F. López, and C. Güell, "Membrane fouling characterization by confocal microscopy during filtration of BSA/dextran mixtures," *J. Membr. Sci.*, vol. 301, no. 1–2, pp. 57–66, Sep. 2007.

[91] M. Zator, M. Ferrando, F. López, and C. Güell, "Microfiltration of protein/dextran/polyphenol solutions: Characterization of fouling and chemical cleaning efficiency using confocal microscopy," *J. Membr. Sci.*, vol. 344, no. 1–2, pp. 82–91, Nov. 2009.

[92] M. Bakhshayeshi, N. Jackson, R. Kuriyel, A. Mehta, R. van Reis, and A. L. Zydney, "Use of confocal scanning laser microscopy to study virus retention during virus filtration," *J. Membr. Sci.*, vol. 379, no. 1–2, pp. 260–267, Sep. 2011.

[93] S. Stehbens, H. Pemble, L. Murrow, and T. Wittmann, "Chapter fifteen - Imaging Intracellular Protein Dynamics by Spinning Disk Confocal Microscopy," in *Methods in Enzymology*, vol. 504, P. M. conn, Ed. Academic Press, 2012, pp. 293–313.

[94] R. Lindken and S. Burgmann, "14 - Laser-optical methods for transport studies in low temperature fuel cells," in *Polymer Electrolyte Membrane and Direct Methanol Fuel Cell Technology*, vol. 2, C. Hartnig and C. Roth, Eds. Woodhead Publishing, 2012, pp. 425–461.

[95] D. Yu, C. Guo, N. Xie, T. Wang, X. Hu, and D. Tang, "Experimental investigation on flow characteristics in open rectangular microgrooves using micro-PIV," *Appl. Therm. Eng.*, vol. 106, pp. 906–915, Aug. 2016.

[96] X.-B. Li, M. Oishi, M. Oshima, F.-C. Li, and S.-J. Li, "Measuring elasticity-induced unstable flow structures in a curved microchannel using confocal micro particle image velocimetry," *Exp. Therm. Fluid Sci.*, vol. 75, pp. 118–128, Jul. 2016.

[97] B. Boissier, F. Lutin, M. Moutounet, and A. Vernhet, "Particles deposition during the cross-flow microfiltration of red wines—incidence of the hydrodynamic conditions and of the yeast to fines ratio," *Chem. Eng. Process. Process Intensif.*, vol. 47, no. 3, pp. 276–286, Mar. 2008.

[98] H. Reingruber, A. Zankel, C. Mayrhofer, and P. Poelt, "A new in situ method for the characterization of membranes in a wet state in the environmental scanning electron microscope," *J. Membr. Sci.*, vol. 399–400, pp. 86–94, May 2012.

[99] Z. L. Wang and J. L. Lee, "Chapter 9 - Electron Microscopy Techniques for Imaging and Analysis of Nanoparticles," in *Developments in Surface Contamination and Cleaning (Second Edition)*, R. Kohli and K. L. Mittal, Eds. Oxford: William Andrew Publishing, 2008, pp. 395–443.

[100] B. Cappella and G. Dietler, "Force-distance curves by atomic force microscopy," *Surf. Sci. Rep.*, vol. 34, no. 1, pp. 1–104, Jan. 1999.

[101] H.-J. Butt, B. Cappella, and M. Kappl, "Force measurements with the atomic force microscope: Technique, interpretation and applications," *Surf. Sci. Rep.*, vol. 59, no. 1–6, pp. 1–152, Oct. 2005.

[102] W. Richard Bowen, N. Hilal, R. W. Lovitt, and Chris. J. Wright, "Characterisation of membrane surfaces: direct measurement of biological adhesion using an atomic force microscope," *J. Membr. Sci.*, vol. 154, no. 2, pp. 205–212, Mar. 1999.

[103] H. Gong, Z. Jin, Q. Wang, J. Zuo, J. Wu, and K. Wang, “Effects of adsorbent cake layer on membrane fouling during hybrid coagulation/adsorption microfiltration for sewage organic recovery,” *Chem. Eng. J.*, vol. 317, pp. 751–757, Jun. 2017.

[104] R. V. Lapshin, “Feature-oriented scanning methodology for probe microscopy and nanotechnology,” *Nanotechnology*, vol. 15, no. 9, pp. 1135–1151, Jul. 2004.

[105] I. Ben Hassan, C. Lafforgue, C. Ellero, A. Ayadi, and P. Schmitz, “Coupling of local visualization and numerical approach for particle microfiltration optimization,” *Microsyst. Technol.*, vol. 21, no. 3, pp. 509–517, Mar. 2015.

[106] Y. Lian, C. Xie, C. Mu, S. Yang, and B. Yao, “Preparation technology of micro-textured tools fabricated by inductively coupled plasma etching,” *Surf. Coat. Technol.*, vol. 370, pp. 177–186, Jul. 2019.

[107] J. Mendret, C. Guigui, P. Schmitz, C. Cabassud, and P. Duru, “An optical method for in situ characterization of fouling during filtration,” *AIChE J.*, vol. 53, no. 9, pp. 2265–2274, 2007.

[108] J. Mendret, C. Guigui, C. Cabassud, and P. Schmitz, “Numerical investigations of the effect of non-uniform membrane permeability on deposit formation and filtration process,” *Desalination*, vol. 263, no. 1, pp. 122–132, Nov. 2010.

[109] M. Honkanen, P. Saarenrinne, T. Stoor, and J. Niinimäki, “Recognition of highly overlapping ellipse-like bubble images,” *Meas. Sci. Technol.*, vol. 16, no. 9, p. 1760, 2005.

[110] C. A. Acuña and J. A. Finch, “Tracking velocity of multiple bubbles in a swarm,” *Int. J. Miner. Process.*, vol. 94, no. 3, pp. 147–158, Apr. 2010.

[111] A. Gupta and D. Yan, Eds., “Chapter 15 - Solid Liquid Separation – Filtration,” in *Mineral Processing Design and Operations (Second Edition)*, Amsterdam: Elsevier, 2016, pp. 507–561.

[112] P. K. Kundu, I. M. Cohen, and D. R. Dowling, Eds., “Chapter 9 - Boundary Layers and Related Topics,” in *Fluid Mechanics (Fifth Edition)*, Boston: Academic Press, 2012, pp. 361–419.

[113] F. A. L. Dullien, *Porous Media: Fluid Transport and Pore Structure*. Academic Press, 2012.

[114] D. Vidal, C. Ridgway, G. Pianet, J. Schoelkopf, R. Roy, and F. Bertrand, “Effect of particle size distribution and packing compression on fluid permeability as predicted by lattice-Boltzmann simulations,” *Comput. Chem. Eng.*, vol. 33, no. 1, pp. 256–266, Jan. 2009.

[115] K. Nakanishi, T. Tadokoro, and R. Matsuno, “On the Specific Resistance of Cakes of Microorganisms,” *Chem. Eng. Commun.*, vol. 62, no. 1–6, pp. 187–201, Dec. 1987.

[116] K. W. Desmond and E. R. Weeks, “Influence of Particle Size Distribution on Random Close Packing,” *Phys. Rev. E*, vol. 90, no. 2, p. 022204, Aug. 2014.

[117] M. Taiebat, P. Mutabaruka, R. Pellenq, and F. Radjai, “Effect of particle size distribution on 3D packings of spherical particles,” *EPJ Web Conf.*, vol. 140, p. 02030, 2017.

[118] A. Rushton and H. E. Khoo, “The filtration characteristics of yeast,” *J. Appl. Chem. Biotechnol.*, vol. 27, no. 1, pp. 99–109, 1977.

[119] M. Schiavone *et al.*, “Evidence for a Role for the Plasma Membrane in the Nanomechanical Properties of the Cell Wall as Revealed by an Atomic Force Microscopy Study of the Response of Saccharomyces cerevisiae to Ethanol Stress,” *Appl. Environ. Microbiol.*, vol. 82, no. 15, pp. 4789–4801, Jul. 2016.

[120] M. Delarue *et al.*, “Self-Driven Jamming in Growing Microbial Populations,” *Nat. Phys.*, vol. 12, no. 8, pp. 762–766, Aug. 2016.

[121] J. D. Stenson, P. Hartley, C. Wang, and C. R. Thomas, “Determining the mechanical properties of yeast cell walls,” *Biotechnol. Prog.*, vol. 27, no. 2, pp. 505–512, Apr. 2011.

[122] A. V. Kyrylyuk, M. A. van de Haar, L. Rossi, A. Wouterse, and A. P. Philipse, “Isochoric ideality in jammed random packings of non-spherical granular matter,” *Soft Matter*, vol. 7, no. 5, pp. 1671–1674, Feb. 2011.

[123] A. Wouterse, S. Luding, and A. P. Philipse, “On contact numbers in random rod packings,” *Granul. Matter*, vol. 11, no. 3, pp. 169–177, May 2009.

[124] L. Meng, P. Lu, S. Li, J. Zhao, and T. Li, “Shape and size effects on the packing density of binary spherocylinders,” *Powder Technol.*, vol. 228, pp. 284–294, Sep. 2012.

[125] S. R. Williams and A. P. Philipse, “Random packings of spheres and spherocylinders simulated by mechanical contraction,” *Phys. Rev. E*, vol. 67, no. 5, p. 051301, May 2003.

[126] G. T. Nolan and P. E. Kavanagh, “Random packing of nonspherical particles,” *Powder Technol.*, vol. 84, no. 3, pp. 199–205, Sep. 1995.

[127] D. M. E. Thies-Weesie and A. P. Philipse, “Liquid Permeation of Bidisperse Colloidal Hard-Sphere Packings and the Kozeny-Carman Scaling Relation,” *J. Colloid Interface Sci.*, vol. 162, no. 2, pp. 470–480, Feb. 1994.

[128] Q. Han, T. A. Trinh, and J. W. Chew, “Cake formation of bidisperse suspensions in dead-end microfiltration,” *J. Membr. Sci.*, vol. 577, pp. 31–40, May 2019.

[129] N. N. Kramadhati, M. Mondor, and C. Moresoli, “Evaluation of the shear-induced diffusion model for the microfiltration of polydisperse feed suspension,” *Sep. Purif. Technol.*, vol. 27, no. 1, pp. 11–24, Apr. 2002.

[130] H. Y. Sohn and C. Moreland, “The effect of particle size distribution on packing density,” *Can. J. Chem. Eng.*, vol. 46, no. 3, pp. 162–167, 1968.

[131] A. E. Smith, Z. Zhang, C. R. Thomas, K. E. Moxham, and A. P. J. Middelberg, “The mechanical properties of Saccharomyces cerevisiae,” *Proc. Natl. Acad. Sci. U. S. A.*, vol. 97, no. 18, pp. 9871–9874, Aug. 2000.

[132] G. K. Batchelor and J. T. Green, “The hydrodynamic interaction of two small freely-moving spheres in a linear flow field,” *J. Fluid Mech.*, vol. 56, no. 2, pp. 375–400, Nov. 1972.

[133] D. Leighton and A. Acrivos, “The shear-induced migration of particles in concentrated suspensions,” *J. Fluid Mech.*, vol. 181, pp. 415–439, Aug. 1987.

[134] M. Roco, *Particulate two-phase flow*, vol. 1002. Butterworth-Heinemann Boston, MA, 1993.

[135] J. F. Richardson and W. N. Zaki, “The sedimentation of a suspension of uniform spheres under conditions of viscous flow,” *Chem. Eng. Sci.*, vol. 3, no. 2, pp. 65–73, Apr. 1954.

[136] R. H. Davis and A. Acrivos, “Sedimentation of Noncolloidal Particles at Low Reynolds Numbers,” *Annu. Rev. Fluid Mech.*, vol. 17, no. 1, pp. 91–118, Jan. 1985.

[137] R. J. Phillips, R. C. Armstrong, R. A. Brown, A. L. Graham, and J. R. Abbott, “A constitutive equation for concentrated suspensions that accounts for shear-induced particle migration,” *Phys. Fluids Fluid Dyn.*, vol. 4, no. 1, pp. 30–40, Jan. 1992.

Annexes

I. Suspension balance model

In this annexe, we address the suspension balance model (SBM) as it related to the present study regarding particle behavior in filtration applications. The suspension balance model is conceived to explain particle migration phenomenon observed in shear flows, known as shear induced migration (SIM). This migration is ascribed to an inhomogeneous stress resulting from the presence of the particles in the suspension, which must be associated with either non-hydrodynamic or many-body interactions, e.g. between three particles or more, which are able to generate a deviation of the particles from their original streamlines to zones with lower shear rates. Batchelor and Green [132] demonstrated that the hydrodynamic interactions between particles doublets make them only rotate around the center of mass or pass by one another, returning to the original streamlines.

The SBM model was first proposed by Nott and Brady (1994) [60] and modified later by Morris and Boulay (1999) [61]. The phenomenon of SIM was recognized and described by Leighton and Acrivos (1987) [133], concluding that irreversible migration was necessary to explain a number of observations in suspension flow in a Couette viscometer. The work of Morris and Boulay demonstrate that a rheological approach in which shear-induced normal stresses provide the driving force for migration is able to explain the migration phenomena observed in curvilinear flows of concentrated suspensions.

Suspension balance modeling has been has been applied primarily to suspensions of monodispersed rigid spherical particles in Newtonian fluids, with some results applicable to general particle geometries and to polydisperse systems. The suspension behavior is considered in Stokes regime with $Re \rightarrow 0$ and $Pe \rightarrow \infty$:

$$Re = \frac{\rho \dot{\gamma} a^2}{\eta}; \quad Pe = \frac{3\pi\eta\dot{\gamma}a^3}{kT}$$

Eq. 29

where ρ and η are the fluid density and viscosity respectively, $\dot{\gamma}$ the shear rate, a the particles radius and kT the thermal energy. It is assumed that microstructural asymmetry necessary to generate anisotropic normal stresses exists at all volume fractions $0 < \phi < \phi_{max}$.

I.1. Mass and momentum conservation equations

The mixture of two phases is known as the bulk suspension. The bulk suspension is analyzed as a continuous medium. Just as each phase, the bulk suspension is subject to conservation equations. In the suspension balance model, the mass and momentum conservation equations are averaged for the particle phase. The general conservation equations are

$$\frac{\partial \rho}{\partial t} + \nabla . (\rho u) = 0$$

Eq. 30

$$\frac{\partial (\rho u)}{\partial t} + u . \nabla (\rho u) = \nabla . \sigma + b$$

Eq. 31

where $\sigma(x,t)$ represents the stress tensor and b the body forces and interparticle forces. The averaging process by Drew and Lahey [134] involves the phase indicator function φ that multiplies the conservation equations. In the particle phase $\varphi = 1$ and in the carrier phase $\varphi = 0$.

Multiplying by the configurational probability $P_N(x_N)$ and integrating over the configurations x_N the resulting particle phase conservation equations for mass and momentum, respectively, are:

$$\frac{\partial \phi}{\partial t} + \nabla . \langle \phi U_p \rangle = 0$$

Eq. 32

$$\rho_p \phi \frac{\partial U_p}{\partial t} + U . \nabla \big(\phi U_p \big) = \nabla . \big(\phi \langle \sigma \rangle_p \big) + n \langle F_H \rangle_p + \langle b \rangle_p - \nabla . \langle x' b' \rangle_p$$

Eq. 33

In Eq. 32 and Eq. 33, ϕ represents the particle volume fraction, $n = 3\phi / 4\pi a^3$ the particle number density, F_H is the hydrodynamic force on particles, $\langle x' b' \rangle_p$ is a stress resulting from interparticle forces, the notation $\langle \cdot \rangle_i$ means an average over the phase i, and primed quantities denotes a fluctuation from average. Eq. 33 can be written as:

$$\rho_p \frac{D(\phi U_p)}{Dt} = \nabla . \Sigma_p + n\langle F_H \rangle_p + \langle b \rangle_p$$

Eq. 34

I.2. Particle mass and momentum coupling

The particle momentum conservation equation at low Reynolds number and without external forces for neutrally buoyant particles yields

$$0 = \nabla . \Sigma_p - \frac{9\eta}{2a^2} \phi f^{-1}(\phi) \big(U_p - \langle u \rangle\big)$$

Eq. 35

where $\langle u \rangle$ is the local average velocity of the bulk suspension and $f^{-1}(\phi)$ is the inverse of the the sedimentation hindrance function and represents the mobility of the particle phase, often described by the standard model proposed by Richardson and Zaki in 1954 [135]:

$$f(\phi) = (1-\phi)^{\alpha}$$

Eq. 36

In the Stokes regime $Re_p = \rho_p \dot{\gamma}/\eta \to 0$, the term on the left hand side of Eq. 34 and the term associated with Reynolds stress in Σ_p scale with Re_p in the dimensionless form of the equation. Another form of the hindrance function from Davis and Acrivos 1985 [136] with dependence in the maximum volume fraction:

$$f(\phi) = \left(1 - \frac{\phi}{\phi_m}\right)(1-\phi)^{\alpha-1}$$

Eq. 37

From Eq. 34 and knowing that the particle flux $j = \phi U_p$ one obtains:

$$j = \phi\langle u \rangle + \frac{2a^2}{9\eta} f(\phi)\, \nabla . \Sigma_p$$

Eq. 38

and for the perpendicular component which correspond to the migration flux j_m:

$$j_m = \phi U_p - \phi\langle u\rangle = \frac{2a^2}{9\eta} f(\phi)\,\nabla.\Sigma_p$$

Eq. 39

Thus the final form of the mass conservation equation is

$$\frac{\partial\phi}{\partial t} + \nabla.\langle\phi U_p\rangle = -\nabla.\left[\frac{2a^2}{9\eta} f(\phi)\nabla.\Sigma_p\right]$$

Eq. 40

I.3. Rheological model for Σ_p

In this model the total stress Σ is decomposed into the fluid phase stress Σ_f and particle phase stress Σ_p. The fluid phase stress is defined as:

$$\Sigma_f = -P_f\boldsymbol{I} + 2\eta_0\boldsymbol{E}$$

Eq. 41

where $\boldsymbol{E} = 1/2\ (\nabla\langle u\rangle + (\nabla\langle u\rangle)^{\mathrm{T}})$ is the local rate of stress tensor, P_f is the local fluid pressure and η_0 is the fluid viscosity. The particular phase contribution to the stress is defined as:

$$\Sigma_p = -\eta_0\dot{\gamma}Q(\phi) + 2\ \eta_0\eta_p(\phi)\boldsymbol{E}$$

Eq. 42

For η_p, the particle contribution to the shear viscosity made dimensionless with η, the shear rate $\dot{\gamma} = (2E{:}E)^{1/2}$ and the normal stresses are introduced by the property tensor Q, defined as follows:

$$Q(\phi) = \eta_n(\phi)\begin{pmatrix} 1 & 0 & 0 \\ 0 & \lambda_2 & 0 \\ 0 & 0 & \lambda_3 \end{pmatrix}$$

Eq. 43

Here $\eta_n(\phi) = \Sigma_{12}^p/\eta\eta$ represents the "normal stress viscosity" and $\lambda_2 = \Sigma_{22}^p/\Sigma_{11}^p$ and $\lambda_3 = \Sigma_{33}^p/\Sigma_{11}^p$ parameters represent ratios of any two particles contributions to bulk normal stress also known as anisotropy parameters. The standard convention 1, 2, 3 represents the flow, gradient and vorticity directions [61]. The particle pressure is given by the expression:

$$\Pi = -\frac{1}{3} tr\Sigma_p = \eta\eta_n\gamma\left(\frac{1+\lambda_2+\lambda_2}{3}\right)$$

Eq. 44

The normal viscosity of the bulk suspension was modeled by Morris and Boulay as :

$$\eta_n = K_n\overline{\phi^2}(1-\bar{\phi})^{-2}$$

Eq. 45

where $\bar{\phi} = \phi/\phi_{max}$ and K_n is a fitting parameter that was set to 0.75 based on a fit to data in a migrated suspension [137].

II. Experiments reproducibility for the filtration of monodispersed spherical particles

The reproducibility of the experiments was investigated. The statistics are done for three experiments and the results are presented for the filtration using C4Pe20 units as they are the used for later comparison with the other suspensions in Chapter V Section I.III. The filtration performance for C4Pe20 units is used as a reference for comparison as the formed cakes exhibited the closest behavior to yeast cakes, i.e. more compact cake.

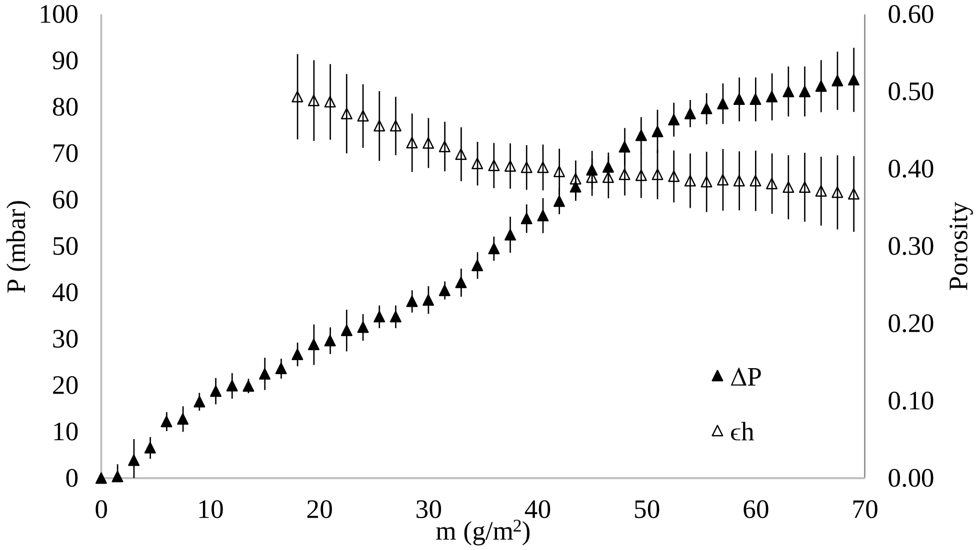

Figure 86. Pressure and porosity variation as a function of the deposited mass per unit filter surface

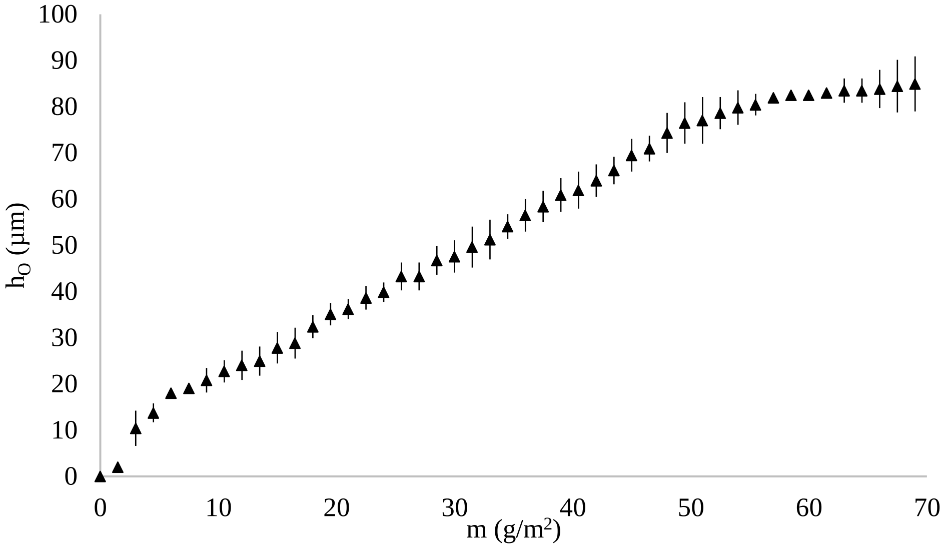

Figure 87. Cake growth as a function of the deposited mass per unit filter surface

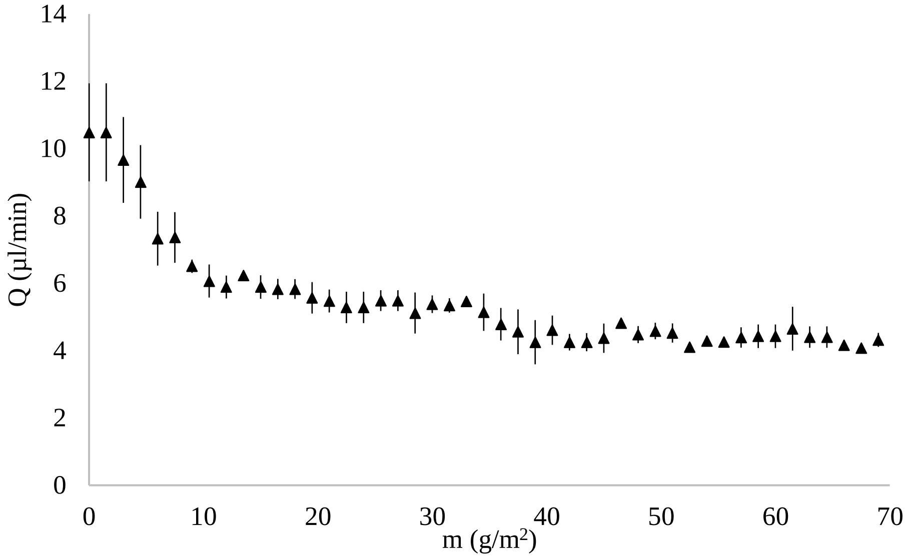

Figure 88. Flowrate reduction throughout the filtration

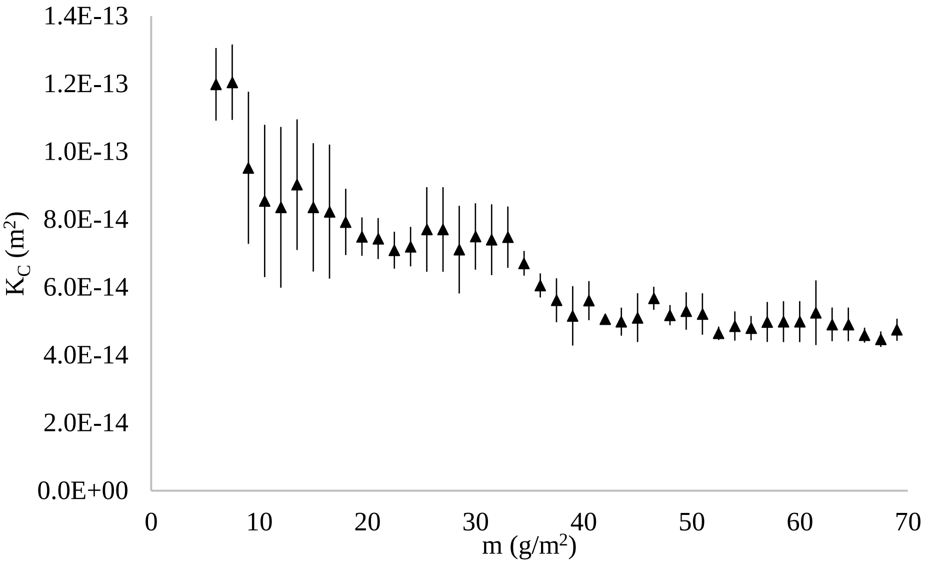

Figure 89. Permeability evolution as a function of the deposited mass per unit filter surface

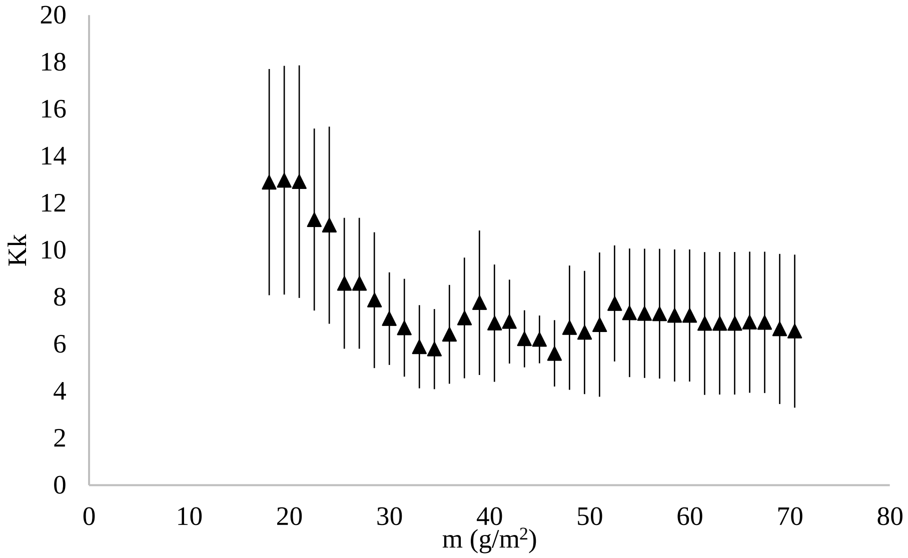

Figure 90. Evolution of K_K throughout the filtration

III. Upper filtration monitoring using confocal microscopy (CLSM)

In-situ situ direct observation of the filtration of a model particle suspension is conducted to explore the confocal microscopy performance of the new Leica SP8 equipment. The new Leica SP8 could lead to enhanced acquisition (compared to previous work [25]) velocities that could allow a dynamic investigation of the filtration.

III.1. Materials

In order to achieve direct real time observation, a specialized micro-filtration module is used (developed in the previous work of Ben Hassan [25]). This module allow the filtration observation using CLSM. The module is in stainless steel and consist in a channel of 60 mm long, 5.18 mm in width and 0.25 mm in height. The system is adapted for commercial microfiltration membranes (Aquamarijn microsieve, Figure 91) and it is covered by a glass slide that allows the observation of the microsieve.

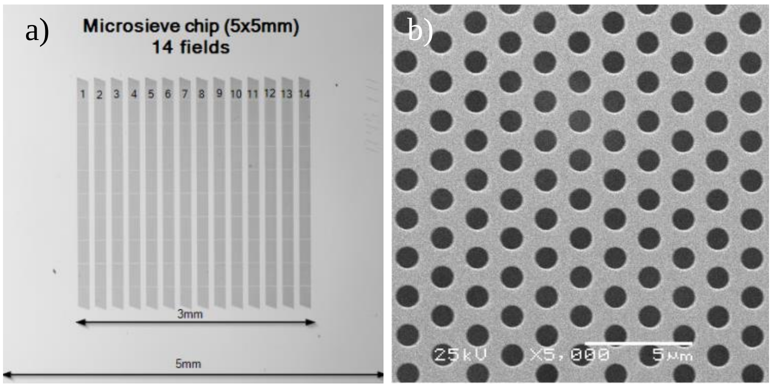

Figure 91. Aquamarijn microsieves.

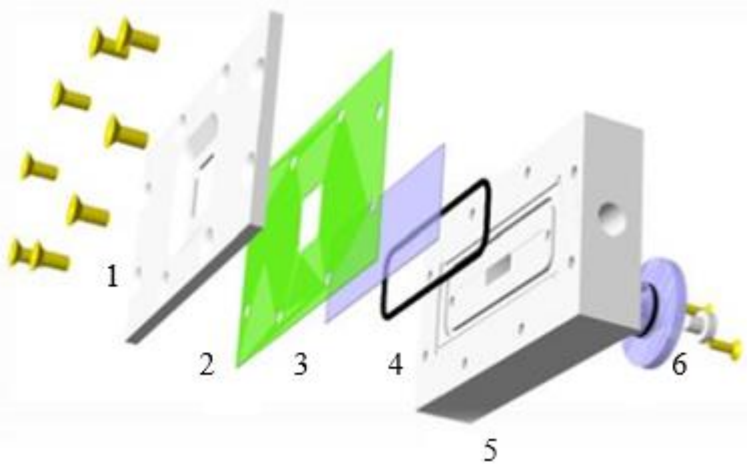

Figure 92. Micro-filtration chamber. 1) Cover, 2) Seal, 3) Glass slide, 4) Seal, 5) Chanel, 6) Microsieve platform

III.2. Protocol

Wettability of the system must be guaranteed; for that, membranes are previously treated with plasma hydrophilic coating and with isopropanol. Before each test, the system is cleaned with ultrapure water to avoid dust particles when the filtration is performed. The entire system is filled with ultrapure water and the gas is removed.

Having the system filled with water the flow is established using a peristaltic pump (Masterflex, Bioblock scientific, USA). The flow rate is set at 1ml/min and the reservoir is filled with the fluorescent model particle suspension. The system run until a constant pressure is reached, at this moment the reservoir valve is open and the suspension filtration starts.

Before starting the filtration, the acquisition is set. The desired microscope objective is selected. For this tests the 10x dry and the 63x water immersion objectives are used, the numerical aperture of the objectives are 0.4 and 0.9 respectively. The microscope is tuned up so the membrane is clearly located.

Particle deposition and the effective formation of one cake layer is observed. For 3D monitoring, the *z* domain must be defined and the spacing between the stack of *xy* planes must be set. Figure 93 shows the filtration monitoring set up.

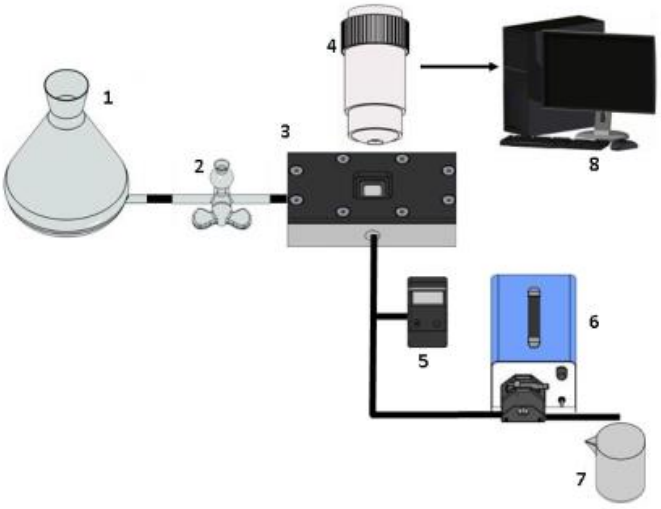

Figure 93. Upper monitoring set up. 1) Ultra-pure water reservoir, 2) Suspension reservoir, 3) Microfiltration chamber, 4) Microscope objective, 5) Manometer, 6) Pump, 7) Permeate, 8) Computer

III.3. Results

Upper filtration monitoring using confocal microscopy (CLSM) was tested for the observation of particle deposition over the membrane as well as the effective formation of multiple layers. Figure 94 shows the micro-filtration process at two different moments, it is possible to appreciate the increasing fouling phenomenon. Figure 94a and b show the increasing fouling at two different times using the 10x/0.4 dry objective while images c and d correspond to 63x/0.9 water objective.

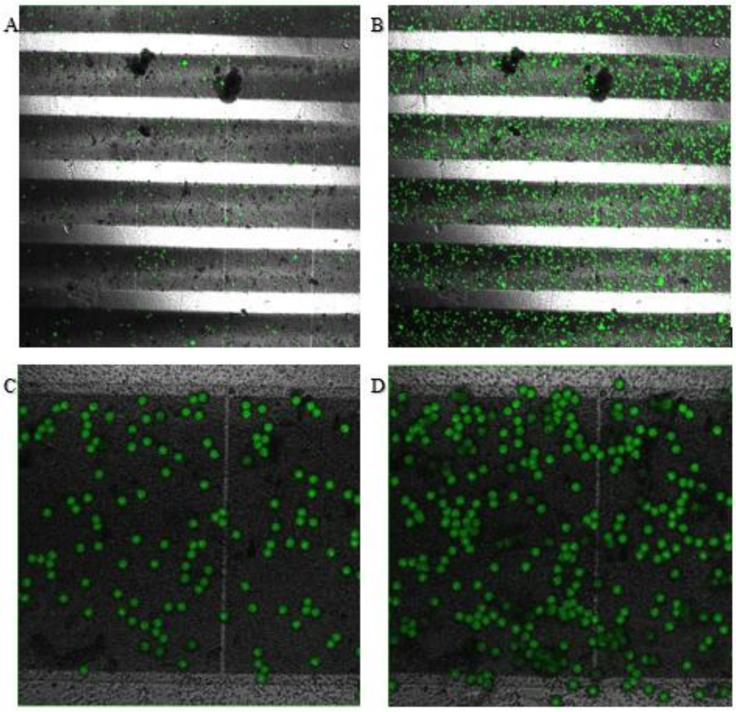

Figure 94. Filtration monitoring at different moments. a, b) x10/0.4 dry objective. c, d) x63/0.9 water objective.

The 3D data acquisition is limited by the scanning time. Different parameters must be set in order to scan the complete investigated domain. These parameters must be optimized in order to find a good compromise between the resolution and acquisition rate. In the conducted experiments, investigated domain remained limited to 15x15x30 µm (x, y z); the acquisition speed was fixed at 1800 Hz, which is the highest in terms of line scanning speed. The scanning pattern is set to bidirectional, which allows reducing the time for scanning the multiple *xy* plane. The pinhole was set to 0.38 AU in order to reduce the light reaching the detector knowing that the signal is strong enough and it could enhance the *z* resolution. This acquisition setting achieved an acquisition time of 20.58s for the entire investigated volume, with 50 *xy* planes scanned.

Not only the acquisition time remains insufficient for the dynamic characterization of particle deposition; in addition, the *z* resolution is low and objects exhibited a distortion of about 20 times the expected dimension. This distortion is mainly caused by the optical aberration induced by the glass (600 µm) in the observation window and it is accentuated when working with high scanning speed. It is possible to attenuate this distortion to achieve a better resolute image and with good acquisition time by reducing the thickness of the glass used for the observation window (170 µm thickness). In addition, finding a good compromise for the number of scanned *xy* planes per volume and the scanning speed should improve *z* resolution. Figure 95 shows a 3D capture from a video recording, where the 3D perception of the deposited particles at given instant is observed.

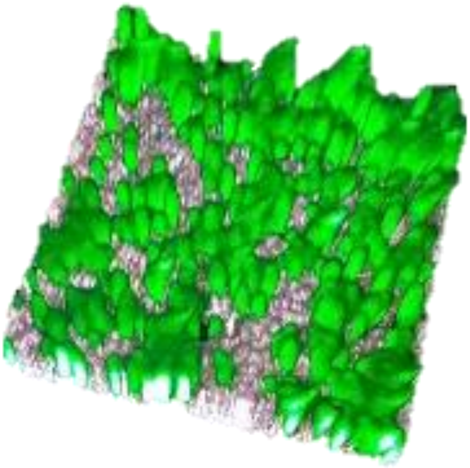

Figure 95. Capture from the 3D cake deposit. Taken from the video recording

III.4. Conclusion

Upper monitoring using CLSM proves to be an interesting *in-situ*, non-invasive technique to analyse filtration cake structure. An adapted observation window, glass thickness of 170 µm should led to a more resolute 3D acquisition. Regarding the acquisition rate, the Leica SP8 microscope is not adapted for capturing de dynamics of the phenomenon. Further tests using spinning disk confocal microscopy SDCLSM could lead to and enhanced acquisition rate. At least, an acquisition rate about 100 scanned volumes per second would be necessary to capture particles movement for low Reynold’s number.